In silico exploration of post-burn contraction using uncertainty quantification

Egberts, G.

DOI
10.4233/uuid:678bd7d9-8aac-4644-b058-2aa8000d7811

Publication date
2023

Document Version
Final published version

Important note
To cite this publication, please use the final published version (if applicable).
Please check the document version above.
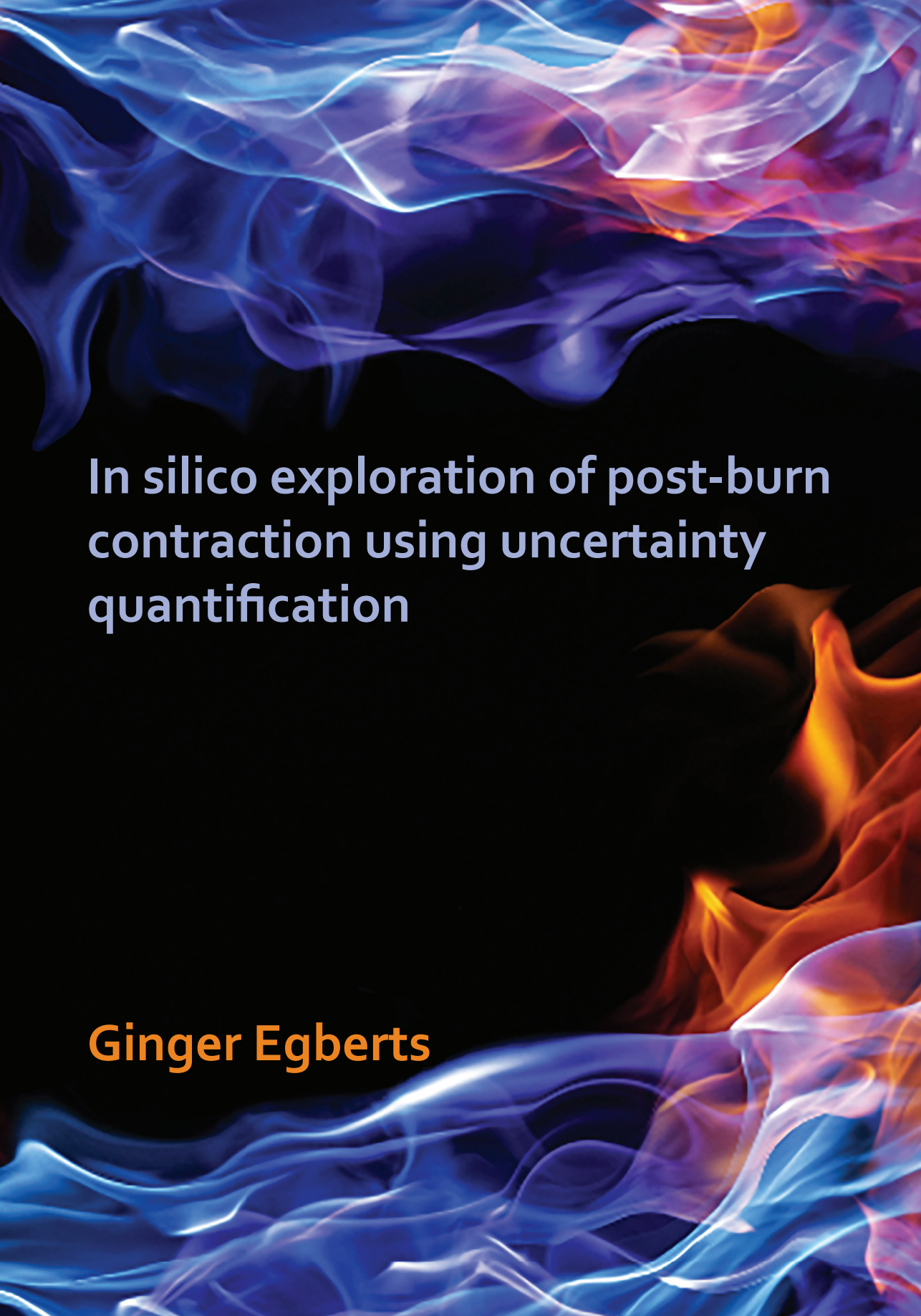
In silico exploration of post-burn contraction using uncertainty quantification

Ginger Egberts

In silico exploration of post-burn contraction using uncertainty quantification

In silico exploration of post-burn contraction using uncertainty quantification

Dissertation

for the purpose of obtaining the degree of doctor
at Delft University of Technology, The Netherlands,
by the authority of the Rector Magnificus, prof. dr. ir. T.H.J.J. van der Hagen,
chair of the Board for Doctorates,
to be defended publicly on
Monday 18 September 2023 at 12:30 o'clock

by

Ginger EGBERTS

Master of Science in Mathematics, Leiden University, the Netherlands
born in Utrecht, the Netherlands

Composition of the doctoral committee:

Rector Magnificus,	chairman
Prof. dr. ir. C. Vuik,	Delft University of Technology, promotor
Prof. dr. ir. F.J. Vermolen	Hasselt University, promotor
Prof. dr. P.P.M. van Zuijlen	Vrije Universiteit Amsterdam, promotor

Independent members:

Prof. dr. I. van Nieuwenhuyse	Hasselt University
Prof. dr. E. Middelkoop	Amsterdam UMC
Prof. D. Weihs	Technion University
Prof. dr. A.A. Zadpoor	Delft University of Technology
Prof. dr. H.M. Schuttelaars	Delft University of Technology, reserve member

In addition, the dissertation is for the purpose of obtaining the degree of doctor of sciences: Mathematics at the Hasselt University, Belgium.

When I saw him lying there with his burns, I felt helpless. Could I mean more than a concerned mother? I started this research with which I can contribute; for that, I will always be grateful.

Summary

Burns can make patients' lives quite miserable. Apart from prominent and thickened, or hypertrophic, scars, the skin may be characterized by contraction. When this contraction is so severe that the patient loses joint mobility, it is called *contracture*. Then a patient may have difficulties with sports or other daily activities. The consequence can be an enormous psychosocial burden for the patient.

Understanding contraction mechanisms is essential to improve and optimize the treatment of contractures. This understanding can arise from clinical (in vivo) and experimental (in vitro) observations but can also be explored using mathematical models (in silico). Mathematical models describe quantitative relations and can explain specific trends and make predictions. Further, in silico models form an alternative for animal experiments. One such mathematical model is the *Biomorphoelastic model for post-burn contraction* [1]. This model arises from conservation laws expressed in partial differential equations on a continuous (macro) scale. We study this model's one- and two-dimensional counterparts.

The biomorphoelastic model for post-burn contraction has multiple steady states, of which some are unstable for specific parameter values. Therefore, we need a control system to stabilize and control the process at and around the steady states. In this work, we predict stability around steady states using linearized models and apply multivariate analysis to assess the local behavior around these steady states. This way, we avoid the parametric dependence of stable and unstable solutions and explain the a priori behavior of the solution. The results show that so-called signaling molecules (growth factors, cytokines, chemokines) involved in wound healing should decay quickly enough for the model to be stable. Slow signaling molecule decay results in lasting signaling, causing continued differentiation of cells that contract the tissue and increased collagen deposition that we link to hypertrophic scarring. Furthermore, the model's convergence is monotonic, except for low viscosity values, and the numerical method has convergence order at least $\mathcal{O}(h^2)$.

There is much variation in the physiological properties of patients, therefore, giving an enormous uncertainty in post-burn contraction. One wonders, for example, why one patient develops a severe contracture and another does not. For the modeling, this is expressed in patient-specific values of the model's input parameters, which give a patient-specific set of output variables. A significant challenge is that many patient-specific input parameter values still need to be discovered and better or more consistently documented in the literature. After all, measurements always contain uncertainty or a margin of error. It is, therefore, necessary to include uncertainty in the modeling.

We assume statistical distributions for the model's input parameters and base these on data from the literature and intuitive arguments. First, we explore the uncertainty in these input parameters by performing a sensitivity analysis. With the sensitivity analysis, we explore to what extent the outcome variables are subject to change when pa-

rameter values are varied and whether the model can make patient-specific contraction predictions. The analysis shows that parameter sensitivity significantly depends on cell proliferation rates. If the proliferation rates are equal for different cells, then the equilibrium collagen concentration significantly affects the outcome variables. This result leads to the discussion of whether we need to make the distinction between different collagen types. The analysis using unequal cell proliferation rates draws attention to the actual contraction mechanism (on a cellular level), and it discusses to what extent tissue contraction cells (myofibroblasts) proliferate. Further, the analysis provides advice for therapies. One should focus on the dermal cells and collagen to limit contraction during 'early' healing. However, to limit scar contraction, one should focus on post-burn signaling. Further, by performing a feasibility study, we show that the model can show significantly different contraction intensities for different groups of parameter values. The groups are chosen to relate to patients of different ages.

A single simulation only provides a possible insignificant scenario from a probabilistic point of view. Therefore, we perform extensive simulations to estimate the mean outcomes, spreads, and statistical distributions for courses of contraction and patient discomfort in the first year after the burn. By drawing samples from the input parameters' statistical distributions, we perform Monte Carlo simulations to further explore these input parameters' uncertainty. With these Monte Carlo simulations, we determine correlations between the outputs and inputs and gain further insight into the reciprocal dependencies. Through the computations, we treat the output statistically by using histograms to model probability density functions, which provide graphical insight into the statistical distribution of the output variables. We then statistically test whether the outcome follows a particular probability distribution. For example, we use the output data to estimate the probability that the post-burn contraction will be more than a certain percentage. This uncertainty quantification method is a significant amount of work translating into computer-intensive computations, and, therefore, we approach the output variables with Bayesian finite-element trained machine learning as an alternative. For this, we use relatively small neural networks that give over 99.5% goodness of fit and spectacular computational accelerations (19354X speedup in 1D and 1815000X speedup in 2D) compared to the numerical approach. We further illustrate the use of these neural networks in an 'online' application. This application shows how clinicians can be offered immediate and quick access to finite element simulations and quick estimation of the probability distribution of the severity of post-burn contraction. In addition to that, this application makes such estimations accessible to clinicians.

In short, we use a mathematical model that simulates post-burn contraction and patient discomfort. We study the stability of this model and quantify the uncertainties in input parameter values through sensitivity analyses and Monte Carlo studies. Because Monte Carlo simulations are computationally intensive, we approximate the output variables with neural networks and demonstrate its application. The model is stable when signaling molecules disappear from the tissue quickly enough. Furthermore, it is discussed whether different collagen types should be added to the model and to what extent tissue-contracting myofibroblasts proliferate (cell division).

Samenvatting

Brandwonden kunnen het leven van patiënten behoorlijk ellendig maken. Afgezien van prominente en verdikte of hypertrofische littekens, kan de huid worden gekenmerkt door contractie. Wanneer deze samentrekking zo hevig is dat de patiënt de gewrichtsmobiliteit verliest, wordt dit *contractuur* genoemd. Dan kan een patiënt moeite hebben met sporten of andere dagelijkse bezigheden. Het gevolg kan een enorme psychosociale belasting voor de patiënt zijn.

Het begrijpen van samentrekkingsmechanismen is essentieel om de behandeling van contracturen te verbeteren en te optimaliseren. Dit begrip kan voortkomen uit klinische (in vivo) en experimentele (in vitro) waarnemingen, maar kan ook worden onderzocht met behulp van wiskundige modellen (in silico). Wiskundige modellen beschrijven kwantitatieve relaties en kunnen specifieke trends verklaren en voorspellingen doen. Verder vormen in silico modellen een alternatief voor dierproeven. Een zo'n wiskundig model is het *Biomorpho-elastic model for post-burn contraction* [1]. Dit model komt voort uit behoudswetten uitgedrukt in partiële differentiaalvergelijkingen op continue (macro)schaal. We bestuderen de een- en tweedimensionale tegenhangers van dit model.

Het biomorfo-elastische model voor contractie na verbranding heeft meerdere stabiele toestanden, waarvan sommige onstabiel zijn voor specifieke parameterwaarden. Daarom hebben we een controle systeem nodig om het proces in en rond de stationaire toestanden te stabiliseren en te beheersen. In dit werk voorspellen we stabiliteit rond stabiele toestanden met behulp van gelineariseerde modellen en passen we multivariate analyse toe om het lokale gedrag rond deze stabiele toestanden te beoordelen. Op deze manier vermijden we de parametrische afhankelijkheid van stabiele en onstabiele oplossingen en verklaren we het a priori gedrag van de oplossing. De resultaten laten zien dat zogenaamde signaalmoleculen (groeifactoren, cytokines, chemokines) die betrokken zijn bij wondgenezing snel genoeg zouden moeten vervallen om het model stabiel te houden. Langzaam verval van signaalmoleculen resulteert in blijvende signalering, wat leidt tot een voortdurende differentiatie van cellen die het weefsel samentrekken en een verhoogde collageenafzetting die we in verband brengen met hypertrofische littekens. Bovendien is de convergentie van het model monotoon, behalve voor lage viscositeitswaarden, en heeft de numerieke methode een convergentievolgorde van ten minste $\mathcal{O}(h^2)$.

Er is veel variatie in de fysiologische eigenschappen van patiënten, wat een enorme onzekerheid geeft in de contractie na de brandwond. Men vraagt zich bijvoorbeeld af waarom de ene patiënt een ernstige contractuur ontwikkelt en de andere niet. Voor de modellering wordt dit uitgedrukt in patiënt-specifieke waarden van de invoerparameters van het model, die een patiënt-specifieke set uitvoervariabelen opleveren. Een belangrijke uitdaging is dat veel patiënt-specifieke invoerparameterwaarden nog moeten worden ontdekt en beter of consistenter moeten worden gedocumenteerd in de litera-

tuur. Metingen bevatten immers altijd onzekerheid of een foutmarge. Het is daarom noodzakelijk om onzekerheid in de modellering op te nemen.

We gaan uit van statistische verdelingen voor de invoerparameters van het model en baseren deze op gegevens uit de literatuur en intuïtieve argumenten. Eerst onderzoeken we de onzekerheid in deze invoerparameters door een gevoeligheidsanalyse uit te voeren. Met de sensitiviteitsanalyse onderzoeken we in hoeverre de uitkomstvariabelen aan verandering onderhevig zijn als parameterwaarden variëren, en of het model patiëntspecifieke contractievoorspellingen kan doen. De analyse laat zien dat parametergevoeligheid in belangrijke mate afhangt van cel-proliferatiesnelheden. Als de proliferatiesnelheden voor verschillende cellen gelijk zijn, heeft de evenwichtscollageenconcentratie een significante invloed op de uitkomstvariabelen. Dit resultaat leidt tot de discussie of we onderscheid moeten maken tussen verschillende soorten collageen. De analyse met behulp van ongelijke cel-proliferatiesnelheden vestigt de aandacht op het eigenlijke contractiemechanisme (op cellulair niveau) en bespreekt in welke mate weefselcontractiecellen (myofibroblasten) prolifereren. Verder geeft de analyse adviezen voor therapieën. Men moet zich concentreren op de dermale cellen en het collageen om contractie tijdens 'vroege' genezing te beperken. Om littekencontractie te beperken, moet men zich echter concentreren op signalering (van signaalmoleculen) na het verbranden. Verder laten we, door een haalbaarheidsstudie uit te voeren, zien dat het model significant verschillende contractie-intensiteiten kan laten zien voor verschillende groepen parameterwaarden. De groepen zijn zo gekozen dat ze betrekking hebben op patiënten van verschillende leeftijden.

Een enkele simulatie geeft slechts een mogelijk onbelangrijk scenario vanuit een probabilistisch oogpunt. Daarom voeren we uitgebreide simulates uit om de gemiddelde uitkomsten, spreidingen en statistische verdelingen voor het verloop van contractie en ongemak voor de patiënt in het eerste jaar na de brandwond te schatten. Door steekproeven te trekken uit de statistische verdelingen van de invoerparameters, voeren we Monte Carlo-simulates uit om de onzekerheid van deze invoerparameters verder te onderzoeken. Met deze Monte Carlo-simulates bepalen we correlaties tussen de uit- en invoer van het model en krijgen we meer inzicht in de onderlinge afhankelijkheden. Door de berekeningen behandelen we de uitvoervariabelen statistisch door histogrammen te gebruiken om kansdichtheidsfuncties te modelleren, die grafisch inzicht geven in de statistische verdeling van de uitvoervariabelen. Vervolgens testen we statistisch of de uitkomst een bepaalde kansverdeling volgt. We gebruiken de uitvoergegevens bijvoorbeeld om de kans in te schatten dat de contractie na het verbranden meer dan een bepaald percentage zal zijn. Deze methode voor het kwantificeren van onzekerheid is een aanzienlijke hoeveelheid werk die zich vertaalt in computer intensieve berekeningen, en daarom benaderen we de uitvoervariabelen met Bayesiaanse eindige-elementen getrainde machine learning als alternatief. Hiervoor gebruiken we relatief kleine neurale netwerken die meer dan 99,5% fitheid en spectaculaire rekenversnellingen opleveren (19354x versnelling in 1D en 1815000x versnelling in 2D) in vergelijking met de numerieke benadering. We illustreren verder het gebruik van deze neurale netwerken in een 'online' applicatie. Deze applicatie laat zien hoe clinici onmiddellijk en snel toegang kunnen krijgen tot eindige-elementensimulates en een snelle schatting van de waarschijnlijkheidsverdeling van de ernst van huidcontractie. Bovendien maakt deze applicatie dergelijke

schattingen toegankelijk voor clinici.

Kortom, we gebruiken een wiskundig model dat contractie na het verbranden en ongemak voor de patiënt simuleert. We bestuderen de stabiliteit van dit model en kwantificeren de onzekerheden in invoerparameterwaarden door middel van gevoeligheidsanalyses en Monte Carlo-onderzoeken. Omdat Monte Carlo-simulaties rekenintensief zijn, benaderen we de uitvoervariabelen met neurale netwerken en demonstreren we de toepassing ervan. Het model is stabiel als signaalmoleculen snel genoeg uit het weefsel verdwijnen. Verder wordt besproken of verschillende soorten collageen aan het model moeten worden toegevoegd en in hoeverre weefsel contracterende myofibroblasten prolifereren (celdeling).

Contents

1

General introduction

1.1 Burn injuries and dermal wound healing

Skin burns are a global problem and are the fifth most common cause of non-fatal childhood injuries. Yearly estimates are around 180 000 deaths and 11 million burn injuries that need medical care [2]. Burns are debilitating, life-threatening, and challenging to assess and manage.

There are many different classifications for burns. For example, a burn can be thermal, electrical, or chemical. Burns are so different from other wound types that there is a separate discipline for this class in medical care. Burns come with a generalized increase in capillary permeability because of heat effects and damage. This increase in capillary permeability is not seen in any other type of wound [3]. Further, almost all full-thickness burns leave no skin tissue behind, which leads to scarring.

Post-burn scars may be immature / mature, atrophic / hypertrophic / keloid, stable / unstable, depigmented (vitiligo) / hyperpigmented, and may also turn malignant [4]. In addition, scars are subject to change. For example, an immature scar can mature, and an atrophic scar can become hypertrophic. Post-burn scars are dry and itchy and need prevention from sunlight exposure.

In recent decades, healthcare has made significant progress so that today, patients can survive even severe burns. However, these injuries will still significantly impact the quality of human life because of aesthetic reasons and the contractions that result from them. Physical, mental, and social complications after a burn can include shock, infection, extreme pain, loss of energy, and prolonged stress. Besides slow wound healing, the prevention of hypertrophic scars and contractures, which always cause a reduction in patient mobility, are significant challenges in burn treatment [5].

In general, the wound healing process comprises four partly overlapping phases that usually act upon each other quickly. The first phase, hemostasis, begins almost immediately after injury and aims primarily at stopping bleeding and initiating the subsequent response. Burn wound healing passes over hemostasis by cause of burning and cauterization of blood vessels. Hence burn wound healing comprises the remaining partly

1

overlapping phases, which are inflammation (reactive), proliferation (reparative), and maturation (remodeling). Within several hours after injury, immune cells clear contaminants and pathogens and prepare the wound for further protection from bacterial infection (the inflammatory response). The secreted growth factors that play a significant role stimulate cells to migrate from the intact peripheral dermis and subcutaneous tissue[1] to the wound. This migration is a hallmark of proliferation; the cells multiply in the wound area.

The subprocesses during the proliferative phase are re-epithelialization (wound closure), angiogenesis[2], fibroplasia, and wound contraction. Re-epithelialization describes the resurfacing of a wound with new epithelium (protective layer). The cellular and molecular processes involved in initiating, maintaining, and completing epithelialization are essential for successful wound closure [6]. Sometimes, re-epithelialization never completes. Limited or no dermal tissue, including the vital collagen, cells, and vascular networks, remains in deep burns. Usually, those wounds will require surgery (skin transplantation) to close the wound.

Fibroplasia encompasses the sub-processes that cause the restoration of the presence of fibroblasts (cells) and the production of a new temporary extracellular matrix (ECM) in the injured area (granulation tissue). Collagen type III fills the granulation tissue as a provisional matrix early. Fibroblasts are the most common cell type in the dermis and the essential cells in connective tissues. Fibroblasts are responsible for the synthesis of all ECM elements (collagen production) and can differentiate into myofibroblasts (a fibroblast phenotype) stimulated by transforming growth factor β [7]. Myofibroblasts are responsible for pulling forces in the skin and stimulate, like fibroblasts, both the production of the new collagen-rich ECM and the release of matrix metalloproteinases (MMPs). The group of MMPs can break down every type of collagen found in human tissue and cleave many signaling molecules (cytokines and growth factors) and their receptors [8, 9]. Myofibroblasts produce a large amount of collagen type III, which the cells attach to and exert tensile forces. These cell-tensile forces cause the tissue to contract. Usually, myofibroblasts disappear by apoptosis when the wound closes [10]. If myofibroblasts persist in a closed wound, they keep exerting tensile forces and show the development of a hypertrophic scar [11]. The spongy collagen III fibrin network is replaced with a firm matrix by regenerating collagen type I at a later stage (remodeling). This last phase, in which the scar matures and attains a balanced structure, can take years. The resulting scar has, on average, 50% strength of unwounded skin (within three months) and 80% on the long-term [12, 13].

1.2 Post-burn contraction

Interestingly, the wound healing process does not stop if the wound is closed. Fibroblasts, myofibroblasts, and collagen deposition play an essential role in post-burn contraction, which is one of the common post-burn complications and usually occurs after healing partial or full-thickness burns. Contraction is an active biological process that

---

[1]The skin is the largest organ of our body and it is also a complicated organ. The skin typically consists of several layers: the top layer is the epidermis, the middle layer is the dermis, and the bottom layer is the subcutis.

[2]Angiogenesis is the physical process through which new blood vessels form from pre-existing vessels.

decreases an area of skin loss in an open wound because of a concentric reduction in the wound's size [4]. In the proliferative phase of wound healing, contraction processes until full scar maturation, after which contraction can become active again. Wound contraction is yet visible in minor wounds: the wound's edges pull in, the wound size reduces, and the wounded area deforms. In adult patients, wounds can become 20–30% smaller over several weeks [14]. Skin contraction occurs in the dermal layer of the skin (the dermis). Myofibroblasts pull on their immediate environment, and because the cell density is large around the injured edges, these edges go 'inward', reducing and deforming the environment.

In principle, contraction is a good phenomenon because it decreases the outer surface area of the wound and hence reduces the possible ingress of contaminants and infectious pathogens. However, it can continue, making it not a solution but a problem for victims of severe burns.

In severe cases, post-burn contraction takes such a large extent that it can cause lifelong limited joint mobility. For example, elbow mobility can be limited because of post-burn contraction, as shown in Figure 1.1.
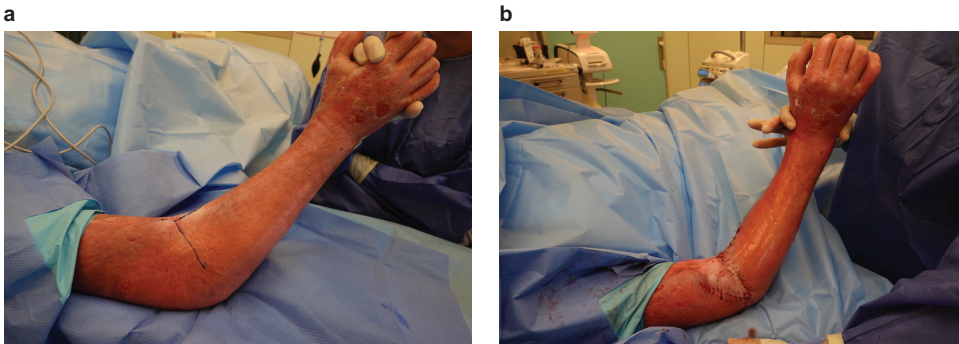
Figure 1.1: Post-burn contraction in an elbow can lead to contracture. The figure shows that the scar tissue is under tension, preventing the patient from stretching the arm. In Figure **a**, we see the marks where the scar tissue is cut open, after which the arm can be stretched further. In Figure **b**, we see a piece of skin placed in the resulting opening. The inserted healthy skin will stretch over time, eventually allowing full elbow function. The figure is published with the consent of the patient.

Patients may have difficulty exercising or with simple daily activities without medical care. In these cases, one refers to a contracture for which we wish to prevent its development because, mostly, contractures need surgery (scar reconstruction). Reported prevalence of burn scar contractures are 58.6% at 3–6 weeks and 20.9% at 12 months post reconstructive surgery after burns.

1.3 Mathematical modeling

Various scientific disciplines study the prevention of contractures, including biology, the medical sciences, and mathematics. The theory of the physiological evolution of burned skin contains quantitative connections that can be represented in mathematical relations. For a couple of decades, several mathematical model frameworks have been set

1

up to predict the evolution of post-wounding skin. These models predict the behavior of experimental and clinical wounds and gain insight into which elements of the wound healing response might substantially influence the contraction [14–20]. Further, the mathematical models provide an alternative for animal experiments.

The majority of the models can be placed into one of three categories: continuum hypothesis-based models, discrete cell-based models, and hybrid models [17]. Here, discrete cell-based models consider individual cell interactions compared to the continuum models that consider cellular densities in a tissue. *Hybrid modeling* is classically defined as coupling a continuous approach with a discrete one to model a complex phenomenon that cannot be described in a standard homogeneous way, mainly because of its inherent multiscale nature [21]. One subcategory of the continuum (partial differential equations–based) hypothesis-based models is the mechano-(bio)chemical model. This formalism and the hybrid model provided the basis for the biomorphoelastic model we use in this study, which Koppenol developed together with Vermolen [1]. This model can simulate permanent wound contraction and reproduce the trends observed in real data.

1.4 Motivation and objectives

There are many developed outcome measures to evaluate contractures and their treatment. However, there are currently no clear indicators for the development of contractures, and it is challenging to alter the post-burn contraction intensity. A better understanding of the post-burn contraction mechanisms might improve its treatment and provide unknown indicators for contractures. Many people have researched the mechanisms in vivo, in vitro, and in silico; however, much remains to be discovered. Today we can predict permanent contraction with the biomorphoelastic model. Therefore, this model is ideally suited to further study the already added mechanisms of contraction.

The equations of the biomorphoelastic model for post-burn contraction are nonlinear and multivariate. Further, multiple steady states are possible. Unfortunately, some of the steady states might be unstable for specific parameter values, thus requiring a control system to stabilize and control the process at and around the steady states. Therefore, one objective of this thesis is to avoid the parametric dependence of stable and unstable solutions and to understand the a priori behavior of the solution. Our method predicts stability around steady states using linearized models and applying multivariable analysis to assess the local behavior around these steady states.

Further, the biomorphoelastic model for post-burn contraction compromises many parameters. Some parameter values are known, while others are unknown and must be estimated. Although an excellent overview of parameter values has been provided [1], parameter values vary between patients and even along a piece of the skin sample. Therefore, two other objectives of this thesis are to show to what extent the model's outcomes are subject to change when parameter values are varied and whether the model can make patient-specific contraction predictions.

The dependency of post-burn contraction on burn wound dimensions (size, depth, location) and patient-specific factors (age, gender, amongst other factors) is a reason for the growing interest in personalized healthcare. To achieve personalized healthcare, we need many model-based predictions. With the detailed biomorphoelastic model

for post-burn contraction, we can show which elements significantly influence contraction, tune these elements, and access the uncertainty by performing Monte Carlo simulations. However, although this method allows for patient-based predictions that can support medical staff in decision-making, there is a downside. To include wound depth, the model must simulate higher dimensions and deal with the curse of dimensionality, leading to even more computer-intensive computations. Hence, the final objective of this thesis is to speed up the predictions of post-burn scar contractions for medical purposes.

1.5 Dissertation outline

This thesis presents six studies based on publications. The mathematical model for which these studies were performed is first presented in Chapter 2, together with the boundary conditions, the applied numerical methods and implementation, and specific model outputs. The studies can be divided into three categories of studies performed in both 1D and 2D: stability analyses, sensitivity analyses, and the application of neural networks. It was decided to divide the thesis into three parts, leading to the following color-coded part and chapter outline.

Part I shows the **stability analyses** for the biomorphoelastic model for post-burn contraction. **Chapter 3** shows the stability analysis for the one-dimensional model and **Chapter 4** shows the stability analysis for the two-dimensional model. The results in these chapters contribute to Chapters 5 and 6.

Part II shows the **sensitivity analyses** for the biomorphoelastic model for post-burn contraction. **Chapter 5** shows the sensitivity analysis for the one-dimensional model and **Chapter 6** shows the sensitivity analysis for the two-dimensional model. The results in these chapters contribute to Chapters 7 and 8.

Part III shows the application of **neural networks** for predicting post-burn contraction. **Chapter 7** shows the neural network for the one-dimensional model and **Chapter 8** shows the neural network for the two-dimensional model.

This thesis concludes in Chapter 9.

2

The mathematical model

2.1 Introduction

In this thesis, we conduct several studies, all for the same mathematical model. We refer to this model as the *Biomorphoelastic model for post-burn contraction*. An extensive description of previously developed mathematical modeling frameworks that served as a basis for this model is given in chapter 2 in [17]. In summary, the biomorphoelastic model for post-burn contraction is an extension of the model developed by Olsen *et al.* [14]. This chapter briefly describes this extension and presents the model for different dimensions.

2.2 The basis of the model and extensions

The model developed by Olsen *et al.* [14] contains equations for fibroblasts, myofibroblasts, signaling molecules, and collagen. Furthermore, the dermal tissue is modeled as an isotropic linear viscoelastic solid. In this model, the fibroblasts are actively motile. In contrast, in the biomorphoelastic model for post-burn contraction, both fibroblasts and myofibroblasts are actively motile. The motivation for this is that Thampatty and Wang have previously shown that both cells are actively motile [22]. As for the random movement of cells, unlike other models, the modeling employs cell density-dependent Fickian diffusion instead of linear Fickian diffusion. The motivation for this is that Hillen and Painter [23] point out that it is far more likely that the random movement of cells depends on the density of these cells. Furthermore, the degradation of both signaling molecules and collagen is incorporated into the model employing proteolytic cleavage by a generic MMP instead of natural decay or very general enzymatic degradation, which were used in the model developed by Olsen *et al.* [14]. Finally, in the biomorphoelastic model for post-burn contraction, the dermis is modeled as an isotropic morphoelastic solid instead of an isotropic linear viscoelastic[1] solid.

---

[1]Viscoelasticity is the property of materials that exhibit both viscous (a measure of its resistance to deformation at a given rate) and elastic characteristics when undergoing deformation.

2.2.1 Morphoelasticity

The biomorphoelastic model for post-burn contraction has been designed for deep tissue injury in which at least the skin's dermal layer (the dermis) has been damaged. To understand morphoelasticity, we hold an elastic band at both ends and pull shortthe pulling results in a stretched elastic ban with a short-term tension. If we let go of the elastic band, it will likely spring back to its original length (elastic behavior); this depends on the applied stress. Now, we stretch the elastic band for a more extended period. The length to which the elastic band springs back then depends on how much we pull and how long we do. We assume the elastic band does not spring back to its original length and is permanently stretched (plastic behavior).

Morphoelasticity encompasses the complicated relations between the different states in one mechanical description. The processes leading to these states may occur simultaneously or consecutively. The theory affirms the existence of mappings between the body in its original state (the undeformed elastic band), the body in its zero stress state (the elastic band after releasing the pulling stress), and the body in its current state (the elastic band while it is actively pulled). With these mappings, it is possible to track the zero-stress state, which reflects the absence of elastic stresses, resulting in a description of the residual stresses after deformation.

The mapping is based on the following principle [24]: the total deformation is decomposed into a deformation because of growth or shrinkage and deformation because of mechanical forces. In a mathematical context, one considers the following three coordinate systems: $\mathbf{X}$, $\mathbf{X}_e(t)$, and $\mathbf{x}(t)$, which, respectively, represent the initial coordinate system, the equilibrium at time t that results because of growth or shrinkage, and the current coordinate system that results because of growth or shrinkage and mechanical deformation. Assuming sufficient regularity, the deformation gradient tensor is written by

$$\mathbf{F} = \frac{\partial \mathbf{x}}{\partial \mathbf{X}} = \frac{\partial \mathbf{x}}{\partial \mathbf{X}_e} \frac{\partial \mathbf{X}_e}{\partial \mathbf{X}} = \mathbf{A}\mathbf{Z}, \tag{2.1}$$

in which the tensor Z represents the deformation gradient tensor because of growth or shrinkage, and A represents the deformation gradient because of mechanical forces [24–26]. Figure 2.1 shows the overview of this mapping.

2.3 The (multidimensional) model

The beauty of the biomorphoelastic model for post-burn contraction is that we can simulate a permanent deformation resulting from post-burn contraction. The results are promising compared to actual real-life data.

The primary variable in this model is the displacement of the skin, i.e., the variable that makes us able to determine the surface of the damaged skin. Here we speak of *damaged skin*, which means both the wound and, in later stages, the scar since a wound and a scar is the same entity at a different time. The permanent dermal displacement is because of the morphoelastic change of the tissue. This displacement generates strains assumed to be infinitesimally small. In short, the model comprises a system of coupled, nonlinear partial differential equations (PDEs). Four equations represent biochemical quantities that play a significant role in skin repair after trauma, such as cell densities and concentrations of signaling molecules and collagen. The other equations track the entries of the
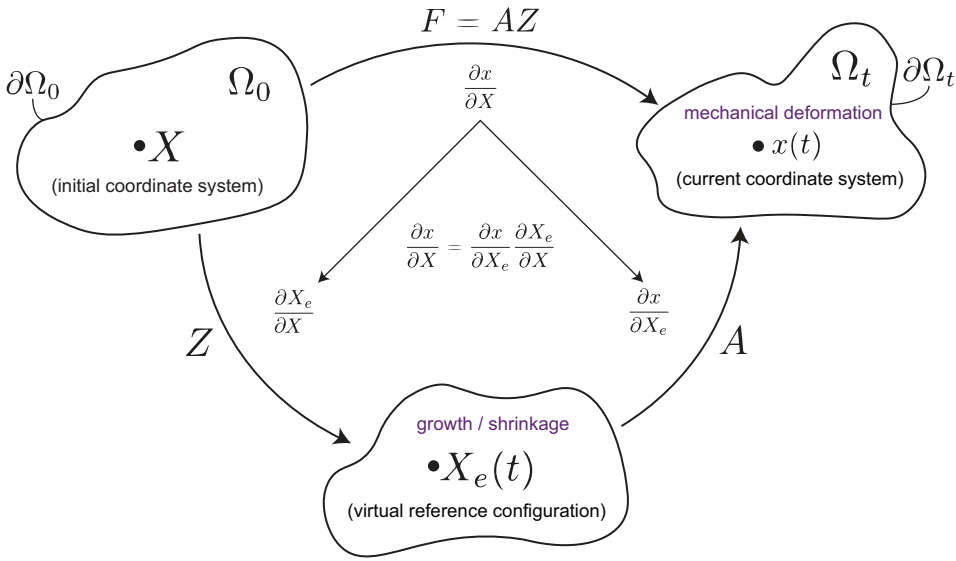
Figure 2.1: Overview of the mapping in morphoelasticity. The initial configuration is stress-free and has a coordinate system $\mathbf{X}$, domain Ω_0 and domain boundary $\partial\Omega_0$. To reach the current configuration with coordinate system $\mathbf{x}(t)$, domain Ω_t and domain boundary $\partial\Omega_t$, the deformation gradient tensor F is decomposed into the deformation gradient A and the deformation gradient tensor Z. The transition from the initial coordinate system and the current coordinate system goes through a virtual reference configuration (zero stress state) with coordinate system $\mathbf{X}_e(t)$. This configuration represents the equilibrium at time t that results from growth or shrinkage.

strain matrix and the components of the displacement velocity vector. The interaction between the model variables leads to a reduction in the wound/scar size.

In the following, we first show the model in a compact, multidimensional form. We discuss the conservation laws for mass and linear momentum and the evolution equation that describes how the infinitesimal effective Eulerian strain changes. Then, we show the equations in one-dimensional form. A significant advantage of the one-dimensional implementation is its short computation time, which allows one to do many simulations within a reasonable time interval.

Variables An essential model variable is the displacement ($\boldsymbol{u}$), i.e., the variable that allows us to determine the area of the wound and, in later stages, the scar. This variable is estimated using a set of other variables that we can divide into biochemical and mechanical. The biochemical variables are the fibroblast density (N), the myofibroblast density (M), the signaling molecule density (c), and the collagen density (ρ). Here we use *collagen* as a collective name for the molecules, fibrils, bundles of collagen, and different collagen types. We use *signaling molecules* as a collective name for growth factors, such as transforming growth factor beta (TGF-β), platelet-derived growth factor and connected tissue growth factor, and cytokines. The signaling molecules are essential in the immune and inflammation response after wound healing. While these molecules migrate to the wound, they induce directed chemotactic migration of cells. For the mechanics, we have

the displacement velocity ($\boldsymbol{v}$) and effective (remaining) Eulerian strain ($\boldsymbol{\varepsilon}$). The effective Eulerian strain is a local measure for the difference between the current and virtual dermal configurations (see Fig. 2.1). Note that we lose the bold fonts for one-dimensional variables.

Material time derivative and passive convection The model involves the material time derivative $\frac{\mathrm{D}z}{\mathrm{D}t} = \frac{\partial z}{\partial t} + \boldsymbol{v} \cdot \nabla z$ and passive convection $z(\nabla \cdot \boldsymbol{v})$, $z \in \{N, M, c, \rho, \boldsymbol{v}\}$. These concepts are introduced because the computational domain is subject to displacement because of the forces exerted by the cells.

2.3.1 The chemicals

The equations of the chemical response have the general form

$$\frac{\mathrm{D}z}{\mathrm{D}t} + z[\nabla \cdot \boldsymbol{v}] = -\nabla \cdot \mathbf{J}_z + R_z, \tag{2.2}$$

with $z \in \{N, M, c, \rho\}$. Here, $\mathbf{J}_z$ and R_z denote the flux and the biochemical kinetics of z, respectively. The fluxes for the (myo) fibroblasts result from random walk and chemotaxis, and the flux of the signaling molecules is only because of diffusion. These functional forms $\mathbf{J}_z$ are

$$\mathbf{J}_N = -D_n(N + M)\nabla N + \chi N \nabla c, \tag{2.3}$$

$$\mathbf{J}_M = -D_n(N + M)\nabla M + \chi M \nabla c, \tag{2.4}$$

$$\mathbf{J}_c = -D_c \nabla c. \tag{2.5}$$

Here, $D_{n/c}$ are the (myo) fibroblast and signaling molecule diffusion constants, and χ is the chemotactic parameter. Equations (2.3) and (2.4) represent migration towards the gradient of the signaling molecules [27–29] and cell density-dependent Fickian diffusion (random walk). Collagen molecules are assumed to have no active transport because they are large, reducing their diffusivity. Since collagen is extracellular, it is, next to diffusion, not subject to other active migration mechanisms. Hence, $\mathbf{J}_\rho = \mathbf{0}$.

The fibroblast proliferation depends on a generic chemokine via an activator/inhibitor mechanism [30]. Furthermore, myofibroblast differentiation only proceeds in the presence of the chemokine [11]. Cell death is taken into account via a linear relation. The myofibroblast dynamics are similar, except that it is assumed that myofibroblasts proliferate only in the presence of the signaling molecules:

$$R_N = r\left[1 + \frac{r^{\max}c}{a_c^I + c}\right][1 - \kappa(N + M)]N^{1+q} - k_1 cN - \delta_n N, \tag{2.6}$$

$$R_M = r\left[\frac{[1 + r^{\max}]c}{a_c^I + c}\right][1 - \kappa(N + M)]M^{1+q} + k_1 cN - \delta_m M. \tag{2.7}$$

Here, $r, r^{\max}$ and a_c^I are the (myo) fibroblast proliferation rate[2], proliferation enhance-

---

[2]In the current formalism, which we took from [1], the (myo) fibroblast proliferation rates are equal. It is well-known that myofibroblasts proliferate much less than fibroblasts [31], so we will later vary the myofibroblast proliferation rate regarding the fibroblast proliferation rate.

ment factor, and half-maximal enhancement factor, respectively. Further, κ is the crowding factor [32], q is a constant used to model equilibrium, k_1 is the differentiation factor[3] [11], and $\delta_{n/m}$ are the (myo) fibroblast apoptosis (cell death) rates.

The above form of the logistic growth forms needs more justification. We do not always know the exact mechanism behind many biological processes, let alone a quantitative description of such a biological mechanism. If others have developed a quantitative description, reliable estimates of parameter values are often lacking. So Koppenol has avoided using quadratic terms in the chemical parts of the model as much as possible unless there is a sound biological reason for this. Therefore, the growth of the (myo) fibroblasts is taken to the power $(1 + q)$ to make the model consistent.

The value of q is a necessary consequence of the other parameter values. Let, therefore, $\overline{N}, \overline{M}, \overline{c}$ define the fibroblast, myofibroblast, and signaling molecule equilibria, respectively. If we take $\overline{M} = 0$ and $\overline{c} = 0$ as the kinetic equilibrium, then solving the reactive term in equation (2.6) for δ_n yields:

$$\delta_n = r[1 - \kappa\overline{N}]\overline{N}^q. \tag{2.8}$$

The signaling molecule and collagen kinetics describe secretion by (myo) fibroblasts [34, 35], where signaling molecules enhance the collagen secretion [36]. Decay is because of cleavage by MMPs [8, 9] of which (myo) fibroblasts handle the release, and collagen [37]:

$$R_c = k_c\left[\frac{c}{a_c^{II} + c}\right][N + \eta^I M] - \delta_c\frac{[N + \eta^{II} M]\rho}{1 + a_c^{III} c}c, \tag{2.9}$$

$$R_\rho = k_\rho\left[1 + \left[\frac{k_\rho^{\max} c}{a_c^{IV} + c}\right]\right][N + \eta^I M] - \delta_\rho\frac{[N + \eta^{II} M]\rho}{1 + a_c^{III} c}\rho. \tag{2.10}$$

Here, $k_{c/\rho}$ are the signaling molecule and collagen secretion rates, and $a_c^{II/IV}$ their inhibition signaling molecule concentrations. Further, $k_\rho^{\max}$ is the collagen secretion enhancement factor [36], and a_c^{III} is the signaling molecule concentration inhibiting MMP release [38]. The parameters η^I and η^{II} represent the proportions of myofibroblasts in the maximum net secretion rates of the signaling molecules/collagen and MMPs, respectively. Further, $\delta_{c/\rho}$ are the coefficients describing decay because of MMP cleavage. The generic MMP affecting the above reaction kinetics is always assumed to be at a local equilibrium concentration. This modeling choice has avoided even more complexity and additional unknown parameter values.

Let $\overline{\rho}$ define the collagen equilibrium. Then, solving the reactive term in equation (2.10) for $\overline{\rho}$ yields $\overline{\rho} = \sqrt{k_\rho/\delta_\rho}$, hence

$$k_\rho = \delta_\rho\overline{\rho}^2 \tag{2.11}$$

is a necessary consequence for the value of k_ρ given the other parameter values.

2.3.2 The mechanics

Two PDEs capture the model mechanics for the displacement velocity and the effective Eulerian strain. The Cauchy stress tensor σ in the displacement velocity equation

---

[3]Although myofibroblasts can differentiate back to fibroblasts under the influence of Prostaglandin E$_2$ (PGE$_2$) [33], we do not consider the re-differentiation of myofibroblasts into fibroblasts.

is related to the effective Eulerian strain and displacement velocity gradients by a visco-elastic constitutive relation. The body force **f** is generated by a pulling force on the extracellular matrix (ECM) by myofibroblasts, which is proportional to the product of the myofibroblast cell density and a function of the collagen concentration[4]:

$$\rho_t \left(\frac{\mathrm{D}\boldsymbol{v}}{\mathrm{D}t} + \boldsymbol{v}[\nabla \cdot \boldsymbol{v}] \right) = \nabla \cdot \sigma + \mathbf{f} = \nabla \cdot \sigma + \nabla \cdot \left(\frac{\xi M \rho}{R^2 + \rho^2} \right) \mathbf{I}. \tag{2.12}$$

Here, ρ_t represents the total mass density of the dermal tissues, ξ is the generated stress per unit cell density and the inverse of the unit collagen concentration, and R is the *body force-inhibiting* constant. The above equation represents the balance of momentum. Although many studies neglect inertial effects (the first two terms), the inertia terms are kept to stay closer to the underlying physics.

The visco-elastic constitutive relation follows the assumption from Ramtani [40, 41], which incorporates the dependence of the Young's modulus of skin on the collagen density. From a mechanical point of view, the tissue is assumed to be isotropic and homogeneous, except for a dependency of the stiffness on the local collagen density:

$$\sigma = \mu_1 \mathrm{sym}(\nabla \boldsymbol{v}) + \mu_2 (\mathrm{tr}(\mathrm{sym}(\nabla \boldsymbol{v}))\mathbf{I}) + \frac{E\sqrt{\rho}}{1+\nu} \left[\boldsymbol{\varepsilon} + \mathrm{tr}(\boldsymbol{\varepsilon}) \frac{\nu}{1-2\nu} \mathbf{I} \right], \tag{2.13}$$

where μ_1 and μ_2 are the shear and bulk viscosities, $E\sqrt{\rho}$ represents Young's modulus (stiffness), and ν is the Poisson's ratio. Despite possibly large deformations in the tissue, linear elasticity is used to avoid the requirement of additional input parameters, of which the value is unknown or, at least, uncertain.

Permanent (plastic) deformation because of the tissue's microstructural changes is incorporated via morphoelasticity, of which the (multidimensional) derivation can be found in [24]. For the equation, a tensor-based approach was used that is also commonly used in the growth of tissues (such as tumors). The 'growth' contribution, which with a negative sign models contraction of the tissue, is assumed to be proportional to the product of the effective Eulerian strain, the (myo) fibroblast cell densities, and to be a function of the collagen density. In particular, the contraction tensor depends on the product of the MMP and the signaling molecule concentrations. It is inversely proportional to the collagen density (note that the collagen density drops out because of the linear dependence of the equilibrium MMP concentration on the collagen density):

$$\frac{\mathrm{D}\boldsymbol{\varepsilon}}{\mathrm{D}t} + \boldsymbol{\varepsilon}\mathrm{skw}(\nabla \boldsymbol{v}) - \mathrm{skw}(\nabla \boldsymbol{v})\boldsymbol{\varepsilon} + (\mathrm{tr}(\boldsymbol{\varepsilon}) - 1)\mathrm{sym}(\nabla \boldsymbol{v}) = -\zeta \frac{[N + \eta^{II} M]c}{1 + a_c^{III} c} \boldsymbol{\varepsilon}. \tag{2.14}$$

Here, ζ is the rate of morphoelastic change, i.e., the rate at which the effective strain changes actively over time.

---

[4]On a molecular basis, this myofibroblast pulling is the contraction mechanism which is the interaction between the actin and myosin filaments that generates their movement relative to one another [39].

2.3.3 The equations in one-dimensional form

The chemical PDEs in the one-dimensional form are:

$$\frac{\partial N}{\partial t} + \frac{\partial (Nv)}{\partial x} = -\frac{\partial}{\partial x}\left(-D_n(N+M)\frac{\partial N}{\partial x} + \chi N\frac{\partial c}{\partial x}\right) +$$
$$r\left[1 + \frac{r^{\max}c}{a_c^I + c}\right][1 - \kappa(N+M)]N^{1+q} - k_1 cN - \delta_n N, \quad (2.15)$$

for the fibroblasts,

$$\frac{\partial M}{\partial t} + \frac{\partial (Mv)}{\partial x} = -\frac{\partial}{\partial x}\left(-D_n(N+M)\frac{\partial M}{\partial x} + \chi M\frac{\partial c}{\partial x}\right) +$$
$$r\left[\frac{[1 + r^{\max}]c}{a_c^I + c}\right][1 - \kappa(N+M)]M^{1+q} + k_1 cN - \delta_m M, \quad (2.16)$$

for the myofibroblasts,

$$\frac{\partial c}{\partial t} + \frac{\partial (cv)}{\partial x} = D_c\frac{\partial^2 c}{\partial x^2} + k_c\left[\frac{c}{a_c^{II} + c}\right][N + \eta^I M] - \delta_c\frac{[N + \eta^{II}M]\rho}{1 + a_c^{III}c}c, \quad (2.17)$$

for the signaling molecules, and

$$\frac{\partial \rho}{\partial t} + \frac{\partial (\rho v)}{\partial x} = k_\rho\left[1 + \left[\frac{k_\rho^{\max}c}{a_c^{IV} + c}\right]\right][N + \eta^I M] - \delta_\rho\frac{[N + \eta^{II}M]\rho}{1 + a_c^{III}c}\rho, \quad (2.18)$$

for collagen. The mechanical PDEs in the one-dimensional form are:

$$\rho_t\left(\frac{\partial v}{\partial t} + 2v\frac{\partial v}{\partial x}\right) = \frac{\partial}{\partial x}\left(\mu\frac{\partial v}{\partial x} + E\sqrt{\rho}\varepsilon\right) + \frac{\partial}{\partial x}\left(\frac{\xi M\rho}{R^2 + \rho^2}\right), \quad (2.19)$$

for the displacement velocity, and

$$\frac{\partial \varepsilon}{\partial t} + v\frac{\partial \varepsilon}{\partial x} + (\varepsilon - 1)\frac{\partial v}{\partial x} = -\zeta\frac{[N + \eta^{II}M]c}{1 + a_c^{II}c}\varepsilon, \quad (2.20)$$

for the effective Eulerian strain.

2.4 The boundary conditions

We locate the xy-plane parallel to the skin's surface, and

$$v = \begin{bmatrix} v_1 \\ v_2 \end{bmatrix}, \quad \text{and} \quad \varepsilon = \begin{bmatrix} \varepsilon_{11} & \varepsilon_{12} \\ \varepsilon_{21} & \varepsilon_{22} \end{bmatrix}. \quad (2.21)$$

Variations over the depth of the skin are disregarded; hence the computations are done on an arbitrary skin depth. Such a configuration can approximate the kinetics of a wound on a non-curved body part, such as a patient's chest or back. Hence, we disregard all dependencies on the depth of the burn into the skin.

If we choose the domain and the initial conditions symmetrical, then the solution inherits this property because of the model's symmetry. Therefore, we can perform calculations on a reduced domain to benefit from a computational workload. We define the *computational domain* by $\Omega_{\mathbf{x}}$ and the *computational domain's boundary* by $\overline{\Omega}_{\mathbf{x}}$. We note that the distance from $\overline{\Omega}_{\mathbf{x}}$ to the modeled burn should be 'sufficiently large' because otherwise, there is too much variable diffusion nearby the boundary $\overline{\Omega}_{\mathbf{x}}$. Further, the computational domain implicitly depends on the time t given that $\mathbf{x} = \mathbf{x}(t)$. It is not allowed to specify any boundary conditions for ρ and $\boldsymbol{\varepsilon}$ because of overdetermination since the equations for ρ and $\boldsymbol{\varepsilon}$ are ordinary differential equations for time t.

Let $\overline{\Omega}_{\mathbf{x}} = \Gamma_{\mathbf{x}}^{o} \cup \Gamma_{\mathbf{x}}^{h} \cup \Gamma_{\mathbf{x}}^{v}$. Here Γ^{o} represents the outer nonsymmetrical boundaries, Γ^{h} represents the horizontal symmetrical boundary where $y = 0$ and Γ^{v} represents the vertical symmetrical boundary where $x = 0$. For the chemicals, the following boundary conditions hold for all time t and all

$$\mathbf{x} \in \Gamma_{\mathbf{x}}^{o}: \quad N(\mathbf{x}; t) = \overline{N}, \quad M(\mathbf{x}; t) = \overline{M}, \quad \text{and} \quad c(\mathbf{x}; t) = \overline{c}, \tag{2.22}$$

$$\mathbf{x} \in \Gamma_{\mathbf{x}}^{p}: \quad \mathbf{J}_{N/M/c} \cdot \mathbf{n} = 0, \tag{2.23}$$

where $p \in \{h, v\}$ and $\mathbf{n}$ is the outward pointing normal vector. We use similar conditions for the mechanics, that is, for all time t and all

$$\mathbf{x} \in \Gamma_{\mathbf{x}}^{o}: \quad \boldsymbol{v}(\mathbf{x}; t) = 0, \tag{2.24}$$

$$\mathbf{x} \in \Gamma_{\mathbf{x}}^{p}: \quad \boldsymbol{v} \cdot \mathbf{n} = 0 \quad \text{and} \quad (\sigma \cdot \mathbf{n}) \cdot \tau = 0, \tag{2.25}$$

where τ is the tangential vector.

2.5 The applied numerical methods and implementation

We solve the model's equations by the finite element method [42] and implement the solution in MATLAB [43]. Before the derivation of the weak formulation, we add the term $\varepsilon_{i,j} [\nabla \cdot \boldsymbol{v}]$ for $i, j \in \{1, 2\}$ to the left-hand side and the right-hand side of the effective Eulerian strain equations. We multiply the equations by a test function $\varphi(\mathbf{x}; t) \in H^{1}(\Omega_{\mathbf{x}})$ and integrate over the domain of computation. Then, we apply Gauss' Theorem and Reynold's Transport Theorem, yielding the weak forms. For a derivation of these forms, we refer to the appendix in Koppenol's thesis [17]. We note that we proved that the effective strain tensor is symmetric for all time t; hence $\varepsilon_{21} = \varepsilon_{12}$ [44].

In a two-dimensional setting, we subdivide the computational domain into a finite number of $m \in \mathbb{N}$ nonoverlapping triangles Δ_{p} (i.e., the elements) that are as equilateral as possible (angles as close to 60 degrees as possible). Let $X_{h}(t) \subset H^{1}(\Omega_{\mathbf{x}})$ the finite element subspace and $\mathbf{a}_{j}, j \in \{1, \ldots, n\}, n \in \mathbb{N}$ the coordinates of these vertices of the elements. We choose the Lagrangian basis functions $\varphi_{i} \in X_{h}(t)$ with $\varphi_{i}(\mathbf{a}_{j}; t) = \delta_{ij}$, with $i, j \in \{1, \ldots, n\}$ as basis functions for the finite-dimensional subspace $X_{h}(t)$, where δ_{ij} denotes the Kronecker delta function.

In a one-dimensional setting, we subdivide the computational domain into a finite number of *line* elements $e_{p} = [x_{p}, x_{p+1}]$. In this case, we let $X_{h}(t)$ the finite element subspace and x_{j}, with $j \in \{1, \ldots, n + 1\}$ the element vertices, and we choose $\varphi_{i}(x_{j}; t) = \delta_{ij}$ with $i, j \in \{1, \ldots, n + 1\}$ as linear basis functions.

Note that the following holds for the chosen subspace $X_h(t) \subset H^1(\Omega_\mathbf{x})$: $\frac{\mathrm{D}\varphi_i}{\mathrm{D}t} = 0$ for all φ_i [45]. We simplify the Galerkin equations using this property. We approximate the integrals over the interior of the elements by a Newton-Cotes rule based on linear basis functions.

We solve the Galerkin equations using backward Euler time integration, and we use a monolithic approach with inner Picard iterations to account for the non-linearity of the equations. In all simulations, the dimension $\mathbf{x}$ is in centimeters and t in days. The Picard iterations converge if the maximum of the relative 1-norms of the difference between successive approximations per variable is smaller than a given bound (10^{-5} for one-dimensional studies, and 5×10^{-2} for two-dimensional studies). We first solve for the chemical part of the model and, subsequently, the mechanical part (for some studies in each iteration); hence, we treat the model's coupling between the mechanics and chemicals sequentially. The maximum number of inner Picard iterations differs between studies and whether the chemicals and the mechanics are solved within a Picard iteration or not. Table 2.1 summarizes these setups for each chapter. We solve the mechanics as a system of equations in all simulations.

Table 2.1: Setup of Picard iterations in the chapters of this thesis.

	Ch. 3	Ch. 4	Ch. 5	Ch. 6	Ch. 7	Ch. 8
All equations together	no	yes	no	yes	yes	yes
# Picard iter. chemicals	not set	6	not set	6	10	6
# Picard iter. mechanics	1		not set			

The rows show whether the equations are solved together within a Picard iteration, the number of inner Picard iterations for the chemicals, and the number of inner Picard iterations for the mechanics. Where we did not set the number of Picard iterations, the Picard iterations continue until the maximum of the relative 1-norms of the difference between successive approximations per variable is smaller than the given bound.

We approximate the local displacements of the dermal layer ($\boldsymbol{u}$) with

$$\boldsymbol{u}(\mathbf{x}; t + \Delta t) \approx \boldsymbol{u}(\mathbf{x}; t) + \boldsymbol{v}(\mathbf{x}; t)\Delta t, \tag{2.26}$$

which translates to

$$u_i^{t+\Delta t} \approx u_i^t + \Delta t\, v_i^{t+\Delta t} \tag{2.27}$$

in a one-dimensional setting. For the displacement we use the initial condition $\boldsymbol{u}(\mathbf{x}; 0) = 0, \quad \forall \mathbf{x} \in \Omega_{\mathbf{x},0}$ in all chapters. Further, we update the mesh (triangulation) in every time integration step, and we determine the quality of this updated mesh in the two-dimensional studies by computing

$$\min_{e_k} |\mathbf{J}_{e_k}| / \max_{e_k} |\mathbf{J}_{e_k}|, \quad e_k \in \Omega,$$

with $\mathbf{J}$ the Jacobian. In case $\min_{e_k} |\mathbf{J}_{e_k}| / \max_{e_k} |\mathbf{J}_{e_k}| < 0.5$, we perform remeshing. Our remeshing strategy is described in Chapter 6 as part of that study.

It is well known that the standard Galerkin method may suffer from oscillatory solution behavior when the equations are convection-dominated for diffusion-convection equations. We use mass lumping and a semi-implicit flux corrected transport limiter [46] that enforces the positiveness of solutions so that loss of monotonicity (that is, spurious oscillations) is suppressed.

2.5.1 Computational domains, modeled burns, and initial conditions

For the simulations in this thesis, we use different domains of computation. In one-dimensional simulations, we define the general computational domain by $\Omega_x = (-L, L)$ cm, and in two-dimensional simulations, we define the general computational domain by $\Omega_{\mathbf{x}} = (-L, L)^2$ cm^2, with $L \in \mathbb{R}$ and $\overline{\Omega}_{\mathbf{x}}$, the closing boundary. Hence, the outer non-symmetrical boundary Γ^o corresponds to all pairs (x, y) where either $x = L$ or $y = L$, the horizontal boundary Γ^h to $y = 0$, and the vertical symmetrical boundary Γ^v to $x = 0$.

In the computational domains, we model the burns as $\Omega_x^w = (-L^w, L^w)$ cm, $L^w < L$ (a piece of a line) in one-dimensional simulations, and $\Omega_{\mathbf{x}}^w = \left\{ (x, y) : \left| \frac{x}{a} \right| + \left| \frac{y}{a} \right| \leq 1 \right\}$ (a symmetrical rotated square) within the square computational domain in two-dimensional simulations.

Regarding the (burn) initial conditions, we assume those to represent the start of the proliferative phase of post-burn healing. The reasoning is that the inflammatory post-burn response is a difficult phase for which the biomorphoelastic model for post-burn contraction needs adjustments before it can simulate inflammation. During inflammation, signaling molecules stimulate fibroblast migration; however, myofibroblast differentiation does not happen yet, and hence the computational domain is not yet subject to displacement. Hence, the initial conditions are the same for the myofibroblast cell density, the displacement velocity density, and the effective Eulerian strain density in all simulations: these densities are initially all zero. We assume that signaling molecules and fibroblasts are initially present in the damaged area. For this, we define the burn boundary's steepness size by s, which accounts for the species' slope on the burn's boundary. We model the slopes of the species with sine functions and provide examples of initial conditions in Chapters 5 and 6. The initial condition of the collagen concentration can differ as we can assume the burn damaged all collagen or part collagen, or we model a skin graft in which the collagen concentration can be in equilibrium.

2.6 Relative area of the wound / scar

Because myofibroblasts pull on the surrounding collagen fibers, the tissue contracts and retracts after these cells disappear. This phenomenon is represented in the resulting displacement variable ($\boldsymbol{u}$). We can convert the density of this variable into a relative density. Suppose the burn initially was 15 cm^2 which then contracts to 10 cm^2. Then the relative area changes in percentage from 100% to about 67%. If the resulting scar retracts asymptotically to 13 cm^2, this has a relative area percentage of approximately 87%, with an associated asymptotic contraction value of 13%. We can use the asymptotic contraction value to detect a future contracture. In our simulations, the displacement density determines the *relative surface area* (RSA) of the damaged skin. Figure 2.2 shows an example of the RSA density and highlights its typical features: the minimum and the asymptotic values.

The minimum RSA value corresponds with the maximum post-burn contraction. Once the RSA has reached its minimum, the scar retracts (i.e., myofibroblasts disappear, and the scar relaxes). After remodeling, the scar no longer changes and ends with a fixed contraction percentage related to the RSA's asymptotic value.

In this thesis, the results show the *minimum of the relative surface area* (RSA$_{\text{min}}$) (i.e., the maximum contraction value) in a time period of one year, the *day on which the min-*
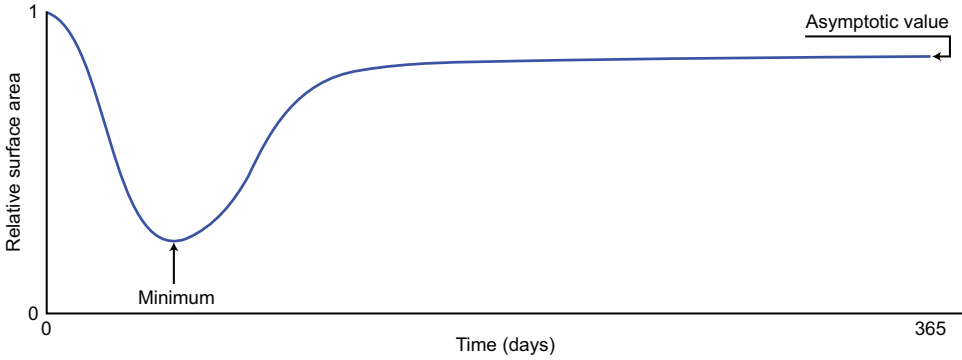
Figure 2.2: An example of the relative surface area (RSA) density highlighted with its minimum and asymptotic values. The minimum value of the RSA corresponds to maximum contraction during healing, and the asymptotic value of the RSA corresponds to the fixed percentage of contraction after scar remodeling.

imum relative surface area is reached (RSA_{day}) (i.e., the day after which the wound / scar retracts), and the *relative surface area on day 365* (RSA_{365}) (i.e., the asymptotic contraction value).

2.7 Strain energy

Contracting wounds and scars cause stress and strain on the skin. We hypothesize that this stress may signal nerves, which may cause the patient to experience nagging, pain, or itchy sensations. Hence, we assume that the total amount of strain energy measures the discomfort a patient experiences. The total strain energy (TSE) is defined by the integral over the strain energy density (per unit volume) [47]:

$$
\begin{aligned}
E_{\boldsymbol{\varepsilon}}(t) &= \int_{\Omega} \frac{1}{2} \left[\varepsilon_{11}\sigma_{11} + 2\varepsilon_{12}\sigma_{12} + \varepsilon_{22}\sigma_{22} \right] \\
&= \int_{\Omega} \frac{1}{2(1-v^2)} E\sqrt{\rho} \left[\varepsilon_{11}^2 + 2v\varepsilon_{11}\varepsilon_{22} + \frac{1}{1+v}\varepsilon_{12}^2 + \varepsilon_{22}^2 \right] \mathrm{d}\Omega \\
&= \int_0^L \int_0^L \frac{2}{1-v^2} E\sqrt{\rho} \left[\varepsilon_{11}^2 + 2v\varepsilon_{11}\varepsilon_{22} + \frac{1}{1+v}\varepsilon_{12}^2 + \varepsilon_{22}^2 \right] \mathrm{d}x\mathrm{d}y.
\end{aligned}
\tag{2.28}
$$

Here, we used the symmetry of the two-dimensional computational domain and integrated the entire tissue, including the undamaged part. Using Hooke's law, the strain energy can be written regarding strain and stress. The integral (2.28) only involves the elastic part of the tensor $\sigma = \sigma_{\text{viscous}} + \sigma_{\text{elastic}}$.
The one-dimensional version of the TSE is:

$$
E_{\varepsilon}(t) = \int_{-L}^{L} \frac{1}{2} E\sqrt{\rho(x,t)} \varepsilon(x,t)^2 \, \mathrm{d}x = \int_0^L E\sqrt{\rho(x,t)} \varepsilon(x,t)^2 \, \mathrm{d}x,
\tag{2.29}
$$

where we again used the symmetry of the domain.
Figure 2.3 shows an example of the TSE density and highlights its typical feature: the maximum value.
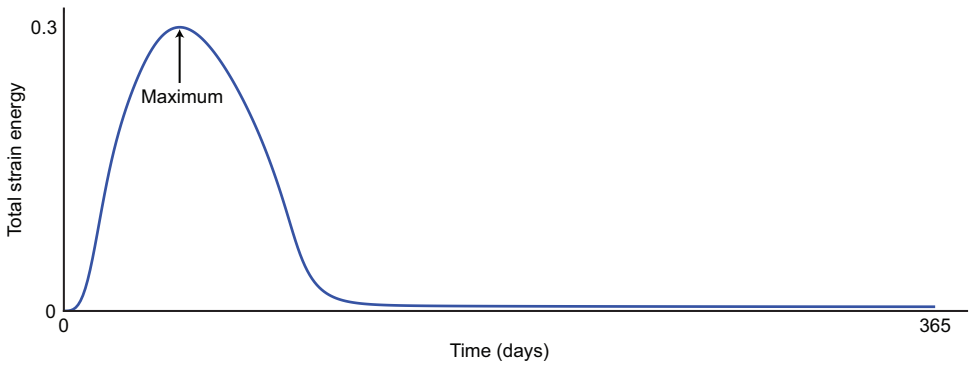
Figure 2.3: An example of the total strain energy (TSE) density highlighted with its maximum value. The TSE's maximum value corresponds to the maximum post-burn discomfort a patient might experience because of contraction.

Throughout this thesis, the results show the *maximum of the total strain energy* (TSE$_{max}$) (i.e., the maximum discomfort that a patient might experience), and the *day on which the maximum of the total strain energy is reached* (TSE$_{day}$) (i.e., the day after which the patient experiences a reduction in discomfort because of less internal stress in the skin).

PART I

Stability of the biomorphoelastic model for post-burn contraction

Introduction to this part

In the following two chapters in this part, we perform stability analyses for the one- and two-dimensional counterparts of the biomorphoelastic model for post-burn contraction. The multivariable multidimensional model has nonlinear equations, and the equilibria (steady states) might be unstable for specific parameter values, or multiple equilibria might be possible. Our method to predict stability around equilibria uses linearized equations and applies multivariable analysis to assess the local behavior around these equilibria. The goal is to avoid the parametric dependence of stable and unstable solutions and to understand the a priori behavior of the solution.

We use a linear stability analysis with Fourier series, where the transformations represent perturbations around equilibria. We analyze the nonlinear equations as a system of equations and provide stability conditions. Here we distinguish between the entire continuous problem, which represents the actual solution to the system of partial differential equations (PDEs), and the semi-discrete problem, which represents the solution of a semi-discrete solution method (i.e., the numerical approximation). In the latter case, the spatial finite difference method is carried out, whereas the time remains continuous. The reasoning for this distinguishment is that the stability of the continuous problem does not always automatically imply the stability of the (semi-) discrete counterpart of the problem.

The stability of the semi-discrete problem can assess the stability of the entire discrete system. Lax's Equivalence Theorem states that a consistent, stable method converges. The global truncation error tends to zero as the step size tends to zero (as $h \to 0$) if the local truncation error (i.e., the difference between the derivatives and difference ratios) tends to zero as the step size goes to zero.

A well-known way to assess numerical stability is by including Gershgorin's Circle Theorem. This theorem is widely used and very general because it is straightforward to generalize stability to general, non-equidistant meshes and cases where the input variables are nonconstant. However, in many examples, the eigenvalue bounds obtained through Gershgorin's Circle Theorem are less accurate than the Von Neumann analysis based on discrete Fourier analysis that provides sufficient conditions for numerical stability [48]. Because of the accuracy and ease of application of the Von Neumann analysis, we apply this analysis on a uniform grid on the system of linearized equations with constant coefficients in Chapter 3. In the stability analysis of the two-dimensional model, we cannot compute the eigenvalues exactly. We, therefore, provide stability conditions using Gershgorins theorem in Chapter 4. Further, in Chapter 4, we give the eigenvalues for a specific case. Biologically this means that the equilibria of the effective strain are determined.

We show that the continuous system's stability implies the semi-discrete system's stability. Besides the stability conditions, we pay attention to the effects of system instability regarding real-life post-burn contraction.

The conclusions of this part are presented after the chapters.

3

Stability analysis of the one-dimensional model

This chapter is based on the publication from [49]. The results from this chapter contribute to the range of parameter values used in Chapter 5. Videos corresponding to some figures in this chapter can be found in the online resources for Chapter 3 where one also finds a data link to the code.

We study the linear stability of the one-dimensional biomorphoelastic model for post-burn contraction to determine the region in the parameter space at which the system is still stable. We present stability constraints for the continuous and (semi-) discrete problems. We show that the truncation error between these eigenvalues associated with the continuous and the semi-discrete problem is of order $\mathcal{O}(h^2)$. Next, we perform numerical validation of these constraints and provide a biological interpretation of the (in)stability. The results show that the parameters of the chemical part of the model need to meet the stability constraint, depending on the decay rate of the signaling molecules, to avoid unrealistic results. For the mechanical part of the model, the results show that the components reach equilibria in a (non) monotonic way, depending on the viscosity value.

3.1 Introduction

In this chapter, we analyze stability around equilibria to study the parametric dependence of stable and unstable solutions for the one-dimensional biomorphoelastic model for post-burn contraction presented in Chapter 2. Section 3.2 presents the stability analysis and Section 3.3 presents the numerical validation of the stability constraints and a biological interpretation of (in)stability.

3.2   Linear stability

We consider the following linearization around the equilibria
$(c, N, M, \rho, v, \varepsilon) = (0, \overline{N}, 0, \overline{\rho}, 0, \overline{\varepsilon})$, where $\overline{N}, \overline{\rho}, \overline{\varepsilon} \in \mathbb{R}_{\geq 0}$:

$$
\frac{\partial \hat{N}}{\partial t} - D_n \overline{N} \frac{\partial^2 \hat{N}}{\partial x^2} + \chi \overline{N} \frac{\partial^2 \hat{c}}{\partial x^2} - r \overline{N}^q ((1+q)(1 - \kappa \overline{N}) - \kappa \overline{N}) \hat{N}
$$
$$
+ \delta_n \hat{N} + r \kappa \overline{N}^{1+q} \hat{M} - \overline{N} \left[\frac{r \cdot r^{\max}}{a_c^I} [1 - \kappa \overline{N}] \overline{N}^q - k_1 \right] \hat{c} = 0,
$$
$$
\frac{\partial \hat{M}}{\partial t} - D_n \overline{N} \frac{\partial^2 \hat{M}}{\partial x^2} + \delta_m \hat{M} - k_1 \overline{N} \hat{c} = 0,
$$
$$
\frac{\partial \hat{c}}{\partial t} - D_c \frac{\partial^2 \hat{c}}{\partial x^2} + \overline{N} \left[\delta_c \overline{\rho} - \frac{k_c}{a_c^{II}} \right] \hat{c} = 0, \tag{3.1}
$$
$$
\frac{\partial \hat{\rho}}{\partial t} + \delta_\rho \overline{\rho}^2 (\eta^{II} - \eta^I) \hat{M} - \delta_\rho \overline{\rho}^2 \overline{N} \left(\frac{k_\rho^{max}}{a_c^{IV}} + a_c^{III} \right) \hat{c} + 2 \delta_\rho \overline{N} \overline{\rho} \hat{\rho} = 0,
$$
$$
\frac{\partial \hat{v}}{\partial t} - \frac{\mu}{\rho_t} \frac{\partial^2 \hat{v}}{\partial x^2} - \frac{E \sqrt{\overline{\rho}}}{\rho_t} \frac{\partial \hat{\varepsilon}}{\partial x} - \frac{E \overline{\varepsilon}}{2 \rho_t \sqrt{\overline{\rho}}} \frac{\partial \hat{\rho}}{\partial x} - \frac{\xi \overline{\rho}}{\rho_t (R^2 + \overline{\rho}^2)} \frac{\partial \hat{M}}{\partial x} = 0,
$$
$$
\frac{\partial \hat{\varepsilon}}{\partial t} + (\overline{\varepsilon} - 1) \frac{\partial \hat{v}}{\partial x} + \zeta \overline{\varepsilon} \overline{N} \hat{c} = 0,
$$

where $\hat{c}, \hat{N}, \hat{M}, \hat{\rho}, \hat{v}$, and $\hat{\varepsilon}$ are variations around the equilibria. Here we used the equilibrium requirement $k_\rho = \delta_\rho \overline{\rho}^2$. First, we analyze the linear stability of the continuous problem and formulate the stability conditions in terms of the input parameters. Then, we analyze the linear stability of the (semi-) discrete problem.

3.2.1   Stability of the continuous problem

We write the variations around the equilibria in terms of a complex Fourier series,

$$
\hat{z}(x, t) = \frac{1}{|\Omega|} \sum_{j \in \mathbb{Z}} c_j^z(t) e^{2 i \pi j x}, \tag{3.2}
$$

for $z \in \{\hat{N}, \hat{M}, \hat{c}, \hat{\rho}, \hat{v}, \hat{\varepsilon}\}$, where $|\Omega|$ denotes the length of Ω and i represents the unit imaginary number.

Substitution of the variations (3.2) into the linearized equations (3.1), multiplication by $e^{-2 i \pi k x}$, and integration over Ω gives

$$
\dot{c}_k^N(t) + D_n \overline{N} (2 \pi k)^2 c_k^N(t) - \chi \overline{N} (2 \pi k)^2 c_k^c(t) + r \kappa \overline{N}^{1+q} c_k^M(t)
$$
$$
- r \overline{N}^q ((1+q)(1 - \kappa \overline{N}) - \kappa \overline{N}) c_k^N(t) + \delta_n c_k^N(t)
$$
$$
- \overline{N} \left[\frac{r \cdot r^{\max}}{a_c^I} [1 - \kappa \overline{N}] \overline{N}^q - k_1 \right] c_k^c(t) = 0, \tag{3.3}
$$
$$
\dot{c}_k^M(t) + D_n \overline{N} (2 \pi k)^2 c_k^M(t) + \delta_m c_k^M(t) - k_1 \overline{N} c_k^c(t) = 0,
$$

for the (myo) fibroblasts,

$$\dot{c}_k^c(t) + D_c(2\pi k)^2 c_k^c(t) + \overline{N}\left[\delta_c\overline{\rho} - \frac{k_c}{a_c^{II}}\right]c_k^c(t) = 0,$$

$$\dot{c}_k^\rho(t) + \delta_\rho\overline{\rho}^2(\eta^{II} - \eta^I)c_k^M(t) - \delta_\rho\overline{\rho}^2\overline{N}\left[\frac{k_\rho^{max}}{a_c^{IV}} + a_c^{III}\right]c_k^c(t) \tag{3.4}$$

$$+ 2\delta_\rho\overline{N}\overline{\rho}c_k^\rho(t) = 0,$$

for the signaling molecules and collagen, and

$$\dot{c}_k^v(t) + \frac{\mu}{\rho_t}(2\pi k)^2 c_k^v(t) - i\frac{E\sqrt{\overline{\rho}}}{\rho_t}(2\pi k)c_k^\varepsilon(t) - i\frac{E\overline{\varepsilon}}{2\rho_t\sqrt{\overline{\rho}}}(2\pi k)c_k^\rho(t)$$

$$- i\frac{\xi\overline{\rho}}{\rho_t(R^2 + \overline{\rho}^2)}(2\pi k)c_k^M(t) = 0, \tag{3.5}$$

$$\dot{c}_k^\varepsilon(t) + i(\overline{\varepsilon} - 1)(2\pi k)c_k^v(t) + \zeta\overline{\varepsilon}\overline{N}c_k^c(t) = 0,$$

for the mechanical part of the model. The derivation of parts of equations (3.3) and (3.5) is given in Appendix 3.4.1. Interchanging the first equation of (3.4) and the second equation of (3.3), and move these above the first equation of (3.3), (3.3)–(3.5) are in the form $y' + Ay = 0$ with

$$A = \begin{bmatrix} A_{11} & 0 & 0 & 0 & 0 & 0 \\ A_{21} & A_{22} & 0 & 0 & 0 & 0 \\ A_{31} & A_{32} & A_{33} & 0 & 0 & 0 \\ A_{41} & A_{42} & 0 & A_{44} & 0 & 0 \\ 0 & A_{52} & 0 & A_{54} & A_{55} & A_{56} \\ A_{61} & 0 & 0 & 0 & A_{65} & 0 \end{bmatrix}. \tag{3.6}$$

We determine the eigenvalues of A by solving $|A - \lambda I| = 0$ for λ, where I represents the identity matrix. For this, we use the first four diagonal values as pivots, ending up with a 2-by-2 matrix containing the mechanical part of the model with determinant $\lambda^2 - A_{55}\lambda - A_{56}A_{65}$. Hence the eigenvalues are the first four diagonal entries and $\lambda = \frac{1}{2}A_{55} \pm \frac{1}{2}\sqrt{A_{55}^2 + 4A_{56}A_{65}}$. Note that the system is linearly stable if and only if the real part of the eigenvalues is non-negative, hence we need:

$$D_n\overline{N}(2\pi k)^2 - r\overline{N}^q((1+q)(1-\kappa\overline{N}) - \kappa\overline{N}) + \delta_n \geq 0,$$

$$D_n\overline{N}(2\pi k)^2 + \delta_m \geq 0,$$

$$D_c(2\pi k)^2 + \overline{N}\left[\delta_c\overline{\rho} - \frac{k_c}{a_c^{II}}\right] \geq 0, \tag{3.7}$$

$$2\delta_\rho\overline{N}\overline{\rho} \geq 0,$$

$$\frac{(2\pi k)^2\mu}{2\rho_t} \pm \frac{1}{2}\sqrt{\left(\frac{(2\pi k)^2\mu}{\rho_t}\right)^2 + 4\frac{(2\pi k)^2 E\sqrt{\overline{\rho}}}{\rho_t}(\overline{\varepsilon} - 1)} \geq 0.$$

Combining the first requirement with (2.8), gives $q\delta_N \leq \kappa r\overline{N}^{1+q}$ ($k = 0$). In addition, it must hold that $\delta_N > 0$ and hence $\kappa\overline{N} < 1$. The third requirement implies that the model

obtains stability for $\delta_c \geq \frac{k_c}{a_c^{II}\overline{\rho}}$. Further, the second and fourth eigenvalues meet the stability condition $\text{Re}(\lambda(A)) \geq 0$ independent of the chosen parameter values, given that the parameter values are positive. Finally, linear stability is obtained for $\overline{\varepsilon} \leq 1$, else a saddle point problem is obtained if $\lambda \in \mathbb{R}$. Note that this is also a physical requirement given that equation (2.14) only holds for small strains. These last two eigenvalues are real-valued as long as $\mu \geq \frac{\sqrt{\rho_t E \sqrt{\overline{\rho}}(1-\overline{\varepsilon})}}{\pi}$ ($k = 1$). If the last-mentioned condition is satisfied for $k = 1$, then the eigenvalues are real-valued for other values of k. For all the other conditions, they hold for all $k \in \mathbb{Z}$ as well. The constant case $k = 0$ implies that these eigenvalues are zero, reflecting the trivial case in which no dynamics exist. This also implies that $\overline{\varepsilon} = 0$ is a stable equilibrium state with real-valued eigenvalues. We summarize these results in Theorem 3.2.1.

Theorem 3.2.1. *Let $\{c, N, M, \rho, v, \varepsilon\}$ satisfy eqs. (2.15)–(2.20). Let $\delta_n = r(1 - \kappa\overline{N})\overline{N}^q > 0$ and $\overline{\rho} = \sqrt{k_\rho/\delta_\rho}$, then:*

1. *The equilibria $(c, N, M, \rho, v, \varepsilon) = (0, \overline{N}, 0, \overline{\rho}, 0, \overline{\varepsilon})$, $\{\overline{N}, \overline{\rho}, \overline{\varepsilon}\} \in \mathbb{R}_{>0}$, are linearly stable if and only if $\delta_c\overline{\rho} \geq \frac{k_c}{a_c^{II}}$, and $q\delta_n \leq \kappa r\overline{N}^{1+q}$ and $\overline{\varepsilon} \leq 1$;*

2. *Given $\overline{\varepsilon} < 1$, then the eigenvalues are real-valued if and only if*
   $$\mu \geq \frac{\sqrt{\rho_t E \sqrt{\overline{\rho}}(1-\overline{\varepsilon})}}{\pi} \ (k = 1);$$

Remark 3.2.1. *Note that $\delta_c \geq \frac{k_c}{a_c^{II}\overline{\rho}}$, for $k = 0$ (constant states). Hence, if constant perturbations are stable, then wavelike perturbations are stable. In case δ_c is not large enough, fast oscillating perturbations will vanish, while slow oscillating perturbations will not vanish and can amplify. Further, if $\overline{\varepsilon} < 1$ and if $\mu < \sqrt{\rho_t E \sqrt{\overline{\rho}}(1-\overline{\varepsilon})}/\pi$, then convergence from variations around $\overline{\varepsilon}$ will occur in a non-monotonic way over time because the eigenvalues of the linearised dynamical system are not real-valued.*

Next, we provide some quantitative examples that illustrate the stability claims. Stability is warranted if there is a sufficient decay of the growth factor. Monotonicity (of convergence) is obtained if there is sufficient damping in viscous forces.

Example   If we let $\delta_c = 5 \times 10^{-4}$ cm^6/(cells g day), $k_c = 4 \times 10^{-13}$ g/(cells day), $a_c^{II} = 10^{-8}$ g/cm^3, and $\overline{\rho} = 0.1125$ g/cm^3, then we have $\delta_c = 5 \times 10^{-4} \geq 3.55 \times 10^{-4} = k_c/(a_c^{II}\overline{\rho})$. Hence, with these parameter values, we meet the stability condition for the signaling molecules. Further, if we let $\overline{N} = 10^4 < 10^6 = \kappa^{-1}$ cells/cm^3, $\delta_n = 0.002$/day, $r = 0.924$ cm^{3q}/(cells^q day) and $q = \log(\delta_N) - \log(r(1 - \kappa\overline{N})/\log(\overline{N}) \approx -0.42$, then we have $q\delta_n = -8.4 \times 10^{-4} \leq 1.9 \times 10^{-4} = \kappa r\overline{N}^{1+q}$. Hence, with these parameter values, we meet the stability condition for the fibroblasts. Note that there is only a distance of 1.45×10^{-4} cm^6/(cells g day) between the left- and right-hand side in the first condition, and a much larger distance of 1.03×10^{-3} between the left- and right-hand side in the second condition. In addition, substitution of $\delta_n = r(1 - \kappa\overline{N})\overline{N}^q$ into the second equation of (3.7), and solving for q with $k = 0$ yields $q \leq \kappa\overline{N}/(1 - \kappa\overline{N}) \approx 0.01$, yielding the upper bound $\delta_n < 1.004$ (with the chosen parameter values). Given that the doubling

time (DT) of fibroblasts ranges from 18 to 20 h [50, 51], and that the average lifespan of fibroblasts varies between 40 and 70 population doublings (PD) [51, 52], using the formula $\delta_n = (\ln 2)/(\text{PD} \times \text{DT}/24)$, yields the save range $0.0119 \leq \delta_n \leq 0.0231$ for the fibroblast apoptosis rate.

3.2.2 Stability of the (semi-) discrete problem

We apply the Von Neumann analysis on a uniform grid on the system of linearized equations with constant coefficients (3.1). The *finite difference method* gives:

$$\lambda N_k = -D_n \overline{N} \frac{N_{k-1} - 2N_k + N_{k+1}}{h^2} + \chi \overline{N} \frac{c_{k-1} - 2c_k + c_{k+1}}{h^2}$$
$$+ \left[\delta_n - r\overline{N}^q ((1+q)(1-\kappa\overline{N}) - \kappa\overline{N}) \right] N_k + r\kappa\overline{N}^{1+q} M_k$$
$$- \overline{N} \left[\frac{r \cdot r^{\max}}{a_c^I} [1 - \kappa\overline{N}]\overline{N}^q - k_1 \right] c_k,$$

$$\lambda M_k = -D_n \overline{N} \frac{M_{k-1} - 2M_k + M_{k+1}}{h^2} + \delta_m M_k - k_1 \overline{N} c_k, \tag{3.8}$$

$$\lambda c_k = -D_c \frac{c_{k-1} - 2c_k + c_{k+1}}{h^2} + \overline{N} \left[\delta_c \overline{\rho} - \frac{k_c}{a_c^{II}} \right] c_k,$$

$$\lambda \rho_k = \delta_\rho \overline{\rho}^2 (\eta^{II} - \eta^I) M_k - \delta_\rho \overline{\rho}^2 \overline{N} \left(\frac{k_\rho^{max}}{a_c^{IV}} + a_c^{III} \right) c_k + 2\delta_\rho \overline{N\rho} \rho_k,$$

for the chemical part of the model, and

$$\lambda v_k = -\frac{\mu}{\rho_t} \frac{v_{k-1} - 2v_k + v_{k+1}}{h^2} - \frac{E\sqrt{\overline{\rho}}}{\rho_t} \frac{\varepsilon_{k+1} - \varepsilon_{k-1}}{2h}$$
$$- \frac{E\overline{\varepsilon}}{2\rho_t\sqrt{\overline{\rho}}} \frac{\rho_{k+1} - \rho_{k-1}}{2h} - \frac{\xi\overline{\rho}}{\rho_t(R^2 + \overline{\rho}^2)} \frac{M_{k+1} - M_{k-1}}{2h}, \tag{3.9}$$

$$\lambda \varepsilon_k = (\overline{\varepsilon} - 1) \frac{v_{k+1} - v_{k-1}}{2h} + \zeta\overline{\varepsilon}\overline{N}\hat{c}_k,$$

for the mechanical part of the model. Let

$$z_k = \sum_{\beta=1}^{n-1} \hat{z}_\beta e^{-2\pi\beta khi}, \tag{3.10}$$

for $z \in \{N, M, c, \rho, v, \varepsilon\}$. Substitution of (3.10) in (3.8)–(3.9), subdivision by $e^{-2\pi\beta khi}$, and using Euler's formula and $2 - 2\cos(2\pi\beta h) = 4\sin^2(\pi\beta h)$ results in

$$\lambda \hat{N}_\beta = \frac{\overline{N}}{h^2} 4\sin^2(\pi\beta h) \left[D_n \hat{N}_\beta - \chi \hat{c}_\beta \right] + \left[\delta_n - r\overline{N}^q ((1+q)(1-\kappa\overline{N}) - \kappa\overline{N}) \right] \hat{N}_\beta$$
$$+ r\kappa\overline{N}^{1+q} \hat{M}_\beta - \overline{N} \left[\frac{r \cdot r^{\max}}{a_c^I} [1 - \kappa_F \overline{N}]\overline{N}^q - k_1 \right] \hat{c}_\beta, \tag{3.11}$$

for the fibroblasts,

$$\lambda \hat{M}_\beta = \left[\frac{D_n \overline{N}}{h^2} 4\sin^2(\pi\beta h) + \delta_m \right] \hat{M}_\beta - k_1 \overline{N} \hat{c}_\beta,$$

$$\lambda \hat{c}_\beta = \frac{D_c}{h^2} 4\sin^2(\pi\beta h)\hat{c}_\beta + \overline{N} \left[\delta_c \overline{\rho} - \frac{k_c}{a_c^{II}} \right] \hat{c}_\beta, \tag{3.12}$$

$$\lambda \hat{\rho}_\beta = \delta_\rho \overline{\rho}^2 (\eta^{II} - \eta^I)\hat{M}_\beta - \delta_\rho \overline{\rho}^2 \overline{N} \left[\frac{k_\rho^{max}}{a_c^{IV}} + a_c^{III} \right] \hat{c}_\beta + 2\delta_\rho \overline{N}\overline{\rho} \hat{\rho}_\beta,$$

for the myofibroblasts, the signaling molecules and collagen, and

$$\lambda \hat{v}_\beta = \frac{\mu}{\rho_t h^2} 4\sin^2(\pi\beta h)\hat{v}_\beta + i\frac{E\sqrt{\overline{\rho}}}{\rho_t h} \sin(2\pi\beta h)\hat{\varepsilon}_\beta$$

$$+ i\frac{E\overline{\varepsilon}}{2\rho_t \sqrt{\overline{\rho}} h} \sin(2\pi\beta h)\hat{\rho}_\beta + i\frac{\xi\overline{\rho}}{2\rho_t (R^2 + \overline{\rho}^2) h} \sin(2\pi\beta h)\hat{M}_\beta, \tag{3.13}$$

$$\lambda \hat{\varepsilon}_\beta = -i\frac{(\overline{\varepsilon}-1)}{h} \sin(2\pi\beta h)\hat{v}_\beta + \zeta\overline{\varepsilon}\overline{N}\hat{c}_\beta,$$

for the mechanical part of the model. The derivation of parts of equations (3.11) and (3.13) is given in Appendix 3.4.2. The equations (3.11)–(3.13) are in the form $\lambda z = Cz$ with the matrix C as in (3.6). Hence, as before, we found the eigenvalues analytically. Note that the discrete system is linearly stable if and only if the real part of the eigenvalues is non-negative, hence we need:

$$\frac{D_n \overline{N}}{h^2} 4\sin^2(\pi\beta h) - r\overline{N}^q ((1+q)(1-\kappa\overline{N}) - \kappa\overline{N}) + \delta_n \geq 0,$$

$$\frac{D_n \overline{N}}{h^2} 4\sin^2(\pi\beta h) + \delta_m \geq 0,$$

$$\frac{D_c}{h^2} 4\sin^2(\pi\beta h) + \overline{N} \left[\delta_c \overline{\rho} - \frac{k_c}{a_c^{II}} \right] \geq 0, \tag{3.14}$$

$$2\delta_\rho \overline{N}\overline{\rho} \geq 0,$$

$$\frac{2\mu}{\rho_t h^2} \sin^2(\pi\beta h) \pm \frac{1}{2} \sqrt{\left(\frac{\mu}{\rho_t h^2} 4\sin^2(\pi\beta h) \right)^2 + 4\frac{E\sqrt{\overline{\rho}}}{\rho_t h^2} (\overline{\varepsilon}-1)\sin^2(2\pi\beta h)} \geq 0.$$

To guarantee linear stability, the first requirement states $q\delta_N \leq \kappa r\overline{N}^{1+q}$, given $\delta_n = r(1 - \kappa\overline{N})\overline{N}^q$. The third requirement states $\delta_c \overline{\rho} \geq \frac{k_c}{a_c^{II}}$. The second and fourth eigenvalues meet the stability condition independent of the chosen parameter values, given that the parameter values are positive. Finally, for the discrete problem, linear stability is also obtained for $\overline{\varepsilon} \leq 1$, and since

$$4\frac{E\sqrt{\overline{\rho}}}{\rho_t h^2} \overline{(1-\varepsilon)} \sin^2(2\pi\beta h) \geq 0, \tag{3.15}$$

stability is guaranteed for all $h \in \mathbb{R}_{>0}$. Hence, we have demonstrated that if the equilibrium is stable in the continuous problem, it is also stable in the semi-discrete problem.

There exists a consistency between the stability criteria of the continuous problem and the stability criteria of the discrete problem. We show this consistency by writing $\sin^2(x)$ as a Taylor series. Substitution into the third and last equation in (3.14) yields:

$$D_c(2\pi\beta)^2 + \mathcal{O}(h^2) + \overline{N}\left[\delta_c\overline{\rho} - \frac{k_c}{a_c^{II}}\right] \geq 0,$$

$$\frac{(2\pi\beta)^2\mu}{2\rho_t} + \mathcal{O}(h^2) \pm \frac{1}{2}\sqrt{\left(\frac{(2\pi\beta)^2\mu}{\rho_t} + \mathcal{O}(h^2)\right)^2 + 4\frac{(2\pi\beta)^2 E\sqrt{\overline{\rho}}}{\rho_t}(\overline{\varepsilon}-1) + \mathcal{O}(h^2)} \geq 0. \tag{3.16}$$

Comparison to the third and last equation of (3.7)

$$D_c(2\pi k)^2 + \overline{N}\left[\delta_c\overline{\rho} - \frac{k_c}{a_c^{II}}\right] \geq 0,$$

$$\frac{(2\pi k)^2\mu}{2\rho_t} \pm \frac{1}{2}\sqrt{\left(\frac{(2\pi k)^2\mu}{\rho_t}\right)^2 + 4\frac{(2\pi k)^2 E\sqrt{\overline{\rho}}}{\rho_t}(\overline{\varepsilon}-1)} \geq 0, \tag{3.17}$$

yields a difference in eigenvalues of order $\mathcal{O}(h^2)$. Note that in the same way, a difference of order $\mathcal{O}(h^2)$ follows for the first two equations of (3.7) and (3.14).
Furthermore, the last equation in (3.14) implies that for real-valued eigenvalues, we need

$$\frac{\mu^2}{\rho_t^2 h^4} 4^2 \sin^4(\pi\beta h) \geq 4\frac{E\sqrt{\overline{\rho}}}{\rho_t h^2}(1-\overline{\varepsilon})\sin^2(2\pi\beta h). \tag{3.18}$$

Writing $\sin^2(2\pi\beta h) = 4\sin^2(\pi\beta h)\cos^2(\pi\beta h)$, multiplication by $\frac{\rho_t^2 h^2}{4^2\sin^4(\pi\beta h)}$ gives

$$\mu^2 \geq \rho_t h^2 E\sqrt{\overline{\rho}}(1-\overline{\varepsilon})\frac{\cos^2(\pi\beta h)}{\sin^2(\pi\beta h)}. \tag{3.19}$$

Hence the numerical criterium

$$\mu \geq \frac{h}{\tan(\pi\beta h)}\sqrt{\rho_t E\sqrt{\overline{\rho}}(1-\overline{\varepsilon})}. \tag{3.20}$$

For consistency, we have

$$\lim_{h\to 0}\frac{h}{\tan(\pi\beta h)} = \lim_{h\to 0}\frac{\pi\beta h}{\tan(\pi\beta h)}\cdot\frac{1}{\pi\beta} = \frac{1}{\pi\beta}$$

and $\frac{h}{\tan(\pi\beta h)} \leq \frac{1}{\pi\beta}$, for $\beta = 1,\ldots,n-1$ ($hn = |\Omega|$). Hence, for monotonic convergence for $\beta = 1$, we see that the convergence is consistent with the convergence of the fully continuous model for $h \to 0$. We summarize the results in Theorem 3.2.2.

Theorem 3.2.2. *Let $\{c, N, M, \rho, v, \varepsilon\}$ satisfy the semi-discrete spatial finite differences version of eqs.* (2.15)–(2.20). *Then the fully continuous problem stability implies stability in the semi-discrete formulation, regardless of the step size. Furthermore, monotonic[1] convergence in the fully continuous problem implies monotonic convergence in the semi-discrete problem formulation, regardless of the step-size.*

[1] If a sequence is either non-increasing or non-decreasing, it is called monotonic.

Corollary 3.2.1. *Let $\{c, N, M, \rho, v, \varepsilon\}$ satisfy the semi-discrete spatial finite differences version of eqs. (2.15)–(2.20). Let $\delta_n = r(1 - \kappa \overline{N})\overline{N}^q$ and $\overline{\rho} = \sqrt{k_\rho/\delta_\rho}$, then the equilibria are unconditionally stable for the trapezoid rule and the Euler backward method as long as $\delta_c \overline{\rho} \geq k_c / a_c^{II}$ and $q\delta_n \leq r\kappa \overline{N}^{1+q}$. Furthermore, the Euler backward method is A-stable.*

Remark 3.2.2. *It is possible that the semi-discrete yields monotonic convergence, whereas the continuous problem does not. The reason for this is that $\frac{h}{\tan(\pi\beta h)} \leq \frac{1}{\pi\beta}$. Hence the inequality for the continuous problem is sharper than for the semi-discrete problem.*

3.3 Numerical validation

To experimentally assess the convergence of the numerical method (see Section 2.5), we use a computational domain of 10 cm in which we model a 4 cm large wound. To account for the steepness of the gradients of the initial fibroblast cell, signaling molecule, and collagen densities, we use an interval of 1 cm over which the initial condition varies between its equilibrium and zero. Within the wound, we assume that there are 2000 fibroblast cells/cm^3, 10^{-8} g/cm^3 signaling molecules, and 0.01125 g/cm^3 collagen present. We model the gradient of the steepness area by sine functions. We divide the computational domain in n elements, where $n \in \{41, 81, 161, 321, 641, 1281\}$. For each simulation, we define $\Delta t = h^2$, where h is the size of the elements, and simulate post-burn contraction for one day. In each simulation, we report the densities of the variables (the solutions) and the relative surface area (RSA) density. We computed the convergence order results as follows. Let $\lim_{h \to 0} z_h(x, 1) = z(x, 1)$ denote the true density of variable $z \in \{N, M, c, \rho, v, \varepsilon\}$ on day 1 and $z_{0.0078}(x, 1) =: z_{h/r}$ the solution in the last simulation (i.e., the reference, which has been computed using the highest numerical resolution). We approximate the errors $\epsilon^z(h) := \int |z - z_h| \mathrm{d}x$ of the solutions on the full computational domain. Since we are interested in the wound boundary, we approximate the errors of the solutions on the wound boundary in particular. For this, we use the following error definition:

$$\epsilon_{|41|}^z(h) = \sum_{i=1}^{41} \left| z_{h/r}(x_{i,41}) - z_h(x_{i,41}) \right|, \tag{3.21}$$

where the grid-points $x_{i,n}$ correspond to the grid-points in the simulation with $n = 41$ nodes. This error is a variant of the L^1-norm. Similarly, we define

$$\epsilon_{L^1}^z(h) = h \sum_{i=1}^{n} \left| z_{h/r}(x_{i,n}) - z_h(x_{i,n}) \right|, \tag{3.22}$$

$$\epsilon_{L^2}^z(h) = \sqrt{h \sum_{i=1}^{n} \left(z_{h/r}(x_{i,n}) - z_h(x_{i,n}) \right)^2}. \tag{3.23}$$

Figure 3.1 shows some results for error $\epsilon_{|41|}^v$, where we show the relations of the errors with the element size h for the displacement velocity and the RSA error.

We see that the absolute error of the displacement velocity decreases consistently as h decreases in Figure 3.1a. The average slope of this graph is 2.1882; hence the order of convergence is about $\mathcal{O}(h^2)$. Further, we see that the absolute RSA error decreases consistently as h decreases in Figure 3.1b. The average slope of this graph is 2.2092, showing
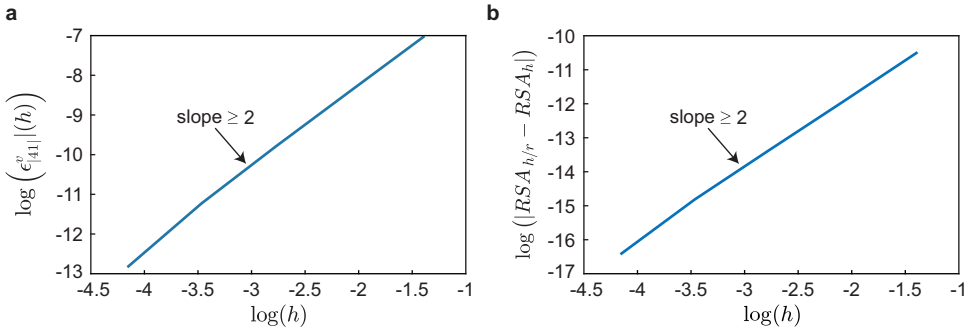
Figure 3.1: Numerical validation of convergence. Shown are the logarithm of the step size h versus the logarithm of the absolute displacement velocity density error on the computational domain on a fixed number of grid points (**a**) and versus the logarithm of the absolute relative surface area (RSA) error (**b**).

an order of convergence of about $\mathcal{O}(h^2)$ as well. We note that all averaged slopes of the logarithms of the absolute errors of the variables and the RSA show an overall consistent convergence of order $\mathcal{O}(h^2)$. One finds these slopes in Table 3.1.

Table 3.1: Overview of the averaged slopes.

Variable	$\epsilon_{|41|}$	ϵ_{L^1}	ϵ_{L^2}	$\epsilon_{boundary}$	Averaged
N	2.1843	2.0160	1.9701	2.1850	2.0889
M	2.1735	2.1203	2.0961	2.1892	2.1448
c	2.1900	2.0964	2.0675	2.0929	2.1117
ρ	2.1911	2.0626	1.9211	2.1708	2.0864
ν	2.1882	2.1891	2.1911	2.1189	2.1718
ε	2.2283	2.2301	2.2521	2.2403	2.2377

The slopes correspond to variable errors on the full computational domain and the wound boundary. The columns show slopes for the different errors, and the rows show the averaged slopes for the variables. The last column shows the averaged slopes of the rows. The reference is the solution in which $h = 0.0078$.

To validate the model's stability, we perturb the initial conditions around equilibria using sine functions, and we vary the parameters δ_c and μ. We use $n = 500$ elements to divide the computational domain between 0 and 1, representing half a domain of the modeled skin on which we perform computations. In all simulations, we use a step of $\Delta t = 5 \times 10^{-1}$ day for time integration (when not stated otherwise), and we fix all parameter values except for δ_c and μ. Table 3.2 shows the values of the fixed parameters.

Table 3.2: Overview of the parameters used for the simulations.

Symbol	Value	Dimension	Reference	
D_n	10^{-7}	cm^5/(cells day)	[53]	
D_c	2.88×10^{-3}	cm^2/day	[54]	

Table 3.2: (continued)

Symbol	Value	Dimension	Reference	
χ	2×10^{-3}	$cm^5/(g\,day)$	[55]	
k_c	4×10^{-13}	$g/(cells\,day)$	[14]	
r	9.24×10^{-1}	$cm^{3q}/(cells^q\,day)$	[50] & [56]	
r^{max}	2	-	[57]	
k_ρ	7.6×10^{-8}	$g/(cells\,day)$	[NC]	
k_ρ^{max}	10	-	[14]	
a_c^I	10^{-8}	g/cm^3	[58] & [14]	
a_c^{II}	10^{-8}	g/cm^3	[14]	
a_c^{III}	2×10^8	cm^3/g	[38]	
a_c^{IV}	10^{-9}	g/cm^3	[59]	
η^I	2	-	[60]	
η^{II}	5×10^{-1}	-	[1]	
k_1	1.08×10^7	$cm^3/(g\,day)$	[7]	
κ	10^{-6}	$cm^3/cells$	[32]	
q	-4.151×10^{-1}	-	[NC]	
δ_n	2×10^{-2}	$/day$	[14]	
δ_m	6×10^{-2}	$/day$	[61]	
δ_c	5×10^{-4}	$cm^6/(cells\,g\,day)$	[14]	
δ_ρ	6×10^{-6}	$cm^6/(cells\,g\,day)$	[61]	
$\overline{N}$	10^4	$cells/cm^3$	[14]	
$\overline{M}$	0	$cells/cm^3$	[14]	
$\overline{c}$	0	g/cm^3	[61]	
$\overline{\rho}$	1.125×10^{-1}	g/cm^3	[14]	
ρ_t	1.09	g/cm^3	[62]	
μ	10^2	$(N\,day)/cm^2$	[1]	
E	2.1×10^2	$N/((g\,cm)^{0.5})$	[63]	
ξ	4.4×10^{-2}	$(N\,g)/(cells\,cm^2)$	[64] & [65]	
R	9.95×10^{-1}	g/cm^3	[1]	
ζ	4×10^2	$cm^6/(cells\,g\,day)$	[1]	

Shown are the symbols, the values, the dimensions, and the references. Here NC denotes that the parameter value is a consequence because of the chosen values for other parameters. This table also shows the parameter values for δ_c and μ that are used for the convergence study.

For the initial conditions, we vary the wavenumber k using three levels (1, 5, and 10). We perturb the fibroblast, collagen, displacement velocity and effective strain initial conditions with sine functions with amplitudes 10 cells/cm^3, 10^{-2} g/cm^3, 0.05 cm/day and 0.5, respectively. We note that, in equilibrium, fibroblasts and collagen fibers are present. For the myofibroblast and signaling molecule initial conditions, we use uniform splines with $2k+1$ knots with values 3 and 6 cells/cm^3 for the myofibroblasts, and 0.5×10^{-15} and 2×10^{-15} g/cm^3 for the signaling molecules. This way, we ensure that the myofibroblast cell density and signaling molecule density values are positive.

For stability, Theorem 3.2.1 requires that $\delta_c \geq \frac{k_c}{a_c^{II}\overline{\rho}}$ in case $k = 0$. Further, given that the

equilibrium density of the effective strain is less than 1, eigenvalues are real-valued if and only if $\mu \geq \sqrt{\rho_t E \sqrt{\overline{\rho}}(1 - \varepsilon_0)}/\pi$ in case $k = 1$. We choose to vary the signaling molecule decay rate δ_c using three levels (2×10^{-4}, 3×10^{-4} and 5×10^{-4}) cm^6/(cells g day), where the first two values do not meet the stability condition. We vary the viscosity parameter μ using two levels (1 and 100) (N day)/cm^2. For the first value, the corresponding eigenvalue is not real-valued.

3.3.1 Stable values

In the first simulation we take $\delta_c = 5 \times 10^{-4}$ cm^6/(cells g day) and $\mu = 100$ (N day)/cm^2 and simulate for 400 days. Figure 3.2 shows the evolution of the variable densities for this setup.

The displacement velocity density rearranges to negative values, shown in Figure 3.2a. As the density moves below zero, the wave's amplitude initially increases, after which the density moves gradually toward the equilibrium $v = 0$ cm/day. Unlike the displacement velocity density, the effective strain density does not change sign, shown in Figure 3.2b. The values on the boundaries of the computational domain initially move away from the equilibrium, where all other values gradually move toward the equilibrium $\varepsilon \approx -0.05$. The boundary condition fixes the signaling molecule density at equilibrium on the left boundary of the computational domain. On the right boundary, the density increases in the first days, after which it decreases to the equilibrium $c = 0$ g/cm^3, shown in Figure 3.2c. Because of the negative values of the displacement velocity density after 12 hours, the mesh moves to the left, most evident in the evolving fibroblast cell density, shown in Figure 3.2d. During the simulation, the fibroblast cell density displaces to the left, and values above the equilibrium gradually move toward the equilibrium $N = 10^4$ cells/cm^3. The fibroblast cell density moves away from the equilibrium on the right boundary of the computational domain as the fibroblasts differentiate into myofibroblasts because of the increased signaling molecule density. After the signaling molecule density is almost zero around the right boundary on day 30, the fibroblast cell density moves toward the equilibrium, reaching it fully around day 400. The effect is the same for the myofibroblast cell density, where the density moves to the left and gradually toward the equilibrium $M = 0$ cells/cm^3, shown in Figure 3.2e. Only the values on the right boundary move away from the equilibrium in the first ten days because of the differentiated fibroblasts. The collagen density evolution is similar to the effective strain density. However, the effect of the local displacements seems more significant for collagen, and it takes much longer before the density reaches the equilibrium $\rho = 0.1125$ g/cm^3, shown in Figure 3.2e. Overall, the model behaves stable given these stable parameter values.

From a biological perspective, minor variations in the number of (myo)fibroblast cells and disturbance of signaling and collagen already initializes wound healing in which contraction appears for 100 days. If there is a disruption in the collagen concentration, the skin recovers this almost immediately. Recovering after signaling disturbance takes longer. Further, the skin's local displacements move toward the center of the wound or the direction of the wound boundary.

3
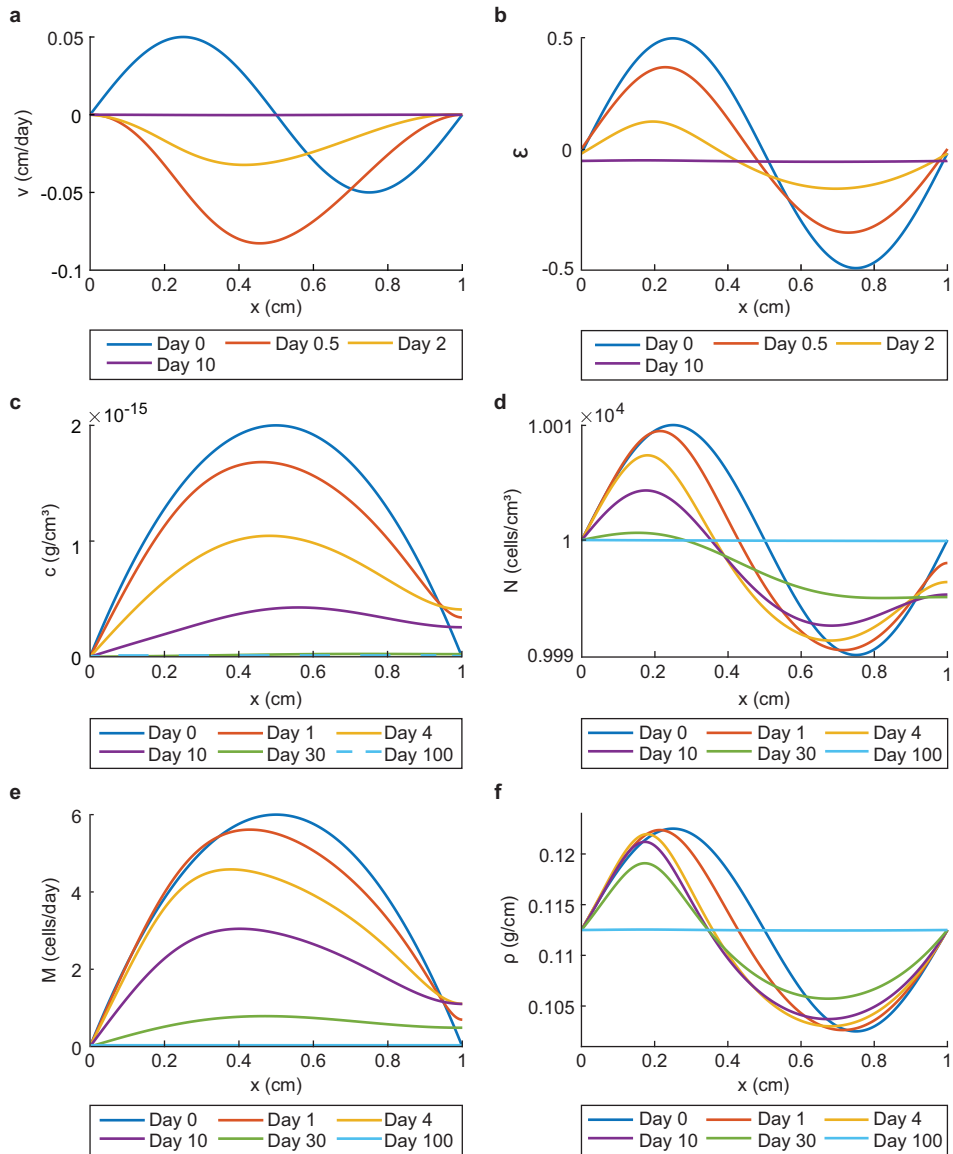
Figure 3.2: Evolution of the perturbed variable densities for $\delta_c = 5 \times 10^{-4}$ cm^6/(cells g day) and $\mu = 100$ (N day)/cm^2. The plots show the displacement velocity (**a**), the effective strain (**b**), the signaling molecules (**c**), the fibroblasts (**d**), the myofibroblasts (**e**), and collagen (**f**).

3.3.2 Unstable signaling molecule decay

The simulations where we take $k = 1$, $\delta_c = 2 \times 10^{-4}$ cm^6/(cells g day) and $\mu = 100$ (N day)/cm^2 show the following. At first, during time integration, the chemicals (almost) reach healthy equilibria. The signaling molecule, myofibroblast cell, fibroblast cell, and

collagen densities reach equilibrium around days 250, 390, 650, and 650, respectively. Further, the displacement velocity and effective strain densities reach equilibria within 15 days. However, from day 660, the signaling molecule density oscillates. The fibroblast cell density oscillates from day 650, and the myofibroblast cell density from day 638. Shortly after the collagen density seems to reach equilibrium around day 650, the density explodes and no longer decreases. Because of singular matrices, we ended this simulation. The Picard iterations did not converge, and no plots were available because of NaN's in all the solutions. We see the same where $k \in \{5, 10\}$.

Theoretically, if the human body or an external factor reduces the decay rate of signaling molecules too much, this does not cause the skin to rupture. However, after a few years, the secretion of signaling molecules can increase significantly, causing such problems. Present fibroblasts fully differentiate into myofibroblasts. The scar will undergo a severe contraction, and collagen will cause tissue to rupture because of excessive production. We believe that the human body protects against lowering the decay rate of signaling molecules to this extent to prevent such a non-realistic occurrence.

3.3.3 Complex eigenvalues

In further simulations we take $\delta_c = 5 \times 10^{-4}$ cm^6/(cells g day) and $\mu = 1$ (N day)/cm^2 and simulate for 600 days. Note that we meet the chemical stability condition and focus on the effect of complex eigenvalues in the model's mechanical part. We initially use a timestep of $\Delta t = 0.01$, change that to $\Delta t = 1$ after two days, and to $\Delta t = 2$ after 50 days. Figure 3.3 shows the results for $k = 1$.

Initially, the displacement velocity density oscillates around zero, moving the mesh to the left and right, shown in Figure 3.3a, and the effective strain density oscillates around the (new) equilibrium, shown in Figure 3.3b. The displacement velocity wave's amplitudes initially increase; however, they decrease shortly afterward. The effective strain wave's amplitudes decrease gradually. The displacement velocity and the effective strain densities reach the equilibria within a few days, the displacement velocity density reaching the equilibrium $\nu = 0$ cm/day first. Note that these results both confirm the non-monotonic convergence from the variations around $\bar{\varepsilon}$ stated in Theorems 3.2.1 and 3.2.2. Subfigures 3.3c–f show that the chemical densities reach equilibria within 600 days, after which the densities remain in equilibrium. We further see the moving mesh. While the displacement velocity density oscillates, the chemical densities move from the right to the left and back until the densities move gradually toward the equilibria. First, the signaling molecule density reaches equilibrium around day 60, shown in Figure 3.3c. Around day 120, the myofibroblast cell density reaches equilibrium, shown in Figure 3.3e. When the displacement velocity density reaches equilibrium, the fibroblast cell density above the equilibrium decreases, shown in Figure 3.3d. The fibroblast cell density below the equilibrium increases, except for the fibroblast cell density around the right boundary of the computational domain, representing the center of the portion of skin that we model. Around the right boundary, the fibroblast cell density decreases until about 23 days, increasing toward the equilibrium. The collagen density changes calmly: the density moves gradually toward the equilibrium after shifting to the left, shown in Figure 3.3f.

Where $k = 5$ (figures not shown), the results show that increasing the wavenumber makes

3
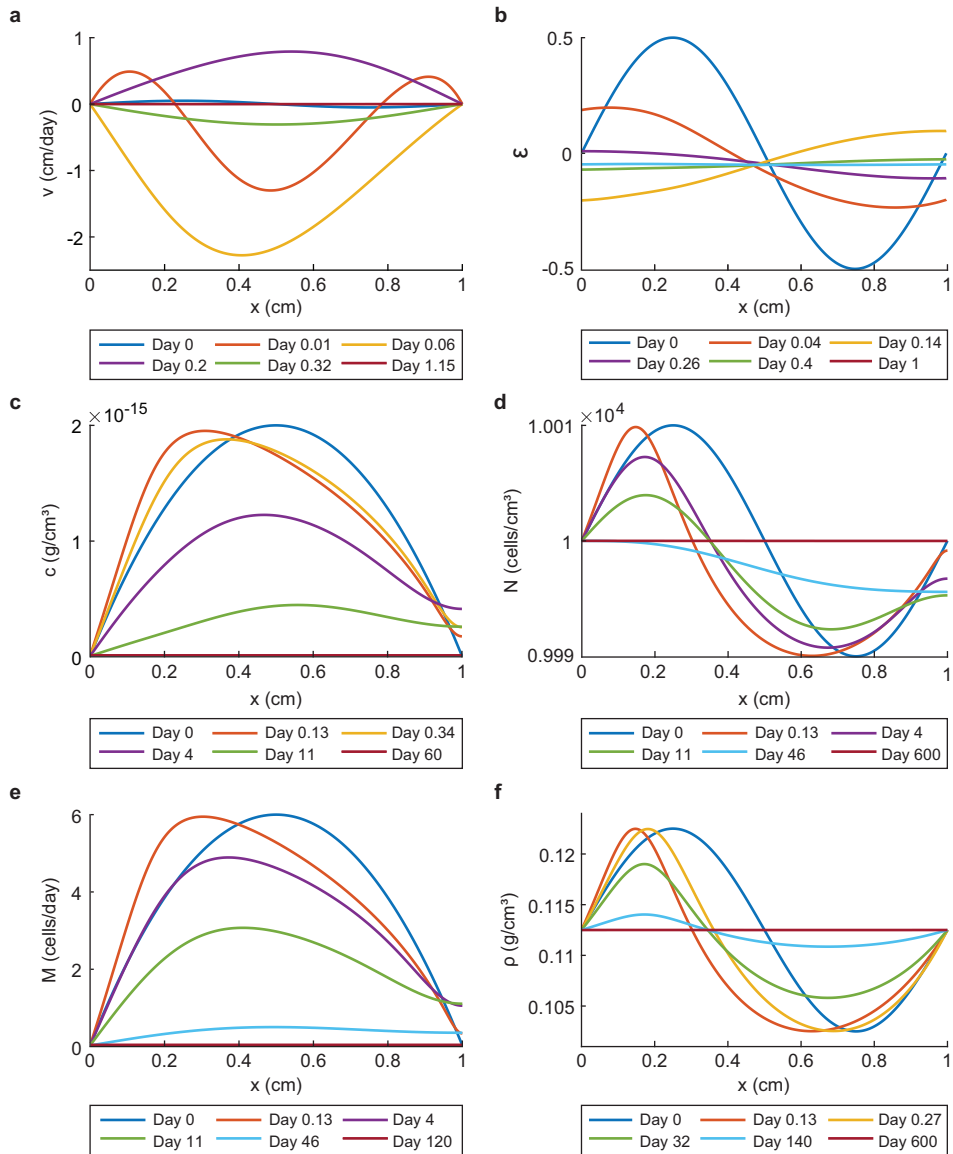
Figure 3.3: Evolution of the perturbed variable densities for $\delta_c = 5 \times 10^{-4}$ cm^6/(cells g day) and $\mu = 1$ (N day)/cm^2. The plots show the displacement velocity (**a**), the effective strain (**b**), the signaling molecules (**c**), the fibroblasts (**d**), the myofibroblasts (**e**), and collagen (**f**).

the initial increase in amplitudes in the displacement velocity density smaller; this amplitude initially increases around 15 minutes, after which it decreases while the density oscillates around the equilibrium. Fading out the waves takes more time, here about 4.8 hours, compared to 1.5 hours where $k = 1$, and the local displacements are much

smaller. The other densities change similarly to where $k = 1$, except for some features. Equilibria are reached around days 112, 210, and 600 for the signaling molecule density, the myofibroblast cell density, and the fibroblast cell and collagen densities, respectively, the first two later than where $k = 1$. The fibroblast cell density waves disappear faster than where $k = 1$, and the cell density moves faster toward the equilibrium. The smaller local displacements are visible in the plots of the chemicals. We have seen that the signaling molecule density shifts to the left between 0 and 3 hours and right between 3 and 8 hours. Further, the density decreases gradually toward the equilibrium, and the waves have already started fading out on day 4.

Comparing the results from the simulation where $k = 10$ (figures not shown) to the simulations where $k \in \{1, 5\}$, we conclude the perturbations disappear faster for higher frequencies and that initially, the chemical and the effective strain densities move faster toward the equilibria. In addition, the initial increase in the signaling molecule wave's amplitude is larger for smaller k. Taken these numerical results together, we can confirm that the one-dimensional biomorphoelastic model for post-burn contraction is stable given that $\delta_c \geq k_c/(a_c^{II}\overline{\rho})$, even for complex eigenvalues.

From a biological perspective, a significant viscosity value mimics an extensive amount of damping, and this damping term makes the equation for the displacement velocity more 'diffusive.' A diffusion equation satisfies a maximum principle. We can only assume the extremes on the domain's boundary unless the solution is constant. This principle implies that the solution must behave more monotonically for large viscosities, as shown by Figure 3.2a. A small value in the viscosity makes the equation for the displacement velocity less diffusive so that the boundary of the computational domain does not bound to the extremes or initially, as shown by Figure 3.3a. Here, the modeled medium is less resistant to the rate of deformation. Given the initial fluctuation in the displacement velocity density, this results in a back-and-forth movement in the displacement and a direct effect in the stress (effective strain) proportional to the shear deformation.

3.3.4 Unstable signaling molecule decay rate not too low

As stated before, the model can numerically be unstable when $\delta_c < k_c/(a_c^{II}\overline{\rho})$. However, we have seen that sometimes for low signaling molecule decay rates not too far below the stated lower bound, the model still converges. In the last simulation we set the wavenumber to $k = 10$, we take $\delta_c = 3 \times 10^{-4}$ cm^6/(cells g day) and $\mu = 100$ (N day)/cm^2, and we simulate for 1000 days. Figure 3.4 shows some early results of the simulation.

The displacement velocity density (figure not shown) reaches equilibrium within ten days, and the effective strain density around day 20. However, the perturbations are still visible. The myofibroblast cell density evolves calmly for the first 65 days, shown in Figure 3.4a. The myofibroblast wave's amplitude decreases, and the density moves toward equilibrium. The signaling molecule density evolves differently, shown in Figure 3.4b. Initially, the signaling molecule wave's amplitude decreases rapidly within one day, shown in Figure 3.5. However, on approximately day 9, the upper bound of the density surpasses the initial upper bound. The signaling molecule density keeps increasing until day 215, affecting the (myo)fibroblast cell densities and the collagen density.

As mentioned, the maximum of the signaling molecule density continues to increase. Figure 3.5 shows how this increase affects the chemicals. The increasing maximum in-
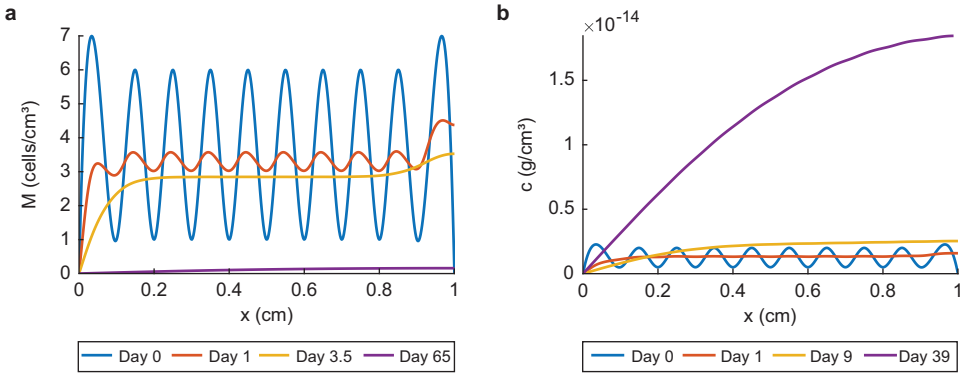
Figure 3.4: (early) Evolution of the perturbed myofibroblast cell density (**a**) and signaling molecule density (**b**) for $\delta_c = 3 \times 10^{-4}$ cm^6/(cells g day) and $\mu = 100$ (N day)/cm^2 and $k = 10$.

creases to day 215 with a value of $c \approx 1.3 \times 10^{-10}$ g/cm^3, shown in Figure 3.5a. In the meantime, the (myo)fibroblast waves' amplitudes decrease significantly within 4.5 days and the cell densities move toward the corresponding equilibria ($N(x) \approx 10^4$ cells/cm^3 on day 25 and $M \approx 0.16$ cells/cm^3 on day 50), shown in Figures 3.5b–c. The cell densities remain nearby equilibria until these move away on days 115 and 80 for the fibroblasts and the myofibroblasts. For the perturbed collagen density, it takes longer for the increased maximum of the signaling molecule density to take effect. The wave's amplitude decreases during the first 100 days, shown in Figure 3.5d. However, the density's maximum increases from day 120 (not visible). Unlike the rapid decrease in other densities waves' amplitudes, decreasing the collagen density wave's amplitude takes more time.

After the signaling molecule density maximum decreases from day 215 on, the myofibroblast cell density, the collagen density, and the fibroblast cell density keep moving away from their equilibria until days 230, 250, and 260, shown in Figures 3.5c, 3.5d, and 3.5b, respectively. In this situation, the chemical densities have reached maxima and minima, and from the mentioned days on, the chemical densities maxima oscillate around a new equilibrium. At the end of the simulation of 1000 days, the new equilibria in the center of the modeled skin are 4.245×10^{-11} g/cm^3, 9723 cells/cm^3, 76 cells/cm^3, and 0.1348 g/cm^3 for the signaling molecules, the fibroblasts, the myofibroblasts, and collagen, respectively. Hence, even though there is little signaling, this signaling is permanent so that myofibroblasts remain present to contract the scar. Further, the scar is thicker because of the increased collagen concentration.

From a biological perspective, if there is an enhanced expression of signaling molecules because of their reduced decay, a wound may heal appropriately at first. However, over time, persistent signaling will lead to over-expression of signaling molecules, resulting in excessive scarring and contraction. The excessive collagen deposition is reminiscent of keloids, and hypertrophic scars, characterized by thicker collagen bundles [66]. In addition, myofibroblasts are abundant in hypertrophic scars. Since aberrant TGF-β signaling in myofibroblasts is associated with the formation of hypertrophic scars [67], likely, such a situation exists precisely because of a lower signaling molecule decay rate. Further, hy-
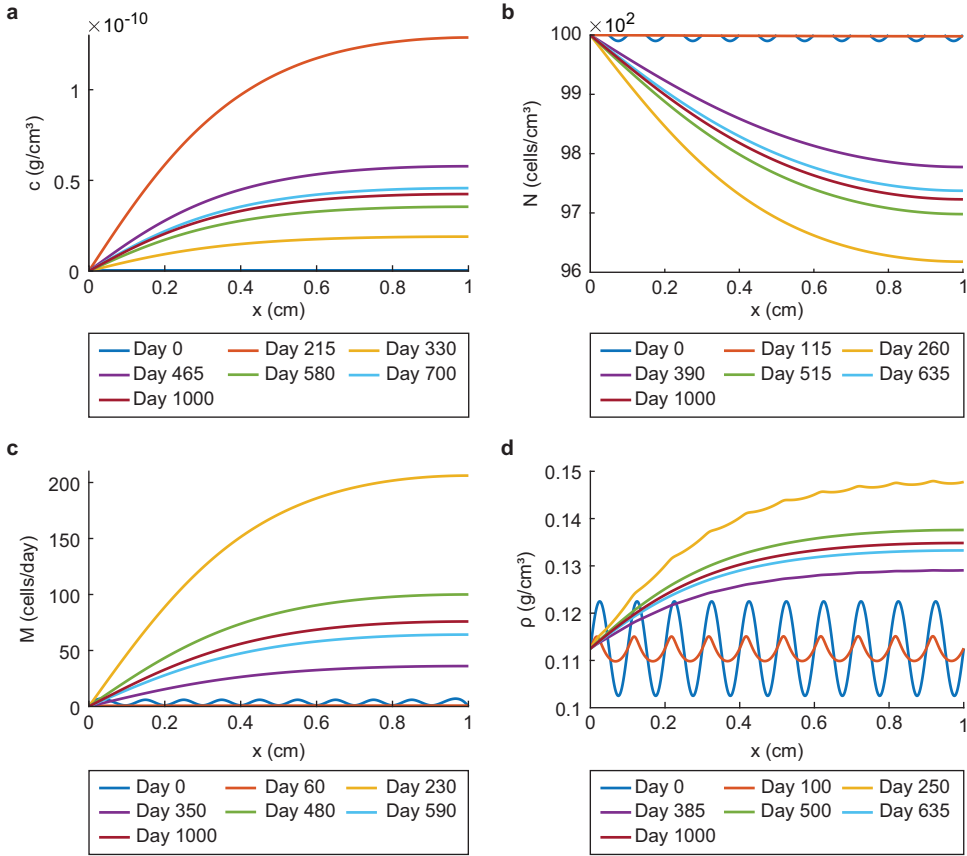
Figure 3.5: Evolution of the perturbed chemical densities for $\delta_c = 3 \times 10^{-4}$ cm^6/(cells g day) and $\mu = 100$ (N day)/cm^2 and $k = 10$. The plots show the signaling molecules (**a**), the fibroblasts (**b**), the myofibroblasts (**c**), and collagen (**d**).

pertrophic scars are not immediately visible after injury. These scars develop 1–2 months after injury, whereas keloids develop months to years after the initial injury, supporting our results. Experimental evidence suggests that fibroblasts from hypertrophic scars might represent a hyper-proliferative phenotype that can be reverted once the stimulation, such as the oversupply of growth factors, is lifted [66]. We verified this by setting the signaling molecule density to healthy equilibrium on day 1000. We saw that this directly initiates the change of the (myo)fibroblast cell densities and collagen density toward the healthy equilibria. First, the myofibroblast cell density reaches equilibrium after 100 days, then 350 days later, the collagen density reaches equilibrium, and finally, 100 days after that, the fibroblast cell density reaches equilibrium. Hence, according to our simulation, reversing the process takes about 1.5 years.

To conclude this section, the model is stable under the condition that the signaling molecule decay rate is not too far decreased to values below the bound $\delta_c \geq k_c/(a_c^{II}\overline{\rho})$.

3.4 Appendix: Derivation of the stability constraints

This appendix shows some derivations of the equations corresponding to the stability analysis. We distinguish between the continuous problem and the discrete problem.

3.4.1 The continuous problem

Substitution of the variations (3.2) into the linearised equations (3.1) yields

$$
\frac{1}{|\Omega|} \sum_{j=-\infty}^{\infty} \dot{c}_j^N(t) e^{2i\pi jx} + \frac{D_n \overline{N}}{|\Omega|} \sum_{j=-\infty}^{\infty} (2\pi j)^2 c_j^N(t) e^{2i\pi jx} - \frac{\chi \overline{N}}{|\Omega|} \sum_{j=-\infty}^{\infty} (2\pi j)^2 c_j^c(t) e^{2i\pi jx}
$$

$$
- \frac{r}{|\Omega|} \overline{N}^q ((1+q)(1-\kappa\overline{N}) - \kappa\overline{N}) \sum_{j=-\infty}^{\infty} c_j^N(t) e^{2i\pi jx} + \frac{r\kappa \overline{N}^{1+q}}{|\Omega|} \sum_{j=-\infty}^{\infty} c_j^M(t) e^{2i\pi jx}
$$

$$
- \frac{\overline{N}}{|\Omega|} \left[\frac{r \cdot r^{\max}}{a_c^I} [1 - \kappa\overline{N}] \overline{N}^q - k_1 \right] \sum_{j=-\infty}^{\infty} c_j^c(t) e^{2i\pi jx} + \frac{\delta_n}{|\Omega|} \sum_{j=-\infty}^{\infty} c_j^N(t) e^{2i\pi jx} = 0,
$$

for the fibroblasts, and

$$
\frac{1}{|\Omega|} \sum_{j=-\infty}^{\infty} \dot{c}_j^v(t) e^{2i\pi jx} + \frac{\mu}{|\Omega|\rho_t} \sum_{j=-\infty}^{\infty} (2\pi j)^2 c_j^v(t) e^{2i\pi jx} - i \frac{E\sqrt{\overline{\rho}}}{|\Omega|\rho_t} \sum_{j=-\infty}^{\infty} (2\pi j) c_j^\varepsilon(t) e^{2i\pi jx}
$$

$$
- i \frac{E\overline{\varepsilon}}{|\Omega|2\rho_t\sqrt{\overline{\rho}}} \sum_{j=-\infty}^{\infty} (2\pi j) c_j^\rho(t) e^{2i\pi jx} - i \frac{\xi\overline{\rho}}{|\Omega|\rho_t(R^2 + \overline{\rho}^2)} \sum_{j=-\infty}^{\infty} (2\pi j) c_j^M(t) e^{2i\pi jx} = 0,
$$

for the displacement velocity.
Multiplication by $e^{-2i\pi kx}$ gives

$$
\frac{1}{|\Omega|} \sum_{j=-\infty}^{\infty} \dot{c}_j^N(t) e^{2i\pi(j-k)x} + \frac{\overline{N}}{|\Omega|} \sum_{j=-\infty}^{\infty} (2\pi j)^2 \left[D_n c_j^N(t) - \chi c_j^c(t) \right] e^{2i\pi(j-k)x}
$$

$$
- \frac{r}{|\Omega|} \overline{N}^q ((1+q)(1-\kappa\overline{N}) - \kappa\overline{N}) \sum_{j=-\infty}^{\infty} c_j^N(t) e^{2i\pi(j-k)x} + \frac{r\kappa \overline{N}^{1+q}}{|\Omega|} \sum_{j=-\infty}^{\infty} c_j^M(t) e^{2i\pi(j-k)x}
$$

$$
- \frac{\overline{N}}{|\Omega|} \left[\frac{r \cdot r^{\max}}{a_c^I} [1 - \kappa\overline{N}] \overline{N}^q - k_1 \right] \sum_{j=-\infty}^{\infty} c_j^c(t) e^{2i\pi(j-k)x} + \frac{\delta_n}{|\Omega|} \sum_{j=-\infty}^{\infty} c_j^N(t) e^{2i\pi(j-k)x} = 0,
$$

for the fibroblasts, and

$$
\frac{1}{|\Omega|} \sum_{j=-\infty}^{\infty} \dot{c}_j^v(t) e^{2i\pi(j-k)x} + \frac{\mu}{|\Omega|\rho_t} \sum_{j=-\infty}^{\infty} (2\pi j)^2 c_j^v(t) e^{2i\pi(j-k)x}
$$

$$
- i \frac{E\sqrt{\overline{\rho}}}{|\Omega|\rho_t} \sum_{j=-\infty}^{\infty} (2\pi j) c_j^\varepsilon(t) e^{2i\pi(j-k)x} - i \frac{E\overline{\varepsilon}}{|\Omega|2\rho_t\sqrt{\overline{\rho}}} \sum_{j=-\infty}^{\infty} (2\pi j) c_j^\rho(t) e^{2i\pi(j-k)x}
$$

$$
- i \frac{\xi\overline{\rho}}{|\Omega|\rho_t(R^2 + \overline{\rho}^2)} \sum_{j=-\infty}^{\infty} (2\pi j) c_j^M(t) e^{2i\pi(j-k)x} = 0,
$$

for the displacement velocity.
Integration over Ω gives the result, hence equations (3.3) and (3.5).

3.4.2 The discrete problem

Substitution of the variations (3.10) in the finite differences equations (3.8)–(3.9) yields

$$\lambda N_k = -\frac{\overline{N}}{h^2} \sum_{\beta=1}^{n-1} \left[D_n \hat{N}_\beta - \chi \hat{c}_\beta \right] \left\{ e^{-2\pi\beta(k-1)hi} - 2e^{-2\pi\beta khi} + e^{-2\pi\beta(k+1)hi} \right\}$$

$$+ \left[\delta_n - r\overline{N}^q ((1+q)(1-\kappa\overline{N}) - \kappa\overline{N}) \right] \sum_{\beta=1}^{n-1} \hat{N}_\beta e^{-2\pi\beta khi} + r\kappa \overline{N}^{1+q} \sum_{\beta=1}^{n-1} \hat{M}_\beta e^{-2\pi\beta khi}$$

$$- \overline{N} \left[\frac{r \cdot r^{\max}}{a_c^I} [1 - \kappa\overline{N}] \overline{N}^q - k_1 \right] \sum_{\beta=1}^{n-1} \hat{c}_\beta e^{-2\pi\beta khi},$$

for the fibroblasts, and

$$\lambda v_k = -\frac{\mu}{\rho_t h^2} \sum_{\beta=1}^{n-1} \hat{v}_\beta \left\{ e^{-2\pi\beta(k-1)hi} - 2e^{-2\pi\beta khi} + e^{-2\pi\beta(k+1)hi} \right\}$$

$$- \frac{E\sqrt{\overline{\rho}}}{\rho_t 2h} \sum_{\beta=1}^{n-1} \hat{\varepsilon}_\beta \left\{ e^{-2\pi\beta(k+1)hi} - e^{-2\pi\beta(k-1)hi} \right\}$$

$$- \frac{E\overline{\varepsilon}}{2\rho_t\sqrt{\overline{\rho}}2h} \sum_{\beta=1}^{n-1} \hat{\rho}_\beta \left\{ e^{-2\pi\beta(k+1)hi} - e^{-2\pi\beta(k-1)hi} \right\}$$

$$- \frac{\xi\overline{\rho}}{\rho_t(R^2+\overline{\rho}^2)2h} \sum_{\beta=1}^{n-1} \hat{M}_\beta \left\{ e^{-2\pi\beta(k+1)hi} - e^{-2\pi\beta(k-1)hi} \right\},$$

for the displacement velocity.

This must be true for arbitrary $\{c_\beta, N_\beta, M_\beta, \rho_\beta, v_\beta, \varepsilon_\beta\}$, hence each factor following $\{c_\beta, N_\beta, M_\beta, \rho_\beta, v_\beta, \varepsilon_\beta\}$ in the sum should be zero. Subdivision by $e^{-2\pi\beta khi}$ gives

$$\lambda N_k = -\frac{D_n\overline{N}}{h^2} \hat{N}_\beta \left\{ e^{2\pi\beta hi} - 2 + e^{-2\pi\beta hi} \right\} + \frac{\chi\overline{N}}{h^2} \hat{c}_\beta \left\{ e^{2\pi\beta hi} - 2 + e^{-2\pi\beta hi} \right\}$$

$$+ \left[\delta_n - r\overline{N}^q ((1+q)(1-\kappa\overline{N}) - \kappa\overline{N}) \right] \hat{N}_\beta + r\kappa\overline{N}^{1+q} \hat{M}_\beta - \overline{N} \left[\frac{r \cdot r^{\max}}{a_c^I} [1-\kappa\overline{N}]\overline{N}^q - k_1 \right] \hat{c}_\beta,$$

for the fibroblasts, and

$$\lambda v_k = -\frac{\mu}{\rho_t h^2} \hat{v}_\beta \left\{ e^{2\pi\beta hi} - 2 + e^{-2\pi\beta hi} \right\} - \frac{E\sqrt{\overline{\rho}}}{\rho_t 2h} \hat{\varepsilon}_\beta \left\{ e^{-2\pi\beta hi} - e^{2\pi\beta hi} \right\}$$

$$- \frac{E\overline{\varepsilon}}{2\rho_t\sqrt{\overline{\rho}}2h} \hat{\rho}_\beta \left\{ e^{-2\pi\beta hi} - e^{2\pi\beta hi} \right\} - \frac{\xi\overline{\rho}}{\rho_t(R^2+\overline{\rho}^2)2h} \hat{M}_\beta \left\{ e^{-2\pi\beta hi} - e^{2\pi\beta hi} \right\},$$

for the displacement velocity.

Using Euler's formula and $2 - 2\cos(2\pi\beta h) = 4\sin^2(\pi\beta h)$ gives the result, hence equations (3.11) and (3.13).

4

Stability analysis of the two-dimensional model

This chapter is based on the publication from [68]. The results from this chapter contribute to the range of parameter values used in Chapter 6. Videos corresponding to some figures shown in this chapter can be found in the online recourses for Chapter 4 where one also finds a data link to the used code.

We analyze the linear stability of the two-dimensional biomorphoelastic model for post-burn skin to determine the region in the parameter space at which the system is still stable. We formulate the stability conditions depending on the decay rate of signaling molecules for both the continuous partial differential equations-based problem and (semi-) discrete representation. We analyze the difference and convergence between the resulting spatial eigenvalues. We show that the truncation error between these eigenvalues associated with the continuous and the semi-discrete problem is of order $\mathcal{O}(h^2)$. We further validate the constraints numerically and provide a biological interpretation of the (in)stability. The results show that signaling molecule decay should be quick enough to avoid unrealistic results. Next to this analysis, we prove that the effective strain tensor remains symmetric if initially symmetric.

4.1 Introduction

In this chapter, we analyze stability around equilibria to study the parametric dependence of stable and unstable solutions for the two-dimensional biomorphoelastic model for post-burn contraction presented in Chapter 2. Section 4.2 presents the stability analysis, and Section 4.3 presents the numerical validation of the stability constraints and a biological interpretation of (in)stability.

4.2 Linear stability

We consider the following linearized equations around the equilibria (N, M, c, ρ, v_1, v_2, ε_{11}, ε_{12}, ε_{22}) = ($\overline{N}$, 0, 0, $\overline{\rho}$, 0, 0, $\overline{\varepsilon_{11}}$, $\overline{\varepsilon_{12}}$, $\overline{\varepsilon_{22}}$), where $\overline{N}, \overline{\rho} \in \mathbb{R}_{\geq 0}$ and $\overline{\varepsilon_{11}}, \overline{\varepsilon_{12}}, \overline{\varepsilon_{22}} \in \mathbb{R}$:

$$\frac{\partial \hat{N}}{\partial t} + \overline{N}\nabla \cdot \left[-D_n\nabla\hat{N} + \chi\nabla\hat{c} \right] - r\overline{N}^q \left[(1+q)(1-\kappa\overline{N}) - \kappa\overline{N} \right] \hat{N} +$$

$$\delta_n\hat{N} + r\kappa\overline{N}^{1+q}\hat{M} - \overline{N}\left[\frac{r \cdot r^{\max}}{a_c^I}(1-\kappa\overline{N})\overline{N}^q - k_1 \right]\hat{c} = 0,$$

$$\frac{\partial \hat{M}}{\partial t} - D_n\overline{N}\nabla \cdot (\nabla\hat{M}) + \delta_m\hat{M} - k_1\overline{N}\hat{c} = 0, \tag{4.1}$$

$$\frac{\partial \hat{c}}{\partial t} - D_c\nabla \cdot (\nabla\hat{c}) + \overline{N}\left[\delta_c\overline{\rho} - \frac{k_c}{a_c^{II}} \right]\hat{c} = 0,$$

$$\frac{\partial \hat{\rho}}{\partial t} + \delta_\rho\overline{\rho}^2(\eta^{II} - \eta^I)\hat{M} - \delta_\rho\overline{\rho}^2\overline{N}\left[\frac{k_\rho^{max}}{a_c^{IV}} + a_c^{III} \right]\hat{c} + 2\delta_\rho\overline{N}\overline{\rho}\hat{\rho} = 0,$$

for the chemical part of the model, where we used that $k_\rho = \delta_\rho\overline{\rho}^2$ must hold in equilibrium,

$$\rho_t\frac{\partial \hat{v}_1}{\partial t} - (\mu_1 + \mu_2)\frac{\partial^2 \hat{v}_1}{\partial x^2} - \frac{\mu_1}{2}\frac{\partial^2 \hat{v}_1}{\partial y^2} - \left[\frac{\mu_1}{2} + \mu_2 \right]\frac{\partial^2 \hat{v}_2}{\partial x\partial y} - \tag{4.2}$$

$$\frac{E\sqrt{\overline{\rho}}}{1+\nu}\left[\frac{\partial\hat{\varepsilon}_{12}}{\partial y} + \frac{\partial\hat{\varepsilon}_{11}}{\partial x} + \frac{\nu}{1-2\nu}\left[\frac{\partial\hat{\varepsilon}_{11}}{\partial x} + \frac{\partial\hat{\varepsilon}_{22}}{\partial x} \right] \right] -$$

$$\frac{E}{2\sqrt{\overline{\rho}}(1+\nu)}\left[\overline{\varepsilon_{12}} + \overline{\varepsilon_{11}} + \frac{\nu}{1-2\nu}(\overline{\varepsilon_{11}} + \overline{\varepsilon_{22}}) \right]\frac{\partial\hat{\rho}}{\partial x} - \xi\frac{\overline{\rho}}{R^2 + \overline{\rho}^2}\frac{\partial\hat{M}}{\partial x} = 0,$$

for v_1 (the equation for v_2 is similar, where x, y and $\hat{v}_1$, $\hat{v}_2$ are interchanged), and

$$\frac{\partial\hat{\varepsilon}_{11}}{\partial t} + \overline{\varepsilon_{12}}\left[\frac{\partial\hat{v}_2}{\partial x} - \frac{\partial\hat{v}_1}{\partial y} \right] + (\overline{\varepsilon_{11}} + \overline{\varepsilon_{22}} - 1)\frac{\partial\hat{v}_1}{\partial x} + \zeta\overline{N\varepsilon_{11}}\hat{c} = 0,$$

$$\frac{\partial\hat{\varepsilon}_{12}}{\partial t} + \overline{\varepsilon_{22}}\frac{\partial\hat{v}_2}{\partial x} + \overline{\varepsilon_{11}}\frac{\partial\hat{v}_1}{\partial y} - \frac{1}{2}\left[\frac{\partial\hat{v}_2}{\partial x} + \frac{\partial\hat{v}_1}{\partial y} \right] + \zeta\overline{N\varepsilon_{12}}\hat{c} = 0, \tag{4.3}$$

for the effective strains $\hat{\varepsilon}_{11}, \hat{\varepsilon}_{12}$ (the equation for $\hat{\varepsilon}_{22}$ is similar as for $\hat{\varepsilon}_{11}$, where x, y and $\hat{v}_1$, $\hat{v}_2$ are interchanged). In equations (4.1)–(4.3), $\hat{N}, \hat{M}, \hat{c}, \hat{\rho}, \hat{v}_1, \hat{v}_2, \hat{\varepsilon}_{11}, \hat{\varepsilon}_{12}$, and $\hat{\varepsilon}_{22}$ are variations around the equilibria. Hence, $N(\mathbf{x}; t) = \overline{N} + \hat{N}(\mathbf{x}; t)$, etc.

Note that we only consider the equation for ε_{12} and not ε_{21}. We demonstrate that if the strain tensor $\boldsymbol{\varepsilon}$ is initially symmetric, then it remains symmetric at all later times [44].

Theorem 4.2.1. *Let equation* (2.14) *hold on an open Lipschitz domain Ω for $t > 0$. Suppose that $\boldsymbol{\varepsilon}$ is symmetric on $t = 0$, then $\boldsymbol{\varepsilon}$ remains symmetric for $t > 0$.*

Proof. Taking the transpose of equation (2.14), gives

$$\frac{D\boldsymbol{\varepsilon}}{Dt} + \boldsymbol{\varepsilon}\,\text{skw}(\nabla\boldsymbol{v}) - \text{skw}(\nabla\boldsymbol{v})\boldsymbol{\varepsilon} + (\text{tr}(\boldsymbol{\varepsilon}) - 1)\text{sym}(\nabla\boldsymbol{v}) = -\zeta\frac{[N + \eta^{II}M]c}{1 + a_c^{III}c}\boldsymbol{\varepsilon},$$

$$\frac{D\boldsymbol{\varepsilon}^T}{Dt} + \boldsymbol{\varepsilon}^T\,\text{skw}(\nabla\boldsymbol{v}) - \text{skw}(\nabla\boldsymbol{v})\boldsymbol{\varepsilon}^T + (\text{tr}(\boldsymbol{\varepsilon}) - 1)\text{sym}(\nabla\boldsymbol{v}) = -\zeta\frac{[N + \eta^{II}M]c}{1 + a_c^{III}c}\boldsymbol{\varepsilon}^T. \tag{4.4}$$

Note that we used $\text{sym}(\nabla \boldsymbol{v})^T = \text{sym}(\nabla \boldsymbol{v})$ and $\text{skw}(\nabla \boldsymbol{v})^T = -\text{skw}(\nabla \boldsymbol{v})$. Subtraction gives

$$\frac{\text{D}}{\text{D}t}(\boldsymbol{\varepsilon} - \boldsymbol{\varepsilon}^T) + (\boldsymbol{\varepsilon} - \boldsymbol{\varepsilon}^T)\,\text{skw}(\nabla \boldsymbol{v}) - \text{skw}(\nabla \boldsymbol{v})(\boldsymbol{\varepsilon} - \boldsymbol{\varepsilon}^T) = -\zeta\frac{[N + \eta^{II}M]c}{1 + a_c^{III}c}(\boldsymbol{\varepsilon} - \boldsymbol{\varepsilon}^T). \tag{4.5}$$

From the above equation, it is clear that $(\boldsymbol{\varepsilon} - \boldsymbol{\varepsilon}^T) = 0$ represents an equilibrium, and hence symmetry of $\boldsymbol{\varepsilon}$ represents an equilibrium. Hence, we conclude that initial symmetry implies no changes in symmetry for later times. Furthermore, we also prove that $\boldsymbol{\varepsilon} - \boldsymbol{\varepsilon}^T$ is the only solution if $\boldsymbol{\varepsilon} - \boldsymbol{\varepsilon}^T = 0$ at $t = 0$.

Performing the matrix scalar product $\boldsymbol{A} : \boldsymbol{B} := \sum_{i,j} A_{ij}B_{ij}$ on the above equation by $\boldsymbol{\varepsilon} - \boldsymbol{\varepsilon}^T$ gives upon setting $\boldsymbol{w} = \boldsymbol{\varepsilon} - \boldsymbol{\varepsilon}^T$ and $\boldsymbol{M} = \nabla \boldsymbol{v}$:

$$\boldsymbol{w} : \frac{\text{D}}{\text{D}t}\boldsymbol{w} + \boldsymbol{w} : (\boldsymbol{w}\,\text{skw}(\boldsymbol{M})) - \boldsymbol{w} : (\text{skw}(\boldsymbol{M})\,\boldsymbol{w}) = -\zeta\frac{[N + \eta^{II}M]c}{1 + a_c^{III}c}\boldsymbol{w} : \boldsymbol{w}. \tag{4.6}$$

Using $\boldsymbol{L} = \text{skw}(\nabla \boldsymbol{v}) = \text{skw}(\boldsymbol{M}) = L_{12}\begin{bmatrix} 0 & 1 \\ -1 & 0 \end{bmatrix}$ $(L_{12} = M_{12} - M_{21})$ and $\boldsymbol{w} = \boldsymbol{\varepsilon} - \boldsymbol{\varepsilon}^T = (\varepsilon_{12} - \varepsilon_{21})\begin{bmatrix} 0 & 1 \\ -1 & 0 \end{bmatrix}$, gives, although $\boldsymbol{w}$ and $\text{skw}(\boldsymbol{L})$ do not commute, that

$$\boldsymbol{w} : (\boldsymbol{w}\boldsymbol{L}) = 0 \quad \text{and} \quad \boldsymbol{w} : (\boldsymbol{L}\boldsymbol{w}) = 0. \tag{4.7}$$

Hence we obtain

$$\boldsymbol{w} : \frac{\text{D}}{\text{D}t}\boldsymbol{w} = -\zeta\frac{[N + \eta^{II}M]c}{1 + a_c^{III}c}\boldsymbol{w} : \boldsymbol{w}. \tag{4.8}$$

Define $||\boldsymbol{w}||^2 := \boldsymbol{w} : \boldsymbol{w}$, then it follows that

$$\frac{1}{2}\frac{\text{D}}{\text{D}t}||\boldsymbol{w}||^2 = -\zeta\frac{[N + \eta^{II}M]c}{1 + a_c^{III}c}||\boldsymbol{w}||^2. \tag{4.9}$$

Integrating over t from $t = 0$ and using $\boldsymbol{w} = 0$ at $t = 0$, gives

$$0 \le ||\boldsymbol{w}||^2 = -\zeta\int_0^t \frac{[N + \eta^{II}M]c}{1 + a_c^{III}c}||\boldsymbol{w}||^2\,\text{d}s \le 0. \tag{4.10}$$

With $\zeta, N, \eta^{II}, M, c, a_c^{III} \ge 0$, this implies that $||\boldsymbol{w}|| = 0$ on $t > 0$ if $||\boldsymbol{w}|| = 0$ on $t = 0$. Hence $\boldsymbol{w} = 0$ for $t > 0$, which represents symmetry, is the only possibility if $\boldsymbol{w} = 0$ on $t = 0$. $\qquad\square$

Remark 1. *Equation* (2.14) *depends on a linear relationship between stress and strain, hence $\boldsymbol{\varepsilon} - \boldsymbol{\varepsilon}^T = 0$ is a solution. However, this solution is not guaranteed to be unique; therefore, initial symmetry may change over time because of computing and rounding errors, for instance.*

This theorem motivates why we only need to consider ε_{12} as a cross term assuming initial symmetry. Further, we demonstrate that small perturbations around symmetry of $\boldsymbol{\varepsilon}$ remain small, which is a characteristic of stability.

Theorem 4.2.2. *Let equation* (2.14) *hold on an open Lipschitz domain Ω for $t > 0$. Let $\boldsymbol{\varepsilon}$ be symmetric for $t \ge 0$, then stability of symmetry is warranted if and only if $K \ge 0$.*

Proof. Let $\boldsymbol{\omega} = \boldsymbol{\varepsilon} - \boldsymbol{\varepsilon}^T$ in equation (4.5), then

$$\frac{D\boldsymbol{\omega}}{Dt} + \boldsymbol{\omega}\,\mathrm{skw}(\nabla\boldsymbol{v}) - \mathrm{skw}(\nabla\boldsymbol{v})\boldsymbol{\omega} + K\boldsymbol{\omega} = \mathbf{0}. \tag{4.11}$$

Write $\mathrm{skw}(\nabla\boldsymbol{v}) = \mathbf{L}$, where $\mathbf{L} = \begin{bmatrix} 0 & L_{12} \\ -L_{12} & 0 \end{bmatrix}$ skew-symmetric (for any $\boldsymbol{v} \in C^2(\Omega)$). Then

$$\frac{D\boldsymbol{\omega}}{Dt} + \boldsymbol{\omega}\cdot\mathbf{L} - \mathbf{L}\cdot\boldsymbol{\omega} + K\boldsymbol{\omega} = \mathbf{0}, \tag{4.12}$$

a system of ordinary differential equations. Writing out, then

$$\frac{D}{Dt}\begin{bmatrix} \omega_{11} & \omega_{12} \\ \omega_{21} & \omega_{22} \end{bmatrix} - L_{12}\begin{bmatrix} \omega_{12}+\omega_{21} & \omega_{22}-\omega_{11} \\ \omega_{22}-\omega_{11} & -\omega_{21}-\omega_{12} \end{bmatrix} + K\begin{bmatrix} \omega_{11} & \omega_{12} \\ \omega_{21} & \omega_{22} \end{bmatrix} = \mathbf{0}. \tag{4.13}$$

Hence

$$\begin{cases} \frac{D}{Dt}\omega_{11} - L_{12}(\omega_{12}+\omega_{21}) + K\omega_{11} = 0, \\ \frac{D}{Dt}\omega_{12} - L_{12}(\omega_{22}-\omega_{11}) + K\omega_{12} = 0, \\ \frac{D}{Dt}\omega_{21} - L_{12}(\omega_{22}-\omega_{11}) + K\omega_{21} = 0, \\ \frac{D}{Dt}\omega_{22} + L_{12}(\omega_{21}+\omega_{12}) + K\omega_{22} = 0. \end{cases} \tag{4.14}$$

In matrix-vector form, let $\boldsymbol{\omega} = [\omega_{11},\omega_{22},\omega_{21},\omega_{22}]'$, then we get

$$\frac{D\boldsymbol{\omega}}{Dt} + \mathscr{B}\boldsymbol{\omega} = \mathbf{0}, \tag{4.15}$$

where

$$\mathscr{B} = \begin{bmatrix} K & -L_{12} & -L_{12} & 0 \\ L_{12} & K & 0 & -L_{12} \\ L_{12} & 0 & K & -L_{12} \\ 0 & L_{12} & L_{12} & K \end{bmatrix}. \tag{4.16}$$

For $K = 0$ (in equilibrium, $c = 0$ in equation (4.5)), this matrix is skew-symmetric (that is $\mathscr{B}^T = -\mathscr{B}$), and hence the eigenvalues are zero or purely imaginary. This implies that $\boldsymbol{\omega} = 0 \Leftrightarrow \boldsymbol{\varepsilon} = \boldsymbol{\varepsilon}^T$ is a null-stable equilibrium. Hence, small perturbations around the symmetry of $\boldsymbol{\varepsilon}$ will remain small, which implies stability. For the case that $K > 0$, it follows that the real part of the eigenvalues are given by K, which gives A-stability as well (perturbations from symmetry vanish as $t \longrightarrow \infty$. For $K < 0$, which corresponds to expansion (instead of contraction in our model), the negative real part of the eigenvalues results in instability of symmetry. Although the current case is not similar to diffusional growth, it is known that diffusional growth in combination with surface processes suffers from Mullins-Sekerka instabilities [69], which exhibits growth of perturbations on spherical surfaces.   □

Remark 4.2.1. *Of course $\boldsymbol{v}$ is non-constant. The only thing that happens is that $\boldsymbol{v} = \boldsymbol{v}(t)$ impacts the angular frequency around the equilibrium $\boldsymbol{\varepsilon} = \boldsymbol{\varepsilon}^T$.*

4.2.1 Stability of the continuous problem

We write the variations around the equilibria in terms of a complex Fourier series,

$$\hat{z}(\mathbf{x};t) = \frac{1}{|\Omega|} \sum_{j,k\in\mathbb{Z}} c_{j,k}^z(t) e^{2i\pi jx} e^{2i\pi ky},\tag{4.17}$$

for $z \in \{\hat{N}, \hat{M}, \hat{c}, \hat{\rho}, \hat{v}_1, \hat{v}_2, \hat{\varepsilon}_{11}, \hat{\varepsilon}_{12}, \hat{\varepsilon}_{22}\}$, where $|\Omega|$ denotes the measure of Ω and i represents the unit imaginary number.

Substitution of the variations (4.17) into the linearized equations (4.1)–(4.3), multiplication by $e^{-2i\pi lx}e^{-2i\pi py}$, integration over $\Omega = (0,1)^2$ ($|\Omega|=1$) and double orthonormality over Ω gives

$$\dot{c}_{l,p}^N(t) + \overline{N}\left[(2\pi l)^2 + (2\pi p)^2\right]\left[D_n c_{l,p}^N(t) - \chi c_{l,p}^c(t)\right] + r\kappa\overline{N}^{1+q} c_{l,p}^M(t) -$$
$$r\overline{N}^q\left[(1+q)(1-\kappa\overline{N}) - \kappa\overline{N}\right] c_{l,p}^N(t) + \delta_n c_{l,p}^N(t) -$$
$$\overline{N}\left[\frac{r\cdot r^{\max}}{a_c^I}(1-\kappa\overline{N})\overline{N}^q - k_1\right] c_{l,p}^c(t) = 0,$$

$$\dot{c}_{l,p}^M(t) + D_n\overline{N}\left[(2\pi l)^2 + (2\pi p)^2\right] c_{l,p}^M(t) + \delta_m c_{l,p}^M(t) - k_1\overline{N}c_{l,p}^c(t) = 0,\tag{4.18}$$

$$\dot{c}_{l,p}^c(t) + D_c\left[(2\pi l)^2 + (2\pi p)^2\right] c_{l,p}^c(t) + \overline{N}\left[\delta_c\overline{\rho} - \frac{k_c}{a_c^{II}}\right] c_{l,p}^c(t) = 0,$$

$$\dot{c}_{l,p}^\rho(t) + \delta_\rho\overline{\rho}^2(\eta^{II} - \eta^I)c_{l,p}^M(t) - \delta_\rho\overline{\rho}^2\overline{N}\left[\frac{k_\rho^{\max}}{a_c^{IV}} + a_c^{III}\right] c_{l,p}^c(t)$$
$$+ 2\delta_\rho\overline{N}\overline{\rho}c_{l,p}^\rho(t) = 0,$$

for the chemical part of the model,

$$\rho_t\dot{c}_{l,p}^{v_1}(t) + \left[(2\pi l)^2(\mu_1 + \mu_2) + \tfrac{1}{2}(2\pi p)^2\mu_1\right] c_{l,p}^{v_1}(t) + (2\pi l)(2\pi p)(\tfrac{1}{2}\mu_1 + \mu_2)c_{l,p}^{v_2}(t) -$$
$$i(2\pi)\left[\frac{E\sqrt{\overline{\rho}}}{1+\nu}\left\{pc_{l,p}^{\varepsilon_{12}}(t) + \frac{1-\nu}{1-2\nu}lc_{l,p}^{\varepsilon_{11}}(t) + \frac{\nu}{1-2\nu}lc_{l,p}^{\varepsilon_{22}}(t)\right\} + \xi\frac{\overline{\rho}}{R^2+\overline{\rho}^2}lc_{l,p}^M(t)\right] -$$
$$i(2\pi l)\frac{E}{2\sqrt{\overline{\rho}}(1+\nu)}\left[\overline{\varepsilon}_{12} + \overline{\varepsilon}_{11} + \frac{\nu}{1-2\nu}\left(\overline{\varepsilon}_{11} + \overline{\varepsilon}_{22}\right)\right] c_{l,p}^\rho(t) = 0,$$
$$\tag{4.19}$$

for the displacement velocity, and

$$\dot{c}_{l,p}^{\varepsilon_{11}}(t) + i(2\pi)\left\{\left[l(\overline{\varepsilon}_{11} + \overline{\varepsilon}_{22} - 1) - p\overline{\varepsilon}_{12}\right] c_{l,p}^{v_1}(t) + l\overline{\varepsilon}_{12}c_{l,p}^{v_2}(t)\right\} + \zeta\overline{N}\overline{\varepsilon}_{11}c_{l,p}^c(t) = 0,$$
$$\dot{c}_{l,p}^{\varepsilon_{12}}(t) + i(2\pi)\left[p(\overline{\varepsilon}_{11} - \tfrac{1}{2})c_{l,p}^{v_1}(t) + l(\overline{\varepsilon}_{22} - \tfrac{1}{2})c_{l,p}^{v_2}(t)\right] + \zeta\overline{N}\overline{\varepsilon}_{12}c_{l,p}^c(t) = 0,\tag{4.20}$$

for the effective strain.

Interchanging the third and first equation of (4.18), these equations together with equations (4.19) and (4.20) are in the form $y' + Ay = 0$ (y the vector of the time-dependent

components) with

$$A = \begin{bmatrix} A_{11} & 0 & 0 & 0 & 0 & 0 & 0 & 0 & 0 \\ A_{21} & A_{22} & 0 & 0 & 0 & 0 & 0 & 0 & 0 \\ A_{31} & A_{32} & A_{33} & 0 & 0 & 0 & 0 & 0 & 0 \\ A_{41} & A_{42} & 0 & A_{44} & 0 & 0 & 0 & 0 & 0 \\ 0 & A_{52} & 0 & A_{54} & A_{55} & A_{56} & A_{57} & A_{58} & A_{59} \\ 0 & A_{62} & 0 & A_{64} & A_{65} & A_{66} & A_{67} & A_{68} & A_{69} \\ A_{71} & 0 & 0 & 0 & A_{75} & A_{76} & 0 & 0 & 0 \\ A_{81} & 0 & 0 & 0 & A_{85} & A_{86} & 0 & 0 & 0 \\ A_{91} & 0 & 0 & 0 & A_{95} & A_{96} & 0 & 0 & 0 \end{bmatrix}. \tag{4.21}$$

We determine the eigenvalues of A by solving $|A - \lambda I| = 0$ for λ, where I represents the identity matrix. First, we perform Gaussian elimination to see that the first four diagonal values can be used as pivots. Hence, the first four eigenvalues are the first four diagonal entries. The system is linearly stable if and only if the real part of all the eigenvalues is non-negative, hence stability for the chemical part of the model is guaranteed if:

$$D_n \overline{N} \left[(2\pi l)^2 + (2\pi p)^2 \right] - r \overline{N}^q ((1+q)(1 - \kappa \overline{N}) - \kappa \overline{N}) + \delta_n \geq 0,$$
$$D_n \overline{N} \left[(2\pi l)^2 + (2\pi p)^2 \right] + \delta_m \geq 0,$$
$$D_c \left[(2\pi l)^2 + (2\pi p)^2 \right] + \overline{N} \left[\delta_c \overline{\rho} - \frac{k_c}{a_c^{II}} \right] \geq 0, \tag{4.22}$$
$$2 \delta_\rho \overline{N} \overline{\rho} \geq 0.$$

These four requirements show that stability for the chemical part of the model is equal to the stability constraints in $\mathbb{R}^1$ [49]. That is, for $\delta_c \geq \frac{k_c}{a_c^{II} \overline{\rho}}$ and $q \delta_n \leq \kappa r \overline{N}^{1+q}$ ($l = p = 0$). We note we need $\delta_n > 0$ and hence $\kappa \overline{N} < 1$. The second and fourth eigenvalues meet the stability condition independent of the chosen parameter values, given that these values are positive. Hence, if the conditions are met for $l = p = 0$, they hold for all $l, p \in \mathbb{Z}$, which correspond to wavelike perturbations.

Further, we end up with a 5×5–matrix B containing the mechanical part of the model. For this 5×5–matrix, we see that the last three columns contain possibly non-zero values at the first two row positions; hence, these columns are linearly dependent. From this, it immediately follows that $\lambda = 0$ is an eigenvalue. Applying Gershgorin's Theorem leads to eigenvalues that can be located anywhere in a union of circles centered around the origin. Hence, Gershgorin's Theorem does not exclude any eigenvalues with a negative real part (they reside in the left half of the complex plane). For this reason, we consider the case that $A_{i,j} = 0$ for $(i, j) \in \{7, 8, 9\} \times \{5, 6\}$. Biologically, this leads to

$$\overline{\epsilon_{11}} = \frac{1}{2}, \qquad \overline{\epsilon_{12}} = 0, \qquad \overline{\epsilon_{22}} = \frac{1}{2}. \tag{4.23}$$

We can see this result as follows. Define $U = \{l, p\}$. Application of Gershgorin's Theorem

on the remainder $A_{i \geq 5, j \geq 5}$ for the effective strain yields

$$|\lambda| \leq \left| i(2\pi) \left[\alpha(\overline{\varepsilon_{11}} + \overline{\varepsilon_{22}} - 1) - \beta \overline{\varepsilon_{12}} \right] \right| + \left| i(2\pi\alpha)\overline{\varepsilon_{12}} \right|$$
$$= (2\pi|\alpha|)(\overline{\varepsilon_{11}} + \overline{\varepsilon_{12}} + \overline{\varepsilon_{22}} - 1) - (2\pi|\beta|)\overline{\varepsilon_{12}}, \tag{4.24}$$

$$|\lambda| \leq \left| i(2\pi\alpha)(\overline{\varepsilon_{11}} - \tfrac{1}{2}) \right| + \left| i(2\pi\beta)(\overline{\varepsilon_{22}} - \tfrac{1}{2}) \right|$$
$$= (2\pi|\alpha|)(\overline{\varepsilon_{11}} - \tfrac{1}{2}) + (2\pi|\beta|)(\overline{\varepsilon_{22}} - \tfrac{1}{2}), \tag{4.25}$$

where $\alpha \in U$ and $\beta \in \{x \in U : x \neq \alpha\}$. Define $\mathscr{B}(a, r) = \{z \in \mathbb{C} : |z - a| < r\}$. Then, the mechanical eigenvalues lie in the union of the disks:

$$\lambda_i \in \mathscr{B}_1 \bigcup \mathscr{B}_2 \bigcup \mathscr{B}_3, \tag{4.26}$$

with

$$\mathscr{B}_1 \left(0, (2\pi|\alpha|)(\overline{\varepsilon_{11}} + \overline{\varepsilon_{12}} + \overline{\varepsilon_{22}} - 1) - (2\pi|\beta|)\overline{\varepsilon_{12}} \right),$$
$$\mathscr{B}_2 \left(0, (2\pi|\alpha|)(\overline{\varepsilon_{11}} - \tfrac{1}{2}) + (2\pi|\beta|)(\overline{\varepsilon_{22}} - \tfrac{1}{2}) \right), \tag{4.27}$$

and $\mathscr{B}_3$ is the disk corresponding to the displacement velocity. Hence, to guarantee linear stability for the effective strain, we need:

$$|\alpha|(\overline{\varepsilon_{11}} + \overline{\varepsilon_{12}} + \overline{\varepsilon_{22}} - 1) - |\beta|\overline{\varepsilon_{12}} = 0,$$
$$|\alpha|(\overline{\varepsilon_{11}} - \tfrac{1}{2}) + |\beta|(\overline{\varepsilon_{22}} - \tfrac{1}{2}) = 0. \tag{4.28}$$

This must hold for all $\alpha, \beta \in \mathbb{Z}$, hence linear stability for wavelike perturbations around equilibria ($\alpha, \beta \in \mathbb{Z}_{\neq 0}$) is obtained for $\overline{\varepsilon_{11}} = \tfrac{1}{2}$, $\overline{\varepsilon_{22}} = \tfrac{1}{2}$ and $\overline{\varepsilon_{12}} = 0$. This implies that $A_{i,j} = 0$ for $i \in \{7, 8, 9\}$, $j \in \{5, 6\}$. We note that with these equilibria, we have $\boldsymbol{\varepsilon} \to \mathscr{O}(1)$, hence describing a physical situation in which the model can no longer be applied. In this case, Gershgorin's theorem cannot be used to access the stability criteria, and there are no other strategies to solve the fourth-order polynomial analytically. In order to 'show' that we have stability for our set of parameter values, we provide an empirical argument based on the numerical approximation of the eigenvalues.

The remaining eigenvalues follow from the 5×5–matrix. The eigenvalue $\lambda = 0$ has algebraic multiplicity 3. The other two eigenvalues follow from the upper left 2×2–block matrix and are in addition to that determined by

$$\lambda^2 - (A_{55} + A_{66})\lambda + A_{55}A_{66} - A_{56}A_{65} = 0. \tag{4.29}$$

We note that $A_{56} = A_{65}$. Hence, the remaining eigenvalues are real-valued. Solving the above equation with the *abc*-formula then gives

$$\lambda = \frac{A_{55} + A_{66} \pm \sqrt{(A_{55} + A_{66})^2 - 4(A_{55}A_{66} - A_{56}^2)}}{2}. \tag{4.30}$$

Here, the discriminant

$$D = \left[(2\pi l)^2 - (2\pi p)^2 \right]^2 (\mu_1 + \mu_2)^2 + \tfrac{1}{4} \left[(2\pi l)^2 - (2\pi p)^2 \right]^2 \mu_1^2 +$$
$$4(2\pi l)^2 (2\pi p)^2 \left(\tfrac{1}{2}\mu_2 + \mu_2 \right)^2 \tag{4.31}$$

is always non-negative. For stability, in this case, a necessary condition is that

$$A_{55} + A_{66} \geq \sqrt{(A_{55} + A_{66})^2 - 4(A_{55}A_{66} - A_{56}^2)}. \tag{4.32}$$

Squaring the left- and the right-hand-side gives

$$A_{55}A_{66} - A_{56}^2 \geq 0. \tag{4.33}$$

Substitution of A_{55}, A_{66} and A_{56} gives

$$-\frac{4}{\rho_t}\left(\frac{1}{\rho_t}\left[(2\pi l)^2(\mu_1 + \mu_2) + \tfrac{1}{2}(2\pi p)^2\mu_1\right]\cdot\left[\tfrac{1}{2}(2\pi l)^2\mu_1 + (2\pi p)^2(\mu_1 + \mu_2)\right] - $$
$$((2\pi l)(2\pi p)(\tfrac{1}{2}\mu_1 + \mu_2))^2\right) \leq 0, \tag{4.34}$$

which reduces to

$$\left[\tfrac{1}{2}((2\pi l)^4 + (2\pi p)^4) + (2\pi l)^2(2\pi p)^2\right](\mu_1^2 + \mu_1\mu_2) \geq 0. \tag{4.35}$$

Hence, for all $\mu_1, \mu_2 \geq 0$ and all $l, p \in \mathbb{Z}$, the stability constraint is satisfied. We note that all eigenvalues are real-valued and that equation (2.14) only holds for minor strains. We summarize these results in Theorem 4.2.3.

Theorem 4.2.3. *Let $\{N, M, c, \rho, v_1, v_2, \varepsilon_{11}, \varepsilon_{12}, \varepsilon_{22}\}$ satisfy equations* (2.2)–(2.14). *Further, let $\delta_n = r(1 - \kappa\overline{N})\overline{N}^q > 0$ and $\overline{\rho} = \sqrt{k_\rho/\delta_\rho}$, then*

1. *The equilibria $(N, M, c, \rho, v_1, v_2, \varepsilon_{11}, \varepsilon_{12}, \varepsilon_{22}) = (\overline{N}, 0, 0, \overline{\rho}, 0, 0, \overline{\varepsilon_{11}}, \overline{\varepsilon_{12}}, \overline{\varepsilon_{22}})$, with $\left\{\overline{N}, \overline{\rho}, \overline{\varepsilon_{11}}, \overline{\varepsilon_{12}}, \overline{\varepsilon_{22}}\right\} \in \mathbb{R}_{>0}$, are linearly stable if and only if $\delta_c\overline{\rho} \geq \frac{k_c}{a_c^l}$, and $q\delta_n \leq \kappa r\overline{N}^{1+q}$ for constant states;*

2. *For (nonconstant) waves around the equilibria, linear stability is met if $\delta_c\overline{\rho} \geq \frac{k_c}{a_c^l}$, $q\delta_n \leq \kappa r\overline{N}^{1+q}$, $\mu_1, \mu_2 \geq 0$, $\overline{\varepsilon_{11}} = \frac{1}{2}$, $\overline{\varepsilon_{22}} = \frac{1}{2}$, and $\overline{\varepsilon_{12}} = 0$;*

Remark 4.2.2. *Note that $\delta_c \geq \frac{k_c}{a_c^l\overline{\rho}}$, for $k = 0$ (constant states). Hence, if constant perturbations are stable, then wavelike perturbations are stable. In case δ_c is not large enough, fast oscillating perturbations will vanish, while slow oscillating perturbations will not vanish and can amplify. Further, the mathematical model is actually not suitable for $\overline{\varepsilon_{11}} = \overline{\varepsilon_{22}} = 0.5$; however, this is still a consequence of the above analysis.*

For the empirical 'proof' of the stability constraints, we only consider the eigenvalues $\boldsymbol{\lambda}$ of the 5×5–submatrix of matrix A. We keep the parameter values as in Tables 3.2 and 4.2 and vary $\overline{\varepsilon_{11}}$ and $\overline{\varepsilon_{22}}$ between -1 and 1 with stepsize 0.01, $\overline{\varepsilon_{12}}$ between -1 and 0.5 with stepsize 0.1, and l and p (integers) between 1 and 100. We define

$$S(\overline{\varepsilon_{11}}, \overline{\varepsilon_{22}}, \overline{\varepsilon_{12}}) = \begin{cases} 1, & \text{if } \forall\, l, p \in \mathbb{Z} : Re(\boldsymbol{\lambda}) \geq \mathbf{0} \\ 0, & \text{otherwise} \end{cases}. \tag{4.36}$$
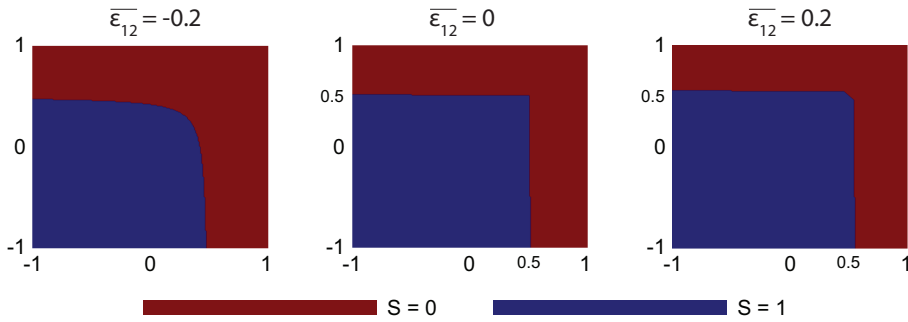
Figure 4.1: Results of the empirical proof of stability for some values of $\overline{\varepsilon_{12}}$. The x- and y-axes show the effective strains $\overline{\varepsilon_{11}}$ and $\overline{\varepsilon_{22}}$, both between -1 and 1. Values for $\overline{\varepsilon_{11}}$ and $\overline{\varepsilon_{22}}$ that yield $Re(\lambda) \geq \mathbf{0}$ for all l, p are colored blue, otherwise red.

Hence, $S = 1$ corresponds to stability, whereas $S = 0$ corresponds to instability. Figure 4.1 shows the results of S for some values of $\overline{\varepsilon_{12}}$. If $\overline{\varepsilon_{12}}$ increases, then the region for stable $\overline{\varepsilon_{11}}$ and $\overline{\varepsilon_{22}}$ values grows. Further, there is symmetry in the line $y = x$. Given the complexity of the fourth-order polynomial, it is unclear what defines these boundaries of stable regions. One can predict that there will not be any stable values for the effective strain in the shown domain if $\overline{\varepsilon_{12}}$ becomes (much) smaller. However, one does not expect the effective strain to become that negative (the model breaks down for these values). Focusing on the origin $(\overline{\varepsilon_{11}}, \overline{\varepsilon_{22}}) = (0,0)$, one can see that for small $|\overline{\varepsilon_{12}}|$, say $|\overline{\varepsilon_{12}}| \leq 0.2$, there is always a stable region around the origin. For values of $|\overline{\varepsilon_{12}}|$ that are larger, which are not interesting from a physical point of view, the stability region may no longer include the origin.

Claim 4.2.1. *Let* $\{N, M, c, \rho, v_1, v_2, \varepsilon_{11}, \varepsilon_{12}, \varepsilon_{22}\}$ *satisfy equations* (2.2)–(2.14). *Let* $\delta_N = r(1 - \kappa \overline{N}) \overline{N}^q > 0$ *and* $\overline{\rho} = \sqrt{k_\rho / \delta_\rho}$, *then for wave-like perturbations around the equilibria, if* $\delta_c \overline{\rho} \geq \frac{k_c}{a_c^{fl}}$, $q \delta_N \leq \kappa r \overline{N}^{1+q}$, *and* $\mu_1, \mu_2 \geq 0$, *then there is a region in the* $(\overline{\varepsilon_{11}}, \overline{\varepsilon_{12}}, \overline{\varepsilon_{22}})-$ *space around* $(\overline{\varepsilon_{11}}, \overline{\varepsilon_{12}}, \overline{\varepsilon_{22}}) = (0,0,0)$ *(the origin), where the model is linearly stable.*

4.2.2 Stability of the (semi-) discrete problem

For the stability of the (semi-) discrete problem, we consider a unit rectangle $\Omega = [0,1]^2$ that we divide into small rectangles with sides h such that $(n+1)h = 1$. At the intersections of the grid lines, we have nodal points where we approximate the variable solutions. We denote the unknowns at node (x_i, y_j) by $z_{i,j}$, $z \in \{N, M, c, \rho, v_1, v_2, \varepsilon_{11}, \varepsilon_{12}, \varepsilon_{22}\}$ and apply finite differences on the eigenvalue problem. Then the *finite difference method*

of the spatial part of the linearized problem (4.1)–(4.3) gives:

$$\lambda N_{i,j} = -D_n \overline{N} \left[\frac{N_{i-1,j} - 2N_{i,j} + N_{i+1,j}}{h^2} + \frac{N_{i,j-1} - 2N_{i,j} + N_{i,j+1}}{h^2} \right] +$$
$$\chi \overline{N} \left[\frac{c_{i-1,j} - 2c_{i,j} + c_{i+1,j}}{h^2} + \frac{c_{i,j-1} - 2c_{i,j} + c_{i,j+1}}{h^2} \right] +$$
$$\left[\delta_n - r\overline{N}^q ((1+q)(1-\kappa\overline{N}) - \kappa\overline{N}) \right] N_{i,j} + r\kappa\overline{N}^{1+q} M_{i,j} -$$
$$\overline{N} \left[\frac{r \cdot r^{\max}}{a_c^I} (1-\kappa\overline{N})\overline{N}^q - k_1 \right] c_{i,j},$$

$$\lambda M_{i,j} = -D_n \overline{N} \left[\frac{M_{i-1,j} - 2M_{i,j} + M_{i+1,j}}{h^2} + \frac{M_{i,j-1} - 2M_{i,j} + M_{i,j+1}}{h^2} \right] + \qquad (4.37)$$
$$\delta_m M_{i,j} - k_1 \overline{N} c_{i,j},$$

$$\lambda c_{i,j} = -D_c \left[\frac{c_{i-1,j} - 2c_{i,j} + c_{i+1,j}}{h^2} + \frac{c_{i,j-1} - 2c_{i,j} + c_{i,j+1}}{h^2} \right] +$$
$$\overline{N} \left[\delta_c \overline{\rho} - \frac{k_c}{a_c^{II}} \right] c_{i,j},$$

$$\lambda \rho_{i,j} = \delta_\rho \overline{\rho}^2 (\eta^{II} - \eta^I) M_{i,j} - \delta_\rho \overline{\rho}^2 \overline{N} \left[\frac{k_\rho^{max}}{a_c^{IV}} + a_c^{III} \right] c_{i,j} + 2\delta_\rho \overline{N}\overline{\rho}\rho_{i,j},$$

for the chemical part of the model, and writing $v_{i,j}^1$ for $v_{1i,j}$ and $\varepsilon_{i,j}^{11}$ for $\varepsilon_{11i,j}$ etcetera gives

$$\rho_t \lambda v_{i,j}^1 = -\left(\mu_1 + \mu_2 \right) \frac{v_{i-1,j}^1 - 2v_{i,j}^1 + v_{i+1,j}^1}{h^2} - \frac{\mu_1}{2} \frac{v_{i,j-1}^1 - 2v_{i,j}^1 + v_{i,j+1}^1}{h^2} - \qquad (4.38)$$
$$\left[\frac{\mu_1}{2} + \mu_2 \right] \frac{v_{i-1,j-1}^2 - v_{i-1,j+1}^2 - v_{i+1,j-1}^2 + v_{i+1,j+1}^2}{4h^2} -$$
$$\frac{E\sqrt{\overline{\rho}}}{1+\nu} \left[\frac{\varepsilon_{i,j+1}^{12} - \varepsilon_{i,j-1}^{12}}{2h} + \frac{1-\nu}{1-2\nu} \frac{\varepsilon_{i+1,j}^{11} - \varepsilon_{i-1,j}^{11}}{2h} + \frac{\nu}{1-2\nu} \frac{\varepsilon_{i+1,j}^{22} - \varepsilon_{i-1,j}^{22}}{2h} \right] -$$
$$\frac{E}{2\sqrt{\overline{\rho}}(1+\nu)} \left[\overline{\varepsilon}_{12} + \overline{\varepsilon}_{11} + \frac{\nu}{1-2\nu} \left(\overline{\varepsilon}_{11} + \overline{\varepsilon}_{22} \right) \right] \frac{\rho_{i+1,j} - \rho_{i-1,j}}{2h} -$$
$$\xi \frac{\overline{\rho}}{R^2 + \overline{\rho}^2} \frac{M_{i+1,j} - M_{i-1,j}}{2h},$$

for v_1 (again, the equation for v_2 is similar), and

$$\lambda \varepsilon_{i,j}^{11} = \overline{\epsilon}_{12} \left[\frac{v_{i+1,j}^2 - v_{i-1,j}^2}{2h} - \frac{v_{i,j+1}^1 - v_{i,j-1}^1}{2h} \right] + (\overline{\epsilon}_{11} + \overline{\epsilon}_{22} - 1) \frac{v_{i+1,j}^1 - v_{i-1,j}^1}{2h} +$$
$$\zeta \overline{N} \overline{\epsilon}_{11} c_{i,j}, \qquad (4.39)$$
$$\lambda \varepsilon_{i,j}^{12} = \left[\overline{\epsilon}_{22} - \frac{1}{2} \right] \frac{v_{i+1,j}^2 - v_{i-1,j}^2}{2h} + \left[\overline{\epsilon}_{11} - \frac{1}{2} \right] \frac{v_{i,j+1}^1 - v_{i,j-1}^1}{2h} + \zeta \overline{N} \overline{\epsilon}_{12} c_{i,j},$$

for the effective strains $\varepsilon_{11}, \varepsilon_{12}$ (again, the equation for ε_{22} is similar). We perform von Neumann eigenvalue and stability analysis. Let

$$z_{k,j} = \frac{1}{n^2} \sum_{\beta=1}^{n} \sum_{\gamma=1}^{n} \hat{z}_{\beta,\gamma} e^{-2\pi\beta khi} e^{-2\pi\gamma jhi}, \tag{4.40}$$

for $z \in \{N, M, c, \rho, v_1, v_2, \varepsilon_{11}, \varepsilon_{12}, \varepsilon_{22}\}$, where i again represents the imaginary unit number. Substitution of (4.40) in equations (4.37)–(4.39), multiplication by $e^{2\pi lkhi} e^{2\pi pjhi}$, using Euler's formula, $2 - 2\cos(2\pi x) = 4\sin^2(\pi x)$ and $\left[e^{ix}e^{iy} - e^{ix}e^{-iy} - e^{-ix}e^{iy} + e^{-ix}e^{-iy} \right]/4 = -\sin(x)\sin(y)$ results in

$$\lambda \hat{N}_{\boldsymbol{\beta}} = \frac{4\overline{N}}{h^2} \left[\sin^2(\pi lh) + \sin^2(\pi ph) \right] \left[D_n \hat{N}_{\boldsymbol{\beta}} - \chi \hat{c}_{\boldsymbol{\beta}} \right] +$$
$$\left[\delta_n - r\overline{N}^q ((1+q)(1-\kappa\overline{N}) - \kappa\overline{N}) \right] \hat{N}_{\boldsymbol{\beta}} +$$
$$r\kappa\overline{N}^{1+q} \hat{M}_{\boldsymbol{\beta}} - \overline{N} \left[\frac{r \cdot r^{\max}}{a_c^I} (1 - \kappa\overline{N})\overline{N}^q - k_1 \right] \hat{c}_{\boldsymbol{\beta}},$$

$$\lambda \hat{M}_{\boldsymbol{\beta}} = \left[\frac{4D_n\overline{N}}{h^2} \left[\sin^2(\pi lh) + \sin^2(\pi ph) \right] + \delta_m \right] \hat{M}_{\boldsymbol{\beta}} - k_1\overline{N}\hat{c}_{\boldsymbol{\beta}}, \tag{4.41}$$

$$\lambda \hat{c}_{\boldsymbol{\beta}} = \left[\frac{4D_c}{h^2} \left[\sin^2(\pi lh) + \sin^2(\pi ph) \right] + \overline{N} \left[\delta_c \overline{\rho} - \frac{k_c}{a_c^{II}} \right] \right] \hat{c}_{\boldsymbol{\beta}},$$

$$\lambda \hat{\rho}_{\boldsymbol{\beta}} = \delta_\rho \overline{\rho}^2 (\eta^{II} - \eta^I) \hat{M}_{\boldsymbol{\beta}} - \delta_\rho \overline{\rho}^2 \overline{N} \left[\frac{k_\rho^{max}}{a_c^{IV}} + a_c^{III} \right] \hat{c}_{\boldsymbol{\beta}} + 2\delta_\rho \overline{N}\overline{\rho}\hat{\rho}_{\boldsymbol{\beta}},$$

for the chemical part of the model,

$$\rho_t \lambda \hat{v}_{\boldsymbol{\beta}}^1 = \frac{4}{h^2} \left[\sin^2(\pi lh)(\mu_1 + \mu_2) + \tfrac{1}{2}\sin^2(\pi ph)\mu_1 \right] \hat{v}_{\boldsymbol{\beta}}^1 + \tag{4.42}$$
$$\frac{\sin(2\pi lh)\sin(2\pi ph)}{h^2} \left(\tfrac{1}{2}\mu_1 + \mu_2 \right) \hat{v}_{\boldsymbol{\beta}}^2 +$$
$$i\frac{E\sqrt{\overline{\rho}}}{h(1+v)} \left[\sin(2\pi ph)\hat{\varepsilon}_{\boldsymbol{\beta}}^{12} + \sin(2\pi lh) \left(\frac{1-v}{1-2v}\hat{\varepsilon}_{\boldsymbol{\beta}}^{11} + \frac{v}{1-2v}\hat{\varepsilon}_{\boldsymbol{\beta}}^{22} \right) \right] +$$
$$i\frac{\sin(2\pi lh)}{h} \left\{ \frac{E}{2\sqrt{\overline{\rho}}(1+v)} \left[\overline{\varepsilon_{12}} + \overline{\varepsilon_{11}} + \frac{v}{1-2v} \left(\overline{\varepsilon_{11}} + \overline{\varepsilon_{22}} \right) \right] \hat{\rho}_{\boldsymbol{\beta}} + \frac{\xi\overline{\rho}}{R^2 + \overline{\rho}^2} \hat{M}_{\boldsymbol{\beta}} \right\},$$

for the displacement velocity v_1 (the equation for v_2 is similar and yields an equal result), and

$$\lambda \hat{\varepsilon}_{\boldsymbol{\beta}}^{11} = i \left\{ \frac{\sin(2\pi lh)}{h}(1 - \overline{\varepsilon_{11}} - \overline{\varepsilon_{22}}) + \frac{\sin(2\pi ph)}{h}\overline{\varepsilon_{12}} \right\} \hat{v}_{\boldsymbol{\beta}}^1 - i\frac{\sin(2\pi lh)}{h}\overline{\varepsilon_{12}}\hat{v}_{\boldsymbol{\beta}}^2 + \zeta\overline{N}\overline{\varepsilon_{11}}\hat{c}_{\boldsymbol{\beta}},$$

$$\lambda \hat{\varepsilon}_{\boldsymbol{\beta}}^{12} = i\frac{\sin(2\pi ph)}{h}(\tfrac{1}{2} - \overline{\varepsilon_{11}})\hat{v}_{\boldsymbol{\beta}}^1 + i\frac{\sin(2\pi lh)}{h}(\tfrac{1}{2} - \overline{\varepsilon_{22}})\hat{v}_{\boldsymbol{\beta}}^2 + \zeta\overline{N}\overline{\varepsilon_{12}}\hat{c}_{\boldsymbol{\beta}},$$
$$\tag{4.43}$$

for the effective strains ε_{11} and ε_{12} (the equation for ε_{22} is similar and yields an equal result). As an example, the derivation of equation (4.42) is given in the Appendix 4.4.

The equations (4.41)–(4.43) are in the form $\lambda z = Cz$ with the matrix C as in (4.21). Hence, the eigenvalues are found in the same way as in the continuous case. Note that, since the overall system has the form $\underline{y}' + A\underline{y} = 0$, the discrete system is linearly stable if and only if the real part of the eigenvalues is non-negative, hence we need:

$$\frac{4D_n\overline{N}}{h^2}\left[\sin^2(\pi lh) + \sin^2(\pi ph)\right] - r\overline{N}^q((1+q)(1-\kappa\overline{N}) - \kappa\overline{N}) + \delta_n \geq 0,$$

$$\frac{4D_n\overline{N}}{h^2}\left[\sin^2(\pi lh) + \sin^2(\pi ph)\right] + \delta_m \geq 0,$$

$$\frac{4D_c}{h^2}\left[\sin^2(\pi lh) + \sin^2(\pi ph)\right] + \overline{N}\left[\delta_c\overline{\rho} - \frac{k_c}{a_c^{II}}\right] \geq 0,$$

$$2\delta_\rho\overline{N}\overline{\rho} \geq 0,$$

$$(4.44)$$

for the chemical part of the model. To guarantee linear stability, the first requirement of equations (4.44) states $q\delta_n \leq \kappa r\overline{N}^{1+q}$, given $\delta_n = r(1-\kappa\overline{N})\overline{N}^q$. The second and fourth eigenvalues meet the stability condition independent of the chosen parameter values, given that the parameter values are positive. Finally, the third requirement states $\delta_c\overline{\rho} \geq \frac{k_c}{a_c^{II}}$. These statements remain the same when the horizontal and vertical step sizes are unequal ($\Delta x \neq \Delta y$).

For the mechanical part of the model, we follow the same procedure as in Section 4.2.1. Again, we end up with a 5×5–matrix D containing the mechanical part of the model. Now, from Gershgorin (not shown) it follows that $\overline{\epsilon_{11}} = \frac{1}{2}, \overline{\epsilon_{12}} = 0$, and $\overline{\epsilon_{22}} = \frac{1}{2}$, and $C_{i,j} = 0$ for $i \in \{7,8,9\}$, $j \in \{5,6\}$. Therefore, for linear stability, we need

$$C_{55}C_{66} - C_{56}^2 \geq 0. \tag{4.45}$$

Substitution of C_{55}, C_{66} and C_{56} gives

$$-4\left(\frac{4}{\rho_t h^2}\left[\sin^2(\pi lh)(\mu_1 + \mu_2) + \tfrac{1}{2}\sin^2(\pi ph)\mu_1\right]\cdot\right.$$

$$\frac{4}{\rho_t h^2}\left[\tfrac{1}{2}\sin^2(\pi lh)\mu_1 + \sin^2(\pi ph)(\mu_1 + \mu_2)\right] -$$

$$\left.\left[\frac{1}{\rho_t}\frac{\sin(2\pi lh)\sin(2\pi ph)}{h^2}(\mu_1 + \mu_2)\right]^2\right) \leq 0, \quad (4.46)$$

which reduces to

$$\mu_1^2\left[8(\sin^4(\pi lh) + \sin^4(\pi ph)) + 4\sin^2(\pi lh)\sin^2(\pi ph)\left[5 - 2\cos^2(\pi lh)\cos^2(\pi ph)\right]\right] +$$

$$\mu_1\mu_2\left[8(\sin^4(\pi lh) + \sin^4(\pi ph)) + 16\sin^2(\pi lh)\sin^2(\pi ph)\left[2 - \cos^2(\pi lh)\cos^2(\pi ph)\right]\right] +$$

$$8\mu_2^2\sin^2(\pi lh)\sin^2(\pi ph)\left[2 - \cos^2(\pi lh)\cos^2(\pi ph)\right] \geq 0. \quad (4.47)$$

Here, we used $\sin(2\pi xh) = 2\sin(\pi xh)\cos(\pi xh)$. Note that the subtractions by the cosines are bounded from above. Therefore, for all μ_1, μ_2 and all $l, p \in \mathbb{Z}$, equation (4.46) is satisfied. To conclude, we have demonstrated that if the equilibrium is stable in the continuous problem, it is also stable in the semi-discrete problem.

There exists a consistency between the stability criteria of the continuous problem and the stability criteria of the discrete problem. We show this by writing $\sin(x)$ and $\sin^2(x)$ as a Taylor series. Substitution into the third equation in (4.44) yields:

$$D_c[(2\pi l)^2 + (2\pi p)^2] + \mathcal{O}(h^2) + \overline{N}\left[\delta_c\overline{\rho} - \frac{k_c}{a_c^{II}}\right] \geq 0. \tag{4.48}$$

Comparison to the third equation in (4.22)

$$D_c[(2\pi l)^2 + (2\pi p)^2] + \overline{N}\left[\delta_c\overline{\rho} - \frac{k_c}{a_c^{II}}\right] \geq 0 \tag{4.49}$$

yields a difference in eigenvalues of order $\mathcal{O}(h^2)$. Note that this difference in the same order is found for the other eigenvalues. We summarize the results in Theorem 4.2.4.

Theorem 4.2.4. *Let $\{N, M, c, \rho, v_1, v_2, \varepsilon_{11}, \varepsilon_{12}, \varepsilon_{22}\}$ satisfy the semi-discrete spatial differences version of equations (4.37)–(4.39), then stability in the fully continuous problem implies stability for the semi-discrete formulation.*

Corollary 4.2.1. *Let $\{N, M, c, \rho, v_1, v_2, \varepsilon_{11}, \varepsilon_{12}, \varepsilon_{22}\}$ satisfy the semi-discrete spatial differences version of equations (4.37)–(4.39). Let $\delta_n = r(1 - \kappa\overline{N})\overline{N}^q$ and $\overline{\rho} = \sqrt{k_\rho/\delta_\rho}$. Then the constant equilibria are unconditionally stable for the trapezoid rule and the Euler backward method as long as $\delta_c\overline{\rho} \geq \frac{k_c}{a_c^{II}}$ and $q\delta_n \leq \kappa r\overline{N}^{1+q}$. Furthermore, the Euler backward method is A-stable.*

4.3 Numerical validation

We need to validate whether the linear stability conditions we have derived also hold in a finite element setting where the fully nonlinearly coupled model is considered. We consider a rectangle $\Omega = [0, L]^2$ that we subdivide into small rectangles (quadrilaterals) with sides $\Delta x = \Delta y$. Then, we convert the regular mesh to a triangulation. The quadrilateral mesh faces are converted to triangles by splitting the faces into triangles according to the cross division of quadrilateral.

We experimentally evaluate the convergence of the numerical method in a domain of $[0, 3.2]^2$ cm^2 with a wound between $[0, 1.2]$ cm^2, which represents a quarter of a domain of the modeled skin on which we perform computations. The transition from healthy to injured skin is steep, and we account for this steepness of gradients through an interval of 0.8 cm. In this transition, the initial conditions vary between the equilibria and the initial wound densities. Within the wound, we assume that 2000 fibroblast cells/cm^3, 10^8 g/cm^3 signaling molecules, and 0.01125 g/cm^3 collagen are present. We model the slope of the variables with sine functions.

We divide the computational domain into $n_x \times n_y = (3.2/h)^2$ elements with $h \in \{0.2, 0.1, 0.05\}$. In order to have mesh convergence of the numerical solution of second order, we choose $\Delta t = h^2$. We simulate contraction for one day and report the densities of the variables (the solutions). We compute the convergence order results using the L_2 error norm. Let $\lim_{h\to 0} z_h(\mathbf{x}, 1) = z(\mathbf{x}, 1)$ denote the true density of variable z on day 1 and $z_{0.05}(\mathbf{x}, 1) =: z_{h_{\text{ref}}}$ the solution in the last simulation (i.e. the reference, the one computed

using the highest numerical resolution). We approximate the errors with the following error definition:

$$\epsilon_{L^2}(z_h) = h\sqrt{\sum_{i=1}^{289}(z_h(\mathbf{x}_{i,289},1) - z_{h_{\text{ref}}}(\mathbf{x}_{i,289},1))^2}, \qquad (4.50)$$

where the grid-points $\mathbf{x}_{i,n}$ correspond to the grid-points in the simulation with $h = 0.2$ ($n = 289$ nodes). Hence, we evaluate the solution to the equations between simulations on a fixed set of initial nodes. Table 4.1 shows the results for the L_2 error.

Table 4.1: Overview of the averaged slopes.

Var.	N	M	c	ρ	ν_1	ν_2	ε_{11}	ε_{12}	ε_{22}
ϵ_{L_2}	2.236	2.815	2.489	2.877	2.923	2.923	2.230	2.276	2.230

The slopes correspond to the L_2 errors of the variables on the total computational domain. The columns show the averaged slopes for the variables. The reference is the solution in which $h = 0.05$.

All the L_2 errors decrease consistently as h becomes smaller (figures not shown), and the values in the table show an order of convergence above $\mathcal{O}(h^2)$.

To validate the stability constraint numerically, we perturb the initial conditions around equilibria using sine functions, and we vary the parameter δ_c. Hence, we fix all parameters except for the signaling molecule decay rate. The fixed parameter values are the same as in Table 3.2, except for the parameters shown in Table 4.2.

Table 4.2: Overview of the parameter values used for the simulations that differ from the parameter values in Table 3.2 or those that are introduced in the two-dimensional model.

Symbol	Value	Dimension	Reference
μ_1	10^2	$(\text{N day})/\text{cm}^2$	[1]
μ_2	10^2	$(\text{N day})/\text{cm}^2$	[1]
ν	4.9×10^{-1}	-	[70]
E	3.2×10	$\text{N}/((\text{g cm})^{0.5})$	[70]

Shown are the symbols, the values, the dimensions, and the references.

For the time integration, we use an initial step of $\Delta t = 10^{-2}$ days until half a day is simulated, after which we increase the timestep by $\Delta t_{\text{new}} = \min\{2, 1.1 \times \Delta t\}$. We use a domain of $[0,1]^2$ cm^2 that we first divide into equilateral elements (rectangles) with $h = 0.05$, then we convert this mesh to an equilateral triangulation by cross division of quadrilaterals. For the initial conditions, we vary the wavenumber using two levels: $k \in \{1,2\}$. We perturb the initial fibroblast cell and collagen density by using a product of sine functions with an amplitude of 10 cells/cm^3 and 10^{-2} g/cm^3, respectively, which is possible because the equilibrium fibroblast cell density and the equilibrium collagen density are non-zero. We use a product of uniform splines with $2k+1$ knots for the initial myofibroblast cell density and signaling molecule density. On the boundaries, the knots have zero

value, and between the values are 3 and 1 cells/cm^3 for the myofibroblasts and 2×10^{-7} and 5×10^{-8} g/cm^3 for the signaling molecules. This way, we ensure that the myofibroblast cell density and the signaling molecule density values are positive. We note that, because of the product of splines, these initial amplitudes become smaller. The initial amplitudes of the displacement velocity density v_1 is 5×10^{-1}. To ensure symmetry, we set the initial condition $v_2(\mathbf{x}; 0) = -v_1(\mathbf{x}; 0)$. We do not perturb the effective strain densities and set $\varepsilon_{11}(\mathbf{x}; 0) = \varepsilon_{12}(\mathbf{x}; 0) = \varepsilon_{22}(\mathbf{x}; 0) = 0$.

For stability, Theorem 4.2.3 further requires that $\delta_c \overline{\rho} \geq k_c / a_c^{II}$ in case $l = 0$. We choose to vary the signaling molecule decay rate δ_c using three levels: $2 \times 10^{-4}, 3 \times 10^{-4}$ and 5×10^{-4} cm^6/(cells g day), where the first two values do not meet the stability condition.

4.3.1 Stable values

In the first simulation, we take $\delta_c = 5 \times 10^{-4}$ cm^6/(cells g day) and $k = 1$, and we simulate over a time interval of 200 days. We note that this signaling molecule decay rate δ_c meets the stability criterium. Figures 4.2–4.4 show the results. The first figure, Figure 4.2, shows the evolution of the displacement velocities for the values of input parameters within the stability regime.
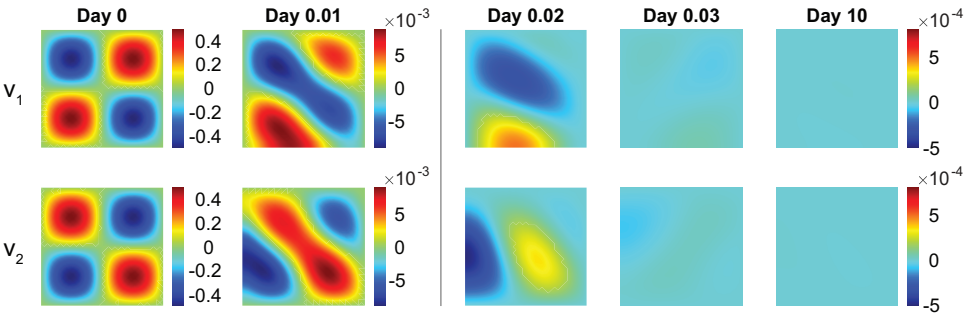
Figure 4.2: Evolution of the displacement velocity densities for $\delta_c = 5 \times 10^{-4}$ cm^6/(cells g day). Tables 3.2 and 4.2 show the values of the other parameters. The upper plots show the displacement velocity v_1, and the lower plots show the displacement velocity v_1. The shown domains are $(0, 1)^2$ cm^2 and the color bars show the displacement velocity in cm/day. For both v_1 and v_2, the first two plots have different color bars, and the last three plots share the same color bar shown on the right.

The displacement velocity densities move to equilibria at a rapid pace. In the first time integration, the densities drop two orders from 5×10^{-1} to 5×10^{-3} within 0.01 day ($\approx$ 15 minutes). The plots show that the peaks in the regions $(x, y) = \{0 \leq x \leq 0.5 \leq y \leq 1 \wedge 0 \leq y \leq 0.5 \leq x \leq 1\}$ merge (i.e., the top left and bottom right corners, negative values for v_1 and positive values for v_2). The peaks in the regions $(x, y) = \{0 \leq x, y \leq 0.5\}$ (i.e., the bottom left corners) shift to the edges of the computational domain, the one in v_1 shifting to the horizontal axis of symmetry, and the one in v_2 shifting to the vertical axis of symmetry. These variations in the displacement velocities are still visible on day 0.02. The peaks in the regions $(x, y) = \{0.5 \leq x, y \leq 1\}$ (i.e., the top right corners) disappear within this time. The densities drop one order further towards equilibria in the next

quarter of an hour. Within ten days, the displacement velocity densities converge to equilibria, following the stability theory.

Figure 4.3 shows the evolution of the effective strains for the values of input parameters within the stability regime.
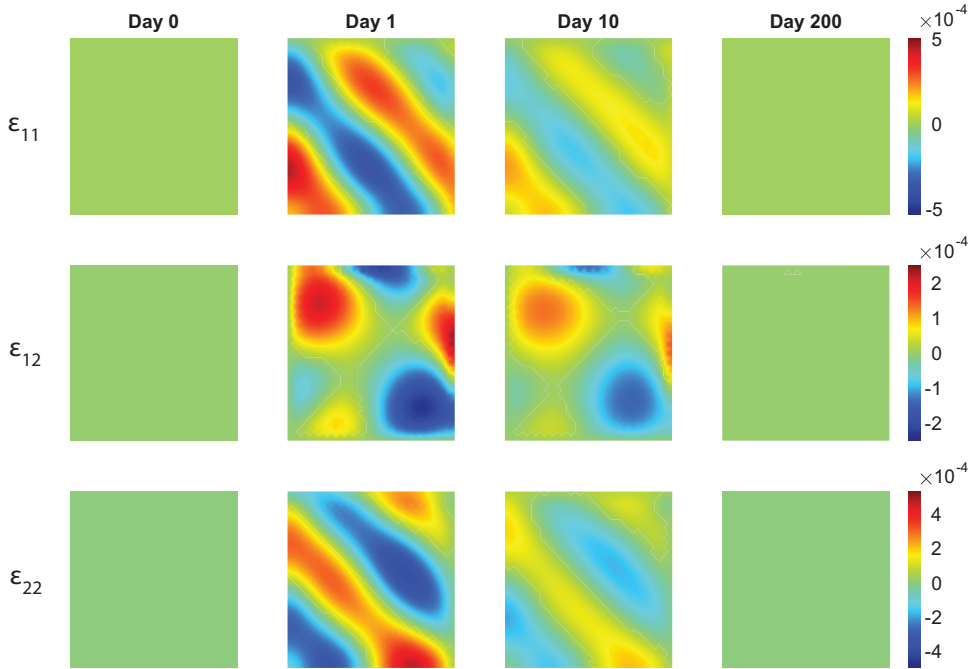
Figure 4.3: Evolution of the effective strain densities for $\delta_c = 5 \times 10^{-4}$ cm^6/(cells g day). Tables 3.2 and 4.2 show the values of the other parameters. The upper, middle and lower plots show the effective strains $\varepsilon_{11}, \varepsilon_{12}$, and ε_{22}. The shown domains are $(0,1)^2$ cm^2, and the color bars show the effective strain (no unit).

The effective strain densities change from the equilibria to perturbations on the first day of the simulation because of the initial perturbations in the other variable densities. We see that diagonal tensions arise in the effective strain densities $\varepsilon_{11}(\mathbf{x};1)$ and $\varepsilon_{22}(\mathbf{x};1)$, while it is more circular for the effective strain density $\varepsilon_{12}(\mathbf{x};1)$. Here, positive and negative values alternate. These diagonal tensions disappear gradually between day 10 and day 200 as the effective strain densities move to the equilibria $\varepsilon_{11}(\mathbf{x};200) = \varepsilon_{12}(\mathbf{x};200) = \varepsilon_{11}(\mathbf{x};200) = \mathbf{0}$. Note that the theory (Theorem 4.2.3 part 1) states that the constant state equilibria $\overline{\varepsilon_{11}}, \overline{\varepsilon_{12}}, \overline{\varepsilon_{22}} \in \mathbb{R}$ are stable.

Figure 4.4 shows the evolution of the chemicals for the values of input parameters within the stability regime. All the plots show that the perturbed chemical densities move gradually toward the equilibria. For the fibroblast cell density, the perturbation leaves a few fibroblasts in the origin of the computational domain on day 25. It takes up to 200 days to move the cell density toward the equilibrium $N = 10^4$ cells/cm^3. For the myofibroblast cell density, no cells are present on day 120 as the perturbed cell density moves
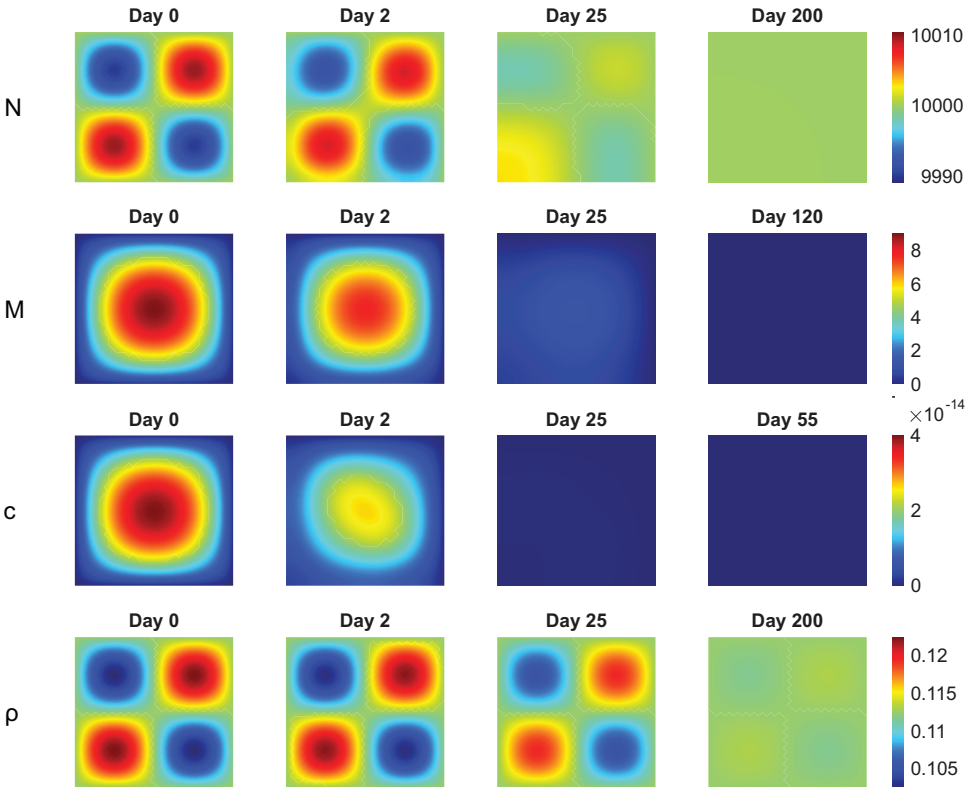
Figure 4.4: Evolution of the chemical densities for $\delta_c = 5 \times 10^{-4}$ cm^6/(cells g day). Tables 3.2 and 4.2 show the values of the other parameters. From top to bottom, the plots show the fibroblasts (N), the myofibroblasts (M), the signaling molecules (c), and collagen (ρ). The shown domains are $(0,1)^2$ cm^2, and the color bars show the (myo) fibroblasts in cells/cm^3 and the signaling molecules and collagen in g/cm^3.

quickly and gradually toward the equilibrium $M = 0$ cells/cm^3. The perturbed signaling molecule density moves even quicker toward the equilibrium $c = 0$ g/cm^3, having the perturbations almost vanished on day 25. The perturbed collagen density takes longer to move to equilibrium as it takes more than 25 days, and on day 200, a slight perturbation is still visible. From this figure, we can conclude that the signaling molecule density moves toward the equilibrium first, after which the myofibroblast cell density moves toward the equilibrium. It takes longer for the fibroblast cell and collagen densities to move toward the equilibria, taking more time for collagen for the current input values. Overall, the perturbations disappear gradually with stable parameter values, and the numerical method behaves stably.

From a biological perspective, minor variations in the fibroblast cell and collagen density already initialize long-term healing. Fibroblasts move toward the center of the wound, and collagen regeneration takes over half a year. Variations arise in the effective strain, after which the tensions disappear.

4.3.2 Unstable signaling molecule decay rate not too low

In the next simulation, we take $\delta_c = 3 \times 10^{-4}$ cm^6/(cells g day) and $k = 2$. We note that this parameter value does not meet the stability criterium. We only present a few figures to avoid too many figures in this chapter.

Likely, as in Figure 4.2, the perturbed displacement velocity densities move gradually toward equilibria in this simulation (figure not shown). In the first step of time integration, the densities align in a similar pattern as we have seen before, decreasing from order $\mathcal{O}(10^{-1})$ to $\mathcal{O}(10^{-3})$. However, in this simulation, in the next timestep, the densities decrease to order $\mathcal{O}(10^{-5})$ in contrast to the order $\mathcal{O}(10^{-4})$ in Figure 4.2.

We see a different evolution for the effective strains and the chemicals. We distinguish between evolution in the *early* and the *later* stage of the simulation.

We see a similar pattern in the early stage of the simulation for the effective strains, as shown in Figure 4.3. For the effective strains ε_{11} and ε_{22}, the tensions in the densities are diagonal and peak on day 5. The peaks diminish in magnitude in the first 51 days (figure not shown). The effective strain ε_{12} density shows the same intensity of variations on day 5, which are circular and alternating between positive and negative values, like in the stable simulation. However, Figure 4.5 shows this pattern changes after 51 days.
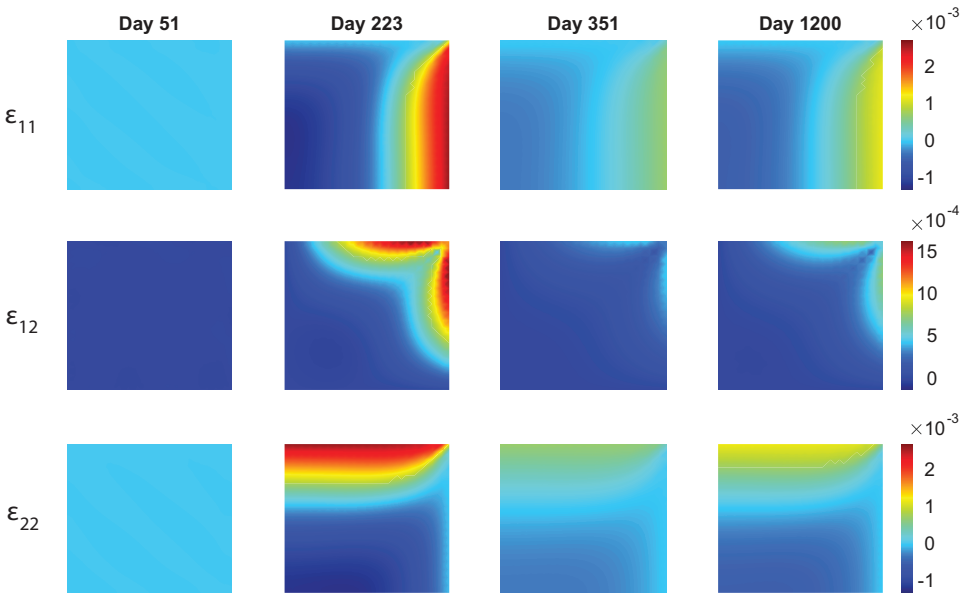
Figure 4.5: Evolution of the effective strain densities for $\delta_c = 3 \times 10^{-4}$ cm^6/(cells g day). Tables 3.2 and 4.2 show the values of the other parameters. The upper, middle and lower plots show the effective strains $\varepsilon_{11}, \varepsilon_{12}$, and ε_{22}. The shown domains are $(0,1)^2$ cm^2, and the color bars show the effective strain.

Unlike the equilibria found in the simulation with stable parameter values, the effective strain densities increase intensely in variation up to day 223 (the second column plots). For the effective strain ε_{11} this is an increase on the right edge of the computational domain, for the effective strain ε_{22} on the top edge, and the effective strain ε_{12} around the top right corner. In opposite directions, these densities decreased. For example, we see

a decrease on the vertical axis of symmetry for the effective strain ε_{11}. After these peaks of intensities in the effective strain densities on day 223, the densities gradually decrease until day 351 and increase in intensity until they reach equilibrium on day 1200. Although it is difficult to see, in this 2D figure, the effective strain densities oscillate around the (new) equilibria. Compared to the simulation with stable parameter values, we see an increase in the intensity of the same order for ε_{12}, albeit with more significant numbers. We note that the order of magnitude may also result from the larger wavenumber ($k = 2$) in the initial perturbations.

The early evolution of the chemicals for $\delta_c = 3 \times 10^{-4}$ cm^6/(cells g day) is comparable to the evolution of the chemicals for $\delta_c = 5 \times 10^{-4}$ cm^6/(cells g day) (figure not shown). In the first 51 days, the perturbed fibroblast and myofibroblast cell densities move gradually toward equilibria, and the perturbed collagen density moves gradually toward equilibrium in the first 119 days. However, the perturbed signaling molecule density does not move to the expected equilibrium. Figure 4.6 shows the early evolution of the signaling molecule density.
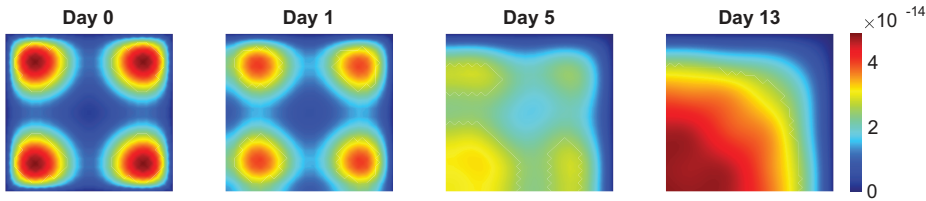
Figure 4.6: Early evolution of the signaling molecule density for $\delta_c = 3 \times 10^{-4}$ cm^6/(cells g day) in the first 13 days. Tables 3.2 and 4.2 show the values of the other parameters. The shown domains are $(0, 1)^2$ cm^2, and the color bars show the signaling molecules in g/cm^3.

Unlike the evolution of the perturbed signaling molecule density for stable parameter values shown in Figure 4.4, the perturbations in the signaling molecule density do not disappear in the first 13 days for an unstable signaling molecule decay rate. The initial peaks of about 4×10^{-14} cm^6/(cells g day) decrease in the first few days. At the same time, these peaks merge and shift toward the origin as they decrease further in the first five days. The peaks continue merging, completed within 13 days; however, the signaling molecule density increases strongly in the origin of the computational domain. In the beginning, this increase does not significantly affect the other chemicals; however, after day 51, it causes a considerable difference.

Figure 4.7 shows the evolution of the chemicals in the later stage of the simulation for $\delta_c = 3 \times 10^{-4}$ cm^6/(cells g day). On day 51, it seems that the chemical densities are in the equilibria $N = 10^4$ cells/cm^3, $M = 0$ cells/cm^3, $c = 0$ g/cm^3, and $\rho = 0.1125$ g/cm^3. However, these densities do not remain in and around equilibria. Note the orders of the signaling molecule concentration: 10^{-10} g/cm^3 on day 200 compared to the order 10^{-14} g/cm^3 on day 13 (see Figure 4.6). After day 13, in the origin of the computational domain, the signaling molecule density increases enormously until day 200, after which the density drops back toward equilibrium until day 317. The signaling molecule density then rises to a new equilibrium on day 1200, which shows a clear oscillation. Since the signaling molecule density increases so much up to day 200 in the origin of the computa-
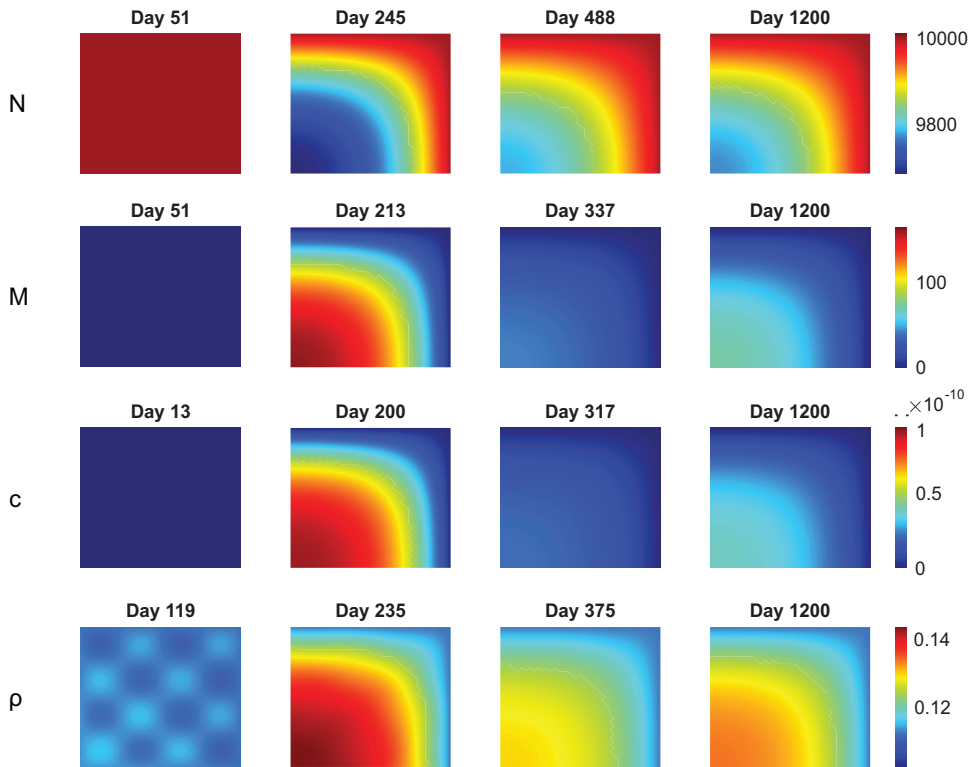
Figure 4.7: Evolution of the chemicals for $\delta_c = 3 \times 10^{-4}$ cm^6/(cells g day). Tables 3.2 and 4.2 show the values of the other parameters. From top to bottom, the plots show the fibroblasts (N), the myofibroblasts (M), the signaling molecules (c), and collagen (ρ). The shown domains are $(0,1)^2$ cm^2, and the color bars show the (myo) fibroblasts in cells/cm^3 and the signaling molecules and collagen in g/cm^3.

tional domain, the fibroblast cell density decreases because of myofibroblast differentiation, and the collagen density increases. These changes in densities are because signaling molecules stimulate the differentiation and production of myofibroblasts (equation (2.7)), stimulate the production of collagen, and inhibit the decay of collagen (equation (2.10)). Further, myofibroblasts also stimulate collagen production.

The myofibroblast cell density reaches a maximum on day 213, the collagen density on day 235, and the fibroblast cell density on day 245. After the signaling molecule density reaches a minimum on day 317, we see that the myofibroblast cell density reaches a minimum on day 337, the collagen density on day 375, and the fibroblast cell density on day 448. After these days, such an oscillating effect around new equilibria is visible, which converges on day 1200. The result is a permanently reduced number of fibroblasts, a permanently increased number of myofibroblasts, and a permanently elevated concentration of signaling molecules and collagen, at the origin of the computational domain (i.e., the center of the burn). Taken together, with an unstable signaling molecule decay rate not too low, the numerical method initially seems to behave like a stable regime.

This stable behavior changes at a later stage of simulation time, where the numerical method behaves stable enough to let the chemical densities reach new equilibria in an oscillatory way.

From a biological perspective, we can state that an increased expression of signaling molecules (because of their reduced decay) can lead to a period in which a wound fluctuates in contraction. This contraction fluctuation is because the number of (migrating) myofibroblasts increases and decreases. In the beginning, the wound can heal well. However, because of the continued signaling, the scar will fluctuate in thickness and stiffness because of the present collagen concentration. The scar is also highly subject to contraction because of the abundance of myofibroblasts present. The abundance of myofibroblasts and the increased collagen concentration may signify hypertrophy.

We may associate the excessive deposition of collagen with keloids, and hypertrophic scars [66]. Abnormal TGF-β signaling in myofibroblasts is associated with the formation of hypertrophic scars [67]. Given our study, it is likely that such a situation arises because of a lower decay rate of signaling molecules. Furthermore, hypertrophic scars develop 1 to 2 months after injury, while keloids develop months to years after the initial injury. This period is consistent with our simulations showing that the abundance of myofibroblasts and collagen occurs after a few months, while the increased expression of signaling molecules occurs within a few weeks. Furthermore, experiments suggest that the hyper-proliferation of fibroblasts in hypertrophic scars can be reversed once their stimulation, such as the abundance of growth factors and cytokines, is abolished [66]. Our 2D simulation partially reflected this. When we turn off the stimulation of signaling molecule expression at a later stage by setting the density to equilibrium, we see the (myo)fibroblast cell densities and the collagen density change. The myofibroblasts seem to disappear, the collagen density recovers, and the fibroblast cell density recovers. However, with three cells/cm^3 myofibroblasts left in the center of the scar after 47 days after this reset, the fibroblast cell density does not increase above 9865 cells/cm^3, and the collagen density does not go below 0.1234 g/cm^3. The numerical method does not converge and decreases the timestep. We, therefore, set the myofibroblast cell density to equilibrium on day 1247 and see the collagen density move to equilibrium within 411 days and the fibroblast cell density within 436 days. Thus, according to this simulation, restoring the fibroblast cell and collagen density is possible when both the signaling molecules and myofibroblasts disappear. Though, it then still takes over a year to repair the defects. Hence, given that the overexpression of signaling molecules occurs in the first weeks, we recommend monitoring this expression to intervene at an early stage when necessary.

4.3.3 Unstable signaling molecule decay rate too low

In the last simulation, we take $\delta_c = 2 \times 10^{-4}$ cm^6/(cells g day) and $k = 2$. We note that this parameter value does not meet the stability criterium. While running the simulation, we see that in the first 40 days, the perturbed fibroblast cell density moves to equilibrium. After 40 days, the fibroblasts persistently differentiate into myofibroblasts, increasing the myofibroblast cell density over the whole computational domain from day 50. This differentiation happens because the signaling molecule density increases, and therefore, also the collagen density increases. Unlike in the last simulation, the displacement velocity does not vanish. For that reason, remeshing is necessary around day 80 of the

simulation. Within a few days, remeshing is necessary again, and at some point, the Picard iterations do not yield convergence anymore because of continuous remeshing. Therefore, we ended this simulation. We see the same for $k = 1$.

From a biological point of view, we believe that the human body protects against lowering the signaling molecule decay rate to this extent to prevent such a non-realistic occurrence where collagen will cause the tissue to rupture because of excessive production.

To conclude this section, the two-dimensional morphoelastic model for post-burn contraction is stable under the condition that the signaling molecule decay rate is not reduced too far to values below the limit $\delta_c \geq \frac{k_c}{a_c^{II} \bar{\rho}}$. We note that in all simulations except the last, the ratio $\min_{e_k} |\mathbf{J}_{e_k}| / \max_{e_k} |\mathbf{J}_{e_k}|$, where $\mathbf{J}$ the triangle Jacobian, was at least 0.9915, hence remeshing was not necessary.

4.4 Appendix: The derivation of equation (4.42)

Substitution of the variations from equation (4.40) into equation (4.38) yields

$$
\begin{aligned}
\rho_t \lambda_{v_1} = {}& \sum_{\beta=1}^{N_x}\sum_{\gamma=1}^{N_y} \hat{v}^1_{\beta,\gamma}\left[-(\mu_1+\mu_2)\frac{e^{-2\pi\beta(k-1)hi}e^{-2\pi\gamma jhi}-2e^{-2\pi\beta khi}e^{-2\pi\gamma jhi}+e^{-2\pi\beta(k+1)hi}e^{-2\pi\gamma jhi}}{h^2} - \right.\\
& \left. \frac{\mu_1}{2}\frac{e^{-2\pi\beta khi}e^{-2\pi\gamma(j-1)hi}-2e^{-2\pi\beta khi}e^{-2\pi\gamma jhi}+e^{-2\pi\beta khi}e^{-2\pi\gamma(j+1)hi}}{h^2} \right] -\\
& \left[\frac{\mu_1}{2}+\mu_2\right]\sum_{\beta=1}^{N_x}\sum_{\gamma=1}^{N_y}\hat{v}^2_{\beta,\gamma}\left[\frac{e^{-2\pi\beta(k-1)hi}e^{-2\pi\gamma(j-1)hi}-e^{-2\pi\beta(k-1)hi}e^{-2\pi\gamma(j+1)hi}}{4h^2}\right.\\
& \left. \frac{-e^{-2\pi\beta(k+1)hi}e^{-2\pi\gamma(j-1)hi}+e^{-2\pi\beta(k+1)hi}e^{-2\pi\gamma(j+1)hi}}{4h^2}\right] + \cdots +\\
& \frac{E\sqrt{\overline{\rho}}}{1+v}\sum_{\beta=1}^{N_x}\sum_{\gamma=1}^{N_y}\left[\hat{\varepsilon}^{12}_{\beta,\gamma}\frac{e^{-2\pi\beta khi}e^{-2\pi\gamma(j+1)hi}-e^{-2\pi\beta khi}e^{-2\pi\gamma(j-1)hi}}{2h}\right.\\
& \frac{1-v}{1-2v}\hat{\varepsilon}^{11}_{\beta}\frac{e^{-2\pi\beta(k+1)hi}e^{-2\pi\gamma jhi}-e^{-2\pi\beta(k-1)hi}e^{-2\pi\gamma jhi}}{2h} +\\
& \left. \frac{v}{1-2v}\hat{\varepsilon}^{22}_{\beta}\frac{e^{-2\pi\beta(k+1)hi}e^{-2\pi\gamma jhi}-e^{-2\pi\beta(k-1)hi}e^{-2\pi\gamma jhi}}{2h}\right] -\\
& \frac{E}{2\sqrt{\overline{\rho}}(1+v)}\left[\varepsilon_{12}+\varepsilon_{11}+\frac{v}{1-2v}\left(\varepsilon_{11}+\varepsilon_{22}\right)\right]\sum_{\beta=1}^{N_x}\sum_{\gamma=1}^{N_y}\hat{\rho}_{\beta,\gamma}\frac{e^{-2\pi\beta(k+1)hi}e^{-2\pi\gamma jhi}-e^{-2\pi\beta(k-1)hi}e^{-2\pi\gamma jhi}}{2h} -\\
& \frac{\overline{\rho}}{\zeta R^2+\overline{\rho}^2}\sum_{\beta=1}^{N_x}\sum_{\gamma=1}^{N_y}\hat{M}_{\beta,\gamma}\frac{e^{-2\pi\beta(k+1)hi}e^{-2\pi\gamma jhi}-e^{-2\pi\beta(k-1)hi}e^{-2\pi\gamma jhi}}{2h}.
\end{aligned}
\tag{4.51}
$$

4

Multiplication by $e^{2\pi lkhi} e^{2\pi pjhi}$ and double orthonormalization yields

$$\rho_t \lambda v_{i,j}^1 = \left[-\left(\mu_1 + \mu_2\right) \frac{e^{2\pi lhi} - 2 + e^{-2\pi lhi}}{h^2} - \frac{\mu_1}{2} \frac{e^{2\pi phi} - 2 + e^{-2\pi phi}}{h^2} \right] \hat{v}_{\boldsymbol{\beta}}^1 - \tag{4.52}$$

$$\left[\frac{\mu_1}{2} + \mu_2 \right] \left[\frac{e^{2\pi lhi} e^{2\pi phi} - e^{2\pi lhi} e^{-2\pi phi}}{4h^2} + \right.$$

$$\left. \frac{-e^{-2\pi lhi} e^{2\pi phi} + e^{-2\pi lhi} e^{-2\pi phi}}{4h^2} \right] \hat{v}_{\boldsymbol{\beta}}^2 -$$

$$\frac{E\sqrt{\overline{\rho}}}{1+v} \left[\hat{\varepsilon}_{\boldsymbol{\beta}}^{12} \frac{e^{-2\pi phi} - e^{2\pi phi}}{2h} + \frac{1-v}{1-2v} \hat{\varepsilon}_{\boldsymbol{\beta}}^{11} \frac{e^{-2\pi lhi} - e^{2\pi phi}}{2h} + \right.$$

$$\left. \frac{v}{1-2v} \hat{\varepsilon}_{\boldsymbol{\beta}}^{22} \frac{e^{-2\pi lhi} - e^{2\pi lhi}}{2h} \right] -$$

$$\frac{E}{2\sqrt{\overline{\rho}}(1+v)} \left[\overline{\varepsilon}_{12} + \overline{\varepsilon}_{11} + \frac{v}{1-2v} \left(\overline{\varepsilon}_{11} + \overline{\varepsilon}_{22} \right) \right] \frac{e^{-2\pi lhi} - e^{2\pi lhi}}{2h} \hat{\rho}_{\boldsymbol{\beta}} -$$

$$\xi \frac{\overline{\rho}}{R^2 + \overline{\rho}^2} \frac{e^{-2\pi lhi} - e^{2\pi lhi}}{2h} \hat{M}_{\boldsymbol{\beta}},$$

for the displacement velocity v_1. Application of Euler's formula, and using $2 - 2\cos(2\pi lx) = 4\sin^2(\pi lx)$ and $\left[e^{ix} e^{iy} - e^{ix} e^{-iy} - e^{-ix} e^{iy} + e^{-ix} e^{-iy} \right] / 4 = -\sin(x)\sin(y)$ yields equation (4.42).

Conclusions of this part

This part forms an entire addition to the existing biomorphoelastic model for post-burn contraction. We presented stability analyses for the fully continuous and the (semi-) discrete (where we have replaced the spatial derivatives with differences) versions of the problem in a one- and two-dimensional setting. We could analytically determine the eigenvalues, which is possible because the linearized equations (3.1) and (4.1)–(4.3) leave out other variables after accounting for the equilibria values. As a result, some eigenvalues meet the stability constraints independent of the chosen parameter values, given that the parameter values involved are positive and realistic. We have shown that linear stability is met for $\bar{\varepsilon} \leq 1$ in 1D, which is also a physical requirement from equation (2.14), and for $\bar{\varepsilon}_{11} = \bar{\varepsilon}_{22} = \frac{1}{2}$ and $\bar{\varepsilon}_{12} = 0$ in 2D. This latter condition is sufficient, meaning the analysis does not exclude any other stable equilibria. Nonlinear effects will, at most, be able to induce constant-state instabilities for the effective strain. Further, in 2D, we have empirically shown that for small $|\overline{\varepsilon_{12}}|$, say $|\overline{\varepsilon_{12}}| \leq 0.2$, there is always a stable region around the origin. For the solution to behave monotonically in 1D, the skin viscosity parameter should be greater or equal to a factor containing the total mass density of dermal tissues, Young's Modulus, and the effective strain equilibrium. Further, another essential stability constraint states that the model is stable for signaling molecule decay that is quick enough.

We have shown consistency between the (semi-) discrete model's eigenvalues and the continuous model's eigenvalues. If the equilibrium solution to the continuous problem is stable, then the equilibrium to the (semi-) discrete problem is stable under the present discretization (if we use the correct discretization method). Further, in 1D, monotonic convergence in the continuous system implies monotonic convergence in the (semi-) discrete system. Conversely, convergence could be monotonic in the (semi-) discrete system and not in the continuous system.

The obtained eigenvalues of the system establish the convergence rate towards the equilibria. We have assessed the convergence of the numerical method experimentally, in which the order of convergence is of order $\mathcal{O}(h^2)$. Since the difference between the chemical eigenvalues from the continuous and (semi-)discrete problem is of the order $\mathcal{O}(h^2)$, the convergence rates towards the equilibrium differ by an order $\mathcal{O}(h^2)$. This order of convergence is better than expected since the discretization method should have local truncation errors of order $\mathcal{O}(h^2)$.

Using numerical simulations, we validated the stability constraints derived from the analysis. If the input values satisfy the stability criterion, the model behaves stable given these stable parameter values. The initial perturbations in the variable densities vanish, and there are local displacements because of the perturbed displacement velocity density. Once this density has reached equilibrium, all the densities move gradually toward the corresponding expected equilibria. We conclude that a small perturbation of order $\mathcal{O}(10^{-15})$ g/cm^3 in the signaling molecule density and a few cells in the (myo)fibroblast cell densities are already responsible for initializing healing that takes more than a year time.

In 1D, we confirmed that the model is stable if the eigenvalues are not real-valued (i.e. if the viscosity is low). In this case, convergence is not monotonic but oscillates because of

increasing amplitudes of the perturbed displacement velocity density, moving the mesh back and forth. We point out that the larger the wavenumber in perturbations, the faster the equilibria are reached and the faster the perturbations disappear. In conclusion, we need real-valued eigenvalues to prevent the model from moving the mesh outside the normal bounds. However, this does not induce instability in terms of equilibria.

The model can numerically be unstable if the parameters do not meet the signaling molecule stability constraint; however, it does not necessarily has to be. If $\delta_c < k_c / (a_c^{II} \overline{\rho})$ is not too far below the bound, then, initially, the model seems stable, and the healing seems proper. The displacement velocity perturbations vanish quickly, and the signaling molecule perturbation shifts such that the density peak moves to the center of the burn in the first two weeks. One would expect the signaling molecule density to decrease from that moment on, given that the other chemicals seem to reach equilibria. However, the increasing signaling affects all the variables except displacement velocity. The densities move away from the expected equilibria and oscillate around new equilibria, where the densities remain, and the numerical method converges. We have linked this situation to real-life occurrences of hypertrophic scars and keloids. From a mathematical point of view, we have provided experimental evidence that one can restore the fibroblast cell and collagen density to healthy equilibria. We proved this restoration by reverting matrix production stimulation and myofibroblast differentiation, which we did by setting the signaling molecule density to (healthy) equilibrium and removing the myofibroblasts.

In case the signaling molecule decay rate is too far below the stability limit, the model is unstable. Initially, the wound healing seems to proceed smoothly; however, the too-slow signaling molecule decay causes such incredibly high signaling that all fibroblasts differentiate, and the collagen density explodes. To this end, the numerical method does not converge and loops over Picard iterations (while remeshing in 2D).

To conclude, the numerical model fully reproduces the stability constraints.

PART II

Sensitivity of the biomorphoelastic model for post-burn contraction

Introduction to the chapters in this part

The biomorphoelastic model for post-burn contraction compromises many (independent) parameters. Some parameter values are known, while others are unknown or poorly documented, and estimating these values is often complicated and sometimes even impossible. Although an excellent overview of parameter values has been provided [1], parameters vary between patients and even along a piece of the skin sample. Therefore, the two objectives of this part are to show to what extent the model's outcomes are subject to change when parameter values are varied and whether the model can make patient-specific contraction predictions.

A (Bayesian) parameter sensitivity analysis can reveal a dependence of the scar area and the total stress-energy of the model parameters. Furthermore, it is good to know which parameter values significantly influence results to determine the research direction for improving and optimizing therapy. Therefore, we are interested in the parameters' sensitivity and the model's feasibility. The sensitivity study aims to show where sensitive parts of the model lie and what the implications of these sensitivities are.

We combine the results from the sensitivity analysis to test the model's feasibility in 1D in Chapter 5. As input to the model, we might choose patient-specific information, such as the genetic background, gender, age, the location of the wound on the body, the depth of the wound, or any other. The literature estimates a significant subset of parameter values for human skin tissue of different ages. For example, the average fibroblast doubling time decreases with age [71], indicating a decrease in fibroblast apoptosis rate with age. Hence, we aim to predict post-burn contraction and discomfort of patients of different ages.

In this part, we simulate burns. Therefore, the computational domain is subject to more significant displacement than in the previous part of this thesis, and therefore, we need to perform remeshing in 2D. In Chapter 6, we discuss the remeshing strategy that we also use in Chapter 8.

The results in this part show the variations in the relative surface area (RSA) density and the total strain energy (TSE) density (for patients of different ages) and contribute to the range of parameter values in Chapters 7 and 8.

The conclusions of this part are presented after the chapters.

5

Sensitivity and feasibility of the one-dimensional model

This chapter is based on the publication from [63]. The code used for this chapter can be found in the online resources for Chapter 5 where one also finds a link to supporting data.

We consider the one-dimensional biomorphoelastic model for post-burn contraction. We perform a sensitivity analysis for many model parameters and use the results for a feasibility study. In the feasibility study, we test whether the model is suitable for predicting the extent of contraction in burns in patients of different ages. To this end, we conduct an extensive literature review to find parameter values and define four different age groups. From the sensitivity analysis, we conclude that the most sensitive parameters are the equilibrium collagen concentration, the fibroblast and myofibroblast apoptosis rates, and the signaling molecule secretion rate.

Further, although we can use the model to simulate significant distinct contraction densities in the different age groups, our results differ from what is seen in the clinic, particularly concerning children and elderly patients. We see more intense contractures in children if the burn injury occurs near a joint because the growth induces extra forces on the tissue. Elderly patients seem to suffer less from contractures, possibly because of excess skin.

5.1 Introduction

In this chapter, we summarize the change in parameter values that come with aging, we perform a sensitivity analysis for many model parameters, and we use the sensitivity analysis results for a feasibility study. The feasibility study's objective is to test whether the model can predict age-dependent post-burn contraction. Section 5.2 presents the

parameter values, and Section 5.3 presents the computational domain and the initial conditions that we use in the simulations. Subsequently, Section 5.4 presents the sensitivity analysis, and Section 5.5 presents the feasibility study.

5.2 Parameter values

This section describes the model's parameter values based on various sources from the literature. Reference [1] is one of the most important sources, in which several parameter values have been estimated that we did not find in the existing literature.

5.2.1 Equilibrium values

Taking into account the reaction term for the signaling molecules and the equilibria $\overline{N}, \overline{M}$ and $\overline{\rho}$, the equilibrium signaling molecule concentration should be $\overline{c} = 0$ g/cm^3.

The estimation of the equilibrium fibroblast count differs per study. One estimates the count to be about $\mathscr{O}(10^4)$ cells/cm^3 [14], and the other estimates it to be about $\mathscr{O}(10^6)$ cells/cm^3 [72]. The estimation of the cell count also differs for the papillary and the reticular dermis[1], where much more fibroblasts exist in the papillary dermis [74, 75]. In our simulations, we have seen that the model works best with the equilibrium distribution of $\mathscr{O}(10^4)$ cells/cm^3. We note that some other parameter values (δ_c, δ_ρ) depend on the chosen order for $\overline{N}$ since we need to consider the matrix metalloproteinase (MMP) density. Furthermore, research has found that among ages 1–10, the fibroblast cell density is nearly twice as high as in any other postnatal age group [76]. Therefore we choose the mean value $\overline{N} = 10^4$ cells/cm^3 and let the value decrease with age.

The myofibroblast count in the skin depends on the skin's condition. Myofibroblasts result from the differentiation of fibroblasts. We assume myofibroblasts are not present since healthy skin contains almost no myofibroblasts. Hence $\overline{M} = 0$ cells/cm^3.

Olsen *et al.* estimate the equilibrium collagen concentration as follows. Roughly 75% of the 15% of other substances than water and fat in 1 ml of human dermal tissue is collagen [14]. This estimate yields $\overline{\rho} \approx 0.75 \times 0.15$ g ml$^{-1} = 0.1125$ g ml^{-1}. Furthermore, the collagen content in human skin decreases at about 2% per year [77]. Therefore, we choose the mean value $\overline{\rho} = 0.1125$ g/cm^3 and let the value decrease exponentially with age.

5.2.2 Initial values

Because of the supply of growth factors during inflammation, the initial signaling molecule concentration is unequal to zero. The value should not exceed 15–50 ng ml^{-1} [14], and is therefore chosen to be $\tilde{c} = 10^{-8}$ g/cm^3.

The (thermal) injury causes the sudden death of cells. The dead cells lose their solid integrity, which causes the release of cytokines. These cytokines trigger the immune response, where several types of immune cells clear up the debris and release signaling molecules, which trigger the fibroblasts to migrate to the damaged region. We assume that several fibroblasts are present. We let this number be 20 percent of the equilibrium

---

[1]The papillary dermis is the superficial layer, lying deep to the epidermis. The papillary dermis is composed of loose connective tissue that is highly vascular. The reticular layer is the deep layer, forming a thick layer of dense connective tissue that constitutes the bulk of the dermis [73].

count. So the mean value is $\tilde{N} = 2 \times 10^3$ cells/cm^3.

5.2.3 Flux values

Sillman *et al.* vary the fibroblast migratory rates depending on the experimental medium used: in the serum-containing medium, the average velocity was as low as 0.23 mm/min. In contrast, in the serum-free keratinocyte medium, the average velocity was as high as 0.36 mm/min [53]. Hence, in serum-containing medium the rate was 7.6176×10^{-7} cm^2/day and in serum-free keratinocyte medium the rate was 1.86624×10^{-6} cm^2/day. All the reported values together yield a mean value of 1.3247×10^{-6} cm^2/day and standard deviation 3.7823×10^{-8} cm^2/day. However, other estimates are 1.44×10^{-5} cm^2/day and 1.2×10^{-5} cm^2/day [14] & [78]. We therefore estimate the value $D_n \approx 10^{-6}$ cm^5/(cells day). Furthermore, we assume that the diffusion of (myo) fibroblasts decreases with age. For the chemotactic parameter, we adopt $\chi = 2 \times 10^{-3}$ cm^5/(cells day) from Murphy *et al.* [55]. For the signaling molecule diffusion parameter, we adopt $D_c \approx 2.88 \times 10^{-3}$ cm^2/day from Haugh [54]. Furthermore, we assume that the diffusion value decreases with age.

5.2.4 Chemical kinetics values

Olsen *et al.* relate the transforming growth factor (TGF)-β inhibitor to the initial growth factor concentration so that $a_c^{II} = 10^{-8}$ g/cm^3 [14]. We adopt this value.

The chemical concentrations required to enhance fibroblast proliferation are somewhat higher than those for chemotactic responses [58]. Experimental evidence indicates that half-maximal enhancement corresponds to concentrations of about ten ng per ml [14]. We adopt this value and take $a_c^I = 10^{-8}$ g/cm^3.

Myofibroblasts produce roughly twice the collagen that is synthesized by fibroblasts [60]. Hence the constant $\eta^I = 2$.

The half-life of TGF-β is about 2 minutes [79], and the half-life of platelet derived growth factor is about 2 minutes as well [80]. So signaling molecules have a decay rate of $-\log(0.5^{24 \times 60/2}) \approx 499$/day. However, Olsen *et al.* decrease the value for two reasons: not all signaling molecules may bind, for example, because of insufficient levels of binding protein present at the wound site, and the bound complex may be recognized by (myo)fibroblasts leading to internalized and metabolized signaling molecules [14]. Therefore, the estimated decay rate is 0.5/day. Other estimates for TGF-β are $0.462 - 0.693$/day [81] and 0.354/day [55, 82]. Given our equilibrium parameter values, the MMP density has order of magnitude $\mathcal{O}(\overline{N}) \times \mathcal{O}(\overline{\rho}) = \mathcal{O}(10^3)$. Hence taking care of the equilibrium dimensions of the model, we end up with a range of $(3.54 - 6.93) \times 10^{-4}$ cm^6/(cells g day). We take the value $\delta_c = 5 \times 10^{-4}$ cm^6/(cells g day).

From the stability analyses in Chapters 3 and 4, it follows that $k_c \leq \delta_c \overline{\rho} a_c^{II}$. Given the parameter values, we set $k_c = 3 \times 10^{-13}$ g/(cells day).

We estimate the constant $\eta^{II} = 0.45$, which is a slight deviation from the constant estimated in [17].

Overall *et al.* estimate $a_c^{III} = (2 - 2.5) \times 10^8$ cm^3/g [38]. We choose the lower limit, hence $a_c^{III} = 2 \times 10^8$ cm^3/g. Furthermore, the MMP production increases with age [83]. Given the equation for the MMPs [1], that is

$$g(N, M, c, \rho) = \frac{[N + \eta^{II} M] \rho}{1 + a_c^{III} c}, \tag{5.1}$$

to let the MMP production increase, we must decrease the inhibiting factor a_c^{III}. Hence, we let the inhibition factor a_c^{III} decrease with age.

We can calculate cell doubling time (DT) using the growth rate (amount of doubling in one unit of time) in the following way: DT = ln(2)/growth rate. The average fibroblast DT is approximately 18–20 h [50, 56]. This gives the range $0.832 \le r \le 0.924$ for the proliferation rate. We choose the upper limit, hence $r = 0.924$ cm^{3q}/(cells^q day). Furthermore, the percentage of proliferative cell nuclear antigen (PCNA)-positive fibroblasts decreases with age, and PCNA can be considered a marker for proliferating cells [76]. We, therefore, let cell division decrease with age.

TGF-β increases fibroblast proliferation by 2–3 times [57]. We choose the lower limit, hence $r^{\max} = 2$.

The skin's fibroblast carrying capacity is known to be approximately $\kappa = 10^{-6}$ cm^3/cells [32]. We adopt this value. Furthermore, skin becomes thinner with age, so we assume crowding occurs faster in elderly skin. Hence we let κ increase with age.

We need to have a stable chemical reaction in case the cell and molecule densities are in equilibrium. The constant q allows us to have a stable reaction in equilibrium for equation (2.15). Given the equilibria, solving for q yields:

$$q = \frac{\log(\delta_n) - \log(r(1 - \kappa\overline{N}))}{\log(\overline{N})}. \tag{5.2}$$

In Desmoulière *et al.*, culturing fibroblasts in the presence of TGF-β increased the percentage of cells expressing alpha smooth muscle activator (α-SMA) from 7.5–45.3%, representing the activation of 37.8% of myofibroblast type cells [7]. This experiment occurred over one week, with a TGF-β dose of 5–10 ng per ml. Suppose the myofibroblast activation follows a linear equation. Then given $y(7) = 7a = 0.378$, we have $a = 0.054$/day. A dose of 5–10 ng per ml yields $0.054/10 \times 10^{-9}$ and $0.054/5 \times 10^{-9}$ cm^3/(g day), giving the range $5.4 \times 10^6 \le k_1 \le 1.08 \times 10^7$ cm^3/(g day). We choose the upper limit. Furthermore, Simpson *et al.* demonstrated a failure of fibroblast-myofibroblast differentiation and showed that this is associated with in vitro aging [71]. Hence we let the differentiating parameter decrease with age.

The average fibroblast DT ranges between 18–20 h [50, 56], and the average lifespan of fibroblasts varies between 40 and 70 population doublings (PD) [52, 84]. Using the formula

$$\delta_n = (\ln 2)/(\text{PD} \times \text{DT}/24), \tag{5.3}$$

we end up with the range $0.0119 \le \delta_n \le 0.0231$. We choose the value $\delta_n = 0.02$/day and let this value decrease with age since, on average, the doubling time of fibroblasts decreases with age [71].

The myofibroblast apoptosis rate was estimated in a previous study for hypertrophic scars [61]. Within this study, it was found that a value of $\delta_m = 0.002$ /day corresponds to hypertrophic scars and that a value of $\delta_m = 0.06$ /day corresponds to normal scars. Other averages are: 8.85% for normal scars and 1.06% for hypertrophic scars [85]. Combination of these results yield the range $0.06 \le \delta_m \le 0.0885$ for normal scars and $0.0106 \le \delta_m \le 0.02$ for hypertrophic scars. For our study we use the lower value $\delta_m = 0.06$/day for normal scars.

The collagen secretion rate k_ρ gives us the opportunity to have a stable reaction in equilibrium for equation (2.18). Given the equilibria, solving yields $k_\rho = \delta_\rho \overline{\rho}^2$.

The synergistic effects of growth factors may accelerate collagen biosynthesis up to tenfold [14]. Hence $k_\rho^{\max} = 10$.

Data suggests that the half-maximal enhancement of collagen synthesis occurs at TGF-β concentrations of 1 ng per ml [59]. We adopt this value, hence $a_c^{IV} = 10^{-9}$ g/cm^3.

For the collagen decay rate, we let $\delta_\rho = 6 \times 10^{-6}$ cm^6/(cells g day) [61]. Furthermore, the collagen turnover decreases with age [77]. Hence we let the proteolytic breakdown of collagen decrease with age.

5.2.5 Mechanical values

Koppenol *et al.* estimated a viscosity value of order $O(10^2)$ for the two-dimensional biomorphoelastic model [1]. In Chapter 3, the stability analysis showed that $\mu \geq \frac{\sqrt{\rho E}}{\pi}$ must hold for the one-dimensional morphoelastic model. Given other parameter values, we can adapt the value $\mu = 100$ (N day)/cm^2. Furthermore, since the viscosity is constant for patients up to their 40s and increases a little after turning 40 [86], we let the viscosity increase with age.

We estimate that the constant E in the Young's Modulus $E\sqrt{\rho}$ is 350 N/((g cm)$^{\frac{1}{2}}$) and let this value increase with age [87, 88].

For the parameters in the body force, we adopt $\xi = 4.4 \times 10^{-2}$ (N g)/(cells cm^2) [64, 65], $R = 0.995$ g/cm^3, and $\zeta = (0 - 9) \times 10^2$ cm^6/(cells g day). We set $\zeta = 4 \times 10^2$/(cells g day) and let this value increase with age because the skin's ability to recover after stretching decreases over a lifetime [89].

Last, but not least, $\rho_t = 1.09$ g/cm^3 for human skin [62]. We assume this density does not change with age.

5.3 The domain and the initial conditions

For the sensitivity analysis and the feasibility study, we use a fixed computational domain defined by $\Omega_x = (-L, L)$ with $\overline{\Omega}_x = [-L, L]$, the closed interval. Similarly, we define the wounded area by the subspace $\Omega_x^w = (-L^w, L^w)$, $L^w < L$. Furthermore, we define the wound boundary's steepness by s, which counts for the slope of the chemicals on the wound boundary. The dimension x is in centimeters and t in days.

We use the following functions for the initial fibroblast and signaling molecule conditions:

$$
N(x,0) = \begin{cases} \overline{N} & \text{if } (*), \\ \frac{\overline{N}+\tilde{N}}{2} + \frac{\overline{N}-\tilde{N}}{2} \sin\left(\frac{\pi}{s}\left(x+\frac{1}{2}s\right)\right) & \text{if } (**), \\ \tilde{N} & \text{if } (***), \end{cases}
$$
$$
c(x,0) = \begin{cases} \overline{c} & \text{if } (*), \\ \frac{\overline{c}+\tilde{c}}{2} + \frac{\overline{c}-\tilde{c}}{2} \sin\left(\frac{\pi}{s}\left(x+L^w-\frac{s}{2}\right)\right) & \text{if } (**), \\ \tilde{c} & \text{if } (***). \end{cases}
\tag{5.4}
$$

$(*): L^w \leq x \leq -L^w$, $(**): \{L^w + x \leq s, L^w - s \leq x \leq L^w\}$, $(***): -L^w + s \leq x \leq L^w - s$. Here $\overline{N}$ and $\overline{c}$ are the fibroblast and signaling molecule densities in healthy dermal tissue, and

$\tilde{N}$ and $\tilde{c}$ in the wound. Figure 5.1 shows an example of possible initial conditions.

a

b
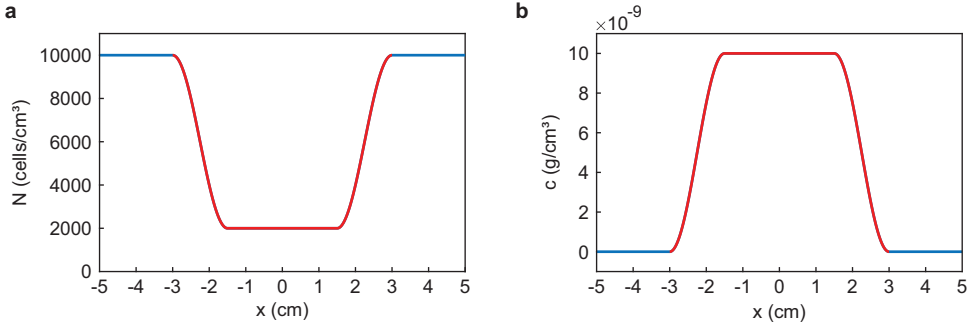
Figure 5.1: An example of two initial conditions showing that fibroblasts (**a**) and signaling molecules (**b**) are present in the wound. The parameter values in this example are: $L = 5$ cm, $L^w = 3$ cm, $s = 1.5$ cm, $\overline{N} = 10^4$ cells/cm^3, $\tilde{N} = 2 \times 10^3$ cells/cm^3, $\overline{c} = 0$ g/cm^3 and $\tilde{c} = 10^{-8}$ g/cm^3.

We use the initial conditions 5.4 to avoid abrupt changes in the densities. We have assumed (some) fibroblasts are present and, because of the secretion by, for instance, macrophages during inflammation, signaling molecules are also present in the wound. We assume that initially, no myofibroblasts are present, a fixed collagen concentration is present, and the displacement of the dermal layer, the displacement velocity, and effective strain initially are zero. Hence for all $x \in \Omega_x$:

$$M(x,0) = \overline{M} = 0, \quad \text{and} \quad \rho(x,0) = \overline{\rho},$$
$$u(x,0) = 0, \quad v(x,0) = 0, \quad \text{and} \quad \varepsilon(x,0) = 0. \tag{5.5}$$

Note that this can represent a skin graft: the skin trauma damages the fibroblasts and induces an inflammatory response that secretes signaling molecules. The skin graft adds a collagen layer.

In the simulations, we use $L = 10$ cm, $L^w = 3.6$ cm (mean value in the sensitivity analysis), $s = 1$ cm, timestep $\Delta t = 1$ day, total simulation time $T = 365$, and we divide the computational domain in $n = 200$ elements.

5.4 Sensitivity analysis

The model contains 34 parameters, of which we vary the following independent 30 to study the sensitivity of these parameters:

- the equilibria $\overline{N}$ and $\overline{\rho}$, and the initial conditions $\tilde{N}, \tilde{c}$ and $\tilde{\rho}$;

- the apoptosis rates δ_n and δ_m, and the decay rates δ_c and δ_ρ;

- the parameters responsible for the enhancement of cell division and molecule secretion a_c^I, a_c^{II} and a_c^{IV}, and the inhibition of MMP secretion a_c^{III};

- the ratios from myofibroblasts to fibroblasts η^I and η^{II}, and chemokine dependent differentiation rate k_1;

- the diffusion and chemotaxis rates D_n, D_c, and χ;

- the proliferation and secretion rates r and k_c, and the maximum factors $r^{\max}$ and $k_\rho^{\max}$;

- the crowding factor κ;

- the parameters ξ and R that influence the force;

- the viscosity μ, Young's-Modulus factor E, morphoelastic factor ζ, and the total mass density of dermal tissues ρ_t.

We organized the analysis as follows. We vary the parameter values by decreasing or increasing each chosen parameter by $\pm\, 0, 5, 10, 15, 20, 25\%$. We also vary the length of the initial wound L^w. This setup means we perform 341 simulations. Namely, we perform 11 simulations for each parameter while leaving the values of the other parameters at the mean value. (For an overview of parameter values, we refer to Table 5.3 in Section 5.5. The mean values are given in Tables 5.3a–d, whereas in Tables 5.3c and 5.3d, the mean values are given in the third column (μ^2).)

The results show the *minimum of the relative surface area* (RSA_min) in a time period of one year, the *day on which the minimum relative surface area is reached* (RSA_day), the *relative surface area on day 365* (RSA_365), the *maximum value of the total strain energy density* (TSE_max), and the *day on which the maximum value of the total strain energy density is reached* (TSE_day).

Given the values in $r \in \mathrm{RSA}_{\{\min, \mathrm{day}, 365\}}$ and $r \in \mathrm{TSE}_{\{\max, \mathrm{day}\}}$ for a variation $j \in \{\pm 25\%\}$, we compute the z-scores for the parameter $i \in \{\overline{N}, \ldots, L^w\}$. The basic z-score for a sample is $z = (x - \overline{x})/s_x$, where $\overline{x}$ is the sample mean and s_x is the sample standard deviation. We define the measure for sensitivity by summing over the absolute values of the z-scores:

$$\mathscr{S}_i^r = \sum_j \left| z_{ij}^r \right|, \tag{5.6}$$

where z_{ij}^r is the z-score of the data in r for parameter i in variation j. For example, $z_{\delta_N, 15\%}^{RSA_{365}}$ represents the z-score of RSA_365 for parameter δ_n in the simulation where the value for δ_n is increased with 15%.

Table 5.1 gives an overview of the sensitivity values in terms of z-scores for the 31 parameters we varied. In the last column, we rounded the sum of the values.

Table 5.1: Sensitivity of the varied parameters in terms of z-scores.

Param.	Dimension	$\mathscr{S}^{\mathrm{RSA_{min}}}$	$\mathscr{S}^{\mathrm{RSA_{day}}}$	$\mathscr{S}^{\mathrm{RSA_{365}}}$	$\mathscr{S}^{\mathrm{TSE_{max}}}$	$\mathscr{S}^{\mathrm{TSE_{day}}}$	$\mathscr{S}^{\mathrm{total}}$
$\overline{\rho}$	g/cm^3	20.35	33.92	15.38	29.19	30.21	129
δ_n	/day	22.55	11.75	23.89	17.85	15.05	91
δ_m	/day	20.52	11.79	23.79	17.25	11.42	85
R	g/cm^3	20.17	10.75	21.51	13.57	13.65	80
k_c	g/(cells day)	16.99	15.12	14.23	10.02	22.49	79
$r^{\max}$	-	17.55	9.88	18.15	13.05	12.10	71

Table 5.1: (continued)

Param.	Dimension	$\mathscr{S}^{\text{RSA}_{\min}}$	$\mathscr{S}^{\text{RSA}_{\text{day}}}$	$\mathscr{S}^{\text{RSA}_{365}}$	$\mathscr{S}^{\text{TSE}_{\max}}$	$\mathscr{S}^{\text{TSE}_{\text{day}}}$	$\mathscr{S}^{\text{total}}$
δ_ρ	$\text{cm}^6/(\text{cells g day})$	8.91	15.13	6.88	13.05	13.55	58
δ_c	g/cm^3	12.00	9.09	11.56	5.10	16.29	54
$k_\rho^{\max}$	-	8.27	12.69	6.45	11.59	12.04	51
a_c^{III}	cm^3/g	8.93	10.75	8.91	11.09	8.92	49
$\overline{N}$	cells/cm^3	9.21	8.83	9.50	10.35	7.58	45
ξ	$(\text{N g})/(\text{cells cm}^2)$	14.89	2.06	14.57	1.18	11.62	44
E	$\text{N}/((\text{g cm})^{1/2})$	13.31	4.16	6.40	4.94	8.48	37
L^w	cm	2.04	9.17	11.52	9.80	4.01	37
η^I	-	8.17	3.36	8.23	4.82	8.25	33
η^{II}	-	6.55	5.71	9.24	6.30	5.61	33
a_c^I	g/cm^3	4.50	9.21	5.73	10.17	2.26	32
ζ	$\text{cm}^6/(\text{cells g day})$	3.85	5.10	1.73	2.99	10.85	25
k_1	$\text{cm}^3/(\text{g day})$	1.33	7.90	2.32	8.49	2.26	22
a_c^{II}	g/cm^3	4.83	2.06	4.78	2.82	4.50	19
$\tilde{c}$	g/cm^3	3.69	3.02	2.07	2.72	4.54	16
r	$\text{cm}^{3q}/(\text{cells}^q \text{ day})$	4.65	1.49	3.69	2.30	4.07	16
$\tilde{N}$	cells/cm^3	3.35	2.96	1.98	3.81	3.32	15
a_c^{IV}	g/cm^3	2.31	3.11	1.53	2.99	3.04	13
ρ_t	g/cm^3	1.82	3.11	1.60	2.99	2.51	12
D_c	cm^2/day	2.15	3.02	1.60	2.88	2.30	12
κ	cm^3/cells	1.89	3.11	1.57	2.99	2.55	12
μ	$(\text{N day})/\text{cm}^2$	1.78	3.11	1.60	2.99	2.42	12
χ	$\text{cm}^5/(\text{g day})$	1.82	3.11	1.60	2.99	2.51	12
$\tilde{\rho}$	g/cm^3	1.42	3.11	1.76	2.99	2.05	11
D_n	$\text{cm}^5/(\text{cells day})$	1.95	2.06	1.60	1.87	2.43	10

The third to seventh columns show the scores on the minimum relative surface area (RSA) $\mathscr{S}^{\text{RSA}_{\min}}$, the day on which the minimum RSA is reached $\mathscr{S}^{\text{RSA}_{\text{day}}}$, the RSA on day 365 $\mathscr{S}^{\text{RSA}_{365}}$, the maximum total strain energy (TSE) $\mathscr{S}^{\text{TSE}_{\max}}$, and the day on which the maximum TSE is reached $\mathscr{S}^{\text{TSE}_{\text{day}}}$. The last column shows the total of the scores $\mathscr{S}^{\text{total}}$.

We can see that the parameter that represents the equilibrium collagen concentration $\overline{\rho}$ with a score of 129 is the most sensitive. It is, therefore, interesting to study the equilibrium collagen concentrations in human skin since collagen concentrations decrease with age [77], and we use this value for the feasibility study in the next section. Parameters that are the least sensitive are the diffusion rate of (myo)fibroblasts D_n with a score of 10 and the initial collagen concentration $\tilde{\rho}$ with a score of 11. Concerning the diffusion D_n, we must note that the mean value is of order $\mathcal{O}(10^{-6})$, which is different from the order used by Koppenol [1], where it is of order $\mathcal{O}(10^{-7})$. This difference may indicate that variations of this parameter have no significant impact on the simulations, while in a different geometry it might be much more sensitive. Concerning the initial collagen concentration $\tilde{\rho}$, we note that the value is varied when the equilibrium collagen concentration is fixed to the mean value ($\overline{\rho} = 0.1125$). If the equilibrium collagen concentration

$\overline{\rho}$ is varied, we fix the initial collagen concentration to 20% of 0.1125, which is the mean value of $\overline{\rho}$ and not the variation.

Other parameters that seem significantly sensitive are the fibroblast apoptosis rate δ_n with a score of 91, the myofibroblast apoptosis rate δ_m with a score of 85, the constant R that influences the force with score 80, and the signaling molecule secretion rate k_c with score 79. However, we must note that Koppenol estimated the mean values for δ_m, R, and k_c for a two-dimensional setting in which he used other values for the parameters [17]. Furthermore, we based the value of k_c on the model's stability constraint $k_c \leq \delta_c a_c^{II} \overline{\rho}$, and since the parameter for the equilibrium collagen concentration is sensitive, it is not a surprise that this secretion parameter is also sensitive. The value for the secretion rate of signaling molecules is not that straightforward. The secretion rate of cytokines differs from the secretion rate of growth factors, yet we model these together in one variable c representing signaling molecules. To prevent the model from unnecessarily complicated computations, we continue modeling with this simplification and bear in mind the sensitivity of the parameter k_c. It is therefore also interesting to study the fibroblast apoptosis rate since the doubling time of fibroblasts decreases with age [71], and we use this value for our age study in the next section.

To visualize the parameters' sensitivity, we present the effect of the parameter values variations on both the RSA and the TSE in Figure 5.2. There is no legend to distinguish the parameters' sensitivity. Instead, we labeled the essential lines with different styles.

Figure 5.2 highlights the effects of decreasing or increasing the five most sensitive parameters: the equilibrium collagen concentration $\overline{\rho}$, the fibroblast and myofibroblast apoptosis rates δ_n and δ_m, the body force-inhibiting constant R and the signaling molecule secretion rate k_c.

Increasing the equilibrium collagen concentration $\overline{\rho}$ gives a larger $\text{RSA}_{\min}$ and RSA_{365}, and a smaller RSA_{day}, TSE_{max} and TSE_{day}. Hence, an elevated equilibrium collagen concentration results in less contraction during proliferation and maturation and less patient discomfort. Further, the incidental effect is that the period of contraction and increasing patient discomfort is shortened. The stated effects are somewhat linear and appear to diminish as the equilibrium collagen concentration increases, most visible in Figure 5.2e. A reduced equilibrium collagen concentration has the opposite effect, and this effect is almost exponential-like in all subfigures, except in Figure 5.2a. Especially, a 25% decrease from the mean value shows a strong negative effect in Figures 5.2c and 5.2d. In reality, it is not likely to change the equilibrium collagen concentration; however, we can use collagen dressings and, for example, vitamin C supplements to reduce contraction and the contraction time.

Further, increasing the myofibroblasts apoptosis rate δ_m and the body force-inhibiting constant R gives a larger $\text{RSA}_{\min}$ and TSE_{day}, and a smaller TSE_{max}. Hence, faster myofibroblast apoptosis and stronger body force inhibition results in less contraction during proliferation and less patient discomfort. Further, the incidental effect is that the period of increasing patient discomfort is extended, in contrast to the effect of increasing $\overline{\rho}$.

Considering the fibroblast apoptosis rate δ_n, we see that decreasing the rate results in a larger $\text{RSA}_{\min}$, TSE_{day} and RSA_{365}, and in a smaller $\text{TSE}_{\max}$. Hence, slower fibroblast apoptosis results in less contraction during proliferation and maturation and less patient discomfort. Further, the incidental effect is that the period of increasing patient discom-
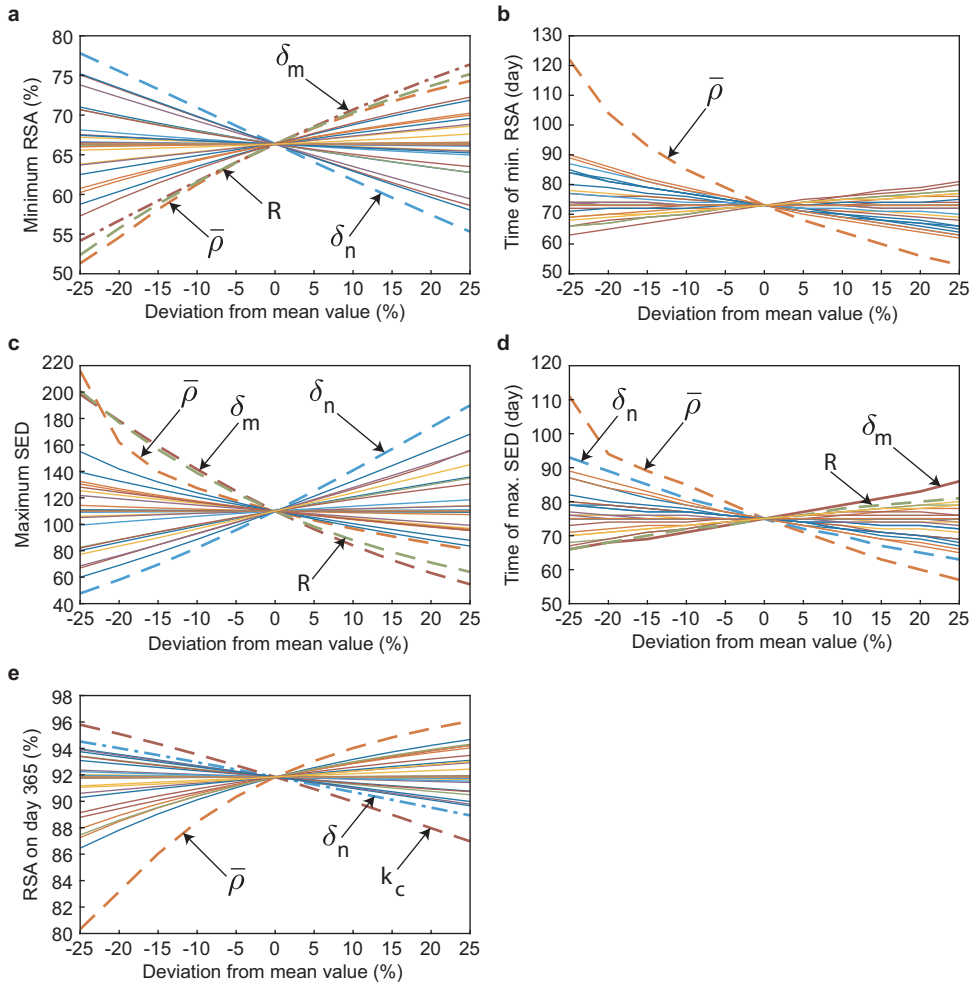
Figure 5.2: Effects of the variations in parameters for the relative surface area (RSA) density and the total strain energy (TSE) density. Shown are the effects on the minimum RSA (**a**), the effects on the day on which the minimum RSA is reached (**b**), the effects on the maximum TSE (**c**), the effects on the day on which the maximum TSE is reached (**d**), and the effects on the RSA on day 365 (**e**). In the figures, δ_n and δ_m are the fibroblast and myofibroblast apoptosis rates, respectively, $\overline{\rho}$ is the equilibrium collagen concentration, k_c is the signaling molecule secretion rate, and R is the body force-inhibiting constant.

fort is extended, as is what happens for faster myofibroblast apoptosis and stronger body force inhibition. Slower apoptosis means more cells survive, hence a relative increase in the proliferation of cells. We can see this from equation (5.2): a lower fibroblast apoptosis rate directly correlates with a smaller value for q and given equation (2.15), we see that if q decreases, the production of fibroblasts increases, also relating to the skin's stiffness. An increase in the fibroblast cell density yields an increase in collagen production and hence an increase in stiffness. Therefore, the tissue's strength increases, and the ef-

fective strain decreases, i.e., $\|\varepsilon\|^2$ becomes smaller. The result is less patient discomfort. Further, surviving fibroblasts take up the space that myofibroblasts could otherwise occupy, explaining why $\mathscr{S}_{\delta_n}^{\mathrm{RSA_{min}}} \geq \mathscr{S}_{\delta_m}^{\mathrm{RSA_{min}}}$ in Table 5.1. We can see this from the body force $\frac{\partial}{\partial x}\frac{\xi M \rho}{R^2+\rho^2}$ that shows less generated isotropic stress for larger R and ρ and smaller M. The result is less scar contraction.

From Figure 5.2e, we see that a decrease in the signaling molecule secretion rate k_c gives a larger RSA$_{365}$. Hence, slower signaling molecule secretion reduces contraction intensity after one year, which is no surprise as, during maturation, inflammatory responses are not favorable. Furthermore, the model's stability constraint $k_c \leq \delta_c a_c^{II} \overline{\rho}$ favors a lower signaling molecule secretion rate.

Taken together, targeting contraction intensity during proliferation is most likely effective in case fibroblast survival and collagen concentration are considered. During maturation, targeting contraction and contractures is more likely to be effective when signaling molecule inhibition and collagen production are considered.

5.5 Feasibility study

To study the feasibility of age-dependent uncertainty quantification, we focus on the effect of skin aging on contraction and patient discomfort. Just like any other organ, aging also affects the skin. Aging has a delaying effect on wound healing and immune responses. Intrinsic aging is the effect of generic and internal influences, such as hormones or metabolic substances. Extrinsic aging is the effect of external influences, such as ultra violet (UV) radiation and environmental toxins [90]. Clear general signs of aging are wrinkles, sagging skin, pigmentary irregularities, increased tendencies to injuries, and the faster opening of healing wounds. These symptoms result from physiological changes such as decreased cell replacement rate. We reviewed various literature sources to find suitable values for the model's parameters. In this way, we can perform simulations for patients of different ages. Based on the results, we have chosen the groups we present in Table 5.2.

Table 5.2: Groups of patients of different ages.

Group	Age
1	0–15
2	16–40
3	41–70
4	71+

In this study, there are five groups of parameters:

1. parameters that are constant along the patients and the computational domain,

2. parameters that are constant along the patients and vary along the computational domain,

3. parameters that vary along the patients and are constant along the computational domain,

4. parameters that vary along the patients and the computational domain,

5. parameters that depend on other parameters.

To assess the uncertainty in the input data, we use a basic Monte Carlo method in which we sample input data from predefined statistical distributions. Regarding spatially heterogeneous parameters, we use sampling from a log-normal distribution. Each sample is a one-dimensional realization and is based on the heterogeneous sampling through a normalized truncated Karhunen–Loéve expansion of a zero-mean stochastic process, by

$$\hat{u}(X) = \sum_{j=1}^{n} \hat{Z}_j \sqrt{\frac{2}{n}} \sin\left((2j-1)\frac{\pi}{2|\Omega_x|} X\right), \tag{5.7}$$

where $\hat{Z}_j \sim \mathcal{N}(0,1)$, hence $\hat{Z}_j$ denotes a set of *iid* stochastic variables that follow the standard normal distribution, $|\Omega_x|$ is the length of the domain of computation, and $-L \leq X \leq L$. From the stochastic variable $\hat{u}(X)$, we show the regeneration of, for example, $\hat{E}$ by

$$\log(\hat{E}(X)) \sim \mu + \sigma \hat{u}, \tag{5.8}$$

in addition to that

$$\hat{E}(X) = \exp\left(\mathcal{M}_E + \mathcal{S}_E \hat{u}(X)\right). \tag{5.9}$$

Hence $\hat{E}(X)$ is a realization of a *lognormal* distribution with mean $\mathcal{M}_E$ (expected value) and standard deviation $\mathcal{S}_E$. These values can be expressed by the arithmetic (sample) mean μ_E and arithmetic standard deviation σ_E:

$$\mathcal{M}_E = \ln\left(\frac{\mu_E}{\sqrt{1 + \frac{\sigma_E^2}{\mu_E^2}}}\right), \quad \mathcal{S}_E = \sqrt{\ln\left(1 + \frac{\sigma_E^2}{\mu_E^2}\right)}. \tag{5.10}$$

In the same way, we can also create heterogeneous, stochastic inputs for other parameters.

To test the model's feasibility, we vary the parameter values based on the results found in the literature on aging skin. We are interested in the differences between the contraction and patient discomfort intensities in the distinct age groups. To quantify these differences, we test the null-hypothesis $H_0 : \mu_A = \mu_B$ versus a two-sided alternative for groups A and B of patients using the following t-statistic:

$$t = \frac{\overline{X}_A - \overline{Y}_B}{s_p}, \quad s_p = \sqrt{\frac{s_a^2 + s_b^2}{n_b}}$$

where $\overline{X}_A$ and $\overline{Y}_B$ are the mean values of the results in distinct age groups A and B, s_p is the estimated standard error of $\overline{X}_A - \overline{Y}_B$, s_a^2 and s_b^2 are the standard deviations in the age groups A and B, and n_b is the number of samples in the age groups. Here we assume that the number of samples in the age groups is equal. We reject the null-hypothesis if $|t| > t_{2(n_b-1)}(\alpha/2)$, with $\alpha = 0.001$.

To reduce the computation time, we performed simulations on half a domain $\Omega^{1/2} = [-L, 0]$. We simulated $n_b = 1950$ burns per age group. Hence, in total, we simulated 7800 burns. Table 5.3 shows the parameter values used for these simulations.

Table 5.3: Parameter values. In subtables (c) and (d), $\mu^i, i \in \{1,2,3,4\}$ denotes the mean value in group i of patients of different age.

(a) The parameter values that are constant along patients and the domain.

Parameter	μ	Dimension
$\overline{M}$	0	cells/cm^3
$\overline{c}$	0	g/cm^3
$\tilde{c}$	10^{-8}	g/cm^3
δ_m	6×10^{-2}	/day
R	0.995	g/cm^3
$r^{\max}$	2	-
η^I	2	-
η^{II}	0.45	-
$k_\rho^{\max}$	10	-

(b) The parameter values that are constant along patients and vary along the domain.

Parameter	μ	σ	Dimension
a_c^I	10^{-8}	3.45×10^{-10}	g/cm^3
a_c^{II}	10^{-8}	6.25×10^{-10}	g/cm^3
a_c^{IV}	10^{-9}	10^{-10}	g/cm^3
ξ	4.4×10^{-2}	1.1×10^{-3}	(N g)/(cells cm^2)
δ_c	5×10^{-4}	9.8×10^{-6}	cm^6/(cells g day)
k_c	3×10^{-13}	3.95×10^{-15}	g/(cells day)
ρ_t	1.09	1.21×10^{-1}	g/cm^3
χ	2×10^{-3}	2.22×10^{-4}	cm^5/(g day)

(c) The parameter values that vary along patients and are constant along the domain. We chose $\bar{N} = 0.2 \cdot \overline{N}$ and $\tilde{\rho} = 0.1 \cdot \overline{\rho}$.

Parameter	μ^1	μ^2	μ^3	μ^4	Dimension
$\overline{N}$	1.5×10^4	10^4	9.5×10^3	9×10^3	cells/cm^3
$\overline{\rho}$	1.25×10^{-1}	1.125×10^{-1}	1.05×10^{-1}	9.75×10^{-2}	g/cm^3

Table 5.3: (continued)

(d) The parameter values that vary along patients and the domain.

Parameter	μ^1	μ^2	μ^3	μ^4	σ	Dimension
D_n	1.2×10^{-6}	10^{-6}	8.5×10^{-7}	7×10^{-7}	1.43×10^{-7}	$\mathrm{cm^5/(cells\ day)}$
D_c	3.25×10^{-3}	2.88×10^{-3}	2.55×10^{-3}	2.2×10^{-3}	3.2×10^{-4}	$\mathrm{cm^2/day}$
r	1.222	9.24×10^{-1}	8.16×10^{-1}	6.11×10^{-1}	7.11×10^{-2}	$\mathrm{cm^{3q}/(cells^q\ day)}$
κ	10^{-6}	10^{-6}	1.5×10^{-6}	2×10^{-6}	1.11×10^{-7}	$\mathrm{cm^3/cells}$
k_1	1.14×10^7	1.08×10^7	1.02×10^7	9.63×10^6	5.68×10^5	$\mathrm{cm^3/(g\ day)}$
a_c^{III}	2.05×10^8	2×10^8	1.95×10^8	1.9×10^8	4.35×10^6	$\mathrm{cm^3/g}$
δ_n	1.9×10^{-2}	2×10^{-2}	2.1×10^{-2}	2.2×10^{-2}	2.27×10^{-4}	$\mathrm{/day}$
δ_ρ	6.11×10^{-6}	6×10^{-6}	5.89×10^{-6}	5.78×10^{-6}	1.09×10^{-7}	$\mathrm{cm^6/(cells\ g\ day)}$
μ	10^2	10^2	1.2×10^2	1.4×10^2	1.11×10	$\mathrm{(N\ day)/cm^2}$
E	3.2×10^2	3.5×10^2	3.8×10^2	4.1×10^2	1.03×10	$\mathrm{N/((g\ cm)^{1/2})}$
ζ	3.8×10^2	4×10^2	4.2×10^2	4.4×10^2	1.82×10	$\mathrm{cm^6/(cells\ g\ day)}$

We used parallel computing with 12 processors, three processors responsible per group, on a 64-bit Windows 10 Pro system with 16 GB RAM and a 3.59 GHz AMD Ryzen 5 3600 6-Core Processor. The total computation time was 13.5 hours. Hence the mean computation time per simulation takes less than half a minute. For the test statistic, we used $t_{3898}(0.0005) = 3.293$. The standard deviations $s_{i,m}^2$ for the age groups $i \in \{1, 2, 3, 4\}$ for RSA$_{\text{min}}$ are

$$s_{1,m}^2 = 1.2158, \quad s_{2,m}^2 = 1.1293, \quad s_{3,m}^2 = 1.2570,$$
$$s_{4,m}^2 = 1.2815.$$

The standard deviations $s_{i,e}^2$ for the age groups $i \in \{1, 2, 3, 4\}$ for RSA$_{365}$ are

$$s_{1,e}^2 = 0.2941, \quad s_{2,e}^2 = 0.3105, \quad s_{3,e}^2 = 0.4003,$$
$$s_{4,e}^2 = 0.4238.$$

To get some insight into the effects of the four groups of Table 5.2, we present results for the RSA and the TSE in Figures 5.3–5.7. Figures 5.4, 5.5 and 5.7 show probability density functions that we computed using the kernel density estimation method.

Figure 5.3 shows four 95% confidence intervals for the post-burn contraction, each confidence interval corresponding to a group of patients.
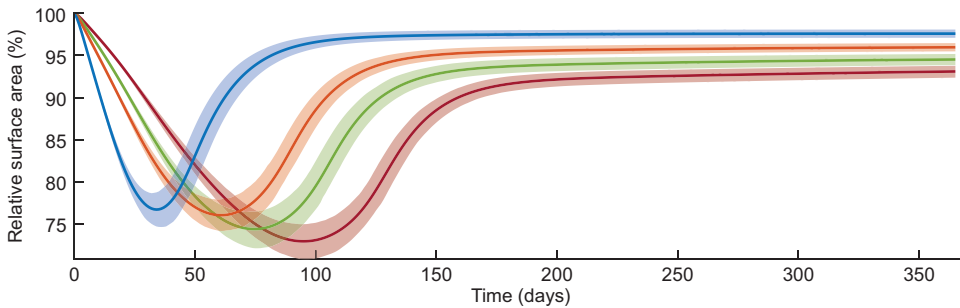
Figure 5.3: Confidence intervals for the post-burn contraction in different patient age groups. The intervals show the mean values and the 95% confidence values of the mean. The range of the values comes from the parameters' variability over the computational domain. From left to right, the lines show groups 1 (blue), 2 (orange), 3 (green), and 4 (red).

We can see that the maximum contraction value is about the same in the first two groups of ages. Higher age groups give a larger scar size reduction and, in addition, a larger contraction intensity. Further, it takes more time for higher ages to reach the maximum contraction intensity.

There seems to be more variability in the permanent deformation in elderly patients. In elderly patients, it takes longer before the wound healing cascade reaches equilibrium than in younger patients. Minima of the RSA were mainly reached on days 34, 61, 74, and 95, with values of 76.7, 76.0, 74.4, and 72.9% for groups 1, 2, 3, and 4, respectively. Unfortunately, these results do not correspond fully to the observations in the clinic. Usually, contraction is of less order in elderly patients, and, in general, retraction takes

a more extended period. We note that the longer retraction period is visible in the two-dimensional model results by Koppenol [1] and that this *stretched retraction period* is handled with the parameter a_c^{III}.

Our simulation results do not meet the clinical observations because of the variety of factors that have not been modeled in our mathematical model yet. In the clinic, one sees more contractures in younger patients in case the injury was in or near a joint. In contrast, the elderly seem to experience less discomfort because of contraction. One reason for this could be that aged skin is less tight than young skin. Looser tissue can move more than skin that is already tight and is, therefore, less likely to cause movement restriction when it contracts.

Figure 5.4 shows the estimated probability density and cumulative distribution function of RSA_{min} for patients in different age groups.
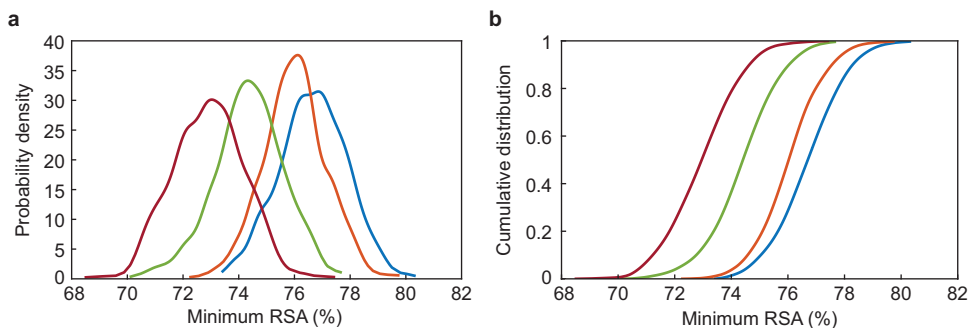
Figure 5.4: Estimated probability density (**a**) and cumulative distribution function (**b**) of the minimum of the relative surface area (RSA) for patients in different age groups. Within the subfigures, from right to left, the lines show groups 1 (blue), 2 (orange), 3 (green), and 4 (red).

Although the groups overlap in Figure 5.4a, the maximal contraction is significantly different ($p < 0.001$) between the groups (see Table 5.4a in Appendix 5.6). The differences in RSA_{min} between consecutive age groups are largest between ages 16–40 (group 2) and 41–70 (group 3) and smallest between ages 0–15 (group 1) and 16–40 (group 2). Given that, in reality, the evolution of the size of the scar is different from our results, we expect that the differences between group 1 and group 2 are larger in reality, possibly the largest.

The overlap between the age groups is also visible in the estimated cumulative distribution function plot in Figure 5.4b, where the functions of the first and second group, and the third and fourth group, almost intersect. From these cumulative distribution functions, we can estimate the probability of maximum contraction intensity. For example, this figure suggests that with a 70% probability, a patient from groups of patients 1, 2, 3, and 4, respectively, can reach 22.6%, 23.4%, 24.9%, and 26.4% contraction. Using such functions in the future can help predict the probability of developing a contracture and intervene in time when possible.

Figure 5.5 shows the estimated probability density and the corresponding cumulative distribution function of RSA_{365} for patients in different age groups.

Eventually, the scar maturates, and because of the skin's morphoelastic behavior, the
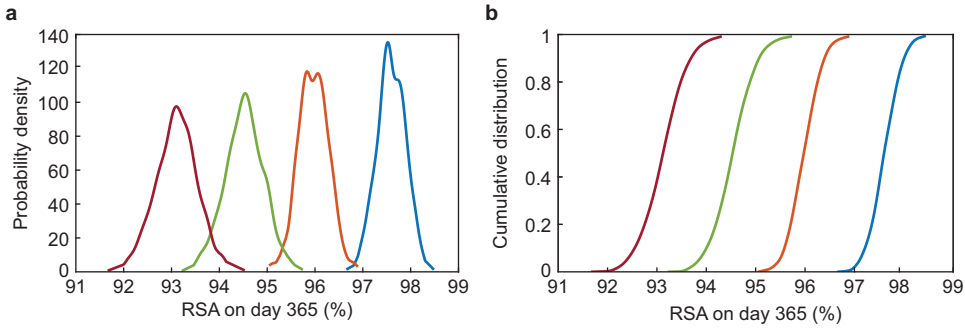
Figure 5.5: Estimated probability density (**a**) and cumulative distribution function (**b**) of the relative surface area (RSA) on day 365 for patients in different age groups. Within the subfigures, from right to left, the lines show groups 1 (blue), 2 (orange), 3 (green), and 4 (red).

scar's size rarely meets its initial configuration again. Here the initial configuration represents the initial size and geometry of the burn wound. Like for minimal contraction values, the overlap between consecutive groups for RSA_{365} in Figure 5.5a are significant ($p < 0.001$, see Table 5.4b in the Appendix 5.6). The differences between consecutive groups are similar to the differences in Figure 5.4a. The probability density functions show a correlation between aging and the spread, confirming the observation found in the confidence intervals that there is larger variability in the intensity of contraction in older adults than in children.

From the cumulative distribution functions in Figure 5.5b, we can estimate the probability of asymptotic contraction intensity. Here we see the mean values $RSA_{365} = 97.6\%$, 95.9%, 94.5%, and 93.3% for groups 1, 2, 3, and 4, respectively, which indicate a possible contracture if the scar is in or near a joint. Given the scar's location, one might estimate the probability that this scar will develop a contracture to a certain extent.

Figure 5.6 shows four 95% confidence intervals for the post-burn patient discomfort, each confidence interval corresponding to a group of patients.
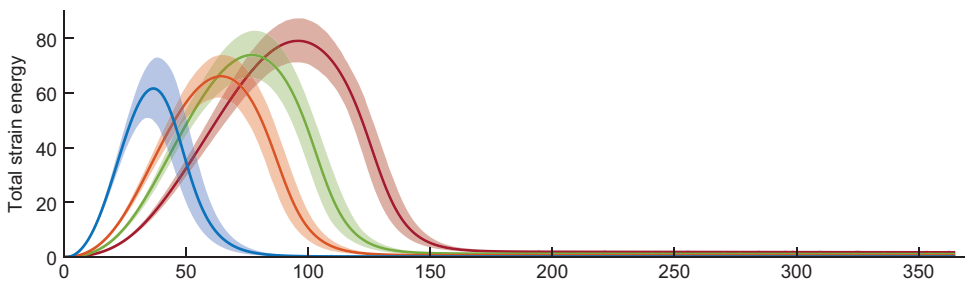
Figure 5.6: Confidence intervals for the patient discomfort in healing burns in different patient age groups. The intervals show the mean values and the 95% confidence values of the mean. The range of the values comes from the variability of the parameters over the computational domain. From left to right, the lines show groups 1 (blue), 2 (orange), 3 (green), and 4 (red).

We see similar maximum discomfort in the first two groups. Higher age groups give a

larger maximum and take more time to reach the maximum. Note that all these results relate to the densities shown in Figure 5.3. Maxima of the TSE densities are reached on days 36, 64, 78, and 95, with values of 62, 66, 74, and 79 for groups 1, 2, 3, and 4, respectively. We note that the discomfort maxima are reached a few days later than the maximum contraction in almost all groups. Because the contraction data in Figure 5.3 does not relate to what doctors see in the clinic, we assume this is the same case for the discomfort data. This assumption means that in real life, children might experience more discomfort than the elderly, in contrast to what we see in Figure 5.6.

Finally, Figure 5.7 shows the estimated probability density and the corresponding cumulative distribution function of TSE_{max} for patients in different age groups.
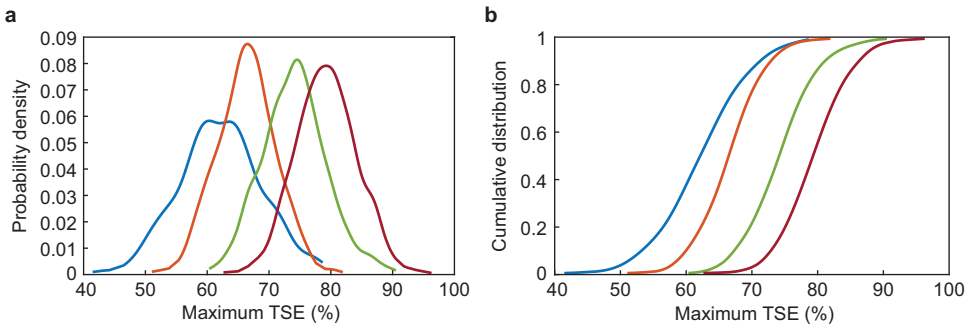
Figure 5.7: Estimated probability density function (**a**) and cumulative distribution function (**b**) of the maximum total strain energy (TSE). Within the subfigures, from left to right, the lines show groups 1 (blue), 2 (orange), 3 (green), and 4 (red).

Like in Figures 5.4 and 5.5, although the probability density functions in Figure 5.7a show an overlap between all the groups, TSE_{max} is significantly different ($p < 0.001$) between the groups (see Table 5.4b in the Appendix 5.6). This overlap is also visible in the cumulative distribution function in Figure 5.7b, where the functions of the first and second groups intersect on the top, and the third and fourth groups almost intersect. From these cumulative distribution functions, we can estimate the probability of maximum discomfort. For example, this figure suggests that with 80% probability, a patient from groups of patients 1, 2, 3, and 4, respectively, can reach a maximum of 67.9, 70.4, 78.5, and 83.6 total strain. Since the figures show a strong correlation between contraction and patient discomfort, we conclude that targeting contraction will also directly target patient discomfort.

5.6 Appendix: Values of the t-statistic

Table 5.4: The values of the t-statistic comparing the minima of the relative surface area (a), the maxima of the total strain energy density (b), and the relative surface area on day 365 (c).

(a) The values of the t-statistic comparing the minima of the relative surface area between patient age groups.

Groups	t-value
1 & 2	17
1 & 3	58
1 & 4	94
2 & 3	43
2 & 4	80
3 & 4	36

(b) The values of the t-statistic comparing the maxima of the total strain energy density between patient age groups.

Groups	t-value
1 & 2	23
1 & 3	63
1 & 4	91
2 & 3	49
2 & 4	83
3 & 4	32

(c) The values of the t-statistic comparing the relative surface area on day 365 between patient age groups.

Groups	t-value
1 & 2	167
1 & 3	273
1 & 4	385
2 & 3	126
2 & 4	241
3 & 4	108

5

6

Sensitivity of the two-dimensional model

This chapter is based on the publication from [91]. The code used for this chapter can be found in the online resources for Chapter 6 where one also finds a link to supporting data.

We consider the two-dimensional biomorphoelastic model for post-burn contraction. We perform a sensitivity analysis for the independent parameters of the model and focus on the effects on features of the relative surface area and the total strain energy density. We conclude that the most sensitive parameters are the Poisson's ratio, the equilibrium collagen concentration, the contraction inhibitor constant, and the myofibroblast apoptosis rate. Next to these insights, we perform a sensitivity analysis for unequal fibroblast and myofibroblast proliferation rates. The impact of this model adaptation is significant.

6.1 Introduction

In this chapter, we perform a sensitivity analysis for the biomorphoelastic model in a two-dimensional setting to complement our previous sensitivity analysis of the model in a one-dimensional setting.

In contrast to the simulations for the two-dimensional stability analysis in Chapter 4, the simulations in this chapter show a larger displacement of the mesh. To this end, we pay close attention to the mesh and our remeshing strategy.

Section 6.2 presents the computational domain and the initial conditions that we use in the simulations, and Section 6.3 presents the applied meshing techniques. Subsequently, Sections 6.4 and 6.5 present the sensitivity analysis for the original model and for the model with different cell proliferation rates.

6.2 The domain and the initial conditions

For the sensitivity analysis in 2D, we use the fixed quarter computational domain defined by $\Omega_{\mathbf{x}} = (0, 10)^2 \subset (-10, 10)^2$ cm^2 with $\overline{\Omega}_{\mathbf{x}} = \bigcup_{b \in \{o,v,h\}} \Gamma_{\mathbf{x}}^b$, the outer nonsymmetrical and symmetrical boundaries (see Section 2.4). Within this domain, we define the initial burn by the subset $\Omega^w(0) = \{(x, y) : \left|\frac{x}{4}\right| + \left|\frac{y}{4}\right| \leq 1\}$, a symmetrical rotated square. We note that we can also split this subdomain in half because of symmetry, though, from a computational point of view, implementation is more appealing for the quarter domain. The initial conditions describe a burn that did not damage all the collagen. Hence, we assume the presence of signaling molecules, fibroblasts and collagen, whereas myofibroblasts are assumed not to be there. Let $d(\mathbf{x})$ be the shortest distance from point $\mathbf{x} \in \Omega^w$ to the wound boundary. Let $\Omega_s^w = \{\mathbf{x} \in \Omega^w(0) \ : \ d(\mathbf{x}) \geq s\}$, then for all $\mathbf{x} \in \Omega_s^w$, we have $z(\mathbf{x}; 0) = \tilde{z} \in \mathbb{R}^+$, the densities in the wound for $z \in \{N, c, \rho\}$. In the intact skin tissue, for all $\mathbf{x} \in \Omega_{\mathbf{x}} \setminus \Omega^w : z(\mathbf{x}; 0) = \overline{z} \in \mathbb{R}^+$, the equilibrium densities for $z \in \{N, c, \rho\}$. For all $\mathbf{x} \in \Omega_{\mathbf{x}} : M(\mathbf{x}; 0) = \overline{M} = 0$. For the wound boundary's steepness, we use half of a period of sine-functions for N, c and ρ to smoothly transition from the burn to the intact tissue, and we take $s = 0.25$ cm. Regarding the mechanical initial conditions, all initial conditions are equal to zero. We show the graphical representation of the initial fibroblast condition in Figure 6.1.
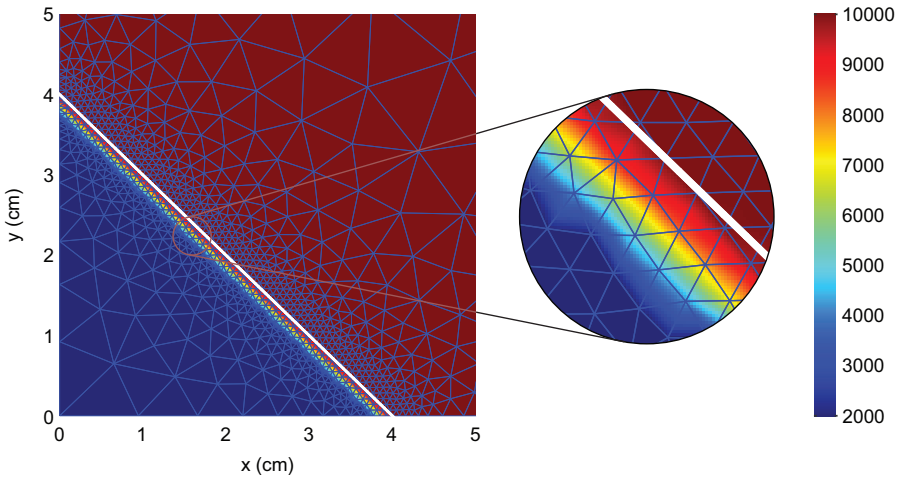
Figure 6.1: Example of the initial fibroblast cell density, with parameter values $\overline{N} = 10^4$ cells/cm^3 and $\tilde{N} = 2 \times 10^3$ cells/cm^3. We also show the initial mesh and the wound boundary (in white). The color bar shows the number of cells per cm^3. Hence, on the wound boundary left-hand-side, there are 2000 cells/cm^3, and on the right-hand-side, there are 10000 cells/cm^3. The plot is zoomed in such that $0 \leq x, y \leq 5$ and provides a closer look to the area of interest.

6.3 Strategy for (re)meshing

For the initial mesh of the computational domain, we use the KOKO mesh generator [92], which we have modifed. We use this mesh generator to fine-tune the mesh density

around the wound edge to get a more accurate approximation of the wound edge (for example, see the fine mesh in Figure 6.1). The 2D KOKO mesh generator uses signed distance and size functions. The signed distance function quickly determines if a point is inside or outside a bounded domain $\Omega \in \mathbb{R}^2$, in our case, a square $[0,10]^2$. The size function $h : \Omega \to \mathbb{R}_+^*$ controls the mesh resolution. The value of $h(d(\mathbf{x}), s)$ gives the relative spatial node distribution over the domain and is not the actual size of the elements. Given the distance $d(\mathbf{x})$ of a node in the mesh to the wound boundary, we define our size function:

$$h(d(\mathbf{x}), s) = \begin{cases} 1, & \text{if } d(\mathbf{x}) \le s \\ 4.5(d(\mathbf{x}) - s) + 1, & \text{if } d(\mathbf{x}) > s \end{cases}, \tag{6.1}$$

such that the triangle size increases linearly with the distance to the wound boundary. Here, $s = 0.25$ cm is the wound boundary's steepness size. The KOKO mesh generator algorithm comprises six steps: initialization, triangulation, mesh smoothing, boundary nodes, termination criteria, and triangle quality. We have adjusted the step where the code projects external nodes to the boundary. We noticed that, sometimes, the KOKO mesh generator gives unacceptable results. Hence, we use a pre-defined polygon and project nodes on the polygon boundary for any points outside the polygon. We compute the distances of the external nodes to the polygon boundary and project the node on the boundary edge closest to the external node.

The KOKO mesh generator termination criterion is based on the relative node displacement on the current iteration. We stop the smoothing process if

$$\max_i \left\| \mathbf{p}_i^k - \mathbf{p}_i^{k+1} \right\| / h_0 < 5 \times 10^{-3},$$

where $\mathbf{p}_i^k$ is the position of node i at the kth timestep, and h_0 is the reference edge length. We take $h_0 = 8 \times 10^{-2}$ cm.

In finite element applications, the error upper bounds depend on the smallest angle in the mesh. In all our simulations, we use the quality measure $\alpha(\Delta)$ that is the smallest ratio of the radius r of the inscribed circle to the radius R of the circumscribed circle of a triangle Δ, i.e.

$$\alpha(\Delta) = 2\frac{r}{R} = \frac{(l_2 + l_3 - l_1)(l_3 + l_1 - l_2)(l_1 + l_2 - l_3)}{l_1 l_2 l_3}, \tag{6.2}$$

where l_1, l_2, l_3 are the side lengths of triangle Δ. A mesh is a good if all triangles have $\alpha_{\min} = \min_{\Delta \in X_h(t)} \alpha(\Delta) > 0.5$. Our initial mesh has $\alpha > 0.618$ for all triangles.

We remesh globally to get a new mesh with a quality at least $\min_k \alpha(\Delta_k) \ge 0.5$ when the quality in the updated mesh drops below $\min_k \alpha(\Delta_k) < 0.5$. For this reason, we use the adapted version of the KOKO mesh generator and provide it with the current wound boundary coordinates so the wound boundary contains grid points. We interpolate all the variables on the new mesh and restart the Picard iterations (for information on our numerical implementation, see Section 2.5).

In our study, we observed that local remeshing was computationally cheaper, taking 1–3 seconds, than global remeshing, which takes 25–40 seconds. However, we had to carry out local remeshing much more frequently than global remeshing, which made local remeshing eventually more expensive from a computational time perspective. Therefore, although hybrid forms could be studied, we continue with global remeshing only.

In case the Picard iterations do not meet the convergence criterion within six iterations, we decrease the timestep to 80% of its current value and restart the Picard iterations. Otherwise, we increase the timestep by a factor of 1.1, with a maximum Δt_{max} depending on the change in the relative surface area (RSA). Initially, the maximal timestep is $\Delta t_{max,1} = 0.5$ day, as long as the RSA is decreasing (contraction). In case the RSA increases (retraction), the maximal timestep changes. If the RSA changes less than 0.1%, the maximal timestep changes to $\Delta t_{max,2} = 2$ days, and if the change is less than 0.01%, the maximal timestep changes to $\Delta t_{max,3} = 100$ days. We start with an initial timestep of $\Delta t = 0.1$ days. Figure 6.2 shows an example of how the RSA, the timestep and the mesh quality develop during a simulation.
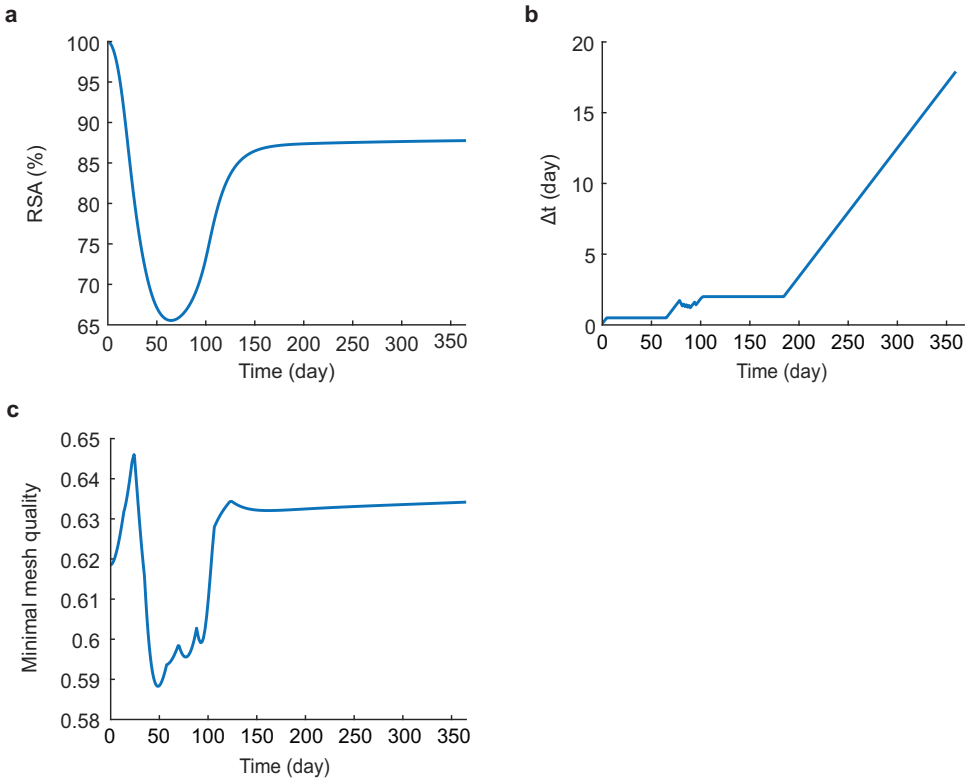
Figure 6.2: Examples of the evolution of the RSA (**a**), the variable timestep (**b**), and the mesh quality (**c**) during a simulation.

Figure 6.2a shows that the RSA drops to about 65% (35% contraction) in 62 days, after which it increases to about 85% (day 150), to an asymptotic RSA of 87.6%. Figure 6.2b shows that the initial timestep of 0.1 day increases to the maximum of $\Delta t_{max,1} = 0.5$ day within five days, after which it stays 0.5 days (that is during contraction). The timestep increases from day 65 until day 78, which is are the first 13 days of retraction after the RSA reached its minimum. Then, the timestep reduces to obtain convergence in the inner Picard iteration loop. That is when the second derivative of the RSA inceases (i.e., during

rapid retraction, increasing in speed). Once the second derivative of the RSA decreases (i.e., when the rapid retraction decreases in speed), the timestep reaches $\Delta t_{\max,2} = 2$ days, which stays constant until the RSA does not change more than 0.1% between time iterations. Subsequently, the timestep increases towards 18 days. Figure 6.2c shows that the mesh quality initially increases when the mesh moves. In this example, when the mesh contracts at the highest rate, the mesh quality decreases rapidly. No remeshing is needed; hence the mesh quality increases when the mesh slowly moves toward maximum contraction (day 48 to 57) and keeps increasing while the mesh retracts (day 57 to 69). When the retraction speed increases, the mesh quality decreases a little (day 69 to 76), however, remeshing is not needed, and the quality starts increasing again (day 76 to 88) until (some) triangles move in wrong positions as the retraction speed is increasing causing the mesh quality to drop (day 88 to 93). Again, no remeshing is needed despite the decrease in mesh quality, and subsequently, the mesh quality starts increasing rapidly again as the timestep increases (day 93 to 106). The remainder period shows that the mesh quality keeps increasing at a slower rate (day 106 to 124), and it decreases slightly while the retraction speed slows down (day 124 to 158), to further increase as the mesh stabilizes (i.e., as the scar completely maturates). In this example, the simulation did not need any remeshing.

6.4 Sensitivity analysis

Out of the 34 model parameters, we vary 30 independent parameters to study the sensitivity of these parameters. These are all the model parameters except for the initial fibroblast cell and collagen densities, the constant q, and the collagen secretion rate k_ρ. We vary the parameter values by decreasing or increasing the mean values by $\pm 5, 15, 25\%$. Hence, we perform 181 simulations: 6 variations × 30 parameters + a single base simulation. On average, a simulation takes less than 8.2 minutes on a 64-bit Windows 10 Pro system with 16 GB RAM 3.59 GHz AMD Ryzen 5 3600 6-Core Processor. We use four processors to solve the chemical part and five processors to solve the mechanical part of the model. Besides the Poisson's ratio parameter, remeshing was only necessary for the highest value for k_c, the signaling molecule secretion rate, the lowest value for δ_c, the signaling molecule decay rate, the lowest value for the body force-inhibiting constant R, and the lowest and second lowest value for $\overline{\rho}$, the equilibrium collagen concentration. We also note that for different geometries, remeshing is needed more often. The parameter values are the same as the mean values in Table 5.3 in Chapter 5, except for the parameter values shown in Table 6.1.

When a new mesh has to be generated, all data has to be interpolated, which results in interpolation errors. Except for low equilibrium collagen values $\overline{\rho}$, the RSA and total strain energy (TSE) densities are smooth in all cases we varied parameter values. We note the stability condition $k_c \le \delta_c a_c^{II} \overline{\rho}$. If the secretion rate k_c is high, and the decay rate δ_c and collagen equilibrium $\overline{\rho}$ are low, these values are closer to the stability bound, explaining why remeshing is necessary. We note that every simulation has a set of parameter values that meets this stability criterion.

As mentioned earlier, the RSA and TSE densities are not smooth for a low equilibrium collagen value. If we decrease the equilibrium by 25%, the simulation needs to perform remeshing 31 times. The RSA is not a smooth density, and the TSE density shows many

Table 6.1: Mean parameter values different from the ones shown in Table 5.3 (where the values are found in group 2 of patients of different age).

Parameter	Value	Dimension
D_c	2.9×10^{-3}	cm^2/day
k_c	4×10^{-13}	$\text{g}/(\text{cells day})$
η^{II}	5×10^{-1}	-
μ_1	10^2	$(\text{N day})/\text{cm}^2$
μ_2	10^2	$(\text{N day})/\text{cm}^2$
E	3.2×10	$\text{N}/((\text{g cm})^{1/2})$
ν	4.9×10^{-1}	-
ξ	5×10^{-2}	$(\text{N g})/(\text{cells cm}^2)$

peaks because of peaks in the collagen density. These peaks result from oscillations in the finite element approximation of the collagen density, presumably because of inter-polation errors. The reason is not necessarily because of instability, since we do not end up in the unstable regime $\overline{\rho} < \frac{k_c}{\delta_c a_c^{II}}$. However, we ended up close to it, and regarding the numerical approximations, we elaborated this criterion for finite differences under constant mesh size. Hence, the 2D finite element case with unstructured meshes can be (slightly) different. Let $\text{devTSE}_{\text{day}}^{\overline{\rho}}(dva)$ denote the deviation from the mean TSE_{day} for deviation $dva \in \{\pm 5, 15, 25\%\}$ from the mean equilibrium collagen value. Although the RSA and TSE densities are smooth, the gradient of $\text{devTSE}_{\text{day}}^{\overline{\rho}}$ changes sign. Therefore, we cannot rely on this simulation result and will interpolate the z-scores of the total strain energy features for a 25% decrease in the equilibrium collagen value. If we de-crease the equilibrium value by 15%, the simulation needs to perform remeshing three times. Hence, we also interpolate the z-score of the total strain energy features for a 15% decrease in the equilibrium collagen value.

Similar to our previous sensitivity study in $\mathbb{R}^1$, the results show the *minimum of the rel-ative surface area* (RSA_{min}, i.e., maximum contraction) in a time of one year, the *day on which the RSA reaches the minimum* (RSA_{day}, i.e., the day after which the wound/scar retracts), the *relative surface area on day 365* (RSA_{365}), the *maximum of the total strain energy density* (TSE_{max}), and the *day on which the total strain energy density reaches the maximum* (TSE_{day}, i.e., the day at which the patient experiences maximal discomfort).

Each parameter $i \in \{D_n, \dots, \tilde{c}\}$ has a z-score for values in $r \in \text{RSA}_{\{:\}} \bigcup \text{TSE}_{\{:\}}$ and variation $j \in \{\pm 5, 15, 25\%\}$ defined by $z_{ij}^r = (x_{ij}^r - \overline{x}_j^r)/s_{x_j^r}$. Here $\overline{x}_j^r$ is the sample mean, and $s_{x_j^r}$ is the sample standard deviation. The sum of the absolute values of the z-scores:

$$\mathscr{S}_i^r = \sum_j \left| z_{ij}^r \right|, \tag{6.3}$$

where z_{ij}^r is the z-score of the data in r for parameter i in variation j, measures the sensitivity.

Table 6.2 shows the sensitivity values of some of the parameters in terms of the z-scores for variation -5%. In the last column, we rounded the sum of the values to the nearest integer.

Table 6.2: Sensitivity of some varied parameter values in terms of z-scores for variation -5%.

Param.	Dimension	$\mathscr{S}^{\text{RSA}_{\min}}$	$\mathscr{S}^{\text{RSA}_{\text{day}}}$	$\mathscr{S}^{\text{RSA}_{365}}$	$\mathscr{S}^{\text{TSE}_{\max}}$	$\mathscr{S}^{\text{TSE}_{\text{day}}}$	$\mathscr{S}^{\text{total}}$
ν	-	2.479	1.971	0.474	5.521	1.833	12
r^{max}	-	0.194	0.239	0.047	0.230	0.208	1
$\overline{\rho}$	g/cm^3	0.013	0.391	0.056	0.173	0.174	1
$\overline{N}$	cells/cm^3	0.154	0.178	0.038	0.213	0.140	1
ξ	(N g)/(cells cm^2)	0.175	0.117	0.044	0.222	0.140	1
η^I	-	0.104	0.117	0.033	0.203	0.208	1
δ_ρ	cm^6/(cells g day)	0.060	0.209	0.014	0.185	0.140	1

The third to seventh columns show the scores on the minimum of the relative surface area (RSA) $\mathscr{S}^{\text{RSA}_{\min}}$, the day on which the minimum RSA is reached $\mathscr{S}^{\text{RSA}_{\text{day}}}$, the RSA on day 365 $\mathscr{S}^{\text{RSA}_{365}}$, the maximum value of the total strain energy (TSE) density $\mathscr{S}^{\text{TSE}_{\max}}$, and the day on which the maximum of the TSE is reached $\mathscr{S}^{\text{TSE}_{\text{day}}}$. The last column shows the total of the scores $\mathscr{S}^{\text{total}}$.

These results show that a relatively small variation of -5% relative to the mean parameter value of ν has a significant impact on all the features for both the RSA and TSE, compared to the variation of the values of the other shown parameters. A variation of -5% on the mean value of Poisson's ratio ν results in a geometry where the wound boundary is bumpy, a phenomenon we do not see when we vary other parameter values. We varied the Poisson's ratio value even more by -15% and -25%, knowing that those simulations would result in even more bumpy boundaries. We do not show the results of these simulations because the timestep decreased significantly, and in almost every iteration, we needed to remesh.

Further, increasing Poisson's ratio above 0.5 is impossible. It is well known that the Poisson's ratio is around 0.49 for soft tissues [70, 93]. Poisson's ratios of more than 0.5 are not physical; if the value equals 0.5, then the material is incompressible. It is well-known that pure elasticity can cause significant accuracy loss by the notorious locking phenomenon in finite element simulations [94].

To visualize the effect of a decreased Poisson's ratio on the resulting mesh and wound boundary, we varied the mean value of $\nu = 0.49$ by taking $\nu \in \{0.48, 0.47, 0.46\}$ and show these results in Figure 6.3.
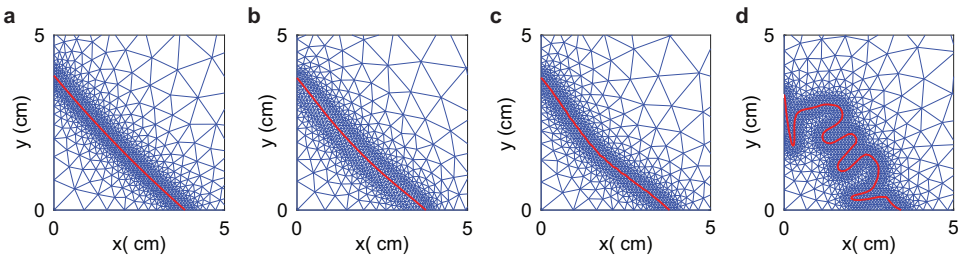
Figure 6.3: Final meshes and wound boundaries on day 365 for different Poisson's ratio values. The figure shows the results for ν equal to 0.49 (**a**), 0.48 (**b**), 0.47 (**c**) and 0.46 (**d**). The plots represent a quarter of the computational domain and are zoomed in such that $0 \leq x, y \leq 5$.

Figure 6.3a shows what the mesh and wound edge look like after a simulation representing a year, with all parameter values equal to the values in Tables 5.3 and 6.1, so $\nu = 0.49$. We note that our definition of the wound edge is sharp, whereas, in clinical practice, the wound edge is more spline-like, though it can also be very sharp. We can see that the wound edge is smooth and curves slightly inwards halfway through. In this simulation, no remeshing was necessary. Figure 6.3b, where the Poisson's ratio is 0.48, shows that the mesh around the wound edge is less dense. Here, we needed to remesh on day 23 only. The wound edge curves more inwards relative to Figure 6.3**a**. However, the wound edge is smooth. In Figure 6.3c, the mesh around the wound edge is denser than in Figure 6.3b because we still needed to remesh on day 85 in this simulation. Further, the wound edge shows small bumps; hence a value of 0.47 for the Poisson's ratio is too low for a smooth wound boundary. Finally, Figure 6.3d results from the simulation where the Poisson's ratio is 0.46. The mesh around the wound edge is dense and explainable after 33 times remeshing, with the last remesh on day 344. The wound edge is visibly bumpy and strongly pulls inwards from the domain symmetry boundaries.

We excluded variations in the Poisson's ratio from further variations.

Table 6.3 shows the sensitivity values in terms of the z-scores for all parameters, except for Poisson's ratio. In the last column, we rounded the sum of the values to the nearest integer.

Table 6.3: Sensitivity of the varied parameter values in terms of z-scores.

Param.	Dimension	$\mathscr{S}^{\mathrm{RSA_{min}}}$	$\mathscr{S}^{\mathrm{RSA_{day}}}$	$\mathscr{S}^{\mathrm{RSA_{365}}}$	$\mathscr{S}^{\mathrm{TSE_{max}}}$	$\mathscr{S}^{\mathrm{TSE_{day}}}$	$\mathscr{S}^{\mathrm{total}}$
$\overline{\rho}$	g/cm^3	9.014	16.690	22.270	14.169	9.125	71
R	g/cm^3	11.510	11.191	12.069	17.874	15.768	68
δ_m	/day	14.356	10.411	11.571	19.595	9.889	66
r^{max}	-	12.035	8.365	10.357	23.206	9.263	63
$\overline{N}$	cells/cm^3	8.349	9.615	9.321	18.784	10.582	57
r	cm^{3q}/(cells^q day)	12.930	7.761	10.620	19.099	5.970	56
k_c	g/(cells day)	5.540	6.141	13.622	19.645	5.322	50
ξ	(N g)/(cells cm^2)	9.707	2.817	9.945	20.528	3.091	46
E	N/((g cm)$^{1/2}$)	8.643	5.666	9.320	12.950	6.494	43
δ_c	g/cm^3	3.069	3.636	13.769	14.679	5.221	40
δ_ρ	cm^6/(cells g day)	3.910	7.051	12.719	12.028	3.930	40
k_ρ^{max}	-	3.696	6.764	12.061	11.991	3.439	38
η^I	-	2.120	2.889	7.733	14.717	9.224	37
a_c^I	g/cm^3	1.883	5.196	5.365	11.783	7.078	31
a_c^{III}	cm^3/g	2.215	4.307	7.605	14.794	2.249	31
ζ	cm^6/(cells g day)	3.306	2.848	10.852	12.077	1.254	30
k_1	cm^3/(g day)	0.924	4.942	5.654	11.354	5.250	28
δ_n	/day	1.533	3.329	6.001	11.872	3.065	26
η^{II}	-	1.204	2.038	6.066	12.218	2.056	24
$\tilde{c}$	g/cm^3	1.903	1.589	6.606	12.029	1.243	23
a_c^{II}	g/cm^3	0.947	1.018	6.086	11.484	3.707	23
μ_2	(N day)/cm^2	1.721	1.589	6.075	11.902	1.896	23

Table 6.3: (continued)

Param.	Dimension	$\mathscr{S}^{\text{RSA}_{\min}}$	$\mathscr{S}^{\text{RSA}_{\text{day}}}$	$\mathscr{S}^{\text{RSA}_{365}}$	$\mathscr{S}^{\text{TSE}_{\max}}$	$\mathscr{S}^{\text{TSE}_{\text{day}}}$	$\mathscr{S}^{\text{total}}$
a_c^{IV}	g/cm^3	1.861	1.717	6.299	12.028	1.254	23
ρ_t	g/cm^3	1.727	1.589	6.106	11.892	1.813	23
χ	cm^5/(g day)	1.727	1.589	6.106	11.892	1.813	23
μ_1	(N day)/cm^2	1.720	1.589	6.074	11.907	1.813	23
κ	cm^3/cells	1.753	1.589	6.120	11.918	1.254	23
D_c	cm^2/day	1.670	1.518	5.814	11.968	1.254	22
D_n	cm^5/(cells day)	1.793	0.999	6.171	12.019	1.223	22

The third to seventh columns show the scores on the minimum of the relative surface area (RSA) density $\mathscr{S}^{\text{RSA}_{\min}}$, the day on which the minimum RSA is reached $\mathscr{S}^{\text{RSA}_{\text{day}}}$, the RSA on day 365 $\mathscr{S}^{\text{RSA}_{365}}$, the maximum value of the total strain energy (TSE) density $\mathscr{S}^{\text{TSE}_{\max}}$, and the day on which the maximum of the TSE is reached $\mathscr{S}^{\text{TSE}_{\text{day}}}$. The last column shows the total of the scores $\mathscr{S}^{\text{total}}$.

This table shows that the equilibrium collagen concentration with a total score of 71 is the next most sensitive parameter. Given that collagen concentrations decrease with age [77], the model shows that the differences in features of RSA and TSE become more intense with age. Other parameters that are sensitive ($\mathscr{S}^{\text{total}} \geq 50$) are the body force-inhibiting constant R, the myofibroblast apoptosis rate δ_M, the maximum factor of (myo) fibroblast cell division rate enhancement $r^{\max}$, the equilibrium fibroblast distribution $\overline{N}$, the (myo) fibroblast proliferation rate r, and the signaling molecule secretion rate k_c. Given the stability constraint $k_c \leq \delta_c a_c^{II} \overline{\rho}$, the sensitivity of the signaling molecule secretion parameter k_c relates to the sensitivity of the equilibrium collagen concentration $\overline{\rho}$ and the signaling molecule decay rate δ_c, rather than to the parameter a_c^{II}.

Parameters that are least sensitive ($\mathscr{S}^{\text{total}} \leq 23$) are all the parameters the least sensitive are the diffusion rate of (myo) fibroblasts en signaling molecules (D_n, D_c), the chemotaxis rate and crowding factor of (myo) fibroblasts (χ, κ), the initial signaling molecule concentration ($\tilde{c}$), the signaling molecule secretion inhibition concentration a_c^{II}, the collagen secretion inhibition factor (a_c^{IV}), the total mass density of dermal tissues ρ_t, and the shear and bulk viscosities (μ_1, μ_2).

To get a visual insight into the sensitivity of the parameters, we present the effect of the variations on the parameters on both the post-burn contraction and the discomfort that a patient might experience in Figure 6.4. The figure has no legend, so the distinction between the sensitivity of the parameters is clear, and we labeled the essential lines with different styles.

Figure 6.4a shows that the most influencing parameters on decreasing the maximum contraction are the proliferation enhancement factor $r^{\max}$, the generated stress per unit cell density ξ, the equilibrium fibroblast cell density $\overline{N}$, the myofibroblast apoptosis rate δ_m, the (myo) fibroblast proliferation rate r, and the body force-inhibiting constant R. Increasing values for δ_m, r and R, and decreasing values for $r^{\max}$, ξ and $\overline{N}$ result in less contraction. From Figure 6.4b, we see that this results in maximal contraction on a later day. In addition, increasing values for the equilibrium collagen concentration $\overline{\rho}$ results in maximal contraction on an earlier day. The reduction in contraction because of increasing values for δ_m and R is not counter-intuitive because myofibroblast pull on the
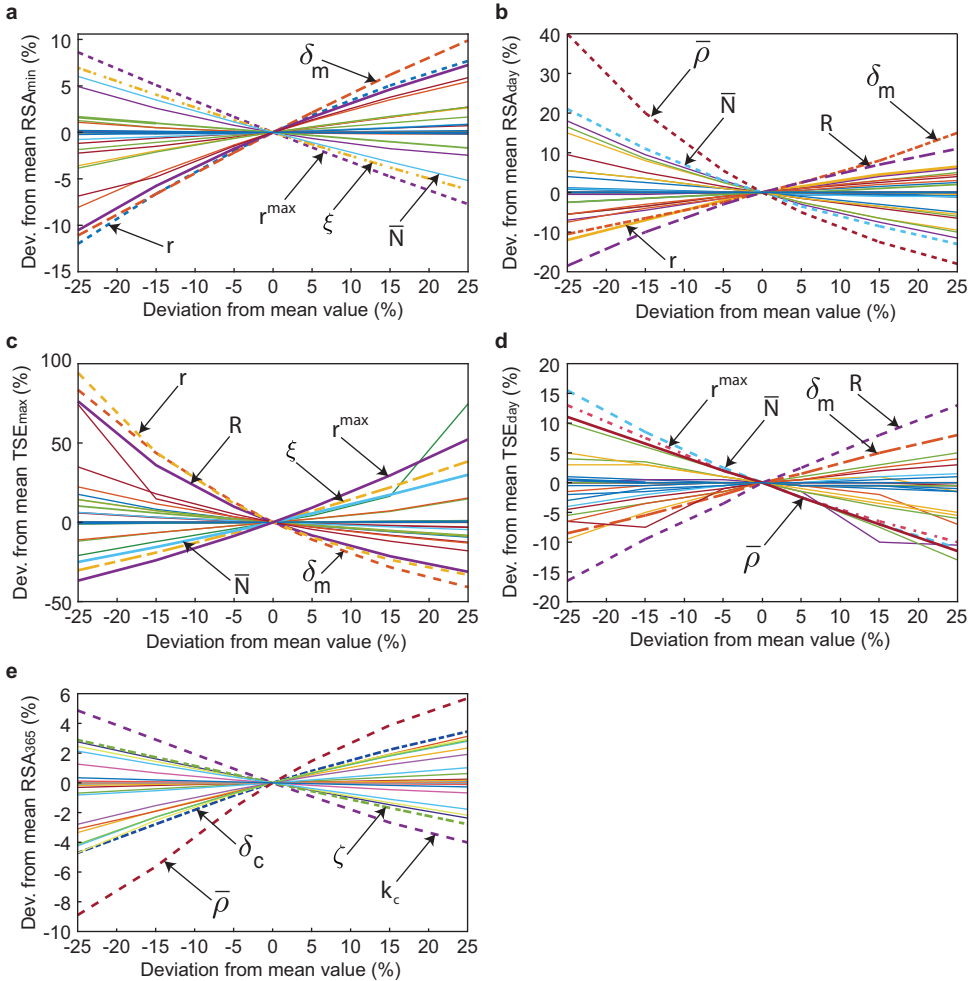
Figure 6.4: Effects of the variations in parameter values for the relative surface area (RSA) and the total strain energy (TSE) density. Shown are the effects on the minimum of the RSA (**a**), the effects on the day the RSA reaches minimum (**b**), the effects on the maximum of the TSE (**c**), the effects on the day the TSE reaches maximum (**d**), and the effects on the RSA on day 365 (**e**). In the figures,

skin and that R reduces the effect. The effect of the reduction in equilibrium collagen concentration is most prominent for the day of maximum contraction: a decrease of 25% delays this day by 40 days relative to the base simulation.

Figures 6.4c & 6.4d summarize the results for the discomfort that the patient might experience. We see that decreasing the maximal contraction by targeting $r^{\max}$, ξ, $\overline{N}$, δ_m, and R results in less maximal discomfort, on a later day. An increase in the equilibrium collagen concentration $\overline{\rho}$ results in maximum discomfort on an earlier day.

In addition, Figure 6.4e features that the signaling molecule secretion rate k_c and decay rate δ_c, the equilibrium collagen concentration $\overline{\rho}$, and the rate of morphoelastic change

ζ can influence decreasing the contraction after one year the most. Increasing values for $\overline{\rho}$ and δ_c, and decreasing the values for k_c and ζ results in less remaining contraction after scar maturation. If fewer signaling molecules are available to enhance the proliferation of (myo) fibroblasts and myofibroblast differentiation, then the tissue is influenced less according to the morphoelastic change in equation (2.14). Further, an increase in collagen concentration results in stiffer tissue that resists contraction and acts as a buffer for effective strain.

6.4.1 Comparison to the case of a 'collagen-rich covered burn' in $\mathbb{R}^1$

The results of our previous sensitivity study in $\mathbb{R}^1$ are partly similar and partly different from the results of our current study. The main reason for this could be because, in our previous study, we set the initial concentration of collagen in the wound equal to the equilibrium concentration of collagen and because the study was in 1D. The initial collagen concentration in our previous 1D study represents the situation where a skin substitute rich in collagen type I covers the wound.

We conclude that the equilibrium collagen concentration $\overline{\rho}$ is the most sensitive parameter in both studies. However, the relative sensitivity of $\overline{\rho}$ in our current study is less because of lower values of the sensitivity scores of all the parameters, implying that the other parameters are substantially less influential in the case of a collagen-rich skin substitute. Furthermore, in our previous study, the fibroblast apoptosis rate was more sensitive than in our current study (factor 3), and the (myo) fibroblast proliferation rate was less sensitive (factor 4). The fibroblast apoptosis rate was almost as sensitive as the myofibroblast apoptosis rate, whereas, in our current study, the fibroblast apoptosis rate is approximately 2.5 times less sensitive.

According to the model, a collagen-rich skin substitute increases the concentration of matrix metallo proteinases that cleave growth factors. As a result, the concentration of growth factors will decrease, stimulating myofibroblast differentiation less. This result is in line with the assumption that myofibroblast differentiation in skin substitutes is very low/absent because of the presence of the substitute that 'replaces' the skin. The result is that more fibroblasts remain present, hence a reason for the increase and decrease of the sensitivity of the fibroblasts apoptosis rate and the (myo) fibroblast proliferation rate, respectively. If the collagen concentration is low/absent, as in our current study, then the fibroblast distribution needs to be replenished because more fibroblasts differentiate into myofibroblasts. From a biological perspective, the lack of collagen in the injured area impairs fibroblast migration. Hence, proliferation becomes more critical to allow the presence of fibroblasts in the injured region, which facilitates myofibroblast differentiation and collagen deposition.

6.5 Implications for different cell proliferation rates

The previous section shows that the proliferation of (myo) fibroblasts significantly influences the post-burn contraction and the discomfort the patient might experience. However, the mathematical model does not provide information on whether this is the proliferation of fibroblasts or myofibroblasts.

Vaughan *et al.* have shown that myofibroblasts proliferate less rapidly than fibroblasts

[31]. Indeed, during myofibroblast differentiation, fibroblasts first gain a proto-myofibroblast phenotype. These proto-myofibroblasts migrate to the wound area and proliferate. They subsequently gain a complete myofibroblast phenotype that expresses a large amount of alpha-smooth muscle actin and takes part in the important deposition of extracellular matrix components. These contractile, fully differentiated myofibroblasts are trapped in the matrix they secrete, adhere tightly to this matrix via focal contacts, and are thought not to proliferate.

In the mathematical model, we do not distinguish between the different phenotypes of proto-myofibroblasts and fully differentiated myofibroblasts. Given the result from Vaughan *et al.*, we study the effect of different cell proliferation rates. We define the fibroblast proliferation rate r_n and the myofibroblast proliferation rate r_m. As in the previous section, we vary the values by ± 5, 15, 25%. Table 6.4 shows the sensitivity of all parameters in terms of z-scores, considering the distinction of the cell proliferation rates. Again, in the last column, we rounded the sum of the values to the nearest integer.

Table 6.4: Sensitivity of the varied parameter values in terms of z-scores in case of different cell proliferation rates.

Param.	Dimension	$\mathscr{S}^{\text{RSA}_{\min}}$	$\mathscr{S}^{\text{RSA}_{\text{day}}}$	$\mathscr{S}^{\text{RSA}_{365}}$	$\mathscr{S}^{\text{TSE}_{\max}}$	$\mathscr{S}^{\text{TSE}_{\text{day}}}$	$\mathscr{S}^{\text{total}}$
R	g/cm^3	2.429	4.303	0.692	7.109	5.008	20
δ_m	/day	2.973	3.883	0.621	8.780	3.023	19
r_m	cm^{3q}/(cells^q day)	3.343	2.982	0.842	9.296	2.044	19
r^{max}	-	2.612	3.381	0.699	7.151	3.361	17
$\overline{\rho}$	g/cm^3	1.821	6.850	1.639	3.508	3.290	17
r_n	cm^{3q}/(cells^q day)	2.728	2.944	0.548	8.405	1.711	16
$\overline{N}$	cells/cm^3	1.836	3.923	0.557	4.505	3.841	15
k_c	g/(cells day)	1.261	2.275	1.154	5.516	1.776	12
ξ	(N g)/(cells cm^2)	2.122	1.050	0.641	5.553	1.283	11
E	N/((g cm)$^{1/2}$)	1.809	2.070	0.429	2.274	1.947	9
δ_c	g/cm^3	0.579	1.574	0.844	3.834	1.587	8
δ_ρ	cm^6/(cells g day)	0.786	2.926	0.761	1.384	1.475	7
η^I	-	0.334	1.089	0.347	2.119	3.331	7
k_ρ^{max}	-	0.738	2.757	0.694	1.349	1.257	7
a_c^I	g/cm^3	0.343	1.903	0.044	1.103	2.047	5
a_c^{III}	cm^3/g	0.353	1.585	0.328	2.150	0.641	5
k_1	cm^3/(g day)	0.100	1.785	0.044	0.530	1.508	4
ζ	cm^6/(cells g day)	0.669	1.037	0.760	0.637	0.235	3
η^{II}	-	0.113	0.757	0.108	1.564	0.475	3
δ_n	/day	0.115	1.161	0.093	0.566	0.798	3
a_c^{II}	g/cm^3	0.069	0.198	0.113	0.652	1.100	2
μ_2	(N day)/cm^2	0.175	0.488	0.103	0.593	0.401	2
a_c^{IV}	g/cm^3	0.219	0.557	0.134	0.613	0.235	2
$\tilde{c}$	g/cm^3	0.232	0.488	0.178	0.615	0.233	2
ρ_t	g/cm^3	0.177	0.488	0.107	0.592	0.375	2
χ	cm^5/(g day)	0.177	0.488	0.107	0.592	0.375	2

Table 6.4: (continued)

Param.	Dimension	$\mathscr{S}^{\text{RSA}_{\min}}$	$\mathscr{S}^{\text{RSA}_{\text{day}}}$	$\mathscr{S}^{\text{RSA}_{365}}$	$\mathscr{S}^{\text{TSE}_{\max}}$	$\mathscr{S}^{\text{TSE}_{\text{day}}}$	$\mathscr{S}^{\text{total}}$
μ_1	$(\text{N day})/\text{cm}^2$	0.174	0.488	0.103	0.593	0.375	2
κ	cm^3/cells	0.185	0.488	0.109	0.595	0.235	2
D_c	cm^2/day	0.159	0.450	0.067	0.605	0.235	2
D_n	$\text{cm}^5/(\text{cells day})$	0.197	0.229	0.117	0.610	0.230	1

The third to seventh columns show the scores on the minimum of the relative surface area (RSA) density $\mathscr{S}^{\text{RSA}_{\min}}$, the day on which the minimum RSA is reached $\mathscr{S}^{\text{RSA}_{\text{day}}}$, the RSA on day 365 $\mathscr{S}^{\text{RSA}_{365}}$, the maximum value of the total strain energy (TSE) density $\mathscr{S}^{\text{TSE}_{\max}}$, and the day on which the maximum of the TSE is reached $\mathscr{S}^{\text{TSE}_{\text{day}}}$. The last column shows the total of the scores $\mathscr{S}^{\text{total}}$.

For relatively insensitive parameters, Table 6.4 shows small differences with Table 6.3 as the parameters k_ρ^{max}, ζ, δ_n and $\tilde{c}$ score slightly lower in sensitivity. The differences for more sensitive parameters are greater than those in Table 6.3. The sensitivity of the equilibrium collagen concentration ranges within the sensitivities of the cell proliferation rates. Further, the variations in sensitivity are greater in the case of equal proliferation rates, given the total z scores. Finally, even though the sensitivity scores differ little, the myofibroblast proliferation rate is slightly more sensitive than the fibroblast proliferation rate.

To provide more insight into the effects of the different proliferation rates, we show the effects on the RSA and TSE in Figure 6.5.
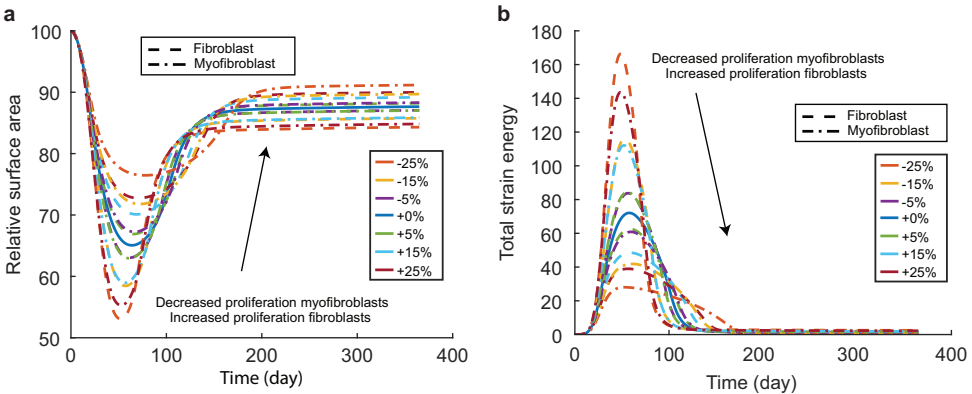
Figure 6.5: Effects of the variations in cell proliferation rates for the contraction and discomfort. Shown are the effects on the relative surface area (**a**) and the effects on the total strain energy (**b**).

These plots clearly show that we need to decrease the myofibroblast proliferation rate, in contrast to what the original model with equal proliferation rates shows. The advice in Section 6.4 to increase the proliferation rate means to increase the fibroblast proliferation rate, implying that the *fibroblast proliferation rate* is more sensitive than the *myofibroblast proliferation rate* in contrast to the result in Table 6.4. Further, Figure 6.5a shows that decreasing the myofibroblast proliferation rate by 25% results in a more extended

retraction period, which is also seen in the clinic. In addition, Figure 6.5b shows that the decreased myofibroblast proliferation rate results in an extended period of persistent discomfort correlated with slower retraction.

Given these results, it is advisable to change the model to distinguish between the roles of fibroblasts, proto-myofibroblasts, and myofibroblasts. We will go into more detail regarding this matter in the discussion of this thesis.

6

Conclusions of this part

We comprehensively described the (ranges of the) parameter values. We estimated some parameter values and others were adopted. Most of the variety in the parameter values was found in literature sources. If ranges of values were found, we chose upper or lower bounds or a fixed averaged value.

We quantified the sensitivity of the biomorphoelastic model for post-burn contraction to highlight the significance of the input parameters on contraction so we can give further research directions. We aim to devise therapies that adjust input parameters to reduce post-burn contraction for most patients.

For our sensitivity analyses, we varied independent parameter values and showed the results for RSA_{min}, RSA_{day}, RSA_{365}, TSE_{max}, and TSE_{day}. The Poisson's ratio is around 0.49 for soft tissues, and variation should be done carefully in future simulations. Disregarding the Poisson's ratio, in the original model, the most sensitive parameter is the equilibrium collagen concentration $\overline{\rho}$ present in the dermal layer accounting for 10.6% of the sensitivity scores in 1D and 6.6% in 2D. Other parameters having a significant sensitivity score in 1D are the (myo)fibroblast apoptosis rates δ_n and δ_m, the body force-inhibiting constant R, and the signaling molecule secretion rate k_c accounting for 7.5%, 7%, 6.6% and 6.5% of the sensitivity scores, respectively. In 2D, the fibroblast apoptosis and signaling molecule secretion rates are less sensitive. If the cell's proliferation rates differ, then the order of sensitivity changes as the body force-inhibiting constant accounts for 9.3% of the sensitivity scores, after which the myofibroblast apoptosis rate and proliferation rate (accounting for 8.8%), and the factor of maximum enhancement of cell proliferation and the equilibrium collagen concentration (accounting for 7.9%) follow.

The least sensitive parameters involve the migration rate parameters D_n, D_c and χ, the crowding factor κ, the viscosity μ, the mass density of dermal tissue ρ_t, and the initial collagen concentration $\tilde{\rho}$, accounting for less than 1% of the sensitivity scores in 1D. We note that we let the initial collagen concentration depend on the equilibrium collagen concentration, which can influence this parameter's sensitivity value. In 2D, the differences in sensitivity scores are minor for equal proliferation rates. However, for unequal cell proliferation rates, the list of parameters accounting for less than 1% of the sensitivity scores extends with the signaling molecule and collagen secretion inhibition concentrations a_c^{II} and a_c^{IV}, and the initial signaling molecule concentration $\tilde{c}$.

Taking a closer look at the sensitivity scores of RSA_{365}, the equilibrium collagen concentration and the signaling molecule secretion rate score highest in sensitivity in 2D. The signaling molecule secretion rate sensitivity shows the importance of the existing stability criterion $k_c \leq \delta_c a_c^{II} \overline{\rho}$. If the parameter values almost reach the stability limit, remeshing is necessary for the finite element method.

Further, the focus for further research differs for the different targets RSA_{min}, RSA_{day}, RSA_{365}, TSE_{max}, and TSE_{day}. We should focus on the (myo) fibroblast proliferation and apoptosis rates to limit the contraction intensity during proliferation with secondary intention. The goal is to inhibit myofibroblast proliferation, stimulate fibroblast proliferation, and stimulate myofibroblast apoptosis. Therapeutic strategies to target myofibroblasts involve inhibition of transforming growth factor (TGF)-β activation, inhibition of mechanotransduction (the sensing of matrix stiffness and response to such stiffness by

cells), and activation of in- and extrinsic apoptosis pathways [95]. We note that decreasing the myofibroblast proliferation rate and stimulating the apoptosis rate delay the day of maximal contraction. Further, an elevated collagen concentration, such as collagen-rich skin substitutes, can reduce contraction intensity and its period. The myofibroblast differentiation parameter k_1 does not rank high in the tables, so there is no clear sign that we should restrict the myofibroblast differentiation.

Many burn interventions target the inflammatory response to promote healing or limit hypertrophy; growth factors ultimately arise from this response. If the goal is to limit contraction intensity at a later stage of healing (during maturation), then we should focus on the growth factors' secretion and decay rates. We have to decrease growth factor secretion and stimulate decay. The results show that, based on the significance of the signaling molecule secretion rate for contraction during remodeling, targeting the inflammatory response has a more significant effect on eventual contractures than on the maximum contraction intensity during healing. We note that decreasing growth factor secretion and increasing decay increases the stability of the chemical part of the model.

A correlation exists between post-burn patient discomfort and maximum contraction. To lower the intensity of discomfort, we should target the same as we do to limit the maximum contraction. The effect on the day when the patient experiences maximum discomfort is the same as on the day of maximum contraction. Hence, when we reduce contraction, we reduce the discomfort a patient experiences.

We furthermore performed a feasibility study to study the effect of aging on post-burn contraction and patient discomfort. We have chosen four groups of patients of different ages and varied the model's parameter values according to observations from literature. We furthermore varied the model's parameter values using Karhunen-Loéve expansions to model the heterogeneity of human skin. In our Monte Carlo method, we performed sampling from statistical distributions to assess the impact of uncertainty in the data on contraction behavior.

The model seems feasible for this approach, showing an increased extent of contraction with age, a delayed maximum amount of contraction in older adults, increased contracture in older adults, and an increased variety of contracture formation in older adults compared to children. The figures show more discomfort in elderly patients and that the maximum discomfort is experienced significantly ($p < 0.001$) earlier in younger children than in other age groups. Next to these results, we see that the extent of discomfort is highly related to the contraction in wound healing.

This study shows that contraction increases with age and shows a significant difference ($p < 0.001$) in the maximum amount of contraction between the different age groups. We found the least significant difference between ages 0–15 and 16–40. Further, the differences in the asymptotic contraction in consecutive age groups are least significant between 41–70 and 70+ years. In consecutive groups, we found the most significant difference between 0–15 and 16–40 years. We have seen the differences in the maximum and asymptotic contraction of a few percentages (less than 10) of order. We have seen a significant difference ($p < 0.001$) between all groups for the maximum discomfort a patient might experience. The difference between ages 16–40 and 41–70 is most significant in consecutive groups. We can conclude that these patients experience the same discomfort, although this happens much faster in children.

PART III
Bayesian finite-element trained machine learning approaches

Introduction to the chapters in this part

Burn wound dimensions (size, depth, location) and patient-specific factors (age, gender, etcetera) influence contraction. This dependency is a reason for the growing interest in personalized healthcare.

Mathematical modeling contributes to this growing interest. Detailed models can give insight into which elements significantly influence the contraction, can tune these elements, and can access the uncertainty by performing Monte Carlo simulations. These techniques allow for patient-based predictions that can support medical staff in decision-making. However, more-dimensional models suffer from long computation times, a downside because many model-based predictions are needed to achieve personalized healthcare. Therefore, this research aims to find a computationally cheaper neural network method. This alternative method should increase the applicability of the mathematical model for parameter studies and healthcare by reducing computation time while maintaining accuracy.

Neural networks and deep learning can reproduce complex relations within a short evaluation time after enough training [96], from which the medical society has benefited for years. For example, Tran *et al.* have used computer vision to classify skin burns [97] and to classify tumors [98]. Furthermore, Brinati *et al.* have used neural networks to find diseases, such as COVID-19, in blood samples [99].

This part explores using surrogate neural networks to replace the expensive numerical predictions of post-burn contraction and patient discomfort. Using surrogate neural models is a common approach. For example, Wang *et al.* considered a long short-term memory neural network to speed up mechanical models used for studying the dynamics of biological systems [100]. Yang *et al.* used a convolutional neural network to speed up the approximation of the stress-strain curve for materials [101]. Navratil *et al.* have shown that a neural network can outperform other, non-intelligent acceleration techniques on both acceleration and accuracy [102]. In particular, Navratil *et al.* compare neural networks to simple procedures, including up-scaling, to speed up the physics-based simulations in oil reservoir modeling. Other authors also applied the neural network surrogate approach to environmental numerical models [103], urban wastewater systems [104], and computational fluid dynamics [105–107].

Chapters 7 and 8 in this part apply neural networks for the one-dimensional and the two-dimensional biomorphoelastic model for post-burn contraction, respectively. We create many data samples using the numerical approach by varying parameter values. Then, we fit two-layer feed-forward neural networks. To illustrate how we can use such a neural network in the future, we implement the optimized networks in (online) applications. The results show a possible speedup of 2000 and two orders of magnitude reduction in average sequence error concerning the simulator in 1D. In 2D, the possible speedup is about 1800000.

The chapters in this part show overlaps. Therefore, in Chapter 8, we refer to the corresponding parts in Chapter 7.

The conclusions of this part are presented after the chapters.

7

A neural network for the one-dimensional model

This chapter is based on the publication from [108]. The codes used for this chapter can be found in the online resources for Chapter 7.

The biomorphoelastic model for post-burn contraction is based on complicated systems of partial differential equations that need finite element-like discretizations to approximate the solution. Since this computational framework can be expensive in computation time and resources, we study the applicability of neural networks to reproduce the finite element results. Our neural network can simulate the post-burn contraction for over one year. The simulations are based on 25 input parameters characteristic of the patient and the injury. One such input parameter is the stiffness of the skin. The neural network results have yielded average goodness of fit (R^2) of 0.9928 (± 0.0013). Further, we obtained a tremendous 19354X speedup with the neural network. We illustrate the applicability of the neural network in an (online) application that considers the age of the patient and the length of the burn.

7.1 Introduction

In this chapter, we study the use of a surrogate neural network to replace the one-dimensional numerical model's relative surface area (RSA) predictions. Section 7.2 presents the neural network. Subsequently, Sections 7.3 and 7.4 present the results and the illustrative (medical) application, respectively.

7.2 The neural network

The biomorphoelastic model for post-burn contraction has many parameters that differ between patients and wounds. Because the model is highly nonlinear, the numerical

evaluation of uncertainty in patient- and wound-specific scar contraction data is expensive. We, therefore, consider a feed-forward neural network to replace the numerical computations. In this section, we define the neural network applied in our study.

7.2.1 Formulation

We consider a burn of length L cm. Together with 24 other independent parameter values, the length makes up the input vector $\mathbf{x}$. Given this input, the wound/scar changes in size over time in the course $\mathbf{y}$. Here, $\mathbf{y}$ is the non-dimensional RSA, determined by the numerical model that uses a one-day timestep and 365 days as total simulation time. The goal is to learn $f(\mathbf{x}; \boldsymbol{\theta}) \approx \mathbf{y}$, with $\boldsymbol{\theta}$ the learnable parameters of the feed-forward network. In our network, we use two hidden layers with 100 neurons each and the *rectified linear unit* [109] to describe the features. We use the sigmoid function on the output layer because the RSA bounds between 0 and 1. This output unit gives our study better (significant) results than other output activation functions. Other activation functions give such poor results ($R^2 < 0$) that returning the expected value is a better choice. Note that the numbers of input and output neurons are 25 and 365. Figure 7.1 shows a graphical overview of the method.
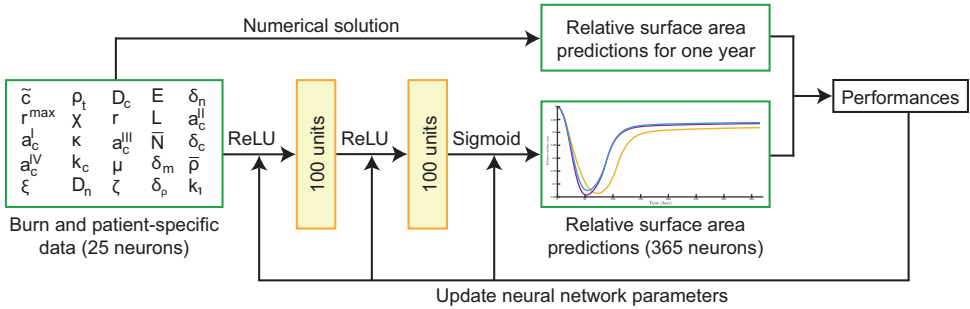
Figure 7.1: Graphical overview of the proposed feed-forward neural network in 1D. The burn and patient-specific data form the input on 25 neurons. The neural network has two hidden layers with 100 units each, activated by the rectified linear unit (ReLU). The sigmoid function activates the output layer by giving the relative surface area (RSA) predictions on 365 neurons that, together with the numerical RSA solutions, yield the neural network's performance. The neural network's parameters are updated until the network meets the required performance.

7.2.2 Training, validating and testing

During the neural network training, we minimize the mean squared error (MSE) loss by using the Adamax algorithm with the standard backpropagation algorithm [110]. We perform a learning rate range test (LRRT) to discover the maximal initial learning rate (ILR) value that can train the model without divergence. We vary ILRs between 0.0001 and 1 and run for 150 epochs in batches of 64 samples. The LRRT takes 12.5 minutes on a 64-bit Windows 10 Pro system with 16 GB RAM and 3.59 GHz AMD Rizen 5 3600 6-Core Processor. Figure 7.2 shows that the optimizers adaptive moment (Adam) and Adamax, a variant of Adam, allow higher ILRs than optimizers root-mean-square propagation (RMSprop) and Nesterov-accelerated adaptive moment (Nadam). Further, these

optimizers reach better scores than the optimizers stochastic gradient descent (SGD), Adadelta, follow the regularized leader (Ftrl), and adaptive gradient (Adagrad). We note that a smaller number of epochs (30) yields the same results. Given these results, we choose an ILR of 0.015 with a standard decaying factor of 0.99. To avoid model overfitting, we use the early stopping regularization. We follow the MSE loss and stop training if 30 epochs show no improvement. Changes between MSE loss smaller than 10^{-5} are qualified as *no improvement*.
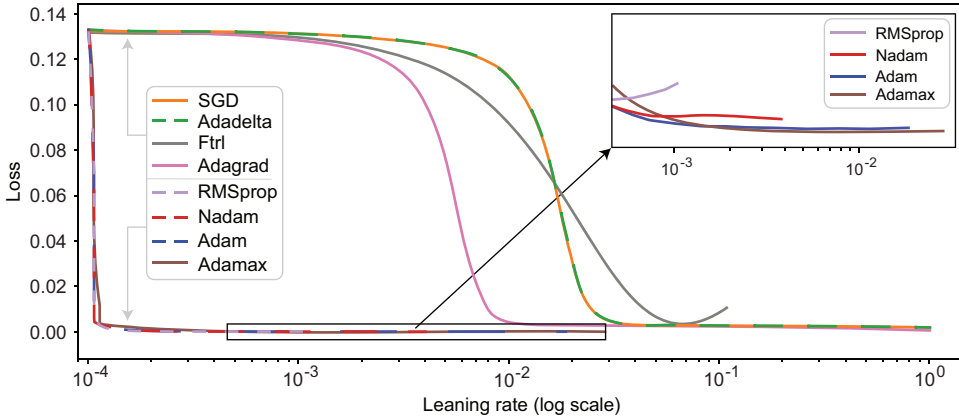
Figure 7.2: Results on the learning rate range test/loss values, showing the moving averages. The Adamax optimizer takes the largest initial learning rate value and provides the smallest loss. Here, the abbreviations are stochastic gradient descent (SGD), follow the regularized leader (Ftrl), adaptive gradient (Adagrad), root-mean-square propagation (RMSprop), Nesterov-accelerated adaptive moment (Nadam), and adaptive moment (Adam). Adadelta extends Adagrad, and Adamax is a variant of Adam based on the infinity norm.

7.2.3 Data

To train and test the neural network, we use a $n = 18000$ Monte Carlo (MC) simulation dataset from the numerical algorithm of size $n \times 25 \times 365$. This dataset is well-varied, as we define a range of acceptable values for each input parameter that varies between patients and simulations. Based on the ranges, we define uniform statistical distributions from which we draw parameter samples. We accept samples that satisfy $k_c < \delta_c \overline{\rho} a_c^{II}$, the chemical stability condition of the biomorphoelastic model for post-burn contraction. Table 7.1 shows the values of the varied and fixed parameters.

Table 7.1: Overview of the parameter values used for the simulations.

Parameter	Value	Dimension	Reference
D_n	$(7–12) \times 10^{-7}$	$cm^5/(cells\ day)$	[53]
D_c	$(2.22–3.2) \times 10^{-3}$	cm^2/day	[54]
χ	$(2–3) \times 10^{-3}$	$cm^5/(g\ day)$	[55]
k_c	$(2.9605–3.0395) \times 10^{-13}$	$g/(cells\ day)$	[14]
r	$0.832–0.924$	$cm^{3q}/(cells^q\ day)$	[50, 56]

Table 7.1: (continued)

Parameter	Range	Dimension	Reference	
$r^{\max}$	2–3	-	[57]	
$k_\rho^{\max}$	10	-	[14]	
a_c^I	$(9\text{–}11)\times10^{-9}$	$\mathrm{g/cm^3}$	[14, 58]	
a_c^{II}	$(9.375\text{–}10.625)\times10^{-9}$	$\mathrm{g/cm^3}$	[14]	
a_c^{III}	$(2\text{–}2.5)\times10^{8}$	$\mathrm{cm^3/g}$	[38]	
a_c^{IV}	$(8\text{–}1.2)\times10^{-10}$	$\mathrm{g/cm^3}$	[59]	
η^I	2	-	[60]	
η^{II}	0.45	-	[63]	
k_1	$(0.54\text{–}1.08)\times10^{7}$	$\mathrm{cm^3/(g\ day)}$	[7]	
κ	$(1\text{–}10)\times10^{-7}$	$\mathrm{cm^3/cells}$	[32]	
δ_n	0.019–0.022	$/\mathrm{day}$	[14]	
δ_m	0.06–0.0885	$/\mathrm{day}$	[63]	
δ_c	$(4.902\text{–}5.098)\times10^{-4}$	$\mathrm{cm^6/(cells\ g\ day)}$	[14]	
δ_ρ	$(5.78\text{–}6.11)\times10^{-6}$	$\mathrm{cm^6/(cells\ g\ day)}$	[61]	
$\overline{N}$	$(1\text{–}1.5)\times10^{4}$	$\mathrm{cells/cm^3}$	[14]	
$\overline{\rho}$	$(9.75\text{–}12.5)\times10^{-2}$	$\mathrm{g/cm^3}$	[14]	
ρ_t	0.89–1.29	$\mathrm{g/cm^3}$	[62]	
μ	10–1000	$\mathrm{(N\ day)/cm^2}$	[TW]	
E	320–410	$\mathrm{N/((g\ cm)^{1/2})}$	[63]	
ξ	$(4.38\text{–}4.42)\times10^{-2}$	$\mathrm{(N\ g)/(cells\ cm^2)}$	[64, 65]	
R	0.995	$\mathrm{g/cm^3}$	[1]	
ζ	380–440	$\mathrm{cm^6/(cells\ g\ day)}$	[1]	
$\tilde{N}$	$0.2\cdot\overline{N}$	$\mathrm{cells/cm^3}$	-	
$\tilde{M}$	0	$\mathrm{cells/cm^3}$	-	
$\tilde{c}$	$(1\text{–}5)\times10^{-8}$	$\mathrm{g/cm^3}$	[1]	
$\tilde{\rho}$	0	$\mathrm{g/cm^3}$	-	
L	3–5	cm	-	

Shown are the symbols, the values, the dimensions, and the references to the mean values. Here TW denotes that the parameter value is estimated in the study.

Each simulation computes the results on a domain of 10 cm with a uniform spatial grid of 202 grid points. We split the large dataset into standardized (using Min-Max scaling) train- and test sets, with 80%/20% train-test split, and run with 10-fold cross-validation.

7.2.4 Performance measures

We include the goodness-of-fit (R^2) statistic, which depends on the L^2 norm. Let $e_i = y_i - \hat{y}_i$ define the residual for the true (finite element) value y_i and the corresponding predicted value $\hat{y}_i$. Then, $R^2 = 1 - \sum_{i=1}^{N} e_i^2 / \sum_{i=1}^{N} (y_i - \overline{y})^2$, with a positive denominator. Note that a small sample standard deviation does not give lower residuals. Hence, the R^2 can become small (and negative) when the results of the finite element simulations show a smaller standard deviation than the mean square error. Further, we compare models

$M \in \mathcal{M}$, where $\mathcal{M}$ is the set of neural networks suitable for our problem. Therefore, since $\sum_{i=1}^{N} (y_i - \overline{y})^2$ will stay constant among the models, maximizing R^2 is minimizing the square error loss, or the L^2 norm. Next, we include the average relative root mean squared error (aRRMSE), often used for (multi-target) regression problems [111]. Finally, we include the average relative error (aRelErr). Although the aRelErr is easy to interpret, this performance measure is unsuitable for the entire set of targets.

7.3 Results

We train the neural network for predicting the RSA. Figure 7.3 shows the best and worst prediction in terms of the MSE, the relative error at each point for the worst prediction, and the relation between the predicted and target values for the samples in the test set.
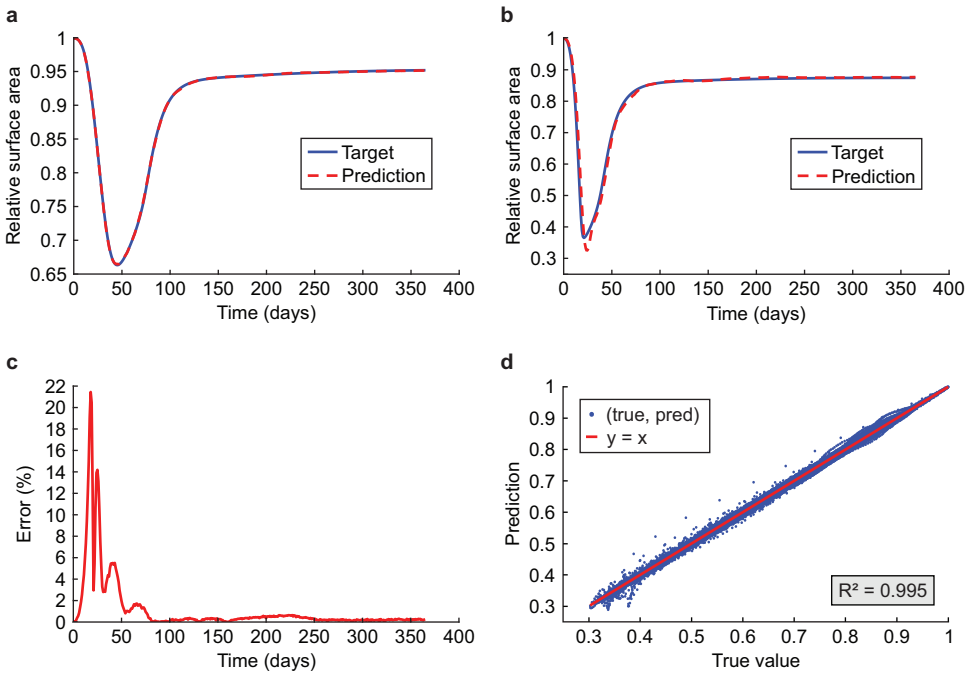
Figure 7.3: Results from the neural network for the relative surface area prediction. The upper two graphs show the best (**a**) and worst (**b**) predictions. The lower two graphs show the relative error of the worst prediction (**c**) and the relation between the predictions and the targets, the line $y = x$, and the R^2 (**d**). Here, we have included the values of the entire set of time values, hence 3600×365 data points.

Figure 7.3a shows that the prediction is indistinguishable from the target in the best-case scenario. Figure 7.3b shows that, in the worst-case scenario, the network estimates the greatest contraction to be around 5% more intensive than the target value. The relative error of the worst prediction increases to 22% and converges to less than 1% for the last RSA value in Figure 7.3c. Finally, Figure 7.3d shows that the predictions are correct, as the (target, prediction) distribution is more or less the $y = x$ line, the latter shown in red for comparison. There are some outliers above and below the $y = x$ line and there is

a dense distribution of outliers in the range $0.31 \leq x \leq 0.39$, showing the model could have trouble predicting such less often occurring contraction values exceeding 60% as is consistent with Figures 7.3b and 7.3c.

To substantiate our observations, Table 7.2 shows the performance measures and the training and validation times.

Table 7.2: Performance of the neural network for predicting contraction.

Performance measure	Cross-validation value	Test value
R^2	0.9928 ± 0.0013	0.9950
aRRMSE	0.0626 ± 0.0080	0.0509
aRelErr	0.0023 ± 0.0003	0.0019
Training time	156 s	-
Validation time	-	0.93 s

The cross-validation trials return a mean $R^2 = 0.9928$, with standard deviation 0.0013. For the test set, we obtained $R^2 = 0.9950$, which fits within the 95% interval of confidence. The R^2 results show accurate predictions. The aRRMSEs are 0.0626 ($\pm$ 0.0080) and 0.0509 for the folds and test set. These results are smaller than 0.1, and according to Despotovic et al. [112], this trained neural network shows excellent reproduction of the finite element data. The aRelErrs of the predictions are only 0.23% ($\pm$ 0.03%) and 0.19%, supporting our claim that the neural network can predict the RSA.

During contraction, the RSA reaches a minimum which, together with the asymptotic value, is interesting from a clinical point of view. Table 7.3 shows the R^2 and the mean absolute error (MAE) for the minimum and asymptotic RSA values over the test set. We further show the general characteristics of the distributions to place the MAE in context. Focusing on these characteristics next to the overall performance makes interpreting the values clearer.

Table 7.3: Performances for the minimum and the asymptotic relative surface area (RSA) values. The table shows the performance measures of the goodness-of-fit (R^2), the mean average error (MAE), and the minimum, maximum, range, and average of the mentioned RSA values.

Characteristic	R^2	MAE	Min	Max	Range	Average
Minimum RSA	0.9981	0.0028	0.3028	0.8095	0.5067	0.5599
Asymptotic RSA	0.9984	0.0008	0.7921	0.9649	0.1728	0.9044

Later in the first year, the predictions are better than the early predictions (not shown here). It is, therefore, not surprising that the R^2 of both the minimum and asymptotic RSA values have a more significant score (0.9984 and 0.9980) than the overall performance score (0.9928). Both scores differ at least four standard deviations from the overall performance. Hence Chebyshev's Theorem states the exceeding probability to be bounded from above by 0.0625. The minimum RSA MAE is 0.55% of the range of values and 0.50% of the average value, supporting the network's performance. However, we note that the neural network could be more accurate for small values, where differences

of 7.5% can occur. Overall, the network can distinguish between the minima within 30 to 80%. The asymptotic RSA value MAE is 0.46% of the range of values and 0.09% of the average value. Hence, the network can also predict the asymptotic contraction intensity. We note that the asymptotic RSA value prediction absolute error is maximal 0.7%. We conclude that the trained network can predict the RSA at various times and for ranges of parameter values.

Finally, the validation time is only 0.93 seconds, in which the network predicts 3600 samples, hence, on average, 0.26 milliseconds per sample. This validation time is significantly faster than the numerical model, which, on average, takes about 5 seconds per simulation (about 5 hours for our test set). Hence, the neural network provides a speedup of 19354X, showing a spectacular acceleration.

7.4 Application of the neural network

The primary asset of the neural network is its quick prediction. In this section, we discuss an application to show the applicability of the neural network and support the claim that fast MC simulations are essential.

We show a basic concept of an application that can assist medical staff when treating patients with burned skin. Knowledge of the courses of contraction and the probabilities of developing a contracture helps to choose the best suitable treatment for each patient if the model considers different therapies in the future. If the probability of developing a contracture (leading to immobility) is significant, a patient needs different treatments than when the probability is small.

We designed a computational application to show the current network's potential. The application reads the patient- and wound-specific information shown in Figure 7.4, such as the patient's age and weight and the wound size and location.
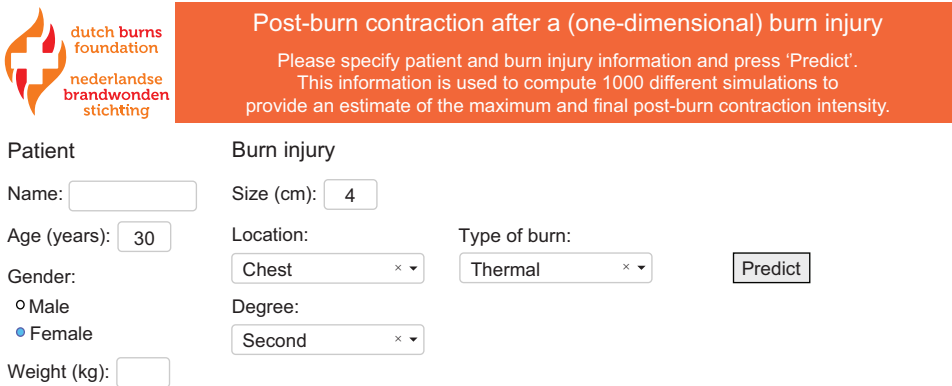
Figure 7.4: The input section of the medical application that predicts post-burn contraction after a patient-specific one-dimensional burn. The user can fill in the patient's name, age, gender, and weight and fill in the burn size, location, degree, and type. Once the *Predict* button is selected, the application runs.

Once the *Predict* button is selected, the application defines the distribution for the input parameters based on the provided information. Currently, it only considers the patient's

age and wound length. In the background, it runs 1000 MC simulations to provide predictions.

The parameter uncertainties are assessed with MC simulations. Based on the literature study in Chapter 4, we use interpolation in the data to find age-related parameter values. First, we define a variable called *age factor*, the patient's age divided by 100. We use this factor to find suitable mean values for the parameters, and for this purpose, we use the parameter value ranges shown in Table 7.1. Although it could be possible that specific parameter values behave more step-like due to, for example, puberty, we assume that linear interpolation between consecutive data points provides a reasonable approximation. We only apply interpolation to age-dependent parameter values and consider if the values increase or decrease with age. Then, we perform random sampling using the normal distribution with these mean values and a fixed portion of the mean values as standard deviation. We cut off values outside the ranges, which can happen because of random sampling. We draw values from a uniform distribution for the age-independent parameter values, with minima and maxima as in the chosen ranges.

We draw 1000 input combinations for each patient, scaled before feeding these to the neural network. The neural network outputs RSA predictions from which we estimate the empirical cumulative probability distribution. With this, we estimate the probability of the asymptotic contraction intensity exceeding a certain threshold, i.e., possibly the probability of developing a contracture.

The results from the MC simulation are post-processed and visualized in the application. The application shows the probabilities $\mathbb{P}(\text{RSA}_{\text{min}} < 0.7)$ (i.e., the probability of the minimum RSA smaller than 0.7) and $\mathbb{P}(\text{RSA}_{365} < 0.9)$ (i.e., the probability of the asymptotic RSA smaller than 0.9), where the threshold values are given in the contraction intensity values 30% and 10%. The user can adapt these threshold values, such that the probabilities are recomputed. Furthermore, the application shows the mean RSA, the 95%-confidence interval of the mean, and the standard deviation from the mean. The mean and its confidence interval are shown in blue, together with the interval $\mu \pm \sigma$ in red. In addition, the application shows the histograms for RSA_{min} and RSA_{365}. Figure 7.5 shows the visualization of the predictions for the RSA.
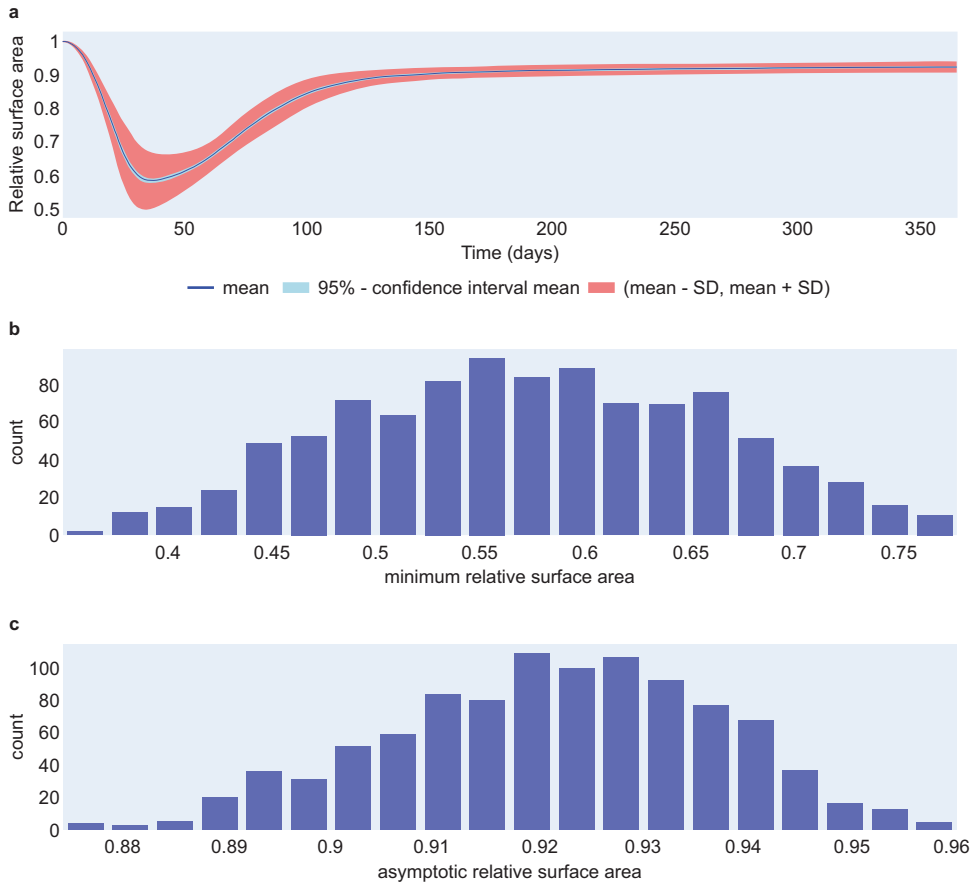
Figure 7.5: The visualization of the relative surface area (RSA) prediction in the application. Shown are the prediction of the RSA in one year (**a**), and the histograms of the minimum RSA (**b**) and the asymptotic RSA (**c**).

8

A neural network for the two-dimensional model

This chapter is based on the publication from [113]. The code for this chapter can be found in the online resources for Chapter 8.

Severe burn injuries often lead to post-burn contraction, leading to stresses in and around the damaged skin region. If this contraction leads to impaired joint mobility, one speaks of contracture. Since the finite element-based simulation of post-burn contraction can be expensive from a computational point of view, we study the use of machine learning to reproduce the expensive finite element simulations cheaply. The current study deals with a feed-forward neural network that we trained with 2D finite element simulations. We focus on the evolution of the scar shape, wound area, and total strain energy, a measure of discomfort, over time. The results show average goodness of fit (R^2) of 0.9979 and a tremendous speedup of 1815000X. Further, we illustrate the applicability of the neural network in an (online) medical application that takes the age of the patient age into account.

8.1 Introduction

In this chapter, we study the use of surrogate neural networks to replace the relative surface area (RSA), the total strain energy (TSE), and wound/scar boundary predictions from the two-dimensional numerical model. Section 8.2 presents the neural network. Subsequently, Sections 8.3 and 8.4 present the results and the illustrative (medical) application, respectively.

8.2 The neural network

In addition to our previous study in 1D, we formulate neural networks to predict the TSE and the wound/scar boundary.

8.2.1 Formulation

We consider a burn of a rotated square shape, as in Section 6.2. The 25 independent parameter values make up the length of the input vector **x**. Given this input, the wound / scar evolves in terms of output variables **y**. Here, $\mathbf{y} \approx f(\mathbf{x}; \theta)$ is either the non-dimensional RSA, the non-dimensional TSE, or the wound/scar boundary, determined by the numerical finite element-based model that uses an *adaptive* timestep (see Section 6.3) and 365 days as total simulation time. Again, the data are post-processed to contain daily predictions and are normalized between 0 and 1, and we use the same feed-forward network as described in Section 7.2.1. The numbers of input and output neurons are 25 and 365 for the RSA and TSE, and 42×365 for the wound/scar boundary because 21 points describe the boundary.

8.2.2 Training, validating and testing

In 2D, we also minimize the mean squared error (MSE) loss by using the Adamax algorithm with the standard backpropagation algorithm, and we perform learning rate range tests (LRRTs) like as in Section 7.2.2. On average, the LRRTs take around 7.2 minutes on our machine. The results for the RSA and the wound/scar boundary are the same as in Figure 7.2; hence, we choose 0.015 for the initial learning rate (ILR) for the RSA and the wound/scar boundary. Further, we initially chose an ILR of 0.045 for the TSE because the LRRT showed high learning rates; however, the results were poor. We perform an LRRT with more epochs and get the ILR of 0.02. After searching the optimal ILR by hand, we find 0.004 to be the optimal ILR for the TSE. We use a standard decaying factor of 0.99 for all learning rates. To avoid model overfitting, we use the early stopping regularization. We follow the validation MSE loss and stop training if 50 epochs show no improvement.

8.2.3 Data

To train and test the neural networks in this chapter, we use a dataset of $n = 5000$ Monte Carlo (MC) simulations from the numerical algorithm of size $n \times 25 \times 365$. As in Chapter 7, we define a *range* of acceptable input parameter values, we define uniform statistical distributions from which we draw parameter samples, and we accept samples that satisfy $k_c < \delta_c \overline{\rho} a_c^{II}$. The (varied) parameter values are the same as the values in Table 7.1 in Chapter 7, except for the parameter values shown in Table 8.1.

Table 8.1: Overview of the parameter values used for the simulations for the neural network in 2D different from the ones shown in Table 7.1.

Parameter	Value	Dimension	Reference
D_n	$(7{-}15) \times 10^{-7}$	$cm^5 / (cells\ day)$	[53]
r^{max}	2–2.3	-	[57]
k_1	$(0.8{-}1.08) \times 10^7$	$cm^3 / (g\ day)$	[7]
$\mu_{1/2}$	10–1000	$(N\ day) / cm^2$	[108]
E	28–34	$N / ((g\ cm)^{1/2})$	[63]
ν	04.9×10^{-1}	-	[70]

Shown are the symbols, the values, the dimensions, and the references to the mean values.

Each simulation computes the results on a domain of 10 cm^2 with a uniform triangulation with 968 nodes. For the simulation setup, we refer to Sections 6.2 and 6.3. We split the large dataset into standardized (using Min-Max scaling) train- and test sets, with an 80%/20% train-test split.

8.2.4 Performance measures
The performance measures are the same as described in Section 7.2.4.

8.3 Results
We train the neural network to predict the RSA, the TSE, and the wound/scar boundary. Figure 8.1 shows the best and the worst prediction in terms of the MSE, the relative error at each point for the worst prediction, and the relation between the predicted and target values for the samples in the RSA test set.
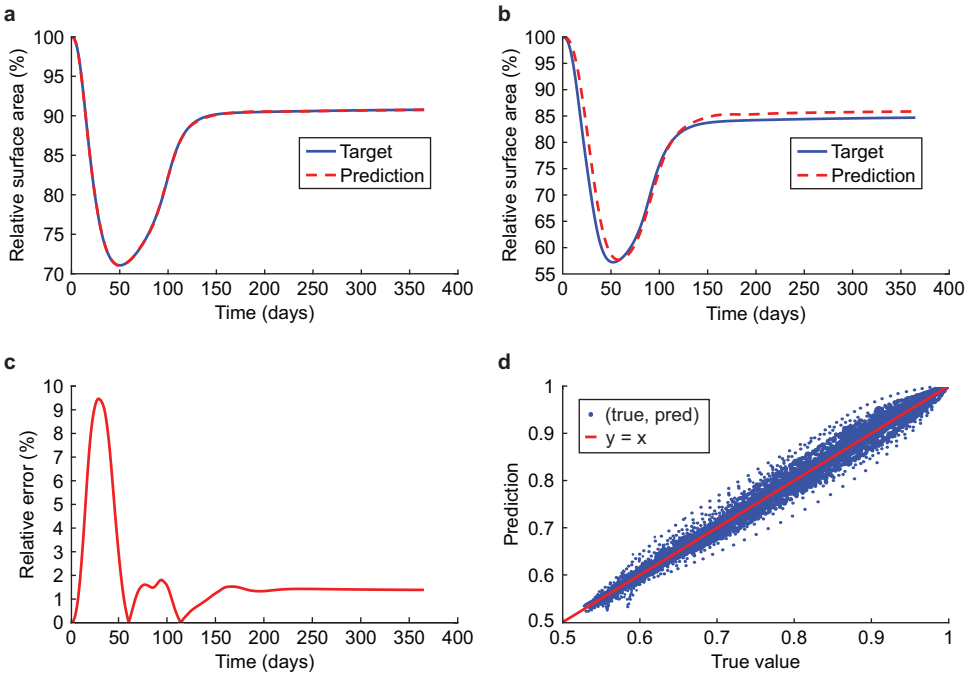
Figure 8.1: Results from the neural network for the relative surface area (RSA) prediction. The upper two graphs show the best (**a**) and worst (**b**) predictions. The lower two graphs show the relative error of the worst prediction (**c**) and the relation between the predictions and the targets, the line $y = x$, and the R^2 (**d**). Here, we have included the values of the entire set of time values, hence 1000 × 365 data points.

Figure 8.1a shows the best-case scenario, where the RSA prediction mostly overlaps the RSA target for the first 130 days and underestimates slightly around day 130. In the worst-case scenario, shown in Figure 8.1b, the neural network shows a delay during contraction and retraction and overestimation after (apprioximately) 120 days. The minimum shifted to day 58, compared to day 52 in the RSA target. After 120 days, the overestima-

tion is about 1% less contraction. The relative error of the worst prediction increases to 9.4% and converges to about 1.39% for the final contraction intensity, as shown in Figure 8.1c. The error peaks around day 30, during steep contraction, while the relative error around the moment of maximum contraction is less than 1%. Finally, Figure 8.1d shows the (target, prediction) distribution is more or less the $y = x$ line. Outliers are because of the worst prediction. The spread in the range $0.75 \leq x \leq 0.95$ shows that the neural network could have trouble predicting contraction values between these values.

Figure 8.2 shows the best and the worst prediction in terms of the MSE, the relative error at each point for the worst prediction, and the relation between the predicted and target values for the samples in the TSE test set.
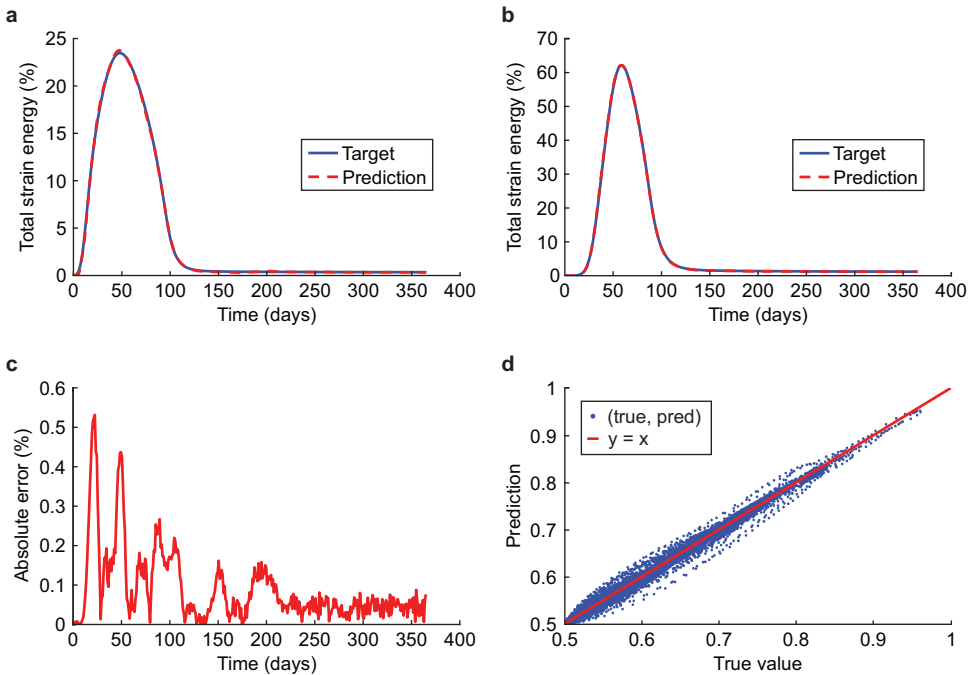
Figure 8.2: Results from the neural network for the total strain energy (TSE) prediction. The upper two graphs show the best (**a**) and worst (**b**) predictions. The lower two graphs show the absolute error of the worst prediction (**c**) and the relation between the predictions and the targets, the line $y = x$, and the R^2 (**d**). Here, we have included the values of the entire set of time values, hence 1000×365 data points.

In the best-case scenario, the TSE prediction mostly overlaps the TSE target, except for the maximum TSE around day 50, as Figure 8.2a shows a slight overestimation. In the worst-case scenario, shown in Figure 8.2b, the prediction by the neural network is almost indistinguishable from the TSE target value. Figure 8.2c shows the relative error of the worst TSE prediction and shows a maximum increase to 0.53% on day 23, which is negligible. Finally, Figure 8.2d shows that the (target, prediction) distribution follows the $y = x$ line. The spread in the lower range shows that the neural network could have trouble predicting small TSE values and that larger values occur sporadically.

The RSA only provides information about the general contraction and lacks any information about localized contractions. Using the displacement of the wound/scar boundary, we can also visualize the contraction and retraction of the wound/scar. Visualizing this movement is intuitively more straightforward to interpret than numeric values. Figure 8.3 shows the results of the neural network we trained to predict the wound/scar boundary.
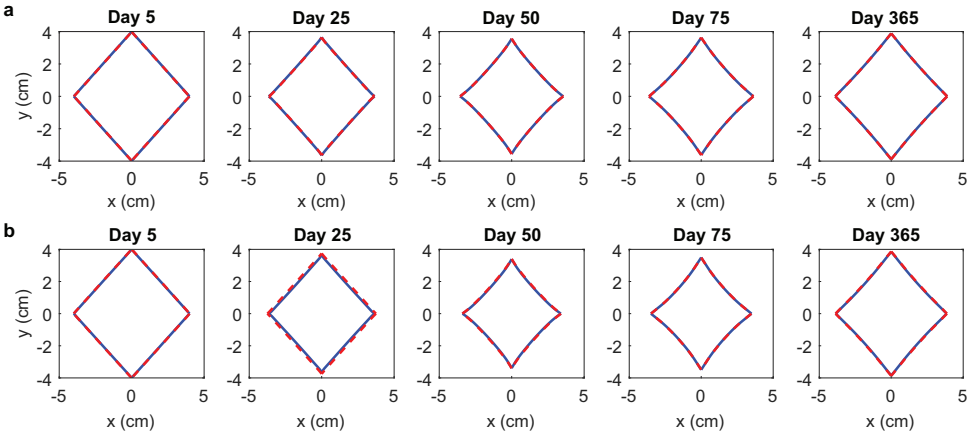
Figure 8.3: Results from the neural network for the wound/scar boundary. The upper graphs show the best predictions (**a**), while the lower graphs show the worst ones (**b**). In each graph, the blue line shows the target, and the red dashed line shows the neural network prediction.

Here, we display targets and predictions on days 5, 25, 50, 75, and 365, with the targets in blue and the predictions in red. The days are shown for the best and the worst prediction in terms of the average relative error. Figure 8.3a shows that the best prediction follows the target closely. The worst prediction, shown in Figure 8.3b, shows a slight deviation from the target boundary (less contraction) in the early phase of contraction before maximum contraction is not yet reached (day 25). Here, the predicted wound boundary is larger than the target boundary, which is also in line with the trends in Figures 8.1b and 8.1c. Further, the graphs show that the neural network can closely predict the wound/scar boundary.

To substantiate our observations, Table 8.2 shows the test sets' performance measures and the training and validation times of the neural networks.

Table 8.2: Performances of the neural networks.

Performance measure	RSA value	TSE value	boundary value
R^2	0.9983	0.9984	0.9969
aRRMSE	0.0787	0.0864	0.0825
aRelErr	0.0018	1.4919	0.0020
Training time	33 s	245 s	295 s
Validation time	0.000069 s	0.000058 s	0.000147 s

8

For all three neural networks, we obtained $R^2 \geq 0.9969$, which fits within the 95% interval of confidence, showing accurate predictions. The aRRMSEs are $0.0787, 0.0864,$ and 0.0825 for the RSA, the TSE, and the wound/scar boundary, respectively. The results are smaller than 0.1, and according to Despotovic et al. [112], these trained neural networks show excellent reproduction of the finite element data. The aRelErrs of the predictions are only $0.018\%, 1.4919\%$ and 0.0020%, supporting our claim that the neural network can predict the RSA, the TSE, and the wound/scar boundary. Finally, the total validation time is only 0.2744 seconds, in which the networks predict 1000 samples; hence, on average, 0.2744 milliseconds per sample. The neural networks are significantly faster than the numerical model, which, on average, takes about 498 seconds per sample. Hence, the neural network provides a speedup of 1815000X, showing a spectacular acceleration the neural networks achieve.

Further, for the minimum and asymptotic RSA values, Table 8.3 shows the R^2 and the mean absolute error (MAE) for the maximum TSE over the test set. During contraction, the RSA reaches a minimum which, together with the asymptotic value, is interesting from a clinical point of view. Focusing on these characteristics than the overall performance makes interpreting the values clearer.

Table 8.3: Performances for the minimum and the asymptotic relative surface area (RSA) values and the maximum total strain energy (TSE) values. The table shows the performance measures of the goodness-of-fit (R^2), the mean average error (MAE), and the minimum, maximum, range, and average of the mentioned values.

Characteristic	R^2	MAE	Min	Max	Range	Average
Minimum RSA	0.9989	0.0016	0.5107	0.8335	0.3228	0.6944
Asymptotic RSA	0.9965	0.0009	0.8067	0.9545	0.1477	0.9032
Maximum TSE	0.9990	0.0029	0.0658	0.9198	0.8540	0.2976

The R^2 of the minimum and asymptotic RSA values and the maximum TSE value are 0.9989, 0.9965, and 0.9990, respectively. Compared to the overall performance scores, the score for the asymptotic RSA is lower, though still above 99%, and the scores for minimum RSA and the maximum TSE are higher than the overall performance scores. The minimum RSA MAE is 0.50% of the range of values and 0.23% of the average value, supporting the network's performance. Overall, the network can distinguish between the minima within the range of 51 to 83%. The asymptotic RSA value MAE is 0.61% of the range of values and 0.10% of the average value. Hence, the network can predict the asymptotic contraction intensity as well. The most significant asymptotic RSA value prediction absolute error is less than 1.17%. Finally, the maximum TSE MAE is 0.34% of the range of values and 0.97% of the average value, showing a better performance in the range of values than the neural network scores for the RSA. We conclude that the trained network can predict the RSA and the TSE at various times and ranges of parameter values.

8.4 Application of the neural network

As stated in Chapter 7, we prefer using a neural network instead of the numerical finite element method to access the MC simulations quickly. We updated the illustrative ap-

plication to show the potential of the networks trained in this study. Like before, we use interpolation in literature data to find age-related parameter values. In short, the application only reads the patients age and then decides the parameter distributions. For illustration, the app shows other patient and wound-specific options that the app does not consider yet. The results from the MC simulations are post-processed and visualized in the application that considers the burn to be a rotated square for $-4 \leq x, y \leq 4$. The app shows the effects of the uncertainties for the RSA, the TSE, and the wound/scar boundary and offers probabilities of contraction intensities. Figure 8.4 shows the addition of the TSE and the wound/scar boundary.

a Prediction of the evolution of patient discomfort in one year

b Histogram of the maximum discomfort

c Wound/scar boundary prediction for one year
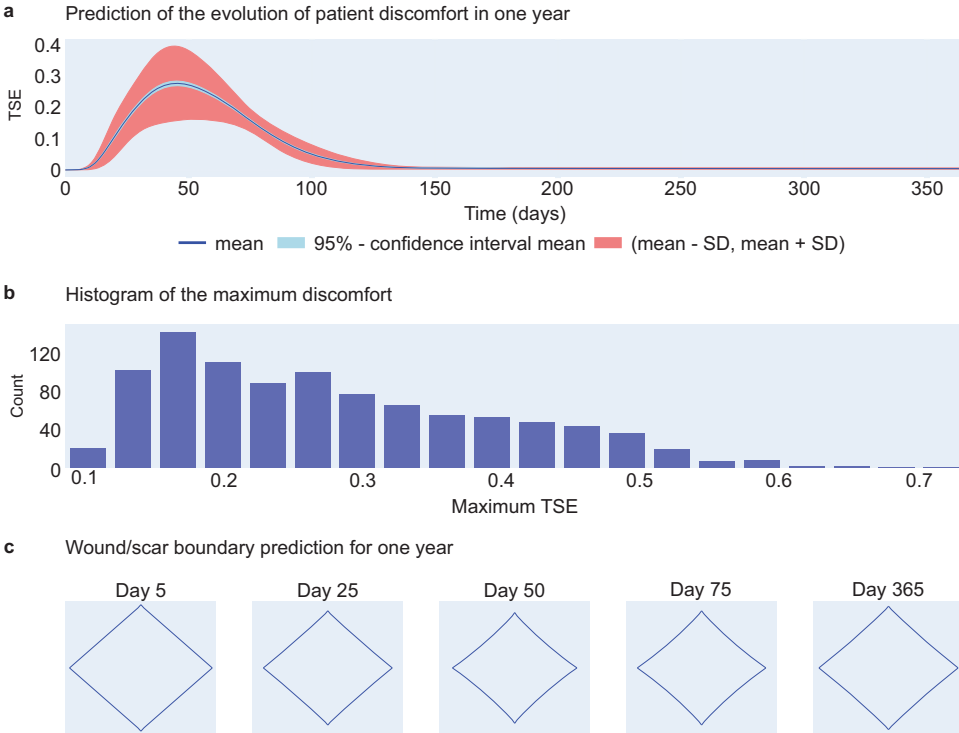
Figure 8.4: The visualization of the total strain energy (TSE) and wound/scar boundary prediction in the application. Shown are the prediction of the TSE in one year (**a**), the histogram of the maximum TSE (**b**), and the wound/scar boundary prediction in one year (**c**).

Conclusions of this part

The numerical approximations to post-burn contraction are less suitable for applications that require many simulations since they are computationally expensive. Therefore, we study neural networks that serve as a low-cost alternative modeling strategy. These neural networks are easy to train and provide quick predictions for post-burn contraction and patient discomfort.

We performed LRRTs to find suitable ILRs, which are 0.015 for the Adamax optimizer for the RSA (in 1D and 2D) and the wound/scar boundary (in 2D). We needed to find the ILR for the TSE by hand and found the optimal value of 0.004.

In 1D, we tested the neural network for predicting the RSA only. The network gives aRellErr = 0.19% and R^2 = 0.995 on the test set. In addition, the network gives accurate predictions of the necessary RSA_{min} and RSA_{365}. For RSA_{min}, it reports MAE = 0.0028 and R^2 = 0.9981, and for RSA_{365}, it reports MAE = 0.0008 and R^2 = 0.9984.

In 2D, we tested the neural networks for predicting the RSA, the TSE, and the wound/scar boundary. On the test set, our networks give aRellErr = 0.0018%, 1.4919% and 0.0020% and R^2 = 0.9983, 0.9984 and 0.9969 for the RSA, the TSE, and the wound/scar boundary. In addition, the networks provide accurate predictions of the minimum and asymptotic RSA values and the maximum TSE values. For the minimum RSA, it reports MAE = 0.0016 and R^2 = 0.9989; for the asymptotic RSA, it reports MAE = 0.0009 and R^2 = 0.9965, and for the maximum TSE, it reports MAE = 0.0029 and R^2 = 0.9990.

Furthermore, the neural networks provide incredible speedups. The neural network in Chapter 7 needs only 0.93 seconds to compute the 3600 predictions. In contrast, the numerical code takes approximately 5 seconds per sample, which is 5 hours for 3600 predictions. Hence this neural network framework is 19354 times faster than the finite element framework demonstrating the spectacular acceleration our neural network achieves. The neural networks in Chapter 8 are 1815000 times faster than the finite element implementation. Overall, our two-layer neural networks' performances are excellent.

We have developed a neural network-based application that takes the patients age (and in 1D, the burn's length) to show its effect on post-burn contraction (and patient discomfort in 2D). The fast computations allow for MC-based predictions to access parameter uncertainty; therefore, the application is an example of how to offer clinicians immediate access to scar contraction simulations. Clinicians can tailor complication-dependent therapies if an efficient and reliable computer framework can predict complications after a burn. Given that the neural networks are effective and inexpensive, such an application increases the application of parameter studies and patient-oriented care. The aim is to optimize the treatment of post-burn contractions.

In conclusion, using neural networks as an alternative to the numerical model is effective and cheap. In addition, it increases the application of parameter studies and patient-based healthcare. The goal is to optimize the treatment of post-burn contractions. If we do, clinicians can adjust therapies depending on complications that an efficient and reliable computational framework can predict.

9

Conclusion and discussion

9.1 General conclusions

This section recapitulates the main conclusions we have drawn from the results obtained in the studies.

9.1.1 Part I

In part I, we presented stability analyses for the one-dimensional and two-dimensional counterparts of the biomorphoelastic model for post-burn contraction. In both settings, stability is guaranteed for

$$\delta_c \geq \frac{k_c}{a_c^{II}\overline{\rho}},\tag{9.1}$$

where δ_c is the signaling molecule decay rate, k_c the signaling molecule secretion rate, a_c^{II} the signaling molecule concentration causing half-maximum secretion, and $\overline{\rho}$ the equilibrium collagen concentration. For values $\delta_c < \frac{k_c}{a_c^{II}\overline{\rho}}$ not too far below the bound, the model can still attain a solution; though slow signaling molecule decay results in lasting signaling. In this case, signaling molecules remain present, causing persistent myofibroblast differentiation and an increased collagen concentration. The resulting scar can be hypertrophic. Stability for the mechanical model's part is met for $\overline{\varepsilon} \leq 1$ in 1D, and for $\overline{\varepsilon}_{11} = \overline{\varepsilon}_{22} = \frac{1}{2}$ and $\overline{\varepsilon}_{12} = 0$ in 2D. These conditions are also physical requirements, given that the equation for the effective Eulerian strain only holds for small strains. Further, when the viscosity is low for complex eigenvalues, the model converges, though not monotonic, but with oscillations. The convergence of the numerical method has order at least $\mathcal{O}(h^2)$.

9.1.2 Part II

In part II, we presented sensitivity analyses for the one-dimensional and two-dimensional counterparts of the biomorphoelastic model for post-burn contraction. In addition, in Chapter 5, we presented an overview of parameter values and a feasibility study

for age-related post-burn contraction. In Chapter 6, we discussed our (re)meshing strategy.

The sensitivity analyses show that parameter value sensitivity depends on the dimensional setting and cell proliferation rates. If the cells have equal proliferation rates, then the equilibrium collagen concentration significantly affects contraction and patient discomfort. The body force-inhibiting constant is the most sensitive parameter if the cells have unequal proliferation rates. In all cases, the myofibroblast apoptosis rate is significantly sensitive. In addition, the signaling molecule secretion rate accounts for significant effects on the contraction intensity after one year and the maximum patient discomfort, which relates to the stability constraint in equation (9.1). If the parameter value gets too close to the stability limit, then remeshing is necessary for the numerical method. Further, the sensitivity of the myofibroblast proliferation rate increases for unequal cell proliferation rates. In 2D, the model considers Poisson's ratio, around 0.49 for soft tissues. We note that when this value increases toward 0.5, the weak form in the finite element method resembles

$$\int_\Omega \nabla \cdot \mathbf{u} \, \nabla \cdot \varphi \, \mathrm{d}\Omega, \tag{9.2}$$

meaning that 'locking' may occur, which is notorious among mechanical engineers. This effect was not a problem in this work because we consider visco-elasticity. However, given the sensitivity of the Poisson's ratio in Chapter 6, variation should be done carefully in future simulations.

Concerning the therapy advice, one should inhibit myofibroblast proliferation and stimulate myofibroblast apoptosis and fibroblast proliferation if the goal is to limit contraction during post-burn proliferation. Further, an elevated collagen concentration can reduce post-burn contraction and shorten its period. If the goal is to limit contraction after scar maturation, one should decrease growth factor secretion and stimulate growth factor decay. The advice is the same if the goal is to decrease patient discomfort.

Further, the model can show significantly different contraction intensities for different groups of parameter values, where the groups are chosen to relate to patients of different ages.

9.1.3 Part III

In part III, we presented neural networks that predict post-burn contraction and patient discomfort, serving as a low-cost alternative modeling strategy. We performed learning rate range tests to find optimal initial learning rates and implemented the resulting neural networks in an (online) application.

The networks give over 99.5% goodness of fit on the test set for (the features of) the contraction, (the features of) the patient discomfort, and the wound/scar boundary, and also show excellent performances. The networks' speedups are incredible: 19354 times faster than the finite element approximations in 1D and 1815000X times faster in 2D, demonstrating spectacular accelerations.

The medical application shows how to offer clinicians immediate access to scar contraction simulations, increasing the application of parameter studies and patient-oriented care.

In conclusion, an alternative to the numerical model is an effective and cheap neural network. If we optimize the treatment of post-burn contraction using such modeling frameworks, clinicians can adjust therapies depending on predicted complications.

9.2 Discussion

For the discussion of this work, we focus on the following topics: the bridge between the clinic and mathematical modeling, parameter values, mathematical model, numerical methods and implementation, and machine learning.

9.2.1 The bridge between the clinic and mathematical modeling

According to Viceconti *et al.*, one should select the model that properly investigates the elements of reality that one wishes to examine [114]. The biomorphoelastic model for post-burn contraction involves elements on a microscale, while clinical observations are on a macro scale. From a clinical point of view, it is uncommon to take burned skin biopsies and blood samples to extract parameter values for the mathematical model. From the mathematical point of view, the model needs significant adjustments to take the macro observations, introduce new, possibly unknown, parameters and equations, and combine different models. Therefore, experimental scientists, computational scientists, and mathematicians need to collaborate.

The goal is to create an accurate mathematical model that supports the clinician and the patient. We need to collect clinical and experimental data and adjust the model to represent the clinical data. Here, one can think of macro observations such as the cause, the location, the depth of the burn, and other patient-specific factors such as gender and age, together with effects such as contraction, hypertrophy, and patient discomfort. A burned hand is much more likely to contract than a burn on the back, and a third-degree burn heals with less surrounding vital tissue than a two-degree burn. The belly's skin is much more likely to stretch than on a wrist, and the skin gets looser with age.

Next to the burn-specific and patient-specific factors, other factors such as nutrition, sports (swimming), and applied treatments play a vital role in post-burn healing. For example, a patient with an open burn wound needs a diet including extra protein because much energy is used at a cellular level. Severe burns cause a profound pathophysiological stress response and a radically increased metabolic rate that can persist for years after injury [115]. Suppose this stress response remains unabated and the increased metabolic needs are not supported. In that case, it can significantly lose lean (fat-free) mass, immune compromise, and delayed wound healing. Regarding sports, patients suffering from tight skin after a burn feel relief when swimming, and moving generally prevents the muscles from becoming weak and forgetting their memory. However, the cells involved in post-burn healing can sense these mechanical stimuli and respond to them, for example, by contracting the damaged tissue. A particular case is the growth of children, where the skin stretches and pulls on the scar. Different treatments are possible, like plastic surgery, a full or partial-thickness skin graft, splinting, bandages with silver, pressure therapy, laser therapy, cryotherapy, and kenacort injections. The goals of the treatments also differ as they can be, for example, to close the wound or to release tension. Further, treatments like skin grafts can be considered in our modeling

framework using other initial conditions. The general question is which factors we need to consider. If so, how can we optimally add these factors to our modeling framework to produce relevant, accurate data in a computationally attractive time?

Guidelines where to start are the Patient Observer Scar Assessment Scale (POSAS) data and the *scar model*. The POSAS is a scar rating scale that measures scar quality from the perspective of the patient and the clinician. It measures scar quality by assessing visual (e.g., color), tactile (e.g., flexibility), and sensory (e.g., itch) features of the scar from the perspective of the observer and patients. Using the POSAS data to adjust the mathematical model, we create a setup where clinicians, patients, and scientists meet on a macro scale. The scar model adds another dimension to the POSAS data. In the scar model, shown in Figure 9.1, the clinician and patient observations are included regarding scar quality. However, the clinician distinguishes between the skin's layers, and the observed visual, tactile, and sensory features correlate via a sublayer where the quality of, for example, keratinocytes and collagen are included.
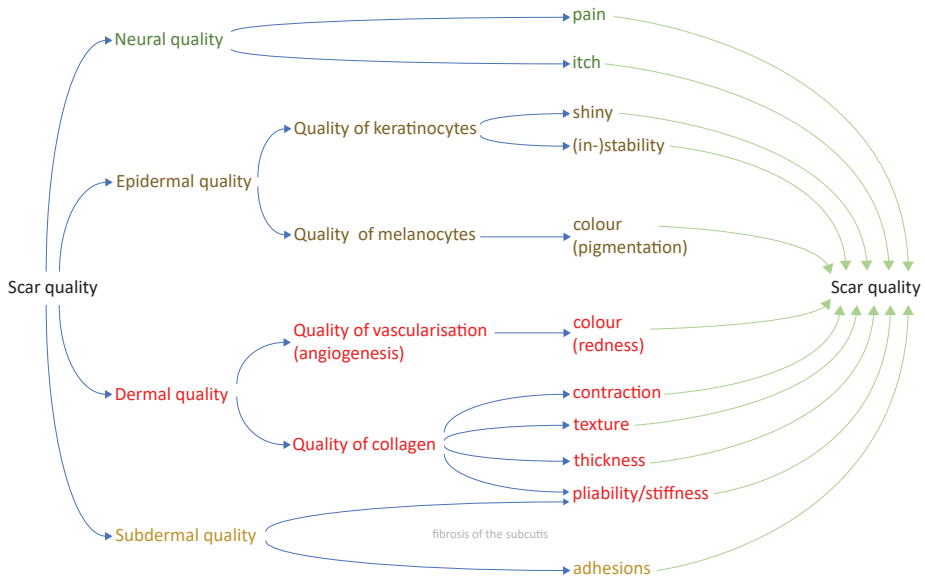
Figure 9.1: The scar model, developed by Paul van Zuijlen. It is the first concept model. The model is continuously under construction and continuously learning as new data feed it.

Given that the biomorphoelastic model for post-burn contraction simulates the skin's dermal layer and does not consider angiogenesis, the first step, for example, is to formally formulate the quality of collagen and link it to the features contraction, texture, thickness, and pliability/stiffness. Using the scar model to adjust the mathematical model, we create a setup where clinicians, patients, and scientists also meet on a micro-scale.

9.2.2 Parameter values

Parameter values are difficult to estimate and sometimes impossible to determine. This difficulty is partly because parameter values differ between patients and the types of wounds, because many values are of cellular and molecular nature, and because parameter values can also depend on each other. For example, the skin's elasticity differs between locations on the body [116]. Estimating parameter values can be done *in vitro* and *in silico*, while *in vivo* is more challenging.

It is necessary to determine patient- and wound-specific parameter values from appropriate data. These data may be of a clinical nature as well as an experimental nature. Depending on the available data, we can perform an a priori parameter estimation followed by an iterated optimization. For the iterated optimization, an objective cost function could be defined, for example, by the mean squared error loss of the relative surface area. We can also set up specific in vitro studies to determine parameter values. However, parameter values resulting from in vitro studies may be different in vivo.

When the proliferation rates of the (cellular) phenotypes are different, then in the current model, the myofibroblast proliferation rate r_m, the equilibrium collagen concentration $\overline{\rho}$ and the body force-inhibiting constant R are the most sensitive parameters. For maximum contraction and patient discomfort, this is the myofibroblast proliferation rate, and for asymptotic contraction, this is the equilibrium collagen concentration (a term for stiffness). Of course, these sensitivities will change when the model is modified. Given the current model, we advise experimentally investigating whether myofibroblasts (actively) proliferate and, if so, at what rate and where their proliferation depends on. Our parameter values study in Chapter 5 determined the cell proliferation rate using measured cell doubling times, which is questionable since cell doubling times can depend on the circumstances cells are in. However, the equations representing the chemical reaction of the cells, equations (2.6) and (2.7), include proliferation enhancement by signaling molecules, cell crowding, differentiation, and apoptosis. For the chemical reaction of myofibroblasts, it has been assumed that myofibroblasts solely divide in the presence of the signaling molecule. Thus, when one studies the multiplication of myofibroblasts in vitro, it will have to be investigated whether this multiplication is indeed dependent on growth factors. If no fibroblasts are present in this study, then the part of myofibroblast differentiation can be disregarded (as the differentiation depends on sufficient mechanical stiffness [117]). Disregarding differentiation means focusing purely on monitoring myofibroblasts that die and how much the population grows.

Another in vitro study may target myofibroblast differentiation using pure human fibroblasts and signaling molecules (TGF-β) and map the dependence on stiffness (collagen). We have assumed that myofibroblast differentiation is linear; however, it could also be that there is also an activator-inhibitor reaction behind this and that we need to estimate the parameter values for this alternative modeling technique. This estimation would, for example, concern the maximum differentiation rate and half-maximal growth factor enhancement of fibroblast differentiation (see [118]).

For the feasibility study and the neural networks in this work, we used linear interpolation to find age-related parameter values, which might be too simplistic. We need more research on the relations between different parameters and influences of factors like skin complexion, age, gender, and the location of the burn on the body.

9

Of course, it is clear that parameter values need to be estimated again when the model changes, and therefore we conclude that parameter estimation involves the collaboration of different scientific fields that continue collecting data, remodeling, and testing until the objective cost function is minimized.

9.2.3 Mathematical model

Our models are unique because we combine the mechanics with shrinkage and microstructural changes of skin, which in turn is coupled with a biochemical model for cells, growth factors (chemokines), and collagen. The current model describes clinical observations very neatly. However, the model still needs to be completed because many factors that play a role in post-burn contraction still need to be included. Post-burn features, such as hypertrophic scarring and the inflammatory wound healing response, are included in other mathematical models and must be linked to the mathematical model in this work. In this subsection, we discuss these parts and the current model's parts that need adjustments.

Hypertrophy   Scars are usually normotrophic but can also be hypertrophic. Normotrophic scars are defined as scars that are not elevated above skin level [119], while hypertrophic scars are raised and tight and often present with changes in color and sensation [120–122]. Clinical data show that these scars' intensity increases in the first three months after injury, after which the intensity gradually decreases, as shown in Figure 9.2.
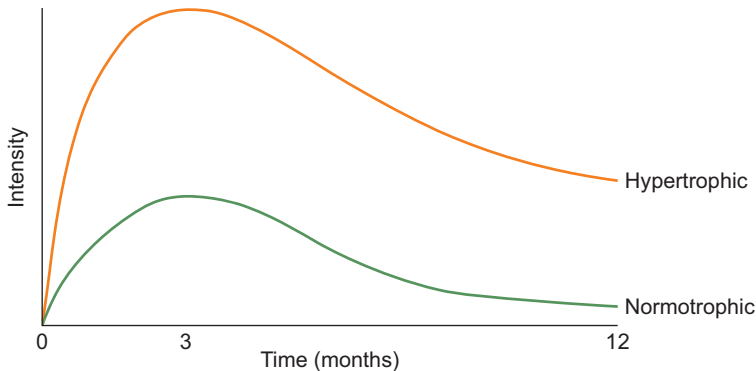
Figure 9.2: A sketch of the intensity of hypertrophic versus normotrophic scars in time. Here, the intensity is not a direct measure of the elevated scar but an overall measure of the intensity of the scar type.

Post-burn hypertrophic scars lead not only to an aesthetic but also to a functional and psychological burden and therefore matter for patients. There needs to be more evidence of the preference for specific treatment plans for these types of scars; therefore, treating them is challenging. In vivo models often focus on mice, rats, rabbits, guinea pigs, and dogs. Cost-effective models exhibit low *transferability* to human conditions, and those that show good transferability (pig models) are cost-intensive [123]. Hence, the benefits of animal testing are not proven, and together with animal suffering, there is a critical ethical aspect. As an alternative to these in vivo models, we could use in sil-

ico models that help predict whether a patient will likely develop hypertrophic scars and require treatment or decide which treatment will likely achieve the best results. The literature mainly contains models for muscle hypertrophy [124, 125], and the literature for post-burn hypertrophy remains scarce. The influence of myofibroblast apoptosis under dermal thickness and hypertrophic scarring was studied before by Koppenol *et al.*; however, not together with (joint) contractures. Hence, it would be interesting to incorporate hypertrophy into the morphoelastic model, for which we need available data sourced from in vivo and in vitro studies. However, validating results from such a model is challenging since hypertrophy depends highly on angiogenesis, which nowadays seems impossible to test in vitro.

Boundary conditions   There are two reasons to study possible boundary conditions to integrate into the mathematical model. One of these reasons emerges when hypertrophy is modeled together with contraction in a three-dimensional environment. Higher-dimensional frameworks account for the wound shape and depth, which is necessary to consider for hypertrophic scars as wound depth plays a crucial role [126]. The boundary conditions in this work can still be used for the modeled piece of skin parallel to the skin's surface, while perpendicular to the skin's surface (modeling the depth of the burn), we need other boundary conditions that allow the skin's surface to move freely.

The computational time for finite element simulations is the other reason for alternative boundary conditions. In this work, the edges of the computational domain are chosen far enough from the burn to account for the variables 'diffusion'. If we define the boundary conditions for the wound edges, this formulation saves many elements over which calculations must be fulfilled.

To give examples of possible boundary conditions, we show in Figure 9.3 graphical representations of what the computational domains can be in such setups.
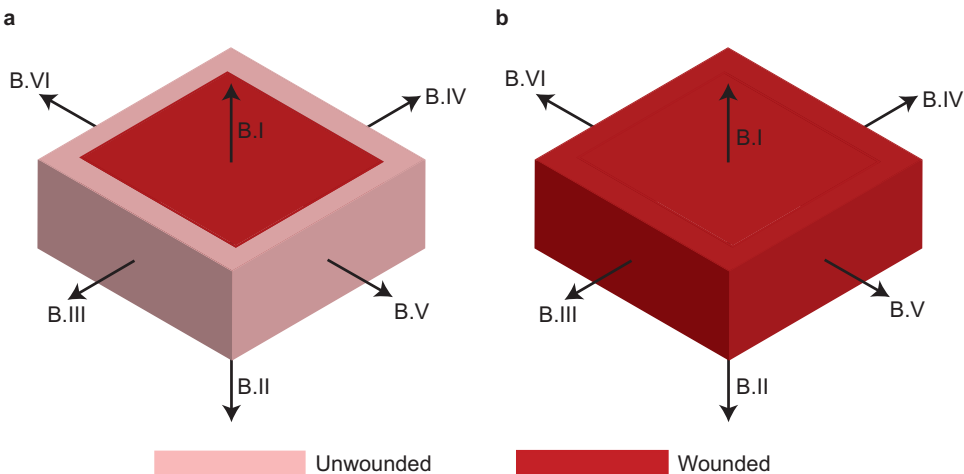
Figure 9.3: Examples of graphical representations of the computational domain when we model hypertrophy and contraction. Here, we show damaged tissue within healthy tissue (**a**) and a completely damaged tissue (**b**).

For the graphical representation in Figure 9.3a, we can use the following boundary conditions. For all $t > 0$ and $\mathbf{x} \in \{\Gamma_{\mathbf{x}}^{I}, \Gamma_{\mathbf{x}}^{II}\}$:

$$\mathbf{n} \cdot \mathbf{J}_N(\mathbf{x}, t) = 0, \quad \mathbf{n} \cdot \mathbf{J}_M(\mathbf{x}, t), \quad \mathbf{n} \cdot \mathbf{J}_c(\mathbf{x}, t) = 0. \tag{9.3}$$

For all $t > 0$ and $\mathbf{x} \in \{\Gamma_{\mathbf{x}}^{III}, \Gamma_{\mathbf{x}}^{IV}, \Gamma_{\mathbf{x}}^{V}, \Gamma_{\mathbf{x}}^{VI}\}$:

$$N(\mathbf{x}, t) = \overline{N}, \quad M(\mathbf{x}, t) = 0, \quad c(\mathbf{x}, t) = 0. \tag{9.4}$$

For the mechanics of the model, we can use the following boundary conditions, where we write $\boldsymbol{v} = (u, v, w)^T$. For all $t > 0$ and

$$\mathbf{x} \in \Gamma_{\mathbf{x}}^{I}: \quad \mathbf{n} \cdot \sigma = \begin{bmatrix} 0 \\ 0 \\ 0 \end{bmatrix}, \qquad \mathbf{x} \in \Gamma_{\mathbf{x}}^{II}: \quad \mathbf{n} \cdot \sigma = \begin{bmatrix} 0 \\ 0 \\ -s^I \rho w \end{bmatrix}. \tag{9.5}$$

For all $t > 0$ and

$$\mathbf{x} \in \{\Gamma_{\mathbf{x}}^{III}, \Gamma_{\mathbf{x}}^{IV}\}: \quad \mathbf{n} \cdot \sigma = \begin{bmatrix} -s^{II} \rho u \\ 0 \\ 0 \end{bmatrix}, \qquad \mathbf{x} \in \{\Gamma_{\mathbf{x}}^{V}, \Gamma_{\mathbf{x}}^{VI}\}: \quad \mathbf{n} \cdot \sigma = \begin{bmatrix} 0 \\ -s^{III} \rho v \\ 0 \end{bmatrix}. \tag{9.6}$$

These boundary conditions imply that the first boundary is allowed to move in any direction, and the second boundary is free to move in the directions of the x- and y-axis and has a spring-like force per unit area in the direction of the z-axis. The third and fourth boundaries are free to move in the directions of the y- and z-axis and have a spring-like force per unit area in the direction of the x-axis. The fifth and sixth boundaries are free to move in the directions of the x- and z-axis and have a spring-like force per unit area in the direction of the y-axis. The spring-like forces are proportional to the collagen concentration and the displacement in the direction of the corresponding axis.

For the graphical representation in Figure 9.3b, we can replace the boundary conditions for boundaries III, IV, V, and VI with spring-like boundary conditions.

If we define a symmetrical burn, then the solution is axisymmetric. We can then use the symmetrical boundary conditions we defined in this work. Further, one could incorporate *pulling and stretching forces* because of children's growth and motility. A first attempt to incorporate children's growth is to add terms to the right-hand side of equation (2.12) representing body forces. Another attempt is to incorporate forces by adding additional terms to the boundary conditions on boundaries III, IV, V, and VI. For the study of pressure therapy, one can add pressing terms to the boundary condition for boundary I.

Strains and constitutive stress-strain relations   We repeat the recommendations for completeness considering the strains and stress-strain relations that Koppenol suggested [17]. In the model of this work, the effective Eulerian strain is assumed to be small. However, the effective strains are more likely to become arbitrarily large, as was assumed in references [61] and [127]. When this assumption is made, equation (2.14) can be replaced by [24]:

$$\frac{\mathrm{D}\mathbf{e}}{\mathrm{D}t} = \mathrm{sym}\left(\mathbf{B}^{-1}\nabla\boldsymbol{v} - \frac{1}{\sqrt{\det\left(\mathbf{B}^{-1}\right)}}\mathbf{B}^{-1}\mathbf{G}\right), \tag{9.7}$$

where

$$\mathbf{e} = \frac{1}{2}\left[\mathbf{I} - \left(\mathbf{A^{-1}}\right)^2\right], \tag{9.8}$$

$$\mathbf{B} = [\mathbf{I} - 2\mathbf{e}]^{-1}, \tag{9.9}$$

and

$$\mathbf{G} = \zeta \frac{[N + \eta^{II} M]c}{1 + a_c^{III} c} \epsilon. \tag{9.10}$$

The tensor $\mathbf{A} = \frac{\partial \mathbf{x}}{\partial \mathbf{X}_e}$ (see Figure 2.1) is the locally-defined deformation gradient tensor that describes how infinitesimal line segments in the hypothetical configuration are transformed into infinitesimal line segments in the current configuration. Here, $\mathbf{x}$ is the current coordinate system, and $\mathbf{X}_e$ is the virtual reference coordinate system.

Further, the visco-elastic constitutive relation in equation (2.13) can be replaced by [127]

$$\sigma = \mu_1 \text{sym}(\nabla \boldsymbol{v}) + \mu_2 \left[\text{tr}\left(\text{sym}(\nabla \boldsymbol{v})\right)\mathbf{I}\right] +$$
$$\left[\frac{E(\rho)}{2[1-2\nu]}\left[\sqrt{\det(\mathbf{B})} - 1\right]\right]\mathbf{I} + \frac{E(\rho)}{2[1+\nu]}\left[\sqrt{\det(\mathbf{B})}\right]^{-\frac{5}{3}}\left[\mathbf{B} - \tfrac{1}{3}\text{tr}(\mathbf{B})\mathbf{I}\right], \quad (9.11)$$

where μ_1 and μ_2 are the shear and bulk viscosities, ν the Poisson's ratio, $E(\rho)$ Young's modulus, and $\mathbf{I}$ the identity tensor. As Koppenol mentioned, this relation might not be representative, and constitutive stress-strain relations for skin tissues such as granulation, dermal, and scar tissue remain to be further studied.

Angiogenesis Angiogenesis, from the Greek word Angêion ($\grave{\alpha}\gamma\gamma\epsilon\tilde{\iota}o\nu$), meaning vessel, is the formation of blood vessels from the existing vasculature. New blood vessel formation is an essential process in wound healing that is thought to mainly manifest as angiogenic sprouting of pre-existing capillaries [119]. Abnormal vascularization can be involved in the development of hypertrophic scars and keloids [128], as compared to normal skin, hypertrophic scars show a higher amount of blood vessels that are more dilated.

Guerra *et al.* state that the existent models of wound healing angiogenesis do not fully describe the process and that upcoming models should include vascular network remodeling and ECM components [129]. Given that hybrid in silico models [130–133] combine the microscale and macroscale analyses, allowing to describe cell behavior and predict the variation of the species concentration simultaneously, we propose to incorporate angiogenesis in a hybrid model.

Inflammation Severe burn injuries induce a complex inflammatory response that can persist for months to a year after the initial burn injury. In burn victims, this response can be over-activated, contributing to secondary wound expansion and excessive scarring, and it can exert systemic effects [134]. These systemic effects include inflammation in the heart that can result in secondary organ failure and, therefore, be life-threatening [135]. It is, therefore, essential to include inflammation in the post-burn modeling framework. This work's model considers the proliferative response after burn injuries, and the initial conditions represent the effect of inflammation. A possible pathway to include

the inflammatory response is to combine this work's model with other (existing or developed) models for inflammation. It is necessary to *upscale* when results from a cell-based model need to be translated to a continuum model. Previous research has been done on upscaling between a cell-based model and this work's continuum model for post-burn contraction [136].

Reepithelialization   For decades, mathematical models for wound healing focused on wound closure. Reepithelialization describes the resurfacing of a wound with new epithelium [6]. Keratinocytes, a major cellular component of the epidermis, are responsible for restoring the epidermis within hours after injury through this process. Under poor circumstances, reepithelialization is impaired, and a wound cannot be considered healed (this happens in all chronic wounds). Therefore, it is interesting to consider reepithelialization and, thus, also the dermal-epidermal interplay in our modeling framework. We suggest combining parts of the models developed by Sherratt and Murray [137], Wearing and Sherratt [138], Vermolen and Javierre [139], and Wang *et al.* [140] to include reepithelialization in the morphoelastic model. Here, one must consider the epidermal-dermal interaction and the dermal-subcutaneous interaction. If the resulting model is hybrid, then its discrete nature enables the modeling of individual keratinocytes. The model can then be easily adjusted to incorporate additional epithelial cell types, such as hair follicles and sweat glands.

The cells   Dermal fibroblasts are not fully differentiated. Hinz *et al.* showed that the myofibroblastic phenotype is regulated by mechanical tension *in vivo* [141]. After an injury, fibroblasts migrate to the wound bed, laying down a collagen- and cellular fibronectin rich ECM. During wound closure, the fibroblasts and collagen become oriented parallel to the wound bed along expected stress lines [142], showing tractional forces. These resulting *proto-myofibroblasts* contain stress fibers, focal adhesions, and extracellular fibronectin fibrils [141]. Unlike normal dermal fibroblasts, wound fibroblasts produce fibronectin messenger ribonucleic acid (mRNA) with two proteins, ectodysplasins A (EDA) and B, leading to EDA fibronectin expression in the granulation tissue [143]. This expression is essential to further myofibroblast differentiation as it stimulates α-SMA activity of transforming growth factor TGF-β1 [144]. Continued mechanical tension and the presence of TGF-β stimulate further diffentiation into myofibroblasts [145, 146] that express a strict organization of fibrils and focal adhesions, exerting forces. These (active) forces are primarily generated by the actin-myosin contractile machinery and transmitted to the ECM using transmembrane proteins of the integrin family in the focal adhesions [147]. Hence, there are fibroblasts (without stress fibers), proto-myofibroblasts having stress fibers that express cytoplasmic actins, and myofibroblasts having stress fibers that express α-SMA (see Figure 9.4).

Further, *in vitro* studies indicate that myofibroblasts can differentiate back to fibroblasts under the influence of Prostaglandin E2 [33], while this de-differentiation remains to be (dis)proven *in vivo*; hence the question mark in Figure 9.4.

The rationale behind the nonproliferation of myofibroblasts is that fully differentiated cells can either do one or the other, proliferating or exerting force. Therefore, myofibroblast proliferation is under discussion. Vaughan *et al.* have shown that myofibrob-
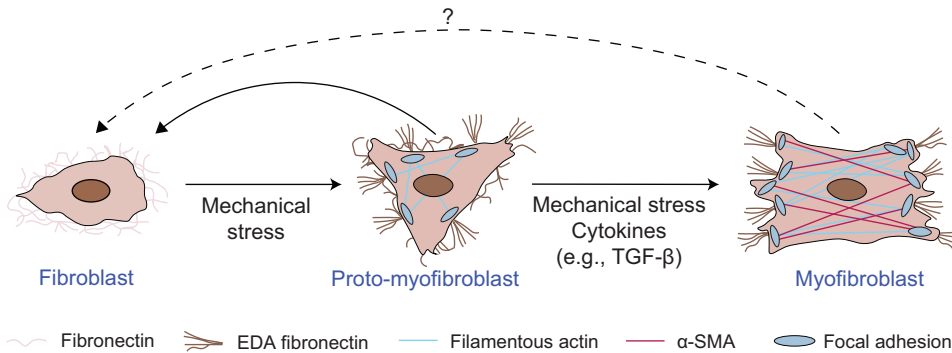
Figure 9.4: The two-stage model of myofibroblast differentiation. *In vivo*, dermal fibroblasts do not show stress fibers, and these cells do not form adhesion complexes with the extracellular matrix. Fibroblasts differentiate into proto-myofibroblasts under mechanical stress. Proto-myofibroblasts show actin-containing stress fibers that complete in adhesion complexes. Further, these cells, including the EDA variant, express cellular fibronectin at the cell surface. Under further mechanical stress and transforming growth factor β (TGF-β), proto-myofibroblasts differentiate into myofibroblasts. The expression of α-smooth muscle actin (α-SMA) characterizes myofibroblasts, showing more extensively developed stress fibers and large (focal) adhesion complexes. Fully differentiated myofibroblasts generate stronger contractile force than proto-myofibroblasts, reflected by the stricter organization of extracellular fibronectin into fibrils. Modified from Tomasek *et al.* Myofibroblasts and mechano-regulation of connective tissue remodeling. *Nature Reviews Molecular Cell Biology* 3:349, 2002.

lasts proliferate more slowly than fibroblasts [31], while other scientists suspect that myofibroblasts do not proliferate at all. Furthermore, it seems likely that the majority of myofibroblasts arise from pre-existing local fibroblasts in the dermis, which gradually acquire the myofibroblast phenotype, as is suggested by the gradual appearance of microfilaments at the electron microscope level and α-SMA positivity at the light microscope level. However, when local fibroblasts cannot satisfy the tissue's requirement for these cells, mesenchymal stem cells, fibrocytes, bone marrow-derived cells, and cells derived from an epithelialmesenchymal transition (EMT) process may represent alternative sources of myofibroblasts. If more myofibroblasts are 'necessary,' and if local sources of fibroblasts are depleted, other cells able to acquire a myofibroblastic phenotype are involved. This point could be consistent with the hypothesis that myofibroblasts do not proliferate.

In the current model, the only difference between the proliferation of fibroblasts and myofibroblasts is that myofibroblasts proliferate only in the presence of growth factors, and the proliferation rate is the same in both cells. In our study in Chapter 6, we have changed the model by defining different proliferation rates, which yielded realistic results. If it appears or is assumed that myofibroblasts do not proliferate and only contract the tissue, then there are two options. The first option is to add a term inspired by the so-called Bernoulli random (flip a coin) process. Another option is adding an equation for proto-myofibroblasts that can proliferate and exert smaller forces than fully differentiated myofibroblasts. Adding a proto-myofibroblast PDE is necessary if we set the myofibroblast proliferation rate to zero because, if we do set the proliferation rate to zero, the model needs considerable adjustments to reproduce the clinically observed contraction

realistically. Further, fibroblasts also cause the tissue to contract, albeit much weaker. This assumption is a good choice, as the simulations then show an initial retraction of the tissue, which is also observed in wounds.

When it comes to chemical response equations in their entirety, several modeling techniques are possible. First, cell proliferation is modeled with adjusted logistic growth models in the current model. Considering the modeling choices, we could keep a linear growth rate and introduce a tuneable quadratic cell death term for fitting equilibrium instead of the constant q in equations (2.6) and (2.7). Second, for the fibroblast differentiation parameter, we assumed a linear relationship in the activation of myofibroblasts, while the activation does not necessarily have to be linear. Further, it was shown that increasing the matrix stiffness leads to myofibroblast activation [148, 149], meaning that myofibroblast differentiation could depend on mechanical stiffness because of perceived stiffness by fibroblasts. We note that increased ECM stiffness and elevated collagen concentration are a hallmark of many tumors [150] and that myofibroblast differentiation requires sufficient mechanical stiffness [151]. Third, myofibroblasts enter a quiescent state or leave the tissue through apoptosis when the tissue's stress is reduced during wound healing [141, 152]. At the same time, these cells keep being activated under chronic mechanical stress or wound splinting [153, 154]. Therefore, we can consider myofibroblast inactivation, stress-dependent apoptosis, and stress-induced activation.

Example stiffness dependent body forces   Valero *et al.* proposed a purely mechanical and self-regulated traction force dependent on the ECM stiffness [118]. The role of the ECM stiffness is considered through a term denoting the force that a cell exerts depending on the ECM's volumetric strain based on the mechanosensing model for an adherent cell developed by Moreo *et al.* [155]. Specifically, this latter model provides the force exerted by the cell (p_{cell}), which is the sum of active and passive forces. The active force comes from the active stress fibers (myosin and actin filaments) and is more significant than the passive force from the microtubules. The active force is transmitted to the ECM. It depends on the deformation of the contractile element, i.e., the actin-myosin filaments for which the force-length relationship comes from the theoretical background for (muscle) sarcomeres[1]. The sliding filament and the cross-bridge theories explain this relationship. The sliding filament theory assumes that length changes are accomplished by relative sliding, and the cross-bridge theory assumes that independent force generators (cross-bridges) cause the relative sliding [156].

Figure 9.5 shows schematics of a frog skeletal muscle sarcomere [157] that might be representative of the myofibroblast actin-myosin machinery. Figure 9.5a shows that myosin motors (orange dots) attach to the actin to connect the actin to the myosin via cross bridges. In the center of the myosin, there are no cross-bridges [158]; this zone is called the midzone. The length of the actin connected to the myosin motors is called the overlap, which extends as the motors pull the actin toward the center. Figure 9.5b shows the force-length relationship of frog skeletal muscle sarcomere with five crucial points representing specific extensions of the sarcomere where the force curve changes. The force is maximal when the overlap is maximal when actin is connected with total length 2 μm

---

[1]A sarcomere, from the Greek words (sarx), meaning flesh, and (meros), meaning part, is the smallest functional unit of striated muscle tissue
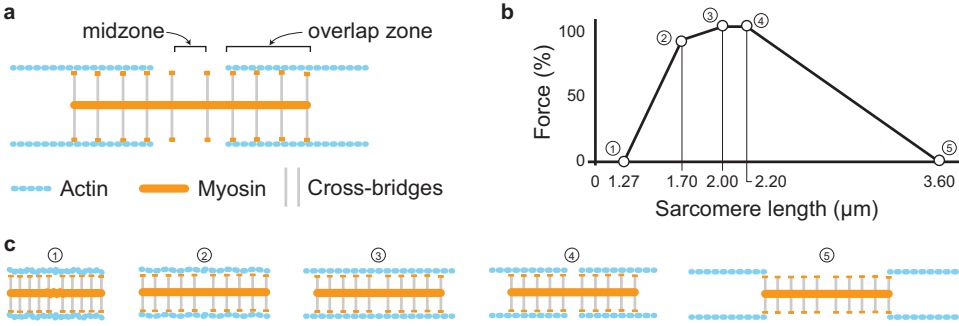
Figure 9.5: Schematic of a sarcomere (**a**), the force-length relationship of frog skeletal muscle sarcomere (**b**), and schematic sarcomeres corresponding to crucial points (1–5) labeled in **b**. Modified from Rassier *et al.* Length dependence of active force production in skeletal muscle. *Journal of Applied Physiology* 86:1445, 1999.

(the third crucial point). As Rassier *et al.* [156] state, sarcomere extension by 0.2 μm (which is the midzone length) does not decrease the force potential because the midzone doe not contain cross bridges (the fourth crucial point). Further, sarcomere extension decreases the force potential linearly to zero when the sarcomere length is maximal (the fifth crucial point). The myosin motors can shrink the sarcomere further than 2 μm because the myosin has a smaller length than the actins. Sarcomere shrinkage up to the myosin length (crucial point 2) decreases the force potential linearly with a smaller slope than when the sarcomere is shrunk further. This force potential decrease might be because of a decreased probability of cross-bridge interaction [159] and interference of cross-bridge interaction [157].

Moreo *et al.* [155] based their modeling on the above theories and used a simplified schematic without considering the cross bridge-free myosin midzone. Their reference 'sarcomere' length (crucial point 3 in Figures 9.5b,c) where the force potential is maximal is represented by $\theta^* = p_{\max}/K_{\mathrm{act}}$, where $p_{\max}$ is the maximum active force and K_{act} is the volumetric stiffness moduli of actin filaments. Further, the lengths corresponding to crucial points 1 and 5 in Figures 9.5b,c are denoted by θ_1 (the shortening strain of the contractile element) and θ_2 (the lengthening strain of the contractile element), respectively. Hence, the active force depends on the ECM volumetric strain $\theta = \mathrm{tr}(\varepsilon)$. Neglecting passive forces, the force exerted by the cells is given by [81]:

$$p_{\mathrm{cell}}(\theta) = \frac{K_{\mathrm{act}}p_{\max}}{K_{\mathrm{act}}\theta_1 - p_{\max}}(\theta_1 - \theta)\mathbb{1}_{[\theta_1,\theta^*]}(\theta) + \frac{K_{\mathrm{act}}p_{\max}}{K_{\mathrm{act}}\theta_2 - p_{\max}}(\theta_2 - \theta)\mathbb{1}_{(\theta^*,\theta_2]}(\theta), \qquad (9.12)$$

where $\mathbb{1}_{[a,b]}$ is the indicator function defined as $\mathbb{1}_{[a,b]}(x) = 1$ if $x \in [a,b]$ and 0 otherwise. In the morphoelastic model, we could insert equation (9.12) in the body force term **f** in equation (2.12):

$$\mathbf{f} = \nabla \cdot \left(p_{\mathrm{cell}}(\theta)\frac{\xi M\rho}{R^2 + \rho^2} \right)\mathbf{I}. \qquad (9.13)$$

In this equation, we can easily add fibroblast traction forces. In addition, stiffness-dependent fibroblast differentiation can be incorporated by adding $\theta^+ = \max(\theta, 0)$ in the differentiation term in equation (2.6).

Matrix metallo proteins   Matrix metalloproteinases (MMPs) are present in acute and chronic wounds [160]. In our model, we introduced MMPs in equations (2.9) and (2.10) and assumed its balance to be instantaneous. This modeling choice might need to be more complex as different MMP types arise during wound healing, each with another possible role. For example, MMP-2 stimulates the activation of MMP-9 [161] that is involved in migrating several cell types [162]. Observations support the idea that MMP-9 is linked to the reepithelialization process and early events [163], whereas MMP-2 is essential during the prolonged remodeling phase [164, 165]. Therefore, we suggest further studying the specific roles of MMPs and the interactions with the modeled species in this work to define time-dependent PDEs for these MMPs to determine the necessity of this consideration.

Collagen I versus III   Because collagen type I is the most abundant type of collagen in the human dermis and has a soft structure, it is the most commonly used type in collagen-based scaffolds. Often skin substitutes comprise the combination of collagen type I with III and V, as in Matriderm [166, 167]. In a later stage of wound healing, the fibroblast cells replace the deposited collagen type III with collagen type I (see Figure 9.6). The success of tissue regeneration depends on the wound size and the biomaterial scaffold's composition. Early granulation tissue with little tensile strength has a deficient collagen type I to type III ratios [168, 169] while mature scar tissue has a high I:III ratio [170]. It has been shown that acellular scaffolds that rely on native cells allow 0.5 cm new tissue growth from the wound edge [171], indicating that more extensive wounds require biomaterials manufactured from cell-seeded matrices.
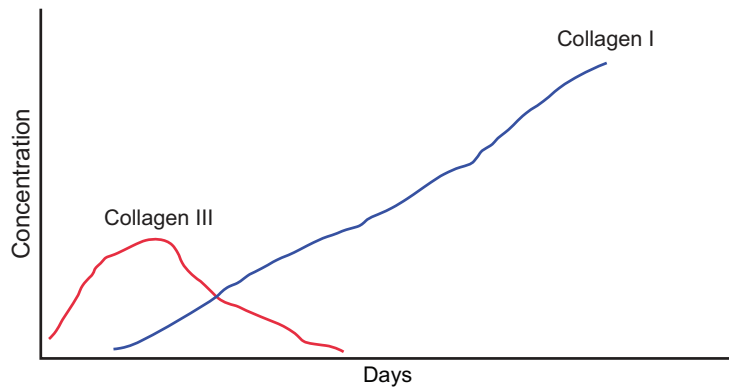
Figure 9.6: Early deposition of collagen type III and later deposition of collagen type I in wound healing. Modified from Witte, M., Barbul, A. General principles of wound healing. *Surgical Clinics of North America* 77:509, 1997.

Replacing the deposited collagen from granulation tissue to scar tissue during contracture formation differs from new tissue generation. It is, therefore, interesting to investigate the effect of *skin substitutes* with differing ratios of collagen type I to collagen type III and for different types of cells. This investigation brings about the combination of different collagen on skin cells and the distinction between tissue generation and healing.

Suppose we know to what extent the skin substitutes' composition in terms of the spatial distribution of the collagen types (that is, the ratio between collagen type I and collagen type III) impacts the amount of maximum contraction and long-lasting contraction. In that case, this knowledge will help manufacturers and clinicians to find the optimal collagen distribution in skin substitutes. So far, it is unknown whether these effects of collagen type I to type III ratio to contraction and patient discomfort have been compared. Further, because collagen type I is more rigid than the flexible collagen type III, local mechanics may vary, and collagen fibers could align because of cell-applied forces. Therefore, the adaption of *skin alignment* can be helpful for predictions. During normal wound healing, scars form from dermal cells that align in parallel. However, if this alignment is disrupted by a biodegradable scaffold that directs cells to grow in a random orientation, then the cells will follow the randomized differentiation program necessary for proper, microstructurally randomized, hence macroscopically isotropic regeneration [172].

Collagen bundles   The collagen orientation of scar tissue is more parallel compared to normal skin [173], and therefore, mechanical tissue properties are different in scars than in normal skin. The current model does not consider the geometrical distribution of collagen bundles; consequently, it is impossible to study the effect of collagen orientation on the tissue's mechanical properties with the current model. Other models, such as the ones developed by Barocas and Tranquilo [15], Olsen *et al.* [174], Dallon *et al.* [16, 18], Cumming *et al.* [175], Boon *et al.* [28], and Koppenol *et al.* [127, 176] do consider collagen orientation. The differences between these mentioned models involve the approaches (tensorial versus vector-based), the scale (continuous versus discrete versus hybrid), and the added chemical and mechanical components. Our suggestion for further development of this work's model is to convert the model to a hybrid model, including collagen orientation, using a tensorial approach. As Koppenol pointed out, equations (2.3) and (2.4) could be replaced with, for instance,

$$\mathbf{J}_N = \Omega^c[-D_n(N + M)\nabla N + \chi N\nabla c], \tag{9.14}$$

$$\mathbf{J}_M = \Omega^c[-D_n(N + M)\nabla M + \chi M\nabla c], \tag{9.15}$$

where

$$\Omega^c = \left[1 - \frac{\text{tr}(\Omega^\rho)}{a_\rho^I + \text{tr}(\Omega^\rho)}\right]\mathbf{I} + \left[\frac{\text{tr}(\Omega^\rho)}{a_\rho^I + \text{tr}(\Omega^\rho)}\right]\hat{\Omega}^\rho. \tag{9.16}$$

Here, the tensor Ω^ρ represents the collagen bundles, $\hat{\Omega}^\rho$ represents the tensor related to the collagen bundles with rows normalized to unit length, and the parameter value a_ρ^I determines the haptotactic[2] cell sensitivity. These equations align the cells with the collagen bundles, which direct the cell movement [177].

Anisotropic and inhomogeneous   Mathematical models that simulate wound healing usually model the cell-ECM system as an isotropic linear visco/morphoelastic solid. This choice is a simplification because of the nonlinear viscoelasticity and anisotropy of soft

---

[2]Haptotaxis is the directional motility or outgrowth of cells.

tissues. Consequently, studying the implications of local mechanics and collagen align-ment is impossible. Therefore, we must model the ECM as an anisotropic (nonlinear) inhomogeneous medium. For this, we can consider the models by Barocas and Tran-quillo [15], Koppenol [176], and Cumming, McElwain, and Upton [175]. This way, we can also include Langer lines of skin tension that are parallel to the natural orientation of collagen, and we can study the direction of contraction in more detail.

9.2.4 Numerical method and implementation

Higher-dimensional models account for the wound shape and depth. The downside, however, is that such models lead to numerical computational complexity. Hence, from a computational point of view, the challenge is to optimize calculations in 3D because of the growing number of elements, arbitrary geometries, and artificial non-positive con-centrations. In 2D, we already applied flux correction techniques, an adaptive meshing algorithm, rotational symmetry, and parallel computing, which will also be helpful in 3D. The next step is to implement these calculations in higher programming languages, such as C++, that compile directly to a machine's native code, allowing it to be fast. Of course, we can still use Matlab to visualize the solutions.

The numerical solutions to multi-dimensional models involve meshes that can get poor quality when the mesh moves because of contraction. Therefore, we need *(adaptive) remeshing techniques*, which, in general, are also computationally expensive and can lead to significant variations in the wound shape. Hence, we need to study these remesh-ing techniques and the use of other elements in more detail to allow for more accurate and quick predictions. We believe that *isogeometric analysis* (IGA) can be helpful since IGA can deal with smooth pieces of the boundary (splines). Because of its high accuracy, the method needs fewer elements and is cost-effective. For example, with IGA, we can model a circle with only two elements, which is impossible to achieve with the finite el-ement method. Barion has provided a promising start using IGA for the morphoelastic model for post-burn contraction in his master thesis [178].

Nevertheless, these computational techniques are expensive and impractical in clini-cal environments. As mentioned earlier, neural networks provide immediate access to the simulations, making these frameworks beautiful for clinical purposes. However, to train these neural networks, we need many numerical simulations. For that purpose, we need to consider other techniques like using *variable data* and (clever) *multi-level Monte Carlo techniques*. To use variable data, we can first study to what extent shorter simulations predict ultimate intensity in contraction and hypertrophy; in other words, how long we have to simulate to make statements with unquestionable certainty. Vari-able data can also mean that we do many short simulations in narrow ranges of param-eter values and fewer long simulations to map the long simulation results onto the short simulations. Multi-level Monte Carlo techniques can involve multiple simulations (sam-ples) with low grid resolution and a few with high resolution. However, other techniques might also be possible, like force-bias Monte Carlo [179] and stochastic collocation [180], that we need to study first.

9.2.5 Machine learning

When the above concepts have been further developed, the idea is that a practitioner can scan the burn wound, for example, using a laser Doppler. This scan includes the shape (geometry) of the burn and the severity of the burn. Such a scan can also contain much noise requiring noise reduction, which neural networks can perform. A convolutional neural network (CNN) can take and process these multi-dimensional images. The CNN can classify these images, for example, an image to be a chest burn or a hand burn, or the cause of the burn, and this information can be helpful in further predictions. The CNN can also detect edges in the images using geometric filters, such as an edge detection filter [181] that uses pixel-based metrics in the convolutional layers. The deeper the network goes, the more details the network can detect, such as hair near the wound edges, which can be a significant detail of the burn as hair follicles might accelerate wound healing [182, 183].

Another approach to map wound shape and size is to use shape similarity [184] and shape matching [185]. This way, we can use standard geometrical objects, such as circles and squares, for which contraction prediction is less complicated. The edge error can measure such mappings error [186]. For these standard geometrical objects, we can use factors such as shape indices [187] (the eccentricity of an elliptical scar, the extent to which a scar is circular, the aspect ratio, etcetera).

From a computational point of view, it is also interesting to study machine learning approaches that work with variable data (e.g., *long short-term memory* (LSTM) [188, 189]). In real life, wounds heal at rates in various etiologies, and applied treatments resolve contractures, after which contraction can develop again. In such cases, we want to predict over a different period. Hence, hybrid approaches like LSTM and *recurrent neural networks* (RNNs) might be necessary to achieve this, though we need many clinical data samples to train such a model.

A disadvantage of the neural network is that the neural network needs to be retrained if the mathematical model changes, though the disadvantage is that retraining costs time and effort. In fact, retraining is also an essential advantage because the model is getting better and better. We note that if the model does not change too much, and if the type of input/output remains the same, one might use *retraining techniques* (instead of full retraining). For this, we can use the trained network as initialization. This re-use might not benefit the low-dimensional models and small neural networks. However, high-dimensional models that use more extensive neural networks might differ in data generation and training time. Therefore, we can use transfer learning that applies the knowledge learned in one or more tasks to develop an efficient hypothesis for a new task [190], or we can use physics-informed neural networks (PINNs) [191] that can ensure we need fewer data to train the model correctly.

The network's performance highly depends on the choices of the hyper-parameters. In this work, we have chosen hyper-parameters based on trial and error. More elaborate tuning of the hyper-parameters could improve the performance results of the trained networks. Furthermore, *hyper-parameter optimization techniques*, such as Hyperopt [192], can optimize the hyper-parameters regarding the validation loss, which is good to keep in mind in further studies.

We must always test whether the machine learning results have been obtained with in-

put data within the training set's domain. The idea is then that the obtained scan is used as an initial condition for the simulations with the neural network model mimicking the mathematical model. The practitioner should then quickly see a histogram of the intensity of the expected post-burn contraction (and any other variables of interest). Further direction is to include the treatments so the practitioner finds the optimal treatment according to the model. The idea is shown schematically in Figure 9.7.
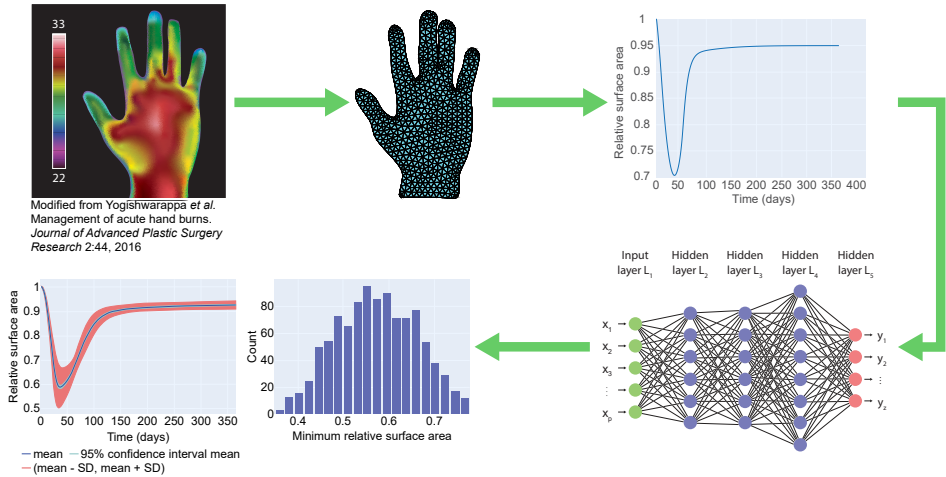
Figure 9.7: Schematic representation of integrating the mathematical model and the neural network in clinical practice. For example, the mathematical model predicts the degree of contraction regarding scar size versus time for many simulations, drawing from probability distributions and different wound shapes and sizes. After training the neural network based on the mathematical model results, the neural network reproduces these results, providing the practitioner with an estimated probability distribution of various scenarios. In the future, this should be expanded with different treatments.

Of course, we still have to deliver a considerable effort equivocate. Practitioners are often experienced physicians who know very well from their observations and colleagues what the most likely scenarios are. Therefore, a clinician should always maintain skepticism regarding model results. Common sense must always come first, and model results can never be unthinkingly adopted. In addition, the model predicts probabilities in specific scenarios. We must remember that improbable events can happen. In other words, the (almost) impossible can happen. So, despite the modeling business, common sense must continue.

Nawoord (Epilogue)

De afgelopen vier jaar heb ik met plezier en af en toe frustratie aan dit prachtige onderzoek gewerkt. In mijn nawoord, waarin ik veel mensen bedank, wil ik de lezer meenemen in een stukje geschiedenis.

Allereerst wil ik mijn grootouders bedanken voor het laten bestaan van mijn ouders. In het bijzonder bedank ik opa Bart, die me al op jonge leeftijd de opdracht gaf om de abc-formule in mijn hoofd op te lossen in plaats van een rekenmachine te gebruiken. Opa Bart besefte dat ik een duidelijke eigen visie had, met eigen ideeën, plannen en werkwijzen. Hij heeft me altijd met humor gestimuleerd om te groeien tot een hechte persoonlijkheid die uitdagingen niet uit de weg gaat. Ik ben blij dat we onze liefde voor wiskunde konden delen.

Mijn ouders betekenen veel voor me en ik ben hen dankbaar. Of ik nou astronaut of actrice wilde worden, piano of saxofoon wilde spelen, wat het ook was, zij hebben me altijd aangemoedigd om mijn passies te volgen. Mijn vader zag dat ik de lat hoog legde en geen genoegen nam met weinig. Hij liet me door de verrekijker kijken om inzicht te krijgen in mijn identiteit, talenten en verlangens. De combinatie van in- en uitzoomen op de details en het overzicht van mijn leven heeft me de afgelopen vier jaar geholpen. Mijn moeder zag mijn uitdagingen en vertrouwde me altijd om ze te overwinnen. Haar vertrouwen in mij is bijzonder, en ik blijf het leuk vinden dat zij, nog voordat ik het zelf wist, wist dat ik een Ph.D. wilde doen. Zij was de eerste die me hierin stimuleerde en is me blijven aanmoedigen, vol vertrouwen dat het me gaat lukken.

Tijdens mijn master wiskunde werd mijn dochter Jazz geboren, en kort daarna verbrandde mijn zoon Dean door een kom hete soep. Deze tragische gebeurtenis resulteerde in een lange herstelperiode waarin het contact met de Nederlandse Brandwonden Stichting ontstond. Tijdens één van de jaarlijkse brandwondendagen ontving ik de toenmalige uitgave van het verenigingsblad *Infocus* en daarin las ik een artikel over het onderzoek van voormalig Ph.D. student D. Koppenol. Koppenol ontwikkelde wiskundige modellen voor het genezen van brandwonden. Ik wilde destijds al deelnemen aan het onderzoek, maar moest eerst mijn opleiding afronden. Dean had destijds een hypertrofisch litteken ontwikkeld en was hiervoor patiënt geworden van Paul van Zuijlen.

Op de dag dat ik mijn master behaalde, was ik aangenaam verrast toen ik de vacature van dit huidige onderzoek bovenaan in de 'feed' van LinkedIn zag staan. Of het nu puur toeval was of van bovenaf in de schoot geworpen, ik wist het zeker: ik wilde dit onderzoek doen en solliciteerde. Voorlopig werd ik uitgenodigd om te solliciteren bij Fred Vermolen. Er waren verschillende perspectieven op dit project en het was een uitdaging om te kiezen tussen de kandidaten. Daarom was besloten om ook met Paul van Zuijlen in gesprek te gaan. In gesprek met Paul realiseerde ik me dat ik hem niet ontmoette als moeder van zijn patiënt, maar als een potentiële collega. De keuze van Paul was beslissend en Fred liet me weten dat ze voor mij hadden kozen. Dit was één van de gelukkigste

momenten in mijn leven. Al die spanning kwam vrij in een vreugdedans waar ik Fred en Paul heel dankbaar voor ben.

In januari 2019 begon ik met het onderzoek waarvoor ik ook cursussen heb gevold. Ik heb erg genoten van de manier waarop Fred de cursus *Toegepaste Eindige Elementen Methoden* doceerde. Ik woonde toen nog in Utrecht en kon voor deze cursus naar de Universiteit Utrecht fietsen. Al snel verhuisde ik naar Pijnacker wat dagelijkse 'live' besprekingen mogelijk maakte, en die waren heel gezellig. In het eerste jaar leerde ik het *Biomorphoelastische model voor contractie in brandwondenlittekens* beter kennen. Ik was blij toen het me eindelijk lukte om goede simulaties in 1D uit te voeren. Tegen de tijd dat ik mijn GO/NO GO-interview had in december 2019, had ik een voorlopige versie van ons eerste artikel waarin ik enige stabiliteit, enige gevoeligheid en de toepasbaarheidsstudie van hoofdstukken 3 en 5 van dit proefschrift had opgenomen. Ik presenteerde dit voor Fred, Paul, Kees Vuik en Neil Budko en nam dankbaar een GO van hen in ontvangst.

Ik kon niet in Pijnacker blijven wonen en moest een nieuw huis vinden wat onmogelijk leek. Mijn ouders waren mijn redders in deze noodsituatie. Zij boden Dean, Jazz en mij aan om bij hen in te trekken, waar we nu wonen. Nogmaals wil ik mijn ouders bedanken omdat hun hulp het mogelijk heeft gemaakt om dit onderzoek af te ronden. Mijn moeder luisterde altijd met belangstelling naar mijn onderzoek, en het is cool dat ze het voor een leek nog zo goed begrijpt!

Mijn zus Joy heeft structureel aangeven dat zij geen twijfels heeft of ik het onderzoek kan uitvoeren en zij heeft mij altijd gestimuleerd situaties van onzekerheid te heroverwegen. Ook in de privésfeer heeft Joy een ongekende waarde betekend voor me en dat doet ze nog steeds. Ik ben dankbaar dat zij dit voor me doet en heeft gedaan. Ik ben blij dat zij mijn zus is, en dat wij zo'n speciale relatie hebben. In deze privésfeer wil ik ook mijn lieve kinderen Dean en Jazz bedanken. Het was echt balen dat ik altijd moest werken, en ik vind het dan zeer mooi om te zien hoe flexibel en begripvol zij hiervoor zijn. ♥

Ik wil alles opschrijven waar ik Fred dankbaar voor ben, maar ik doe de lezer een plezier, want als ik dit zal doen, zal dit hoofdstuk nog een tijdje doorgaan. ☺ Ik ben blij dat ik Fred heb leren kennen. Wij praatten in dergelijke mate over niet-werkgerelateerde zaken dat wij regelmatig in de laatste minuten van de discussies over werk spraken. Ik denk dat dit onze samenwerking ten goede is gekomen en had me geen betere begeleider kunnen wensen. Ik wil Fred niet alleen bedanken voor alle geboden begeleiding en inzichten, maar ook voor wie hij is en hoe hij tegen het leven aankijkt. Ik denk nu terug aan de online bijeenkomst waar ik vroeg wat er mis was zijn wenkbrauwen, niet wetende dat er een gekke functie aan stond. En de keer dat de online discussie werd versierd met digitale vlaggetjes. En natuurlijk de altijd mooi gekleurde duimpjes. Ik heb veel van Fred geleerd en veel met hem gelachen. Ik wil Fred ook bedanken voor zijn vertrouwen in mij en in het bijzonder voor het naar een hoger niveau tillen van dit werk en het laten uitvoeren van mijn ideeën.

Ik wil ook Paul nogmaals bedanken. Paul heeft mij zoveel geleerd op medisch gebied en blijft me nieuwe dingen leren. Hij heeft goede tips gegeven over het schrijven van artikelen, en zijn kennis is onmisbaar. Ik denk nu terug aan toen Paul Dean had geopereerd, waarna wij op de verkoeverkamer een gesprek hadden over myofibroblasten. Dat moment was voor mij een keerpunt. Als moeder voelde ik me machteloos na Deans verbranding, maar als onderzoeker hoopte ik dat ik het verschil kon maken. Pauls visie

op brandwondenonderzoek is inspirerend en helder en komt in zijn volledigheid op mij over. Ik heb het geluk dat ik hieraan kan bijdragen en dat mijn visie een rol kan spelen. Tijdens het afronden van mijn proefschrift mocht ik ook een dag meelopen in de operatiekamer bij Paul. Op deze dag heb ik wederom veel geleerd, vanuit de praktijk. Het was een bijzondere ervaring, met een enkele keer flauwvallen, en deze draagt bij aan de uitbreiding van het vervolgonderzoek.

Fred, Paul en ik probeerden maandelijks af te spreken voor overleg. In één van deze bijeenkomsten bleek de behoefte aan specifieke expertise. Paul bracht me in contact met myofibroblast-expert Alexis Desmoulière. In de daaropvolgende tijd had ik fascinerende gesprekken met Alexis en een enorme boost in mijn kennis van myofibroblasten. Alexis gaf duidelijke antwoorden op mijn kritische vragen en besprak nog veel meer bijkomende factoren in wondgenezing. We schreven allemaal samen een artikel waarin we deze essentiële punten erkenden, wat resulteerde in een duidelijke toekomstvisie voor het verbeteren van het wiskundige model. Ik ben Alexis dankbaar voor deze samenwerking, en voor zijn vriendelijkheid en betrokkenheid.

Tijdens dit onderzoek was ik ook een tijdje met ziekteverlof. Ik stootte mijn hand en kon hem al snel niet meer gebruiken. Typen en piano spelen was niet meer mogelijk. Geen enkele arts wist zeker wat er mis was, en het duurde zes weken voordat ik weer aan het werk kon. In die periode kreeg ik een telefoontje van Kees Vuik. De afgelopen jaren hebben Kees en ik elkaar nog maar een paar keer gezien en gesproken. Ik waardeer het enorm dat Kees me belde om te vragen hoe het met me ging. Ik ben Kees dankbaar voor zijn vriendelijkheid, betrokkenheid en vertrouwen in dit onderzoek, en dat hij promotor is van dit onderzoek.

In mijn dankwoord neem ik ook de Nederlandse Brandwondenstichting en Stichting Proefdiervrij op. De financiële steun van de stichtingen maakte het mogelijk om dit onderzoek uit te voeren en te publiceren in wetenschappelijke tijdschriften. Uiteraard wil ik ook de donateurs en collectanten van de Nederlandse Brandwonden Stichting bedanken voor hun bijdrage aan dit proefschrift. Bedankt!

De laatste persoon die ik wil bedanken is mijn geliefde Jesse Russell. Hij is al jaren mijn steunpilaar. We hebben veel gelachen en mooie momenten samen gehad. Hij heeft me enorm geholpen om persoonlijke problemen te overwinnen en inzicht te krijgen. Ik ben blij dat we elkaars leven delen, en ik kan niet wachten om permanent samen te zijn.

Kortom, tijdens deze promotieperiode heb ik veel geleerd en ben ik gegroeid met dank aan iedere genoemde persoon. Ik heb mijn wiskundige en medische kennis aangevuld, en ik heb ook nieuwe vriendschappen gesloten die ik niet zou willen missen. Gelukkig gaan dit onderzoek, de waardevolle samenwerkingen en de vriendschappen verder dan hier nu ik aan mijn post-doctorale onderzoek werk. Ik kan mijn kennis verder uitbreiden met de geweldige mensen die ik als mijn vrienden beschouw.

Tot slot, om niet te vergeten, dank ik God dat Hij mij bijstaat.

Bibliography

1. Koppenol, D. & Vermolen, F. Biomedical implications from a morphoelastic continuum model for the simulation of contracture formation in skin grafts that cover excised burns. *Biomechanics and Modeling in Mechanobiology* **16,** 1187–1206 (2017).

2. WHO. *World Health Organisation, Fact sheet, Burns, 06-03-2018* `https://www.who.int/en/news-room/fact-sheets/detail/burns`. Accessed on 04-12-2019. 2018.

3. Tiwari, V. Burn wound: How it differs from other wounds? *Indian Journal of Plastic Surgery* **45,** 364–373 (2012).

4. Goel, A. & Shrivastava, P. Post-burn scars and scar contractures. *Indian Journal of Plastic Surgery* **43,** 63 (2010).

5. Wang, Y. *e.a.* Burn injury: challenges and advances in burn wound healing, infection, pain and scarring. *Advanced Drug Delivery Reviews* **123,** 3–17 (2018).

6. Rousselle, P., Braye, F. & Dayan, G. Re-epithelialization of adult skin wounds: cellular mechanisms and therapeutic strategies. *Advanced Drug Delivery Reviews* **146,** 344–365 (2019).

7. Desmoulière, A., Geinoz, A., Gabbiani, F. & Gabbiani, G. Transforming growth factor-β1 induces alpha-smooth muscle actin expression in granulation tissue myofibroblasts and in quiescent and growing cultured fibroblasts. *The Journal of Cell Biology* **122,** 103–111 (1993).

8. Mast, B. & Schultz, G. Interactions of cytokines, growth factors, and proteases in acute and chronic wounds. *Wound Repair and Regeneration* **4,** 411–420 (1996).

9. Sternlicht, M. & Werb, Z. How matrix metalloproteinases regulate cell behavior. *Annual review of cell and developmental biology* **17,** 463–516 (2001).

10. Desmoulière, A., Redard, M., Darby, I. & Gabbiani, G. Apoptosis mediates the decrease in cellularity during the transition between granulation tissue and scar. *The American journal of pathology* **146,** 56–66 (1995).

11. Tomasek, J., Gabbiani, G., Hinz, B., Chaponnier, C. & Brown, R. Myofibroblasts and mechano-regulation of connective tissue remodelling. *Nature Reviews Molecular Cell Biology* **3,** 349–363 (2002).

12. Enoch, S. & Leaper, D. Basic science of wound healing. *Surgery (Oxford)* **26,** 31–37 (2008).

13. Young, A. & McNaught, C. The Physiology of Wound Healing. *Surgery (Oxford)* **29,** 475–479 (2011).

14. Olsen, L., Sherratt, J. & Maini, P. A mechanochemical model for adult dermal wound contraction and the permanence of the contracted tissue displacement profile. *Journal of Theoretical Biology* **177,** 113–128 (1995).

15. Barocas, V. & Tranquillo, R. An anisotropic biphasic theory of tissue-equivalent mechanics: the interplay among cell traction, fibrillar network deformation, fibril alignment, and cell contact guidance. *Journal of Biomechanical Engineering* **119,** 137–145 (1997).

16. Dallon, J., Sherrat, J. & Maini, P. Mathematical modelling of extracellular matrix dynamics using discrete cells: fiber orientation and tissue regeneration. *Journal of Theoretical Biology* **199,** 449–471 (1999).

17. Koppenol, D. *Biomedical implications from mathematical models for the simulation of dermal wound healing* proefschrift (Delft University of Technology, 2017).

18. McDougall, S., Dallon, J., Sherrat, J. & Maini, P. Fibroblast migration and collagen deposition during dermal wound healing: mathematical modelling and clinical implications. *Philosophical Transactions of the Royal Society A: Mathematical, Physical and Engineering Sciences* **364,** 1385–1405 (2006).

19. Tranquillo, R. & Murray, J. Continuum model of fibroblast-driven wound contraction: inflammation-mediation. *Journal of Theoretical Biology* **158,** 135–172 (1992).

20. Menon, S., Hall, C., McCue, S. & McElwain, D. A model for one-dimensional morphoelasticity and its application to fibroblast-populated collagen lattices. *Biomechanics and Modeling in Mechanobiology* **16,** 1743–1763 (2017).

21. Stéphanou, A. & Volpert, V. Hybrid modelling in biology: a classification review. *Mathematical Modelling of Natural Phenomena* **11** (red. Volpert, V.) 37–48 (2015).

22. Thampatty, B. & Wang, J. A new approach to study fibroblast migration. *Cell Motility and the Cytoskeleton* **64,** 1–5 (2006).

23. Hillen, T. & Painter, K. A user's guide to PDE models for chemotaxis. *Journal of Mathematical Biology* **58,** 183–217 (2008).

24. Hall, C. *Modelling of some biological materials using continuum mechanics* proefschrift (Queensland University of Technology, 2008).

25. Goriely, A. & Amar, M. On the definition and modeling of incremental, cumulative, and continuous growth laws in morphoelasticity. *Biomechanics and Modeling in Mechanobiology* **6,** 289–296 (2006).

26. Rodriguez, E., Hoger, A. & McCulloch, A. Stress-dependent finite growth in soft elastic tissues. *Journal of Biomechanics* **27,** 455–467 (1994).

27. Postlethwaite, A., Keski-Oja, J., Moses, H. & Kang, A. Stimulation of the chemotactic migration of human fibroblasts by transforming growth factor beta. *Journal of Experimental Medicine* **165,** 251–256 (1987).

28. Boon, W., Koppenol, D. & Vermolen, F. A multi-agent cell-based model for wound contraction. *Journal of Biomechanics* **49,** 1388–1401 (2016).

29. Dallon, J., Sherrat, J. & Maini, P. Modeling the effects of transforming growth factor-β on extracellular matrix alignment in dermal wound repair. *Wound Repair and Regeneration* **9,** 278–286 (2001).

30. Murray, J. *Mathematical Biology II* 844 p. ISBN: 0387952284 (Springer New York, 2011).

31. Vaughan, M., Odejimi, T., Morris, T., Sawalha, D. & Spencer, C. A new bioassay identifies proliferation ratios of fibroblasts and myofibroblasts. *Cell Biology International* **38,** 981–986 (2014).

32. Vande Berg, J., Rudolph, R., Poolman, W. & Disharoon, D. Comparative growth dynamics and actin concentration between cultured human myofibroblasts from granulating wounds and dermal fibroblasts from normal skin. *Lab Invest* **61,** 532–538 (1989).

33. Garrison, G. *e.a.* Reversal of myofibroblast differentiation by erostaglandin E2. *American Journal of Respiratory Cell and Molecular Biology* **48,** 550–558 (2013).

34. Barrientos, S., Stojadinovic, O., Golinko, M., Brem, H. & Tomic-Canic, M. Perspective article: Growth factors and cytokines in wound healing. *Wound Repair and Regeneration* **16,** 585–601 (2008).

35. Baum, C. & Arpey, C. Normal cutaneous wound healing: clinical correlation with cellular and molecular events. *Dermatologic Surgery* **31,** 674–686 (2006).

36. Ivanoff, J., Talme, T. & Sundqvist, K.-G. The role of chemokines and extracellular matrix components in the migration of T lymphocytes into three-dimensional substrata. *Immunology* **114,** 53–62 (2005).

37. Lindner, D. *e.a.* Differential expression of matrix metalloproteases in human fibroblasts with different origins. *Biochemistry Research International* **2012,** 1–10 (2012).

38. Overall, C., Wrana, J. & Sodek, J. Transcriptional and post-transcriptional regulation of 72-kda gelatinase/ type IV collagenase by transforming growth factor-beta in human fibroblasts. *Journal of Biological Chemistry* **266,** 14061–14071 (1991).

39. Cooper, G. *The Cell: A Molecular Approach* 2nd Edition. ISBN: 9780878931064 (Sinauer Associates Inc, 2000).

40. Ramtani, S. Mechanical modelling of cell/ECM and cell/cell interactions during the contraction of a fibroblast-populated collagen microsphere: theory and model simulation. *Journal of Biomechanics* **37,** 1709–1718 (2004).

41. Ramtani, S., Fernandes-Morin, E. & Geiger, D. Remodeled-matrix contraction by fibroblasts: numerical investigations. *Computers in Biology and Medicine* **32,** 283–296 (2002).

42. Van Kan, J., Segal, A. & Vermolen, F. *Numerical Methods in Scientific Computing* Second (Delft Academic Press, 2014).

43. MATLAB. *versions 9.8.0 (R2020a) and 9.11.0 (R2021b)* (The MathWorks Inc., 2010).

44. Egberts, G., Smits, D., Vermolen, F. & van Zuijlen, P. in *Lecture Notes in Computational Science and Engineering* 1119–1127 (Springer International Publishing, 2020).

45. Dziuk, G. & Elliot, C. Finite elements on evolving surfaces. *IMA Journal of Numerical Analysis* **27,** 262–292 (2007).

46. Möller, M., Kuzmin, D. & Kourounis, D. Implicit FEM-FCT algorithms and discrete Newton methods for transient convection problems. *International Journal for Numerical Methods in Fluids* **57,** 761–792 (2008).

47. Sadd, M. *Elasticity: Theory, applications, and numerics* Chapter 6 (Elsevier / Academic Press, Amsterdam Boston, 2014).

48. Fletcher, C. *Computational Techniques for Fluid Dynamics 1* (Springer Berlin Heidelberg, 1998).

49. Egberts, G., Vermolen, F. & van Zuijlen, P. Stability of a one-dimensional morphoelastic model for post-burn contraction. *Journal of Mathematical Biology* **83** (2021).

50. Alberts, B. *e.a. The molecular biology of the cell* Second (Garland Publishing, 1989).

51. Ghosh, K. *e.a.* Cell adaptation to a physiologically relevant ECM mimic with different viscoelastic properties. *Biomaterials* **28,** 671–679 (2007).

52. Moulin, V., Mayrand, D., Laforce-Lavoie, A., Larochelle, S. & Genest, H. *Regenerative medicine and tissue engineering - cells and biomaterials* 195–208 (IntechOpen, 2011).

53. Sillman, A. *e.a.* Human dermal fibroblasts do not exhibit directional migration on collagen I in direct-current electric fields of physiological strength. *Experimental Dermatology* **12,** 396–402 (2003).

54. Haugh, J. Deterministic model of dermal wound invasion incorporating receptor-mediated signal transduction and spatial gradient sensing. *Biophysical Journal* **90,** 2297–2308 (2006).

55. Murphy, K., Hall, C., Maini, P., McCue, S. & MacElwain, D. A fibrocontractive mechanochemical model of dermal wound closure incorporating realistic growth factor kinetics. *Bulletin of Mathematical Biology* **74,** 1143–1170 (2012).

56. Gosh, K. *e.a.* Cell adaptation to a physiologically relevant ECM mimic with different viscoelastic properties. *Biomaterials* **28,** 671–679 (2007).

57. Strutz, F. *e.a.* TGF-β1 induces proliferation in human renal fibroblasts via induction of basic fibroblast growth factor (FGF-2). *Kidney International* **59,** 579–592 (2001).

58. Grotendorst, G. in. 1ste ed. In: Cohen 1, Diegelmann R, Lindblad W (eds) Wound healing: biochemical and clinical aspects, 237–246 (W.B. Saunders, Philidelphia, Pennsylvania, 1992).

59. Roberts, A. *e.a.* Transforming growth factor type beta: rapid induction of fibrosis and angiogenesis in vivo and stimulation of collagen formation in vitro. *Proceedings of the National Academy of Sciences* **83,** 4167–4171 (1986).

60. Rudolph, R. & Vande Berg, J. The myofibroblast in Dupuytren's contracture. *Journal of Hand Clinics* **7.** Discussion 693-4, 683–692 (1991).

61. Koppenol, D., Vermolen, F. & Niessen, F. A mathematical model for the simulation of the formation and the subsequent regression of hypertrophic scar tissue after dermal wounding. *Biomechanics and Modeling in Mechanobiology* **16,** 15–32 (2017).

62. Icrp. *ICRP Publication 110* Table A.1 p. 51. 168 p. ISBN: 0702041866 (SAGE Publications Ltd, 2010).

63. Egberts, G., Vermolen, F. & van Zuijlen, P. Sensitivity and feasibility of a one-dimensional morphoelastic model for post-burn contraction. *Biomechanics and Modeling in Mechanobiology* **20,** 2147–2167 (2021).

64. Maskarinec, S., Franck, C., Tirell, D. & Ravichandran, G. Quantifying cellular traction forces in three dimensions. *Proceedings of the National Academy of Sciences* **106,** 22108–22113 (2009).

65. Wrobel, L. *e.a.* Contractility of single human dermal myofibroblasts and fibroblasts. *Cell Motility and the Cytoskeleton* **52,** 82–90 (2002).

66. Tuan, T. & Nichter, L. The molecular basis of keloid and hypertrophic scar formation. *Molecular Medicine Today* **4,** 19–24 (1998).

67. Zhang, T. *e.a.* Current potential therapeutic strategies targeting the TGF-β/Smad signaling pathway to attenuate keloid and hypertrophic scar formation. *Biomedicine & Pharmacotherapy* **129,** 110287 (2020).

68. Egberts, G., Vermolen, F. & van Zuijlen, P. Stability of a two-dimensional biomorphoelastic model for post-burn contraction. *Journal of Mathematical Biology* **86** (2023).

69. Caroli, B., Caroli, C. & Roulet, B. The Mullins-Sekerka instability in directional solidification of thin samples. *Journal of Crystal Growth* **76,** 31–49 (1986).

70. Liang, X. & Boppart, S. Biomechanical properties of in vivo human skin from dynamic optical coherence elastography. *IEEE Transactions on Biomedical Engineering* **57,** 953–959 (2010).

71. Simpson, R. *e.a.* Age-related changes in pericellular hyaluronan organization leads to impaired dermal fibroblast to myofibroblast differentiation. *The American Journal of Pathology* **175,** 1915–1928 (2009).

72. Miller, C. *e.a.* Validation of a morphometric method for evaluating fibroblast numbers in normal and pathologic tissues. *Experimental Dermatology* **12,** 403–411 (2003).

73. T. Brown, K. K. Histology, Dermis (jan 2023). ppublish.

74. Harper, R. & Grove, G. Human skin fibroblasts derived from papillary and reticular dermis: differences in growth potential in vitro. *Science* **204,** 526–527 (1979).

75. Randolph, R. & Simon, M. Dermal fibroblasts actively metabolize retinoic acid but not retinol. *Journal of Investigative Dermatology* **111,** 478–484 (1998).

76. Gunin, G., Kornilova, N., Petrov, V. & Vasilyeva, O. Age changes in the number and proliferation of fibroblasts in the human skin. *Advances in Gerontology* **1,** 299–303 (2011).

77. Farage, M., Miller, K. & Maibach, H. in *Textbook of Aging Skin* 1–18 (Springer Berlin Heidelberg, 2015).

78. Simpson, M., Lo, K. & Sun, Y. Quantifying the roles of random motility and directed motility using advection-diffusion theory for a 3T3 fibroblast cell migration assay stimulated with an electric field. *BMC Syste* **11,** 39 (2017).

79. Wakefield, L. *e.a.* Recombinant latent transforming growth factor β1 has a longer plasma half-life in rats than active transforming growth factor β1, and a different tissue distribution. *Journal of Clinical Investigation* **86,** 1976–1984 (1990).

80. Bowen-Pope, D., Malpass, T., Foster, D. & Ross, R. Platelet-derived growth factor in vivo: levels, activity, and rate of clearance. *Blood* **64,** 458–469 (1984).

81. Javierre, E., Moreo, P., Doblaré, M. & García-Aznar, J. Numerical modeling of a mechano-chemical theory for wound contraction analysis. *International Journal of Solids and Structures* **46,** 3597–3606 (2009).

82. Yang, L., Qiu, C., Ludow, A., Ferguson, M. & Brunner, G. Active transforming growth factor-beta in wound repair. *The American Journal of Pathology* **154,** 105–111 (1999).

83. Ashcroft, G. *e.a.* Age-related differences in the temporal and spatial regulation of matrix metalloproteinases (MMPs) in normal skin and acute cutaneous wounds of healthy humans. *Cell and Tissue Research* **290,** 581–591 (1997).

84. Azzarone, B., Failly-Crepin, C., Day-Garosjean, L., Chaponnier, C. & Gabbiani, G. Abnormal behavior of cultured fibroblasts from nodule and nonaffected aponeurosis of Dupuytrens disease. *Journal of Cellular Physiology* **117,** 353–361 (1983).

85. Moulin, V. *e.a.* Normal skin wound and hypertrophic scar myofibroblasts have differential responses to apoptotic inductors. *Journal of Cellular Physiology* **198,** 350–358 (2003).

86. Xu, F. & Tianjian, L. *Introduction to skin biothermomechanics and thermal pain* (Springer, 2011).

87. Pawlaczyk, M., Lelonkiewicz, M. & Wieczorowski, M. Age-dependent biomechanical properties of the skin. *Advances in Dermatology and Allergology* **5,** 302–306 (2013).

88. Pond, D., McBride, A., Davids, L., Reddy, B. & Limbert, G. Microstructurally-based constitutive modelling of the skin-linking intrinsic ageing to microstructural parameters. *Journal of Theoretical Biology* **444,** 108–123 (2018).

89. Krueger, N. & Luebberding, S. in, 309–317 (Springer-Verlag Berlin Heidelberg, 2017).

90. Wiegand, C., Raschke, C. & Elsner, P. in *Textbook of Aging Skin* (red. Farage, M., Miller, K. & Maibach, H.) 55–65 (Springer Berlin Heidelberg, Berlin, Heidelberg, 2017). ISBN: 978-3-662-47398-6.

91. Egberts, G., Desmoulière, A., Vermolen, F. & van Zuijlen, P. Sensitivity of a two-dimensional biomorphoelastic model for post-burn contraction. *Biomechanics and Modeling in Mechanobiology* **22,** 105–121 (2022).

92. Koko, J. A Matlab mesh generator for the two-dimensional finite element method. *Applied Mathematics and Computation* **250,** 650–664 (2015).

93. Li, C., Huang, Z. & Wang, R. K. Elastic properties of soft tissue-mimicking phantoms assessed by combined use of laser ultrasonics and low coherence interferometry. *Optics Express* **19,** 10153 (2011).

94. Braess, D. Finite elements: theory, fast solvers and applications in solid mechanics. *Measurement Science and Technology* **13,** 1500–1500 (2002).

95. Hinz, B. & Lagares, D. Evasion of apoptosis by myofibroblasts: a hallmark of fibrotic diseases. *Nature Reviews Rheumatology* **16,** 11–31 (2019).

96. Funahashi, K. On the approximate realization of continuous mappings by neural networks. *Neural Networks* **2,** 183–192 (1989).

97. Tran, H., Le, T. & Nguyen, T. The degree of skin burns images recognition using convolutional neural network. *Indian Journal of Science and Technology* **9** (2016).

98. Mohsen, H., El-Dahshan, E., El-Horbaty, E. & Salem, A. Classification using deep learning neural networks for brain tumors. *Future Computing and Informatics Journal* **3,** 68–71 (2018).

99. Brinati, D. *e.a.* Detection of COVID-19 infection from routine blood exams with machine learning: a feasibility study. *Journal of Medical Systems* **44** (2020).

100. Wang, S. *e.a.* Massive computational acceleration by using neural networks to emulate mechanism-based biological models. *Nature Communications* **10** (2019).

101. Yang, C., Kim, Y., Ryu, S. & Gu, G. Prediction of composite microstructure stress-strain curves using convolutional neural networks. *Materials & Design* **189,** 108509 (2020).

102. Navrátil, J. *e.a.* Accelerating physics-based simulations using end-to-end neural network proxies: an application in oil reservoir modeling. *Frontiers in Big Data* **2** (2019).

103. Krasnopolsky, V. M. & Chevallier, F. Some neural network applications in environmental sciences. Part II: advancing computational efficiency of environmental numerical models. *Neural Networks* **16,** 335–348 (2003).

104. Raduly, B., Capodaglio, A. G., Lindblom, E. & Gernaey, K. V. *Model reduction using neural networks applied to the modeling of integrated urban wastewater systems* in *ECMS 2006 Proceedings edited by: W. Borutzky, A. Orsoni, R. Zobel* (ECMS, 2006).

105. Amini, S. & Mohaghegh, S. Application of machine learning and artificial intelligence in proxy modeling for fluid flow in porous media. *Fluids* **4,** 126 (2019).

106. Eichinger, M., Heinlein, A. & Klawonn, A. *Stationary flow predictions using convolutional neural networks* tech. rap. (Center for Data en Simulation Science, 2019).

107. Guo, X., Li, W. & Iorio, F. *Convolutional neural networks for steady flow approximation* in *Proceedings of the 22nd ACM SIGKDD International Conference on Knowledge Discovery and Data Mining* (ACM, 2016).

108. Egberts, G., Schaaphok, M., Vermolen, F. & van Zuijlen, P. A Bayesian finite-element trained machine learning approach for predicting post-burn contraction. *Neural Computing and Applications* **34,** 8635–8642 (2022).

109. Glorot, X. & Bengio, Y. *Understanding the difficulty of training deep feedforward neural networks* in *Proceedings of the 13th International Conference on Artificial Intelligence and Statistics* **9** (2010).

110. Rumelhart, D., Hinton, G. & Williams, R. Learning representations by back-propagating errors. *Nature* **323,** 533–536 (1986).

111. Borchani, H., Varando, G., Bielza, C. & Larrañaga, P. A survey on multi-output regression. *Wiley Interdisciplinary Reviews: Data Mining and Knowledge Discovery* **5,** 216–233 (2015).

112. Despotovic, M., Nedic, V., Despotovic, D. & Cvetanovic, S. Evaluation of empirical models for predicting monthly mean horizontal diffuse solar radiation. *Renewable and Sustainable Energy Reviews* **56,** 246–260 (2016).

113. Egberts, G., Vermolen, F. & van Zuijlen, P. High-speed predictions of post-burn contraction using a neural network trained on 2D-finite element simulations. *Frontiers in Applied Mathematics and Statistics* **9** (2023).

114. Viceconti, M., Olsen, S., Nolte, L.-P. & Burton, K. Extracting clinically relevant data from finite element simulations. *Clinical Biomechanics* **20,** 451–454 (2005).

115. Clark, A., Imran, J., Madni, T. & Wolf, S. Nutrition and metabolism in burn patients. *Burns & Trauma* **5** (2017).

116. Kalra, A. & Lowe, A. An overview of factors affecting the skins uoungs modulus. *Journal of Aging Science* **4** (2016).

117. Van de Water, L., Varney, S. & Tomasek, J. Mechanoregulation of the myofibroblast in wound contraction, scarring, and fibrosis: opportunities for new therapeutic intervention. *Advances in Wound Care* **2,** 122–141 (2013).

118. Valero, C., Javierre, E., García-Aznar, J. & Gómez-Benito, M. A cell-regulatory mechanism involving feedback between contraction and tissue formation guides wound healing progression. *PLoS ONE* **9,** 92774 (2014).

119. Van der Veer, W. *e.a.* Time course of the angiogenic response during normotrophic and hypertrophic scar formation in humans. *Wound Repair and Regeneration* **19,** 292–301 (2011).

120. Ladak, A. & Tredget, E. Pathophysiology and management of the burn scar. *Clinics in Plastic Surgery* **36,** 661–674 (2009).

121. Gauglitz, G., Korting, H., Pavicic, T., Ruzicka, T. & Jeschke, M. Hypertrophic scarring and keloids: pathomechanisms and current and emerging treatment strategies. *Molecular Medicine* **17,** 113–125 (2010).

122. Friedstat, J. & Hultman, C. Hypertrophic burn scar management. *Annals of Plastic Surgery* **72,** S198–S201 (2014).

123. Rössler, S. *e.a.* In vivo models for hypertrophic scars: a systematic review. *Medicina* **58,** 736 (2022).

124. Torres, M., Trexler, E., Smith-Ryan, A. & Reynolds, A. A mathematical model of the effects of resistance exercise-induced muscle hypertrophy on body composition. *European Journal of Applied Physiology* **118,** 449–460 (2017).

125. Herold, J. & Sommer, A. A mathematical model-based approach to optimize loading schemes of isometric resistance training sessions. *Sports Engineering* **24** (2020).

126. Chiang, R. *e.a.* Current concepts related to hypertrophic scarring in burn injuries. *Wound Repair and Regeneration* **24,** 466–477 (2016).

127. Koppenol, D. *e.a.* A mathematical model for the simulation of the contraction of burns. *Journal of Mathematical Biology* **75,** 1–31 (2017).

128. Amadeu, T. *e.a.* Vascularization pattern in hypertrophic scars and keloids: a stereological analysis. *Pathology - Research and Practice* **199,** 469–473 (2003).

129. Guerra, A., Belinha, J. & Jorge, R. Modelling skin wound healing angiogenesis: a review. *Journal of Theoretical Biology* **459,** 1–17 (2018).

130. Sun, S., Wheeler, M., Obeyesekere, M. & Junior, C. Nonlinear behaviors of capillary formation in a deterministic angiogenesis model. *Nonlinear Analysis: Theory, Methods & Applications* **63,** 2237–2246 (2005).

131. Machado, M. *e.a.* Dynamics of angiogenesis during wound gealing: a coupled in vivo and in silico study. *Microcirculation* **18,** 183–197 (2011).

132. Bookholt, F., Monsuur, H., Gibbs, S. & Vermolen, F. Mathematical modelling of angiogenesis using continuous cell-based models. *Biomechanics and Modeling in Mechanobiology* **15,** 1577–1600 (2016).

133. Pillay, S., Byrne, H. & Maini, P. Modeling angiogenesis: a discrete to continuum description. *Physical Review E* **95,** 012410 (2017).

134. Korkmaz, I. *The local and systemic inflammatory responses after burn* proefschrift (Vrije Universiteit, 2019).

135. Jeschke, M. *e.a.* Burn size determines the inflammatory and hypermetabolic response. *Critical Care* **11,** R90 (2007).

136. Peng, Q. & Vermolen, F. Upscaling between an agent-based model (smoothed particle approach) and a continuum-based model for skin contractions. *Journal of Mathematical Biology* **85** (2022).

137. Sherratt, J. & Murray, J. Models of epidermal wound healing. *Proceedings of the Royal Society of London,* 29–36 (1990).

138. Wearing, H. & Sherratt, J. Keratinocyte growth factor signalling: a mathematical model of dermal–epidermal interaction in epidermal wound healing. *Mathematical Biosciences* **165,** 41–62 (2000).

139. Vermolen, F. & Javierre, E. A finite-element model for healing of cutaneous wounds combining contraction, angiogenesis and closure. *Journal of Mathematical Biology* **65,** 967–996 (2011).

140. Wang, Y. *e.a.* A multiscale hybrid mathematical model of epidermal-dermal interactions during skin wound healing. *Experimental Dermatology* **28,** 493–502 (2019).

141. Hinz, B., Mastrangelo, D., Iselin, C., Chaponnier, C. & Gabbiani, G. Mechanical tension controls granulation tissue contractile activity and myofibroblast differentiation. *The American Journal of Pathology* **159,** 1009–1020 (2001).

142. Gabbiani, G., Ryan, G. & Majno, G. Presence of modified fibroblasts in granulation tissue and their possible role in wound contraction. *Experientia* **27,** 549–550 (1971).

143. Rousselle, P., Montmasson, M. & Garnier, C. Extracellular matrix contribution to skin wound re-epithelialization. *Matrix Biology* **75-76,** 12–26 (2019).

144. Serini, G. *e.a.* The fibronectin domain ED-A is crucial for myofibroblastic phenotype induction by transforming growth factor-β1. *Journal of Cell Biology* **142,** 873–881 (1998).

145. Vaughan, M., Howard, E. & Tomasek, J. Transforming growth factor-β1 promotes the morphological and functional differentiation of the myofibroblast. *Experimental Cell Research* **257,** 180–189 (2000).

146. Brown, R. Enhanced fibroblast contraction of 3D collagen lattices and integrin expression by TGF-β1 and -β3: mechanoregulatory growth factors? *Experimental Cell Research* **274,** 310–322 (2002).

147. Bershadsky, A., Balaban, N. & Geiger, B. Adhesion-dependent cell mechanosensitivity. *Annual Review of Cell and Developmental Biology* **19,** 677–695 (2003).

148. Wang, J., Zohar, R. & McCulloch, C. Multiple roles of α-smooth muscle actin in mechanotransduction. *Experimental Cell Research* **312,** 205–214 (2006).

149. Van Putten, S., Shafieyan, Y. & Hinz, B. Mechanical control of cardiac myofibroblasts. *Journal of Molecular and Cellular Cardiology* **93,** 133–142 (2016).

150. Provenzano, P. *e.a.* Collagen density promotes mammary tumor initiation and progression. *BMC Medicine* **6** (2008).

151. Wipff, P.-J., Rifkin, D., Meister, J.-J. & Hinz, B. Myofibroblast contraction activates latent TGF-β1 from the extracellular matrix. *Journal of Cell Biology* **179,** 1311–1323 (2007).

152. Desmoulière, A., Badid, C., Bochaton-Piallat, M.-L. & Gabbiani, G. Apoptosis during wound healing, fibrocontractive diseases and vascular wall injury. *The International Journal of Biochemistry & Cell Biology* **29,** 19–30 (1997).

153. Aarabi, S. *e.a.* Mechanical load initiates hypertrophic scar formation through decreased cellular apoptosis. *The FASEB Journal* **21,** 3250–3261 (2007).

154. Gurtner, G. *e.a.* Improving cutaneous scar formation by controlling the mechanical environment. *Annals of Surgery* **254,** 217–225 (2011).

155. Moreo, P., García-Aznar, J. M. & Doblaré, M. Modeling mechanosensing and its effect on the migration and proliferation of adherent cells. *Acta Biomaterialia* **4,** 613–621 (2008).

156. Rassier, D., MacIntosh, B. & Herzog, W. Length dependence of active force production in skeletal muscle. *Journal of Applied Physiology* **86,** 1445–1457 (1999).

157. Gordon, A., Huxley, A. & Julian, F. The variation in isometric tension with sarcomere length in vertebrate muscle fibres. *The Journal of Physiology* **184,** 170–192 (1966).

158. Walker, S. & Schrodt, G. I segment lengths and thin filament periods in skeletal muscle fibers of the rhesus monkey and the human. *The Anatomical Record* **178,** 63–81 (1974).

159. Godt, R. & Maughan, D. Influence of osmotic compression on calcium activation and tension in skinned muscle fibers of the rabbit. *Pflügers Archiv - European Journal of Physiology* **391,** 334–337 (1981).

160. Caley, M., Martins, V. & O'Toole, E. Metalloproteinases and wound healing. *Advances in Wound Care* **4,** 225–234 (2015).

161. Schmoldt, A., Benthe, H. & Haberland, G. Digitoxin metabolism by rat liver microsomes. *Biochemical pharmacology* **24,** 1639–1641. ISSN: 1873-2968 (1975). ppublish.

162. Legrand, C. *e.a.* Airway epithelial cell migration dynamics: MMP-9 role in cell-extracellular matrix remodeling. *Journal of Cell Biology* **146,** 517–529 (1999).

163. Vu, T. & Werb, Z. in *Matrix Metalloproteinases* 115–148 (Elsevier, 1998).

164. Agren, M. Gelatinase activity during wound healing. *British Journal of Dermatology* **131,** 634–640 (1994).

165. Stricklin, G., Li, L. & Nanney, L. Localization of mRNAs representing interstitial collagenase, 72-kDa gelatinase, and TIMP in healing porcine burn wounds. *Journal of Investigative Dermatology* **103,** 352–358 (1994).

166. Keck, M. *e.a.* Construction of a multi-layer skin substitute: simultaneous cultivation of keratinocytes and preadipocytes on a dermal template. *Burns* **37,** 626–630 (2011).

167. Böttcher-Haberzeth, S., Biedermann, T. & Reichmann, E. Tissue engineering of skin. *Burns* **36,** 450–460 (2010).

168. Gay, S. *e.a.* Immunohistochemical evidence for the presence of collagen type III in human arterial walls, arterial thrombi, and in leukocytes, incubated with collagen in vitro. *Klinische Wochenschrift* **53,** 899–902 (1975).

169. Bailey, A., Sims, T., Lous, M. L. & Bazin, S. Collagen polymorphism in experimental granulation tissue. *Biochemical and Biophysical Research Communications* **66,** 1160–1165 (1975).

170. Shuttleworth, C., Forrest, L. & Jackson, D. Comparison of the cyanogen bromide peptides of insoluble guinea-pig skin and scar collagen. *Biochimica et Biophysica Acta (BBA) - Protein Structure* **379,** 207–216 (1975).

171. Dorin, R., Pohl, H., Filippo, R. D., Yoo, J. & Atala, A. Tubularized urethral replacement with unseeded matrices: What is the maximum distance for normal tissue regeneration? *World Journal of Urology* **26,** 323–326 (2008).

172. Atala, A., Irvine, D., Moses, M. & Shaunak, S. Wound healing versus regeneration: role of the tissue environment in regenerative medicine. *MRS Bulletin* **35,** 597–606 (2010).

173. Van Zuijlen, P. *e.a.* Collagen morphology in human skin and scar tissue: no adaptations in response to mechanical loading at joints. *Burns* **29,** 423–431 (2003).

174. Olsen, L., Maini, P., Sherratt, J. & Dallon, J. Mathematical modelling of anisotropy in fibrous connective tissue. *Mathematical Biosciences* **158,** 145–170 (1999).

175. Cumming, B., McElwain, D. & Upton, Z. A mathematical model of wound healing and subsequent scarring. *Journal of The Royal Society Interface* **7,** 19–34 (2009).

176. Koppenol, D., Vermolen, F., Niessen, F., van Zuijlen, P. & Vuik, K. A biomechanical mathematical model for the collagen bundle distribution-dependent contraction and subsequent retraction of healing dermal wounds. *Biomechanics and Modeling in Mechanobiology* **16,** 345–361 (2016).

177. Guido, S. & Tranquillo, R. A methodology for the systematic and quantitative study of cell contact guidance in oriented collagen gels. Correlation of fibroblast orientation and gel birefringence. *Journal of Cell Science* **105,** 317–331 (1993).

178. Barion, A. *An isogeometric analysis approach for morphoelastic models - application to skin contractures* masterscriptie (Delft University of Technology, 2020).

179. Mees, M., Pourtois, G., Neyts, E., Thijsse, B. & Stesmans, A. Uniform-acceptance force-bias Monte Carlo method with time scale to study solid-state diffusion. *Physical Review B* **85,** 134301 (2012).

180. Xiu, D. in *Handbook of Uncertainty Quantification* 1–18 (Springer International Publishing, 2015).

181. Mousavi, S. & Mosavi, S. *A new edge and pixel-based image quality assessment metric for colour and depth images* in *2022 9th Iranian Joint Congress on Fuzzy and Intelligent Systems (CFIS)* (IEEE, 2022).

182. Stojadinovic, O., Ito, M. & Tomic-Canic, M. Hair cycling and wound healing: to pluck or not to pluck? *Journal of Investigative Dermatology* **131,** 292–294 (2011).

183. Heidari, F. *e.a.* Bulge hair follicle stem cells accelerate cutaneous wound healing in rats. *Wounds : a compendium of clinical research and practice* **28,** 132–141. ISSN: 1943-2704 (2016). ppublish.

184. Andreou, I. & Sgouros, N. Computing, explaining and visualizing shape similarity in content-based image retrieval. *Information Processing & Management* **41,** 1121–1139 (2005).

185. Veltkamp, R. *Shape matching: similarity measures and algorithms* in *Proceedings International Conference on Shape Modeling and Applications* (IEEE Computer Society, 2001).

186. Humber, M., Boschetti, L. & Giglio, L. Assessing the shape accuracy of coarse resolution burned area identifications. *IEEE Transactions on Geoscience and Remote Sensing* **58,** 1516–1526 (2020).

187. Bimbo, A. & Pala, P. *Shape indexing by structural properties* in *Proceedings of IEEE International Conference on Multimedia Computing and Systems* (IEEE Comput. Soc, 1997).

188. Hochreiter, S. & Schmidhuber, J. Long short-term memory. *Neural Computation* **9,** 1735–1780 (1997).

189. Graves, A. & Schmidhuber, J. Framewise phoneme classification with bidirectional LSTM and other neural network architectures. *Neural Networks* **18,** 602–610 (2005).

190. Silver, D. & Bennett, K. Guest editor's introduction: special issue on inductive transfer learning. *Machine Learning* **73,** 215–220 (2008).

191. Grimm, V., Heinlein, A., Klawonn, A., Lanser, M. & Weber, J. Estimating the time-dependent contact rate of SIR and SEIR models in mathematical epidemiology using physics-informed neural networks. *ETNA - Electronic Transactions on Numerical Analysis* **56,** 1–27 (2021).

192. Bergstra, J., Komer, B., Eliasmith, C., Yamins, D. & Cox, D. Hyperopt: a Python library for model selection and hyperparameter optimization. *Computational Science & Discovery* **8,** 014008 (2015).

List of Publications

Articles

1. **Egberts G.**, Smits D., Vermolen F., Van Zuijlen P. (2020) Some mathematical properties of morphoelasticity. *Lecture Notes in Computational Science and Engineering, Springer International Publishing*, p. 1119–1127.

2. **Egberts G.**, Vermolen F., Van Zuijlen P. (2021) Sensitivity and feasibility of a one-dimensional morphoelastic model for post-burn contraction. *Biomechanics and Modeling in Mechanobiology*, **20**, 2147–2167

3. **Egberts G.**, Vermolen F., Van Zuijlen P. (2021) Stability of a one-dimensional morphoelastic model for post-burn contraction. *Journal of Mathematical Biology*, **83**, article 24

4. **Egberts G.**, Schaaphok M., Vermolen F., Van Zuijlen P. (2022) A Bayesian finite-element trained machine learning approach for predicting post-burn contraction. *Neural Computing and Applications*, **34**, 8635–8642

5. **Egberts G.**, Desmoulière A., Vermolen F., Van Zuijlen P. (2023) Sensitivity of a two-dimensional biomorphoelastic model for post-burn contraction. *Biomechanics and Modeling in Mechanobiology* , **22**, 105–121

6. **Egberts G.**, Vermolen F., Van Zuijlen P. (2023) High-speed predictions of post-burn contraction using a neural network trained on 2D-finite element simulations. *Frontiers in Applied Mathematics and Statistics*, **9**, 1098242

7. **Egberts G.**, Vermolen F., Van Zuijlen P. (2023) Stability of a two-dimensional morphoelastic model for post-burn contraction. *Journal of Mathematical Biology*, **86**, article 59

8. **Egberts G.**, Vermolen F., Peng Q., Korkmaz H., Van Zuijlen P. How can mathematics be used to improve burn care? (in progress)

Online resources

1. Egberts G., Vermolen F., Van Zuijlen P. Data supporting the paper: Stability of a one-dimensional morphoelastic model for post-burn contraction. *4TU.ResearchData*, **2023**

2. Egberts G., Vermolen F., Van Zuijlen P. Code supporting the paper: Stability of a one-dimensional morphoelastic model for post-burn contraction. *4TU.ResearchData*, **2023**

3. Egberts G., Vermolen F., Van Zuijlen P. Data supporting the paper: Sensitivity and feasibility of a one-dimensional morphoelastic model for post-burn contraction. *4TU.ResearchData*, **2023**

4. Egberts G., Vermolen F., Van Zuijlen P. Code supporting the paper: Sensitivity and feasibility of a one-dimensional morphoelastic model for post-burn contraction. *4TU.ResearchData*, **2023**

5. Egberts G., Vermolen F., Van Zuijlen P. Code supporting the paper: A Bayesian finite-element trained machine learning approach for predicting post-burn contraction. *4TU.ResearchData*, **2023**

6. Egberts G., Desmoulière A., Vermolen F., Van Zuijlen P. Data supporting the paper: Sensitivity of a two-dimensional biomorphoelastic model for post-burn contraction. *4TU.ResearchData*, **2023**

7. Egberts G., Desmoulière A., Vermolen F., Van Zuijlen P. Code supporting the paper: Sensitivity of a two-dimensional biomorphoelastic model for post-burn contraction. *4TU.ResearchData*, **2023**

8. Egberts G., Vermolen F., Van Zuijlen P. Code supporting the paper: High-speed predictions of post-burn contraction using a neural network trained on 2D-finite element simulations. *4TU.ResearchData*, **2023**

9. Egberts G., Vermolen F., Van Zuijlen P. Data supporting the paper: Stability of a two-dimensional morphoelastic model for post-burn contraction. *4TU.ResearchData*, **2023**

10. Egberts G., Vermolen F., Van Zuijlen P. Code supporting the paper: Stability of a two-dimensional morphoelastic model for post-burn contraction. *4TU.ResearchData*, **2023**